Advances in Quantitative Precipitation Estimation with Polarimetric C-Band Radar Networks

DISSERTATION
ZUR
ERLANGUNG DES DOKTORGRADES (DR. RER. NAT.)
DER
MATHEMATISCH-NATURWISSENSCHAFTLICHEN FAKULTÄT
DER
RHEINISCHEN FRIEDRICH-WILHELMS-UNIVERSITÄT BONN

vorgelegt von
Ju-Yu Chen
陳如瑜
aus
Kaohsiung City, Taiwan

Bonn, 2023

Diese Arbeit ist die ungekürzte Fassung einer der Mathematisch-Naturwissenschaftlichen Fakultät der Rheinischen Friedrich-Wilhelms-Universität Bonn im Jahr 2023 vorgelegten Dissertation von Ju-Yu Chen aus Kaohsiung City, Taiwan.

This paper is the unabridged version of a dissertation thesis submitted by Ju-Yu Chen born in Kaohsiung City, Taiwan to the Faculty of Mathematical and Natural Sciences of the Rheinischen Friedrich-Wilhelms-Universität Bonn in 2023.

1. Gutachterin: PD Dr. Silke Trömel
2. Gutachter: Prof. Dr. Clemens Simmer

Tag der Promotion: 13 Oct. 2023
Erscheinungsjahr: 2023

Abstract

Areal quantitative precipitation estimation (QPE) with high spatial and temporal resolution is crucial to feed nowcasting and hydrological models. Ground-based weather radars are the best-suited tool for this purpose. Despite the upgrades of the German C-band radar network to polarimetry, the operational QPE products offered by the German Meteorological Service (DWD, Deutscher Wetterdienst) are still based mainly on the traditional radar variable, reflectivity Z, leading to large uncertainties. To enhance QPE quality from DWD radars, this study presents several novel polarimetric QPE algorithms at C-band. These include i) hybrid rainfall estimators based on specific attenuation A and specific differential phase K_{DP}, denoted as $R(A, K_{DP})$, ii) a polarimetric vertical profile of reflectivity (PVPR) correction method for Z biases within and above the melting layer (ML), and iii) a K_{DP}-based snowfall estimator. Additionally, a warm-rain event is investigated to develop approaches that mitigate the impacts of vertical precipitation gradients below the ML on QPE.

The S-band $R(A)$ algorithm has been proven to be a powerful tool for rainfall estimation and has recently been operational in the U.S.A. The attenuation parameter α required for the A calculation, however, is susceptible to the variability of drop size distributions (DSD), which is more accentuated at C-band compared to S-band due to stronger resonance effects. This limits the applicability of $R(A)$ to C-band radars. To overcome this challenge, this study derives DSD-dependent α values based on the slope of differential reflectivity Z_{DR} against Z. Furthermore, in cases of heavy rain where Z > 40 dBZ, the $R(A)$ relationship at C-band becomes relatively sensitive to the DSD variability and therefore $R(K_{DP})$ is used. The resulting hybrid algorithms $R(A, K_{DP})$ surpass in quality the DWD real-time QPE product, particularly for convective rain where the normalized root-mean-square error (NRMSE) is reduced by 13% and the normalized mean bias (NMB) by 16%.

On 14 July 2021, western Europe experienced severe floods caused by intense stratiform precipitation, for which the above rainfall algorithms underestimated surface rain with an NMB of -30% owing to the increased rain rates below the observing altitudes of the operational radars. Since most existing vertical profile of reflectivity (VPR) correction techniques focus on data within and above the ML, this study proposes a vertical profile (VP) correction method that considers vertical precipitation gradients near the surface for both Z and K_{DP}. This correction method involves i) projecting radar observations from the bottom of the ML down to 700 m taking range-defined quasi-vertical profiles (RD-QVP) as references, and ii) deriving rainfall relationships from vertically-pointing radar data in the lower few hundred meters, in order to better capture warm-rain processes. Moreover, observations from a local X-band radar are utilized to fill gaps in the operational radar network. Results show that the VP correction method reduces the NRMSE and NMB values of the estimates by more than 20%, and with the additional use of the gap-filling radar, the $R(A, K_{DP})$ retrievals even outperform the hourly gauge-adjusted QPE product from DWD.

When the radar beam intersects and exceeds the height of the ML, significant errors in surface precipitation estimates are induced due to Z biases caused by partially frozen and clumped hydrometeors within the ML and beam-broadening effects above it. Current VPR

correction approaches mitigating the biases rely solely on Z and do not explore the potential of polarimetry. Here, the - as far as is known - first PVPR correction method for C-band is developed. This method reconstructs the intrinsic VPR and estimates Z biases within and above the ML based on the statistics of polarimetric profiles. For pure and uniform stratiform rain, the rainfall retrieval based on the corrected Z has an up to 20% lower NRMSE value than the hydrometeor-type-specific rainfall retrieval suggested by Giangrande and Ryzhkov (2008); and for estimates above the ML, the PVPR-corrected retrieval is more accurate than the polarimetric snowfall retrieval proposed in this study.

The PVPR correction method is rendered inapplicable when snowfall reaches the ground. Additionally, the accuracy of snowfall estimation using Z is restricted due to the high diversity of snowflakes. To solve this issue, Bukovčić et al. (2020) introduced a generalized polarimetric snowfall estimator using K_{DP} and demonstrated its efficacy with S-band radar observations. This estimator considers changes in the shape and orientation of snowflakes or ice crystals by incorporating an assumed aspect ratio ar and width of the canting angle distribution σ in a power-law snowfall relationship. Our adjustment of the algorithm to C-band yields better estimates than conventional Z-based retrievals, and it additionally mirrors the typically higher ice concentration within the dendritic growth layer (DGL) at higher levels.

The novel QPE algorithms exhibit promising results and hold potential for real-time applications to C-band radar networks throughout Europe. These advancements profit from the strong cooperation with DWD in the program “Near-Realtime Quantitative Precipitation Estimation and Prediction (RealPEP)”. Currently, the algorithms are implemented in DWD’s operational platform “Polarimetric Radar Algorithms (POLARA)” in order to assess their stability, feasibility, and robustness for online applications. In the near future, optimization of the algorithms will continue based on evaluations using long-term databases in POLARA.

Contents

Chapter 1

Introduction

Ground-based weather radars offer core information for areawide quantitative precipitation estimation (QPE) due to their high spatial and temporal resolution. The resulting QPE data serve as input for observation-based nowcasting, data assimilation for short-term weather forecasts, and flash-flood predictions, and are also used for the validation of numerical models (Clark et al. 1972; Sun 2005; Stephan et al. 2008; Zacharov et al. 2010; Saadi et al. 2022). Thus, reliable and timely radar-based QPE is one of the most important tasks for radar meteorologists and hydrologists. Since 2014, the German Meteorological Service (DWD, Deutscher Wetterdienst) has upgraded its C-band radar network to polarimetry. However, the current operational QPE products from DWD, Radar-Online-Aneichung (RADOLAN), still rely mainly on linear reflectivity at horizontal polarization Z_h. Z_h is strongly influenced by the structure of hydrometeor size distributions and measurement errors, which leads to large uncertainties in QPE. Moreover, DWD's most accurate gauge-adjusted product RW is delayed by at least 30 minutes after each completed hour, making it useless for real-time applications. Therefore, polarimetric precipitation retrieval algorithms at C-band are mandatory.

In recent decades, the quality of radar-based QPE has greatly improved through the additional use of polarimetric radar variables, such as differential reflectivity Z_{DR}, specific differential phase K_{DP} (Seliga and Bringi 1976; Zrnić and Ryzhkov 1999; Matrosov et al. 2005a; Steinert et al. 2013), and specific attenuation A (Ryzhkov et al. 2014; Diederich et al. 2015a/b; Chen et al. 2021a). Z_{DR} is indicative of hydrometeor shape and provides information on the average raindrop size within a sampling volume. Phase-based observables such as K_{DP} and A have superiorities for QPE over Z_h and Z_{DR}, as they are less affected by the variability of raindrop size distributions (DSD) or ice particle size distributions (PSD), and immune to radar miscalibration, attenuation, partial beam blockage (PBB), and radome effects. Furthermore, A-based rainfall retrievals, also referred to as $R(A)$, inherit all the advantages of $R(K_{DP})$ but are less noisy or oversmoothed in light rain and comparable in spatial resolution to that of $R(Z_h)$. Despite their restriction to liquid rain, these features make $R(A)$ particularly beneficial for generating seamless rainfall composites derived from radar observations at various wavelengths.

Weather radars are capable of monitoring various types of hydrometeors in the atmosphere, such as rain, graupel/hail, snowflakes/ice crystals, and mixed-phase particles. Therefore, accurately estimating precipitation at the surface requires the consideration of the different hydrometeor types in polarimetric QPE algorithms. This study proposes a set of specific algorithms for C-band that aim to address the challenges associated with the current state of the art in the field. These algorithms include i) hybrid rainfall algorithms $R(A, K_{DP})$, ii) a vertical profile (VP) correction method for reflectivity Z and K_{DP} below the melting layer (ML) and the use of gap-filling radars during warm rain, iii) a polarimetric vertical profile of reflectivity

(PVPR) correction method for observations made within and above the ML, and iv) a snowfall estimator $S(Z_h, K_{DP})$. A summary of the challenges and motivations behind these algorithms is provided below, with a detailed discussion of their historical development to be presented in the following chapter.

QPE below the ML

Rain is the most common precipitation in Germany. Recent advances have demonstrated the benefits of radar-derived A using the ZPHI method [the attenuation correction for measured Z using the total constraint differential phase shift Φ_{DP}, see Testud et al. 2000 and Eqs. (2)-(6) in their paper] for rainfall estimation at S- and X-band (Ryzhkov et al. 2014; Wang et al. 2019; Cocks et al. 2019; Zhang et al. 2020a; Diederich et al. 2015a/b). Wang et al. (2019) first pointed out that the DSD sensitivity of the attenuation parameter α, required to estimate A, needs to be accounted for in the ZPHI method. To this goal, they exploited the change of Z_{DR} with Z - known as the Z_{DR} slope - to derive α values for each radar scan. Trömel et al. (2014a), however, demonstrated that resonance effects related to large raindrops and hail at C-band enhance the dependence of α on the DSD variability, and render its change with Z_{DR} non-monotonic, which further complicates the methodology in addition to the stronger attenuation at this frequency range compared to S-band. Accordingly, only a few research studies on $R(A)$ applications for C-band exist in the literature (Giangrande et al. 2014; Wang et al. 2014 and 2017; Boodoo et al. 2015; Chen et al. 2021a).

Since coefficients in the power-law $R(A)$ relations strongly vary with different DSD types at C-band, Wang et al. (2017) formulated relations for three rain types in Taiwan. In addition, Ryzhkov and Zrnić (2019) compared large DSD datasets from Oklahoma in the U.S.A. and the western Pacific area, and found that $R(K_{DP})$ may outperform $R(A)$ at C-band in heavier continental rain, which contains large raindrops originating from the melting of graupel or hail. Consequently, hybrid estimators $R(A, K_{DP})$ are suggested for C-band to compensate for shortcomings of $R(A)$ algorithms in rain mixed with hail or rain dominated by large resonance-size drops. Note that in hail-contaminated regions, Wang et al. (2019) recommended performing segment-wise integration for pure rain along the rays in the ZPHI method, as this method does not account for the extra attenuation from hail within the rays. Nevertheless, this application may introduce significant errors in QPE due to unreliable Φ_{DP} within a short-range interval.

Advances in radar polarimetry are obstructed by the measurement geometry, wherein precipitation is monitored at greater heights with increasing distance from the radar. This property poses difficulties in estimating rainfall with vertical intensity changes caused by precipitation formation below the lowest radar beam, leading to systematic inaccurate estimates. One example is warm-rain formation (Porcacchia et al. 2017) whose occurrence rate increases due to global warming (IPCC 2022). Simulations by Kumjian et al. (2014) showed that during the coalescence-dominated growth process, the radar variables Z, Z_{DR}, and K_{DP} increase towards the ground as mass from cloud drops or drizzle is shifted to larger particles. Rainfall estimates are then negatively biased and thus might fail to activate flooding alerts. McLaughlin et al. (2009) and Antonini et al. (2017) demonstrated that a denser network composed of small X-band radars could act as cost-effective gap fillers, with increased low-altitude coverage and finer spatial resolution compared to current operational networks.

Vertical profile of reflectivity (VPR) corrections also reduce biases resulting from the uncaptured vertical variability of precipitation intensity below radar observation heights via near-surface Z estimates using observation- or model-based profile information (Koistinen 1991; Kitchen et al. 1994; Seo et al. 2000; Germann and Joss 2002; Matrosov et al. 2007; Anagnostou et al. 2010; Zhang and Qi 2010). The majority of existing VPR correction methods, however, assume a constant Z from the ML height down to the ground, disregarding potential precipitation-generating processes below the ML, and only correct Z biases within and above the ML (Andrieu and Creutin 1995; Matrosov et al. 2007). Additionally, most reference profiles rely on climatology, which may not adequately handle extreme cases. Chen et al. (2020) introduced one of the first VPR corrections aimed at addressing vertical Z gradients below the ML for QPE. They employed Z observations from vertically-pointing profilers located in four zones with different hydrological properties as references for the VPR correction, leading to a halved bias in QPE. Any similar corrections for radar polarimetry, however, had not been explored until the recent work of Chen et al. (2022), which will be presented in detail later in this dissertation.

QPE within and above the ML

A perennial issue confronting radar-based QPE is rainfall estimation at ranges where the radar signals intersect or pass through the ML. The ML contains mixed-phase particles, which result in enhanced Z, known as the bright band (BB), leading to a significant overestimation of surface rain. When the beam overshoots the ML and progressive beam-broadening effects distort the profiles of radar observables, rainfall is considerably underestimated. These Z biases require correction before observations aloft are used to estimate surface precipitation. Multiple attempts exist to address this problem through the reconstruction of intrinsic VPR, but none of them utilizes polarimetry to their full potential.

When snowfall reaches the ground, QPE becomes even more challenging because of the intricate microphysical properties of hydrometeors associated with density, shape, orientation, etc. Therefore, researchers utilized a number of Z_h -based algorithms for different climatological regions or snow types with different success (Matrosov 2007; Liu 2008; Kulie and Bennartz 2009; Matrosov et al. 2009; Hiley et al. 2011; Wolfe and Snider 2012; Huang et al. 2015; von Lerber et al. 2017; Cooper et al. 2017). Nevertheless, using Z_h alone still limits the accuracy of the estimates due to its high uncertainty in the face of snowflake diversity. Recently, Bukovčić et al. (2020) investigated the effect of snow diversity on the polarimetric variables and proposed a combination of Z_h and K_{DP} for snowfall estimation, which led to improvements for the S-band radar network in the U.S.A. However, concerns remain regarding the use of K_{DP} owing to the expected loss of K_{DP} information towards the surface, resulting from increasing randomness of snowflake orientation and decreasing density. While the advantages of this approach have not yet been showcased at C-band, the higher magnitude of K_{DP}, at least 2-3 times higher than that of S-band, makes it in principle more exploitable at C-band.

The central objective of this study is to improve the QPE quality of DWD's countrywide C-band polarimetric radar network through the application of innovative techniques with the potential for real-time operation. To begin with, rainfall relations are optimized using locally measured DSDs. Next, challenges specific to C-band radar and observational limitations during

warm-rain processes are thoroughly examined and taken into account while developing the rainfall algorithms. Furthermore, the potential of polarimetry is explored and expanded for snow quantification. Finally, the efficacy of the algorithms is assessed by their application to several precipitation events, validation against ground-based measurements, and comparison with the benchmark algorithms and DWD QPE products. In Chapter 2, the fundamental knowledge of radar-based QPE, such as DSD/PSD, radar polarimetry, potential error sources that affect QPE performance, and the evolution of QPE algorithms, are introduced. Chapter 3 describes the data sources used and their processing, while Chapter 4 elaborates on the methodologies for estimating liquid, mixture, and solid precipitation, as well as their assessment. The application of the algorithms to diverse precipitation events and a discussion on their benefits, drawbacks, and possible improvements are presented in Chapters 5 and 6, respectively. Chapter 7 concludes the study with key findings and provides an outlook.

Chapter 2

Basics of Radar Polarimetry and To-Date Precipitation Retrievals

The development and understanding of radar-based QPE reside in the connections between hydrometeor size distribution, meteorological integral parameters such as rain/snow rates, and several polarimetric radar variables. This chapter provides an introduction to these relationships, followed by an overview of potential error sources in radar-based QPE and their corresponding solutions. Subsequently, it reviews the history and current state-of-the-art of radar-based QPE algorithms, helping readers grasp the direction and focus of this research. For more in-depth and thorough interpretations of radar polarimetry and its relevance, the monographs authored by Bringi and Chandrasekar (2001), Zhang (2016), and Ryzhkov and Zrnić (2019) are highly recommended.

2.1 Hydrometeor size distribution

The discussion on the characteristics of hydrometeor size distribution involves the consideration of the hydrometeor phase. The DSD refers to the number concentration of raindrops at given diameter sizes within a volume and is expressed as

$$N(D) = \int_{D_{min}}^{D_{max}} N(D) dD, \tag{2.1}$$

where $N(D)$ is the volume density of drops per unit drop diameter in $m^{-3}mm^{-1}$; D is the diameter of drops in mm. The minimum diameter of drizzle D_{min} can be smaller than 0.5 mm, while the largest raindrop diameter D_{max} known so far as reported in Gatlin et al. (2015) is 9.7 mm. Marshall and Palmer (1948) proposed an exponential relation to describe the shape of DSD:

$$N(D) = N_0 e^{-\Lambda D}, \tag{2.2}$$

where N_0 is a constant value of 8000 $m^{-3}mm^{-1}$, and Λ is a function of rain rate R given by

$$\Lambda(R) = 4.1R^{-0.21}. \tag{2.3}$$

The unit for Λ is mm^{-1}, while the unit for R is mm h^{-1}.

The Marshall-Palmer relation, however, is insufficient for representing the diverse DSDs observed in nature, often overestimating the number of small raindrops. Ulbrich (1983) then introduced a three-parameter gamma distribution:

$$N(D) = N_0 D^{\mu} e^{-\Lambda D}. \tag{2.4}$$

Apart from the slope parameter Λ that mainly determines the concentration of large raindrops, Eq. (2.4) includes a shape parameter μ controlling the number of small raindrops. This gamma DSD also encompasses the form of Eq. (2.2) as μ is set to zero.

Later, Cao et al. (2008) noted that the values of Λ and μ can change with climatological regimes, precipitation systems, and even their evolution, rendering the previously assumed $\Lambda(R)$ relation or the $\Lambda(\mu)$ constraint from Zhang et al. (2001) inadequate. To enable a more universal comparison and analysis of DSD characteristics across various environmental conditions, Testud et al. (2001) and Bringi et al. (2003) suggested the use of normalized raindrop concentration N_w and mass-weighted mean diameter D_m, which are derived without any assumptions or constraints. The equations for these two parameters are given by

$$N_w = \frac{4^4}{\pi \rho_w} \frac{10^3 LWC}{D_m^4}, \text{ and} \tag{2.5}$$

$$D_m = \frac{\int_{D_{min}}^{D_{max}} N(D) D^4 dD}{\int_{D_{min}}^{D_{max}} N(D) D^3 dD}, \tag{2.6}$$

where ρ_w is the density of water (1 g cm^{-3}) and

$$LWC \text{ (liquid water content)} = \frac{\pi}{6} \rho_w \int_{D_{min}}^{D_{max}} N(D) D^3 dD \tag{2.7}$$

in g m^{-3}. Bringi et al. (2003) fitted a line of $Log_{10}(N_w)$-D_m based on a large dataset of tropical stratiform rain, demonstrating the consistency of DSD characteristics in stratiform rain over the world. Subsequent studies by Tokay et al. (2008) and Chen (2013) also utilized N_w and D_m to classify different types of precipitation. Generally, small N_w values and higher D_m values indicate a relatively high fraction of larger drops, which may occur in the pre-convective regime of continental rain (Fig. 2.1 in blue), while frontal rain in the middle latitudes gives small N_w and D_m values. High N_w values with smaller D_m values are typical for tropical rain formed predominantly via the warm-rain process (Fig. 2.1 in green), while deep continental showers with abundant raindrops often exhibit high N_w values with larger D_m values.

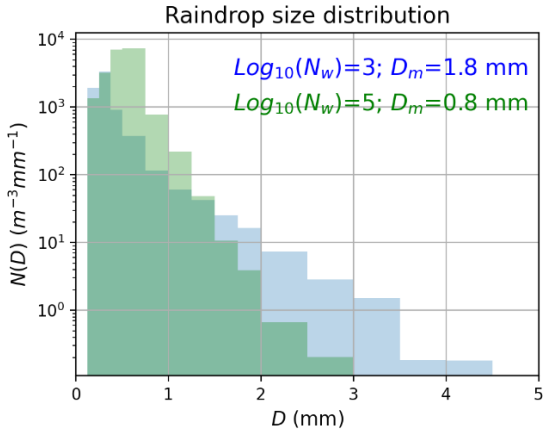

Figure 2.1 Two examples of the raindrop size distribution (DSD), one in blue with a lower value of normalized raindrop concentration N_w and a higher value of mass-weighted mean diameter D_m, the other one in green with a higher N_w value and a smaller D_m value. $N(D)$ represents the volume density of drops per unit drop diameter; D denotes the diameter of drops.

In addition to rain type, microphysical processes such as aerodynamic breakup, collisional breakup, collision coalescence, and evaporation can also alter DSD during raindrop falling. Kumjian et al. (2014) simulated these processes and found that, in a steady-state (or near-steady) situation, decreases toward the ground in D_m and increases in N_w are evident when rain is undergoing aerodynamic breakup or collisional breakup, with the latter exhibiting a more pronounced tendency. In contrast, when collision-coalescence processes are dominant, D_m increases and N_w decreases. Evaporation primarily impacts and depletes small raindrops, leading to a slight increase in D_m (Kumjian and Ryzhkov 2010; Xie et al. 2016).

The variability in DSD is strongly related to the quantities of R, which is expressed as

$$R = \frac{386.6\,\pi}{6}\int_{D_{min}}^{D_{max}} N(D)D^{3.67}dD, \tag{2.8}$$

as well as other radar variables to varying degrees, making it one of the main error sources in radar-based QPE. More details on this topic will be presented in the following two sections.

Exponential relations are commonly used to describe PSDs (Gunn and Marshall 1958). However, the parameters N_0 and Λ for ice particles (including graupel, hail, snowflakes, and ice crystals) are temperature-dependent and vary significantly due to their complex microstructure associated with shape, density, orientation, and phase composition. Delanoë et al. (2005 and 2014) derived normalized size distribution N_i for ice crystals and snowflakes by replacing LWC with

$$IWC \text{ (ice water content)} = \frac{\pi}{6}\int_{D_{min}}^{D_{max}} \rho_s(D)N(D)D^3dD, \tag{2.9}$$

in Eq. (2.5). IWC is in a unit of g m^{-3} and the size D here means the equivolume diameter of ice crystals or snowflakes. The density of these ice particles, denoted as ρ_s, can be estimated using empirical relations, e.g., the one from Brandes et al. (2007):

$$\rho_s(D) = 0.178D^{-0.922}. \tag{2.10}$$

The liquid equivalent snowfall rate S, i.e., snow water equivalent (SWE), also can be formulated using PDS as follows

$$S = 6\times10^{-4}\,\pi\int_{D_{min}}^{D_{max}} \frac{\rho_s(D)}{\rho_w} V_{Ts}(D)N(D)D^3dD, \tag{2.11}$$

where V_{Ts} is the fall velocity of snowflakes in m s^{-1}. According to the observations made by Brandes et al. (2007), V_{Ts} can be expressed as

$$V_{Ts}(D) = 0.9\left(\frac{P_0}{P}\right)^{0.5}D^{0.15}. \tag{2.12}$$

P_0 and P indicate the atmospheric pressures at mean sea level (MSL, $P_0 =$ 1013.25 mb) and at the measured height above the MSL, respectively. The factor $(P_0/P)^{0.5}$ represents the terminal velocity adjustment due to the change in air density with altitudes, as noted by Brandes et al. (2008).

2.2 Radar dual-polarimetry

Weather radar systems actively transmit microwave radiation, which interacts with hydrometeors in the air, and receive backscattered power, namely the portion of the signal reflected by the target to the antenna. Traditional weather radar only provides reflectivity at horizontal polarization Z_h, which can be expressed by the co-polar backscatter coefficient S_{HH} with units in mm^6m^{-3} (Doviak and Zrnić 2006):

$$Z_h = \frac{4\lambda^4}{\pi^4|k_w|^2}\langle|S_{HH}|^2\rangle \tag{2.13}$$

(Z_H stands for reflectivity at horizontal polarization in dBZ). λ is the radar wavelength in mm, k_w indicates the dielectric constant factor for water, and $\langle|S_{HH}|^2\rangle$ represents the ensemble (probabilistic) average of S_{HH} within a unit volume. The first subscript of S_{HH} refers to the horizontal (H) polarization of the incident field transmitted by the radar, and the second one denotes the horizontal (H) polarization of the backscattered field.

The computation of Z_h assumes the measured hydrometeors are spherical, and can be represented by the equation

$$Z_h = \frac{\langle|k|^2D^6\rangle}{|k_w|^2}, \tag{2.14}$$

where k is the dielectric constant factor of the targets, and the angular bracket means integration over the ensemble of particles. For raindrops where $|k|^2 = |k_w|^2$, Z_h can be written respecting DSD as

$$Z_h = \int_{D_{min}}^{D_{max}} N(D)D^6dD. \tag{2.15}$$

Apparently, Z_h is directly related to both the size and concentration of raindrops, and is easily biased towards larger raindrops due to its sixth moment of D.

For frozen ice particles, e.g., graupels and hailstones whose dielectric constant and density remain unchanged with size, Z_h is expressed as

$$Z_h = \frac{|k_i|^2}{|k_w|^2}\int_{D_{min}}^{D_{max}} N(D)D^6dD, \tag{2.16}$$

where k_i is the dielectric constant factor of solid ice. Hailstones can produce large Z_h values due to their size, which can reach up to 20 cm in diameter as documented by the National Severe Storms Laboratory (NSSL, https://www.nssl.noaa.gov/education/svrwv101/hail/) in the U.S.A. It is noteworthy that the ratio $|k_i|^2/|k_w|^2$ is less than one, causing Z_h values of graupels or small hails to be lower than those of rain with identical size distribution.

Dry snow, on the other hand, requires the consideration of its density variation with size in Eq. (2.14), resulting in the expression of

$$Z_h = \frac{|k_i|^2}{|k_w|^2\rho_i^2}\int_{D_{min}}^{D_{max}} \rho_s^2(D)N(D)D^6dD. \tag{2.17}$$

Here, the solid ice density ρ_i is equal to 0.92 g cm^{-3}. As per the exponent value in Eq. (2.10),

ρ_s is almost inversely proportional to D, and thus Z_h of dry snow is approximately the fourth moment of D. In addition, given that $|k_i|^2$ is smaller than $|k_w|^2$ and dry snow has low density, Z_h values observed in snow are usually much lower than those in rain despite the large size of snowflakes.

In the case of melting (mixed-phase) hydrometeors, the calculation of Z_h is influenced not only by the hydrometeor size distribution (Fabry and Szyrmer 1999; Zawadzki et al. 2005), but also by the mass water fraction (Aydin and Zhao 1990; Aydin et al. 1991; Ryzhkov et al. 2013a). E.g., in continental convective rain, large values of Z_h shown may arise from the presence of melting graupels and hailstones. The intensity of Z_h within the ML is also affected by melting snowflakes, but in a more complex manner. The factors involved include i) changes in dielectric constant factor from snow to water, ii) reduced particle size owing to density changes, and iii) decreased particle concentration (based on the conservation of particle concentration flux during melting). Furthermore, pronounced resonance effects at C-band may cause Z_h values to drop when particle size exceeds 20 mm.

Dual-polarimetric radar operates by transmitting and receiving microwaves at both horizontal and vertical polarization, allowing radar meteorologists to gain a deeper insight into the physical properties of the observed hydrometeors. By analyzing the differences between the signals received in each polarization, information on the size distribution, shape, orientation, and composition of the hydrometeors can be retrieved. Some of the polarimetric radar variables that can be measured include:

i. Differential reflectivity:

The differential reflectivity Z_{DR} (in dB) is a parameter that provides information about the shape of hydrometeors within a radar volume. It is defined as the logarithmic ratio of the reflected power between the horizontal and vertical polarizations:

$$Z_{DR} = 10\log_{10}(\frac{Z_h}{Z_v}) = Z_H - Z_V, \tag{2.18}$$

where

$$Z_v = \frac{4\lambda^4}{\pi^4|K_w|^2}\langle|S_{VV}|^2\rangle \tag{2.19}$$

is the reflectivity at vertical polarization in a linear unit and Z_V is in dBZ. Similarly, S_{VV} is the co-polar scattering amplitude at the vertical channel. Note that Z_{dr} is differential reflectivity expressed in a linear scale.

In heavy rain with big raindrops, the shape of the raindrop becomes more oblate, leading to a much higher value of Z_H than Z_V, i.e., an increased Z_{DR} value. Thus, Z_{DR} can be considered relative to the average size of raindrops within a volume. For larger raindrops from melting graupels or hails, Z_{DR} values can reach 2-3 dB and even up to 8 dB for resonance-size D larger than 5 mm at C-band, where this resonance feature is more significant at higher temperatures.

Randomly tumbling hailstones in the air result in a spherical shape with near-zero Z_{DR} and strong Z. In the case of aggregated snowflakes, Z_{DR} is usually small due to the low values of k_i and ρ_s, and the chaotic orientation. Pristine ice crystals such as plates, columns, needles, and dendrites, however, may have large values of Z_{DR} because of their

low aspect ratio ar (a/b and $a < b$ for oblate spheroids) and relatively high density. Z_{DR} of melting hails is higher than that of dry hails owing to the increasing dielectric constant and less tumbling movement stabilized by the water on their surface. In stratiform rain, a Z_{DR} peak is observed near the bottom height of the ML (H_b). This peak is more remarkable in the case of melting aggregated snowflakes with larger sizes and oblate shapes, and less noticeable for the melting of rimed snow.

ii. Differential phase shift:

The total differential phase shift Φ_{DP} is a crucial parameter for both radar data quality control and radar-based QPE. It is calculated as the difference between the cumulative phase shift at two radar channels Φ_H and Φ_V:

$$\Phi_{DP} = \Phi_H - \Phi_V = \varphi_{DP} + \delta, \tag{2.20}$$

where φ_{DP} represents the propagation differential phase and δ is the backscatter differential phase, both in degree. The value of δ is strongly associated with radar wavelength and temperature, and it increases with particle size in rain. At C-band where resonance effects are more pronounced compared to S- and X-band, δ may exceed 40 deg or drop as low as -20 deg for raindrops with D > 5 mm, dry/melting hailstones of resonance size, and wet snow within the ML (Ryzhkov and Zrnić 2019). Such variation is one of the major contributors to the noise in Φ_{DP} measurements from the DWD radars. To obtain accurate φ_{DP} for further applications, δ needs to be carefully separated from the radar-observed Φ_{DP}.

iii. Specific differential phase:

The specific differential phase K_{DP} (deg km^{-1}) is a powerful phase-based radar variable for precipitation estimation. For raindrops, K_{DP} can be approximated as

$$K_{DP} \approx \frac{0.03\pi F_o}{\lambda} \int_{D_{min}}^{D_{max}} \frac{L_a - L_b}{L_a L_b} N(D) D^3 dD, \tag{2.21}$$

where F_o is the orientation factor associated with the width of the canting angle distribution σ in radians:

$$F_o = \frac{1}{2} e^{-2\sigma^2} \left(1 + e^{-2\sigma^2}\right), \tag{2.22}$$

and L_a and L_b are the shape parameters given by

$$L_a = \frac{1+g^2}{g^2} \left(1 - \frac{\tan^{-1} g}{g}\right), \text{ and} \tag{2.23}$$

$$L_b = \frac{1-L_a}{2}. \tag{2.24}$$

The parameter g in Eq. (2.23) is a function of ar:

$$g = \sqrt{\left(\frac{1}{ar}\right)^2 - 1}. \tag{2.25}$$

According to Eq. (2.21), K_{DP} has an inverse relationship with radar wavelength, indicating that radars with shorter wavelengths are more effective in detecting K_{DP}. K_{DP} value is dependent on both the size and concentration of raindrops but less weighted by larger sizes compared to Z, as it is a lower-order moment of D. Simulations made by Sachidananda and Zrnić (1986) demonstrated that K_{DP} scales proportionally with $D^{4.24}$. Additionally, based on a large dataset of DSDs measured in Oklahoma, Ryzhkov and Zrnić (2019) reported that K_{DP} is more sensitive to the DSD variability in smaller drops with a size D < 1 mm compared to larger drops.

For dry aggregated snow, K_{DP} is close to

$$K_{DP} \approx \frac{0.27\pi|k_i|^2 F_o}{\lambda \rho_i^2} \int_{D_{min}}^{D_{max}} (L_a - L_b)\rho_s^2 N(D) D^3 dD. \tag{2.26}$$

Similar to Z_{DR}, K_{DP} also has smaller values in snow compared to rain due to the low values of k_i and ρ_s, as well as their orientation. K_{DP} values increase slowly with the size of snowflakes because they are roughly proportional to the first moment of D. In contrast, K_{DP} values of pristine ice crystals can be even higher than those of rain. Dry graupel and small hail yield low K_{DP} values for the same reason as Z_{DR}. At C-band, K_{DP} values can drop below zero due to resonance effects on large raindrops, dry/wet hailstones, and melting snow. Since K_{DP} contains information about particle orientation, it proves particularly useful for studying snowflakes, which can display complex, asymmetrical shapes with varying orientations.

In practice, the slope of the range dependence of processed Φ_{DP} (assuming $\approx \varphi_{DP}$) is used to estimate K_{DP} (Rinehart 2004):

$$K_{DP} = \frac{1}{2}\frac{\Delta\Phi_{DP}}{\Delta r}, \tag{2.27}$$

where r is the range distance in km.

iv. Co-polar correlation coefficient:

The co-polar correlation coefficient ρ_{HV} represents the correlation of radar signal powers between two channels and can be expressed as

$$\rho_{HV} = \frac{\langle S_{VV} S_{HH}^* \rangle}{\sqrt{[\langle |S_{HH}|^2 \rangle \langle |S_{VV}|^2 \rangle]}}, \tag{2.28}$$

where * denotes the complex conjugate. ρ_{HV} does not provide any information about precipitation amounts. Instead, it indicates the uniformity of particles within a sampled volume in terms of their shape, size, orientation, and phase composition. Typically, outside of the ML where liquid and solid precipitation take place, ρ_{HV} values are close to one. However, within the ML where snowflakes start melting, ρ_{HV} values can decrease to 0.9. In rain or snow, deviations of ρ_{HV} from one are usually attributed to statistical measurement errors, non-uniform beam filling (NBF) effects, and, especially at C-band, resonance effects. For non-meteorological signals such as interference noises, insects, and ground clutter, ρ_{HV} values could be less than 0.8 and thus a threshold value of ρ_{HV} is recommended to remove these signals.

v. Linear depolarization ratio:

The linear depolarization ratio L_{DR} can be obtained only through a dual-channel radar system, which is capable of transmitting linearly polarized signals and receiving power from the orthogonal channels. Usually, L_{DR} is expressed in dBZ and defined following Bringi and Chandrasekar (2001) as

$$L_{DR} = 10\log_{10}\left(\frac{\langle|S_{HV}|^2\rangle}{\langle|S_{HH}|^2\rangle}\right). \tag{2.29}$$

$\langle|S_{HV}|^2\rangle$ represents the ensemble average representative of the cross-polar scatterers S_{HV} with the transmission at horizontal polarization and reception at vertical one.

L_{DR} is sensitive to the shape and orientation of raindrops and closely correlated with Z_{DR}. In dry aggregated snow with low density and an average ar of 0.6, L_{DR} values typically fall below -26 dB (Herzegh and Jameson 1992). Rimed snow further reduces L_{DR} values due to the net effect of its higher density and more spherical shape [i.e., the impact of shape is larger than that of density on L_{DR}, Ryzhkov et al. (2017)]. Pristine ice crystals with high density and less spherical shape, on the other hand, lead to higher values of L_{DR}.

Owing to its sensitivity to the water content of mixed-phase hydrometeors and strong resonance effects, L_{DR} values increase with wet hail size. Herzegh and Jameson (1992) and Brandes and Ikeda (2004) also demonstrated that the L_{DR} values within the ML exceed -18 dB, which is considerably greater than those observed in pure rain and dry aggregated snow. Consequently, L_{DR} provides valuable information for ML detection and hail discrimination.

Notably, current scanning strategies and the use of a single transmitter for simultaneous transmission and reception of waves at two polarizations preclude the production of L_{DR} measurements by the radars used in this work (Doviak et al. 2000).

The last polarimetric radar variables introduced here are specific attenuation at horizontal and vertical polarizations, A_H and A_V, as well as specific differential attenuation, A_{DP} defined as

$$A_{DP} = A_H - A_V \tag{2.30}$$

with all in units of dB km^{-1}. A_H and A_V, however, cannot be directly observed by radars. Instead, they can be estimated in rain from the measured Z, Φ_{DP} and the attenuation parameter α using the ZPHI method (Testud et al. 2000). α is defined as the ratio of A to K_{DP}, expressed in units of dB deg^{-1}. Its sensitivity to the DSD variability is particularly pronounced for small raindrops at all band frequencies, and for big drops of resonance size at C-band. Additionally, α increases with decreasing temperature. Further details on estimating A and α for rainfall retrieval are presented in the following section and section 4.2, respectively.

In summary, the hydrometeor size distribution serves as the foundation for determining rain/snow rates and radar variables. As a result, simulations based on measured DSDs/PSDs from disdrometers are frequently used to investigate the impacts of DSD/PSD variability on the relationships between precipitation rates and polarimetric variables, and the consequent impact on radar-based QPE.

2.3 Error sources of radar-based QPE

Accurate measurement of the power-associated variables Z and Z_{DR} is a challenge due to errors stemming from radar miscalibration, attenuation along the path, PBB, radome effects, etc. While the phase-based variables K_{DP} and A are immune to these issues, they can still suffer from noise in Φ_{DP} caused by the effects of NBF and backscattering (resonance), particularly in the presence of large δ. Moreover, heavy filtering and smoothing applied to Φ_{DP} for noise suppression can lead to spatial degradation. To mitigate these uncertainties, a series of quality check procedures are essential in radar meteorology. Here are some well-known and widely used methods in the field:

i. Miscalibration of Z:

The accuracy of 1 dBZ for Z is deemed desirable in weather radar measurements. To achieve this, external calibrations using metal points, solar radio emissions, or disdrometer measurements are frequently performed (Ulaby et al. 1982; Sekelsky 2002; Atlas 2002; Chandrasekar et al. 2015). Subsequently, with the advent of polarimetric radar, the phase-based variable Φ_{DP} has emerged as a constraint, leading to the proposal of various self-consistency methods for Z calibration (Gorgucci et al. 1992 and 1999; Scarchilli et al. 1996; Vivekanandan et al. 2003). In their works, the $K_{DP}(Z_h, Z_{DR})$ relation in the form of

$$K_{DP}(Z_h, Z_{DR}) = f(Z_{DR}){Z_h}^a \tag{2.31}$$

has been utilized in rainy conditions to calculate K_{DP} (Goddard et al. 1994; Illingworth and Blackman 2002). The function $f(Z_{DR})$ in this equation is represented by a third-degree polynomial (Gourley et al. 2009). In situations where the quality of Z_{DR} is uncertain, K_{DP} can be estimated via a power-law relation based solely on Z_h (Lee et al. 2015; Chen et al. 2021b). Given that the integral of calculated K_{DP} over a ray or within a rainy segment (i.e., $\Delta\Phi_{DP}^{cal.}$) is assumed to be consistent with the total span of radar-observed differential phase shift $\Delta\Phi_{\mathrm{DP}}$ within the same interval, the offset of reflectivity at horizontal polarization, denoted as Z_H^{offset}, can be derived by the ratio of $\Delta\Phi_{DP}^{cal.}$ to $\Delta\Phi_{\mathrm{DP}}$:

$$\Delta\Phi_{DP}^{cal.} = 2\int_{r_1}^{r_2} K_{DP}[Z_h(r), Z_{DR}(r)]dr, \tag{2.32}$$

$$Z_H^{offset} = 10\frac{1}{\gamma}Log_{10}\frac{\Delta\Phi_{DP}^{cal.}}{\Delta\Phi_{DP}}. \tag{2.33}$$

In Eq. (2.32), the range interval (r_1, r_2) only contains the region below the ML, or a small rainy radial segment. In Eq. (2.33), the constant γ is the exponent a in Eq. (2.31) or the exponent of Z_h in the $K_{DP}(Z_h)$ relation. Note that Z_h and Z_{DR} are attenuation-corrected in this context.

ii. Miscalibration of Z_{DR}:

Numerous methods exist for Z_{DR} calibration, with the most common approach involving bird-bath scans, which are azimuthal scans conducted at a 90-deg elevation angle (Gorgucci et al. 1999; Hubbert et al. 2008). Since Z_{DR} is assumed to be zero when raindrops are viewed at vertical incidence, the average value of Z_{DR} from the vertical scan is directly regarded as its systematic bias. When a vertical scan is unavailable, an alternative approach

is to use the mean value of Z_{DR} in light rain from plan position indicator (PPI) scans at low angles. The rationale behind this approach is that small raindrops are nearly spherical and the values of Z_{DR} in light rain are similar regardless of rain type. To apply this approach, the light-rain area must be carefully defined, typically by selecting data with Z_H < 20 dBZ, signal-to-noise ratio SNR > 20 dB, and $\Delta\Phi_{\mathrm{DP}}$ < 20 deg. The latter two conditions ensure the high quality of measurements without significant noise and attenuation. The offset of Z_{DR} can then be quantified by subtracting the mean of those chosen data from that of simulated Z_{DR} within the same range of simulated Z_H derived from the measured DSDs (see section 4.1 regarding this simulation).

Other methods for determining the systematic bias of Z_{DR} include using data from dry aggregated snow at mid-to-high latitudes (Ryzhkov and Zrnić 1998; Brandes and Ikeda 2004), Bragg scatter at S-band (Melnikov et al. 2011), cross-polar measurements (Hubbert et al. 2003) and ground clutter (Melnikov et al. 2017).

iii. Attenuation of Z:

Attenuation is the gradual loss of power as radar energy travels through the atmosphere and is absorbed or reflected by gas or hydrometeors. Gas-induced attenuation is negligible, while the power-related radar variables at shorter wavelengths are highly susceptible to precipitation-induced attenuation. Within the range-bin interval (r_1, r_2) of rain, the two-way path-integrated specific attenuation (PIA in dB), i.e., the total amount of attenuated reflectivity ΔZ, can be estimated from $\Delta\Phi_{DP}$ and α for attenuation correction:

$$PIA = \alpha_0[\Phi_{DP}(r_2) - \Phi_{DP}(r_1)] = \alpha_0\Delta\Phi_{DP}, \tag{2.34}$$

where α_0 represents the attenuation parameter α specific to rain. It is worth noting that α_0 is DSD- and temperature-dependent, but in practice, it remains constant within the interval (r_1, r_2).

To obtain a more precise estimate, ΔZ can be calculated by integrating A along the rainy ray. The ZPHI method used to estimate A follows:

$$A(r) = \frac{Z_a(r)^b C(b,PIA)}{I_a(r_1,r_2)+C(b,PIA)I_a(r,r_2)}, \tag{2.35}$$

where

$$I_a(r_1, r_2) = 0.46b\int_{r_1}^{r_2}[Z_a(s)]^b\, ds, \tag{2.36}$$

$$I_a(r, r_2) = 0.46b\int_{r}^{r_2}[Z_a(s)]^b ds \text{ and} \tag{2.37}$$

$$C(b, PIA) = e^{0.23bPIA} - 1. \tag{2.38}$$

In Eqs. (2.35)-(2.38), Z_a represents the measured, uncorrected apparent Z_h or Z_v, the parameter b is the exponent in the power-law $A_{H/V}(Z_{h/v})$ relations and is assumed to be a constant of 0.86 and 0.87 for two channels, respectively. In Eqs. (2.36) and (2.37), s denotes the slant range in km.

The α values in hail are considerably higher than those in rain (Schmidt et al. 2020). Also, the assumed $A(Z_{h/v})$ relations and α_0 used in the ZPHI method are only valid for rain. To overcome this limitation, Gu et al. (2011) proposed a reliable attenuation correction method for heavy rain mixed with hail at C-band, based on the ZPHI algorithm. In this method, the calculation of A using Eq. (2.35) is modified by substituting Eq. (2.34) with

$$PIA_{HS} = \alpha_0[\Phi_{DP}(r_2) - \Phi_{DP}(r_1)] + \Delta\alpha\Delta\Phi_{DP}(\mathrm{HS}), \tag{2.39}$$

where HS refers to convective cores with the presence of hail, known as hot spots, and $\Delta\alpha$ denotes the difference between the α values within and outside HS. The method determines $\Delta\alpha$ values through an iterative process of incrementing $\Delta\alpha$ in Eq. (2.39) until it satisfies the condition given by

$$\int_{\mathrm{OHS}} A(r, \Delta\alpha)dr = \frac{\alpha_0}{2}\Delta\Phi_{DP}(\mathrm{OHS}), \tag{2.40}$$

where OHS indicates the radar bins located outside HS. Once $\Delta\alpha$ is determined, $\Delta Z(r)$ can be estimated according to the radar bin location with respect to HS:

$$\Delta Z(r) = \begin{cases} \alpha_0\Delta\Phi_{\mathrm{DP}}(r) & if\ r < r_3 \\ \alpha_0\Delta\Phi_{\mathrm{DP}}(r) + \Delta\alpha[\Delta\Phi_{\mathrm{DP}}(r) - \Delta\Phi_{\mathrm{DP}}(r_3)] & if\ r_3 < r < r_4, \\ \alpha_0\Delta\Phi_{\mathrm{DP}}(r) + \Delta\alpha\Delta\Phi_{\mathrm{DP}}(\mathrm{HS}) & if\ r > r_4 \end{cases} \tag{2.41}$$

where (r_3, r_4) is the range-bin interval of HS. After deriving ΔZ, the entire process is repeated again, but using the latest corrected Z for better HS detection.

For the data within the ML, Bellon et al. (1997) found that the BB attenuation could be 3-5 times the rain-equivalent attenuation, while it is hard to quantify precisely. Conversely, attenuation due to dry snow and small graupel is very low and thus ignorable.

iv. Attenuation of Z_{DR}:

Estimating two-way path-integrated differential attenuation PIA_{DP}, namely ΔZ_{DR}, in rain is similar to the estimation of PIA in Eq. (2.34), where $\Delta\Phi_{DP}$ is used with the factor β, representing the ratio of A_{DP} to K_{DP} in dB deg^{-1}. A more precise correction considering the contributions from HS can also be made by following the approach outlined in Eq. (2.41). To determine $\Delta\beta$ (the difference in β values inside and outside the HS), ΔZ_{DR} behind the HS ($r > r_4$) needs to be first quantified using

$$\Delta Z_{DR} = Z_{DR}(Z_H) - Z_{DR}^{obs.}, \tag{2.42}$$

where $Z_{DR}^{obs.}$ indicates the radar-observed differential reflectivity, while $Z_{DR}(Z_H)$ is viewed as the expected (true) value of Z_{DR} derived from the quality-controlled Z_H. Note that only data points with Z_H values below 40 dBZ are selected for calculation, to reduce the impacts of DSD variability on the derived Z_{DR} in heavy rain. $\Delta\beta$ then can be written as

$$\Delta\beta(r) = \frac{\Delta Z_{DR}(r) - \beta\Delta\Phi_{\mathrm{DP}}(r)}{\Delta\Phi_{DP}(HS)}, \tag{2.43}$$

where $r > r_4$. In the rainy segment following the first HS, Eq. (2.43) can be simplified by assuming ΔZ_{DR} behind the HS mostly results from hail and thus deleting the second term (Ryzhkov et al. 2013b).

The correction method for Z_{DR} within the ML is currently unknown due to limited studies, while the attenuation of Z_{DR} above the ML is very small and can be neglected.

v. Partial beam blockage:

PBB is a common issue that arises from terrain or local obstacles such as buildings or trees near radar sites when the radar beams are still at low altitudes. To estimate the impact of beam blockage on Z at each azimuth and elevation, a digital elevation model is used based on the beam's geometry and occultation (Ryzhkov and Zrnić 2019). Thus, the Z bias resulting from PBB can be minimized by utilizing data from higher elevation scans in the affected regions or by applying a correction based on the blocking factor. Moreover, Shakti et al. (2013) employed X-band radars as gap fillers over a mountainous region, whereas Zhang et al. (2013) and Gou and Chen (2021) corrected PPB through a self-consistency method similar to that used for Z calibration. The related bias of Z_{DR} is less conspicuous compared to that of Z.

vi. Radome effect:

When rainwater coats or snow accumulates on the surface of a radome, it can introduce wet radome effects that cause biases in Z_H and Z_{DR} (Hudak et al. 2006; Kurri and Huuskonen 2008; Frech 2009). These effects are dependent on factors such as precipitation intensity, radome material, and radar wavelength. Chen et al. (2021b) indicated that Z_H^{offset} obtained via the self-consistency method also includes power loss from the wet radome effects. The impact on Z_{DR}, however, may result in azimuthal biases, which vary with wind speed and direction, making it difficult to correct (Bechini et al. 2006).

In addition to precipitation, the installation of lightning protection in the radome may potentially induce another type of radome effect, thereby affecting the transmission of signal power. Notably, this effect brings about a discernible bias in Z_{DR} that is characterized by a consistent and fixed pattern over time. Nevertheless, research in this area is limited.

vii. Beam-broadening effect:

Beam-broadening effects can largely degrade the quality of radar observations at far ranges from radar sites. As the beam width widens, the occurrence of the NBF effects may increase, and SNR values, an indicator of the noise level, typically decrease.

a. Non-uniform beam filling:

Ryzhkov (2007) developed simple analytical formulas to estimate the NBF-induced biases in Z_{DR}, Φ_{DP}, and ρ_{HV}, while in practice the associated correction study is insufficient and restricted.

b. Noise:

When SNR falls below 20 dBZ, statistical errors in the phase-based variables become more significant. Additionally, the quantitative use of power-related observations like ρ_{HV} and Z_{DR} is badly affected due to their high sensitivity to the noise-induced biases. As the ρ_{HV}-threshold method for non-weather signal removal is frequently applied in the field, noise correction for ρ_{HV} becomes important. The corrected ρ_{HV} can be

obtained following Ryzhkov and Zrnić (2019):

$$\rho_{HV} = \rho_{HV}^{obs.}(1 + \frac{1}{snr}), \tag{2.44}$$

where $\rho_{HV}^{obs.}$ is observed co-polar correlation coefficient and snr is the signal-to-noise ratio in a linear unit estimated via

$$SNR = Z_H - 20\,log_{10}(r) + C. \tag{2.45}$$

In Eq. (2.45), SNR, Z_H, and C are in units of dB, while r is the distance in km. The accuracy of SNR estimation relies on the value of the constant C, which can be determined by examining the flatness of the scatterplot of corrected ρ_{HV} against SNR below 20 dB.

viii. Backscattering effects on Φ_{DP}:

Backscattering and resonance effects can impact both the quantity and quality of radar variables. To process Φ_{DP} and retrieve K_{DP}, numerous methods have been published (Hubbert and Bringi 1995; Ryzhkov et al. 2005; Lang et al. 2007; Maesaka et al. 2012; Vulpiani et al. 2012 and 2015; Giangrande et al. 2013; Schneebeli et al. 2014; Reimel and Kumjian 2021). The primary goals of these methods are to smooth noise, mitigate the deviation in Φ_{DP} caused by δ, and provide reliable K_{DP}. Users can select their preferred window size for smoothing based on the type of investigated precipitation, the radial bin-resolution, and the quality of Φ_{DP}.

ix. Ground clutter contamination:

Traditional techniques for removing ground clutter from radar observations include the use of clutter maps generated from statistical data collected during clear-air conditions, or the application of classification methods based on the analysis of Doppler spectra (Siggia and Passarelli Jr 2004). The former, however, is limited in its ability to eliminate sporadic ground clutter caused by anomalous propagation due to super-refraction. The latter may mistakenly filter out useful signals when precipitation movement is perpendicular to the radial viewing direction from the radar at the observed location, which leads to near-zero Doppler velocity W, as is the case with ground clutter. The advent of polarimetry has enabled more efficient and accurate ground clutter removal methods. E.g., the utilization of ρ_{HV} thresholds or polarimetric ground clutter identification methods based on fuzzy-logic algorithms have demonstrated greater success in addressing these concerns.

Apart from errors originating from radar observation itself, other uncertainty sources such as the DSD/PSD variability, vertical variation of precipitation, and wind advection are also critical for radar-based QPE. Accounting for these uncertainties is essential to enhance the accuracy and reliability of QPE results. A corresponding discussion on this matter is provided below:

i. DSD/PSD variability:

The DSD/PSD variability is an error source for QPE that all radar variables will face, albeit to varying degrees. DSD characteristics exhibit significant variation across locations, cases, and even within a developing storm. In the case of rain, it is possible for a radar

volume with a high/small value of N_w/D_m to yield a value of any radar variable equal to that of another volume with a completely different DSD, i.e., a small/high value of N_w/D_m, even though the former volume typically produces a stronger rain intensity than the latter. In this scenario, QPE error due to the DSD variability is expected. Fig. 2.2 displays the sensitivity of rainfall retrievals based on different radar variables at C-band to the DSD variability, as simulated using DSDs measured in Germany. The scatter of R against Z_h is generally broad across the entire range since Z_h is the higher-order moment of D (Fig. 2.2a). In light rain, K_{DP} shows the highest sensitivity to DSD variations among all variables, whereas having the smallest sensitivity in heavy rain (Fig. 2.2b). In Figs. 2.2c/d, $R(A_{H/V})$ hold the narrowest scatter in light rain compared to all other variables. In heavy rain, however, there is a deviation from the line observed in the data points representing continental rain (defined as points with $Log_{10}(N_w) < 3$ in cyan). Note that A_V is less sensitive to the DSD variability in heavy rain than A_H. As a result, hybrid rainfall estimators, that use different radar variables in different rain conditions, are widely suggested and implemented in operation to reduce the impacts of DSD variability on QPE (e.g., Figueras i Ventura and Tabary 2013 in French; Jung et al. 2018 in South Korea; Zhang et al. 2020a in the U.S.A.).

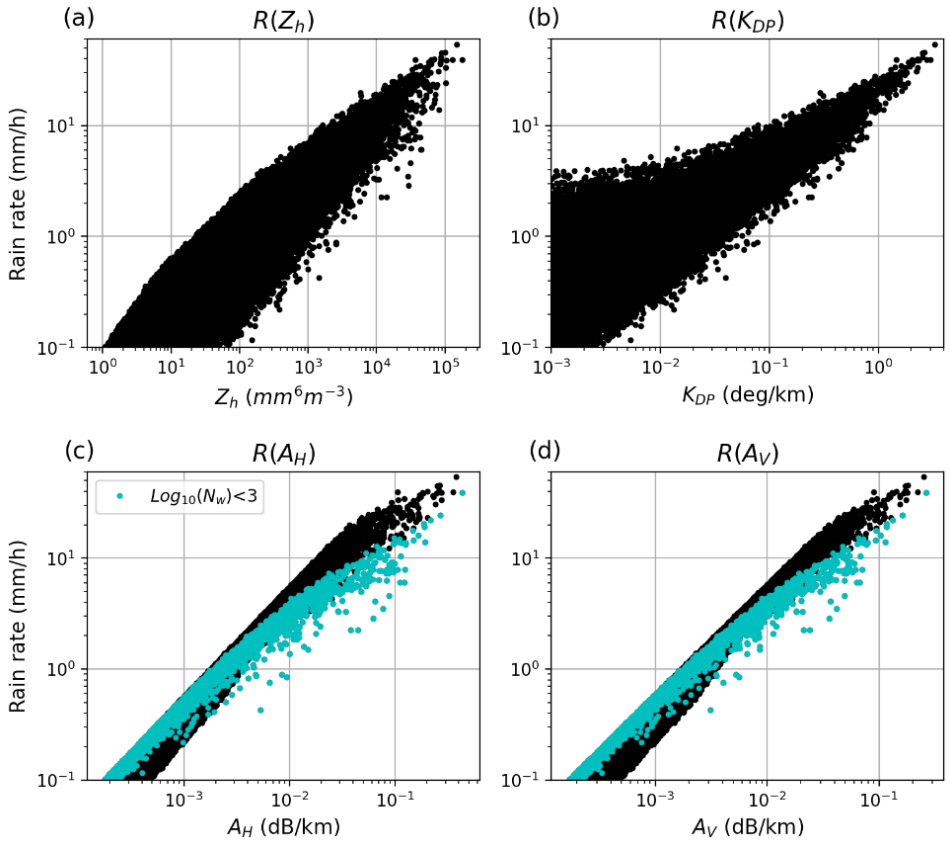

Figure 2.2 Scatterplots of rain rates R against (a) linear reflectivity at horizontal polarization Z_h, (b) specific differential phase K_{DP}, (c) specific attenuation at horizontal polarization A_H and (d) specific attenuation at vertical polarization A_V. The radar variables are simulated at C-band using DSD measurements made in Germany. The cyan dots in (c) and (d) indicate the points with $Log_{10}(N_w)$ less than three.

Compared to raindrops, snowflakes exhibit a higher degree of variation in PSD, which has led to a limited understanding of their properties and difficulty in accurately quantifying snowfall. Simulations conducted by Bukovčić et al. (2018) and illustrated in their Figs. 6 and 7 indicated that both the $S(K_{DP})$ and bivariate $S(Z_h, K_{DP})$ retrievals improve the estimation of IWC and snowfall beyond the Z_h-based retrievals, with $S(Z_h, K_{DP})$ giving the lowest errors. The improvements are attributed to K_{DP}, which is mostly linearly proportional to the D of snowflakes, while Z_h represents the fourth moment of D. As A cannot be estimated for ice particles, the application of $S(A)$ is not discussed.

ii. Variations of the vertical structure of precipitation:

Microphysical processes occurring within atmospheric columns can lead to vertical variations in precipitation. These variations can in turn affect the accuracy of surface QPE when radar beams monitor precipitation at high altitudes. This problem is compounded in areas with complex topography, where persistent PBB and frequent orographic enhancement of rain at lower levels take place (Lee et al. 2018). In such scenarios, VP corrections that project radar observations to the surface and gap-filling radars with low observing heights are recognized as promising solutions (Kitchen et al. 1994; Chen et al. 2020; Gehring et al. 2020; Chen et al. 2022).

iii. Wind advection:

The impact of wind drift on radar-based QPE cannot be overlooked, as it can cause precipitation to fall in unexpected regions. Advection adjustment schemes, such as those based on estimated hydrometeor trajectories obtained from model output (Lauri et al. 2012) or on temporal interpolation of radar images (Thorndahl et al. 2014; Wang et al. 2015), are typically employed to mitigate this issue. Spatial smoothing, by averaging retrieved precipitation fields within a certain distance, can also provide a relatively simple solution (Berndt et al. 2014). Tracking snowflakes with low V_{TS} for adjustment, however, remains a challenge, as they may be carried by the wind flow to distant locations from where they are measured. The issue is further complicated by the presence of large vertical wind shear.

2.4 The history and current status of radar-based QPE methodologies

Radar-based QPE has undergone significant developments over several decades. This section provides a historical overview of the evolution of radar-based QPE algorithms, highlighting the key innovations and milestones that have shaped the field. The current state of the art in radar-based QPE methodologies, including recent advances and promising research directions, is also discussed.

Below the ML

Prior to the establishment of dual-polarimetric radar networks, early rainfall estimates were primarily based on Z_h. Given the fact that Z_h is highly sensitive to the DSD variability, various Z_h-based rainfall algorithms were applied according to climatological regimes, seasons, and precipitation types (Battan 1973; Zhang et al. 2016). In the initial stages, power-law $R(Z_h)$ relations were obtained by fitting radar-observed echoes aloft to gauge-measured rain rates at the surface (Marshall and Palmer 1948). Subsequently, with the increasing installment of disdrometer instruments, rainfall relations were derived mainly from simulations based on measured DSDs (Ryzhkov and Zrnić 2019).

In recent decades with the aid of polarimetric radar variables, QPE performance has been greatly improved (Zrnić and Ryzhkov 1999). The first polarimetric variable exploited was Z_{DR}, which helps characterize the average drop size within the sampled volume (Scarchilli et al. 1993; Zrnić et al. 2000). Z_{DR} alone, however, does not provide information on particle concentration and thus $R(Z_{DR})$ cannot be used for rainfall estimation. As a consequence, the bivariate relation $R(Z_h, Z_{DR})$ was proposed and expected to increase the quality of QPE by incorporating additional DSD messages (Seliga et al. 1981; Jameson 1991). Nevertheless, this approach requires reliable calibration and attenuation correction, especially for Z_{DR} where a desired accuracy of 0.1 dB is needed for QPE purposes (Sachidananda and Zrnić, 1987). While $R(Z_h, Z_{DR})$ may turn out a counterproductive attempt for shorter-wavelength radars due to larger uncertainties in attenuation than S-band, Z_{DR} enhances the capability of hydrometeor classification algorithms (HCA), as noted by Bringi et al. (1984), Aydin et al. (1986), and Park et al. (2009). In their work, polarimetric HCAs have shown advantages over non-polarimetric HCAs with limited discrimination. This advancement has driven the development of hydrometeor-type-specific rainfall algorithms that are widely used in many operational environments (Steinert et al. 2013).

Later on, the phase-based measurement Φ_{DP} has gained attention in the field. It improves QPE by offering K_{DP} as well as reliable attenuation correction methods for power-related variables. Specifically, K_{DP} exhibits lower sensitivity to DSD variations, and immunity to radar miscalibration, moderate attenuation, (wet) radome effect, and PBB (Zrnić and Ryzhkov 1996). $R(K_{DP})$ is particularly suggested for heavy rain due to the demand for heavy spatial averaging to counteract the noise in light rain, resulting in a loss of accuracy (Zrnić and Ryzhkov 1999). For situations where rain is mixed with hail, K_{DP} better estimates liquid precipitation than Z_h, as it is less affected by water-coated hail, which appears as large raindrops in Z_h-based retrievals, leading to an overestimation of rainfall (Balakrishnan and Zrnić 1990; Ryzhkov et al. 2013b). Note that $R(K_{DP})$ is more advantageous for radars at C- or X-band and thus can be applied to a wider range of rain intensities.

Most recently, another phase-based variable A has emerged as a powerful information source for QPE, gradually replacing the use of $R(Z_h)$ and $R(K_{DP})$ in light-to-moderate rain (Ryzhkov et al. 2014; Diederich et al. 2015 and 2015b). Its success lies not only in its low sensitivity to the DSD variability in these rain intensities (Atlas and Ulbrich 1977), but also in its higher spatial resolution compared to $R(K_{DP})$. A_V is even expected to provide greater accuracy of QPE than A_H in areas with strong attenuation, where Z_H may be buried in noise while Z_V can still be reliably measured (Diederich et al. 2015b). Nevertheless, A is a relatively new tool for rainfall retrieval, and scientists are still working on optimizing it based on the ZPHI method (Testud et al. 2000).

The main challenge in using A for accurate rainfall estimation is the sensitivity of α to the DSD variability. To overcome this challenge, α estimators based on the change of Z_{DR} with respect to Z_H (called Z_{DR} slope) or Z_{DR} itself have been studied (Ryzhkov et al. 2022). The Z_{DR} slope method is especially beneficial in case no bird-bath scans are available for Z_{DR} calibration, as it is not affected by the potential radar system biases of Z and Z_{DR}. This method has already been applied to S-band (Wang et al. 2017 and 2019; Zhang et al. 2020a). However, Zhang et al. (2020a) and Chen et al. (2021a) have pointed out that the α adjustment using Z_{DR} slope on a scan basis may not be robust enough due to the inhomogeneity of precipitation

regimes within a scan. At S-band, this problem can be resolved by including a ratio factor of α derived from Z to scan-wise α in the power-law $R(A)$ relation, as the exponent value for S-band is close to one (Zhang et al. 2020b). Conversely, at C-band where the exponent value is relatively low, an optimization of α along radial rays for different rain types is recommended, but remains challenging (Huang et al. 2020; Ryzhkov et al. 2022). The difficulties in implementing this approach are discussed in section 4.2.

Since A is only valid in the pure-rain segment, Wang et al. (2017 and 2019) excluded the contribution of intense convective cells with potential hail contamination from the integration path in the ZPHI algorithm. This exclusion strategy, however, did not account for the extra attenuation from hail cores, which should propagate to the radar bins behind. As a result, A and thus $R(A)$ were overestimated in the former rainy segments and underestimated in the latter (Chen et al. 2021a). This is especially problematic for shorter-wavelength radars with pronounced attenuation effects. To further increase the accuracy of radar-derived A and thus QPE, the integration in the ZPHI algorithm should be reset for each pure-rain segment.

The vertical gradients of radar variables and rain intensities may increase towards the surface below the ML during warm-rain processes or precipitation enhancement over complex terrain. However, the radar beams, which rise with distance from the radar site, may not detect these changes. In such cases, utilizing gap-filling X-band radars to monitor rain at lower altitudes and applying VP corrections for radar variables or derived rain rates have proven to be effective (McLaughlin et al. 2009; Antonini et al. 2017; Chen et al. 2020). Chen et al. (2020) used observations from profiler radars as a VP reference and estimated Z near the surface by adding the Z-difference between the surface and the observing height of the scanning radar seen in the referred VP to the observations of the scanning radar (see Fig. 3a in their paper). It has reduced negative biases by at least 30% in two case studies. Chen et al. (2022) extended this method by using range-defined quasi-vertical profiles (RD-QVP, Tobin and Kumjian 2017) as VP references and likewise correcting for K_{DP}.

Within and above the ML

In rain events characterized by low ML heights, radar beams tend to sample mixed-phase and solid precipitation at short ranges. In situations like this, Z_h-based estimators are still widely used owing to the incomplete understanding of the relationship between precipitation rates and polarimetric variables for melting and solid particles. A method to address issues related to BB contamination and beam overshooting of the ML is QPE based on hydrometeor type. E.g., Giangrande and Ryzhkov (2008) introduced additional multipliers of 0.6 and 2.8 to the $R(Z_h)$ relations for wet snow within the BB and dry snow/crystals above, respectively, which are currently implemented in the operational radar network in the U.S.A. This methodology, however, is heavily reliant on temperature information and always produces discontinuities in the rainfall fields associated with the switching between different hydrometeor types.

Several articles have attempted to mitigate the overestimation of rainfall in BB-contaminated areas and the underestimation caused by weaker echoes of snowflakes and beam-broadening effects via reconstructing the intrinsic VPR (Koistinen 1991; Kitchen et al. 1994; Seo et al. 2000; Germann and Joss 2002; Matrosov et al. 2007; Anagnostou et al. 2010; Zhang and Qi 2010, among others). The apparent vertical profile of reflectivity (AVPR) method presented by Zhang and Qi (2010) is one of the most successful techniques. In this algorithm,

convective and stratiform regions are first discriminated based on the vertical integrated liquid (VIL) parameter, allowing identification of BB-affected areas within the stratiform region. Subsequently, the mean AVPR from radar observations and model outputs are combined to efficiently compute the VPR. The resulting VPR is then used to correct the observed local profile of Z for rainfall estimation at the surface. The AVPR-corrected precipitation fields were found to be continuous, unlike those derived from the HCA-based method. Until recently, Ryzhkov et al. (2022) recommended the utilization of polarimetry for the VPR correction, which involves better detection of BB range and more precise estimation of Z biases. This technique is expected to increase the accuracy of ensuing QPE.

Due to the large sensitivity of Z to PSD, similar to the retrieval of rain rate using $R(Z_h)$, a variety of power-law $S(Z_h)$ relations have been employed to quantify snowfall according to the climatological regions and hydrometeor classifications (Matrosov 2007; Liu 2008; Kulie and Bennartz 2009; Matrosov et al. 2009; Hiley et al. 2011; Wolfe and Snider 2012; Huang et al. 2015; von Lerber et al. 2017; Cooper et al. 2017). To better classify ice particles, additional measurements from multi-frequency microwave sensors (Huang et al. 2019) or disdrometers (Tao et al. 2021; Shen et al. 2022) can be used to estimate the parameters of PSD, and optimize the coefficients in $S(Z_h)$ relations. Recent studies have focused on overcoming the challenge associated with the vast diversity of snowflakes using polarimetry. Hassan et al. (2017) introduced the first polarimetric snowfall estimator at C-band that combined Z_{dr} with Z_h to better measure large aggregates. Similarly, Bukovčić et al. (2018) proposed snowfall estimators using K_{DP} for S-band. Later, Bukovčić et al. (2020) developed the generalized bivariate $S(Z_h, K_{DP})$ and $S(Z_{dr}, K_{DP})$ relations that are applicable to different climatologies and radars at various wavelengths. These relations incorporated adjustable assumptions regarding the σ and ar of snowflakes and ice crystals, and were applied to several snowstorms in the U.S.A. The outcomes indicated that the polarimetric retrievals demonstrated better agreement with ground-based measurements than the $S(Z_h)$ retrieval. The decreasing information of K_{DP} due to increasing aggregation of snowflakes towards the ground, however, may be a drawback of $S(Z_h, K_{DP})$ and $S(Z_{dr}, K_{DP})$ retrievals at S-band, but less problematic for C- and X-band radars.

At the end of this section, radar-based QPE algorithms based on variational schemes and artificial intelligence (AI) techniques (e.g., machine learning) are briefly overviewed. Variational approaches are capable of dynamically integrating models, radar measurements, and climatological (background) information based on physical constraints. By accounting for the properties of precipitation microphysics in various rainfall algorithms and minimizing radar observation errors, they have led to further improvements in QPE (Chang et al. 2016; Huang et al. 2018 and 2020). In addition to this, the rapid progress in computer science and supercomputer has accelerated the development of AI-based algorithms, which have also gained popularity in the field of radar meteorology. Recent research has utilized long-term databases from precipitation radars and ground-based sensors to train and refine models for radar-based QPE (Zhang et al. 2021; Yo et al. 2021; Hassan et al. 2022). AI-based algorithms have also enhanced radar-based QPE by providing improved hydrometeor classification (Roberto et al. 2017; Wang et al. 2017; Lu and Kumar 2019) or advanced radar-gauge merging methods (Zhang et al. 2022).

Chapter 3

Precipitation Sensors and Data Processing

This chapter covers the collection and processing of data from ground-based instruments that provide DSD information, and radar observations used for precipitation retrieval.

3.1 Ground-based instruments providing DSD information

In this study, DSDs measured by local disdrometers or retrieved from vertically-pointing radars are utilized as inputs to T-matrix scattering calculations for radar variable simulations (Waterman 1971). The following subsections introduce the working principles of these devices and the associated data processing techniques.

3.1.1 Thies Clima Laser Precipitation Monitor

Measurements of Thies Clima Laser Precipitation Monitor (LPM) disdrometers from DWD are chosen to investigate the impact of DSD variability on key parameters of rainfall retrievals at C-band. LPM, an optical laser-based disdrometer, utilizes an infrared beam with a wavelength of 785 nm and a total horizontal area of 45.6 cm^2 (228 mm $\times$ 20 mm $\times$ 0.75 mm) to observe D and fall velocity V_T (m s^{-1}) of individual hydrometeors, from which DSDs are estimated. It separates particles into 22 D- and 20 V_T- classes resulting in a D-V_T matrix with 440 bins saved as telegrams transmitted every minute by the instrument (Bloemink et al. 2005). The data used in this study and their processing procedures follow Chen et al. (2021a), but with additional details provided below.

Northwestern Germany and the coast in the north are under the maritime influence, exhibiting DSD characteristics similar to those of tropical rain with relatively high N_w and small D_m values. In contrast, the climate becomes more continental-like farther inland and towards the south. In such transition zone from the European marine regime to the continental regime in Germany, it is crucial to gather representative DSDs. However, due to limited access to the DWD LPM data, measurements from 68 LPMs operated within a 150-km range of six DWD C-band radars are selected. These radars include Hannover (HNR), Essen (ESS), Boostedt (BOO) radar in the northwest, and Isen (ISN), Memmingen (MEM), Eisberg (EIS) radar in southeast part of Germany (Fig. 3.1 purple triangles and dots). From these disdrometers, thirty rain days covering various types of precipitation across different seasons from 2015 to 2017 are chosen and listed in Table 3.1. In total, 1,020,000 1-minute DSDs were collected, including the LPM measurements from the rooftop of the Institute for Geosciences, Department of Meteorology at the University of Bonn (Fig. 3.1 cyan dot) between October 2011 and April 2019.

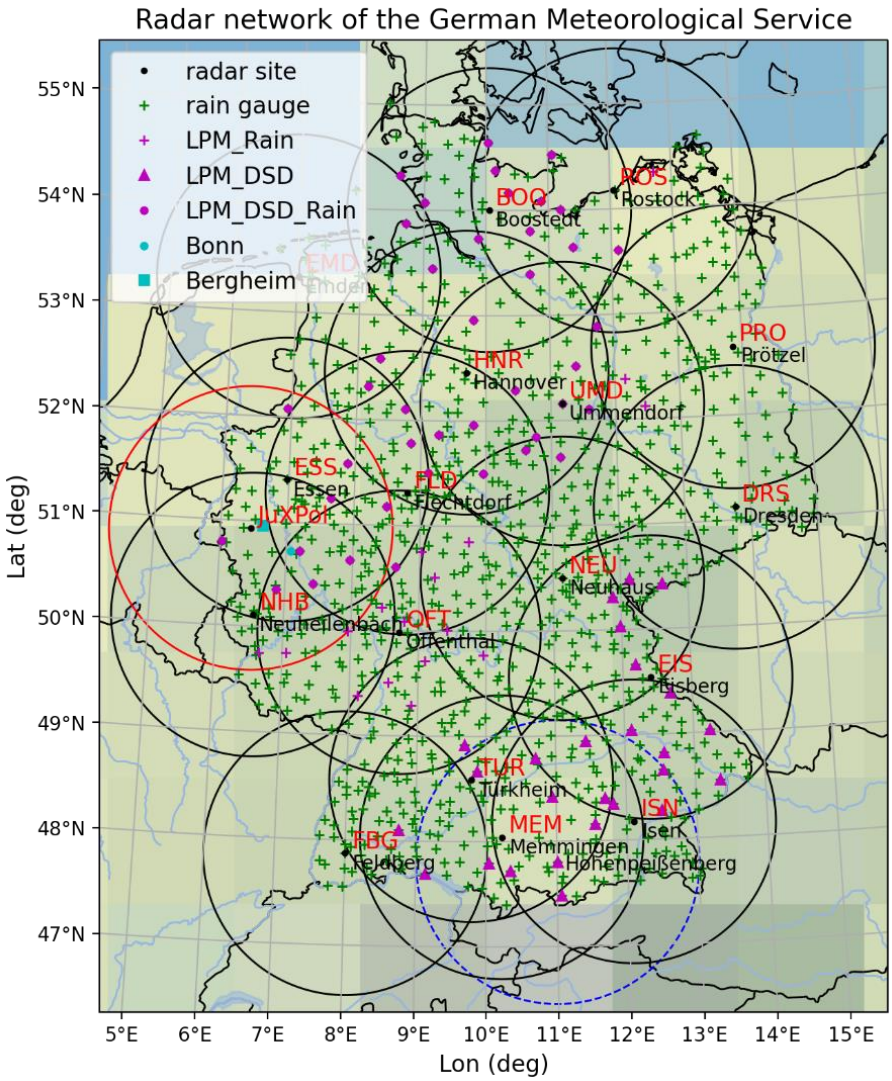

Figure 3.1 Spatial coverage of the current radar network operated by the German Meteorological Service (DWD, Deutscher Wetterdienst), and a local research radar operated by the Laboratory for Clouds and Precipitation Exploration (CPEX-LAB). Distributions of the ground-based precipitation sensors from DWD and the University of Bonn are also depicted. The black circles correspond to the measurement ranges (150 km) of the operational radars, and the measurement range of the research radar in Hohenpeißenberg is represented with the blue dotted circle. The red circle highlights the measurement range of the local X-band research radar, JuXPol, situated near Jülich. The green/purple crosses mark the locations of rain gauges/Thies Clima Laser Precipitation Monitor (LPM) disdrometers utilized for quantitative precipitation estimation (QPE) evaluations. The purple triangles are the LPMs used for QPE algorithm developments, and the purple dots are those used for both QPE evaluations and algorithm developments. The cyan dot indicates the location of the Institute for Geosciences, Department of Meteorology, University of Bonn where the LPM and Micro Rain Radar (MRR) are co-located. The cyan square is the MRR installed in the village of Bergheim.

Table 3.1 Dates on which the measurements of Thies Clima Laser Precipitation Monitor (LPM) disdrometers from the German Meteorological Service (DWD, Deutscher Wetterdienst) were used for quantitative precipitation estimation (QPE) algorithm developments. The locations correspond to radar sites within a 150-km range of which the selected LPMs were installed.

location	date [yyyy/mm/dd]
HNR, ESS, BOO	2015/10/15-16, 2015/11/14-15, 2015/11/30, 2015/12/11-12, 2016/06/20, 2016/06/23-25, 2017/03/19, 2017/07/19, 2017/07/24-25, 2017/09/30, 2017/10/05
ISN, MEM, EIS	2015/10/13-14, 2015/11/20, 2015/12/01, 2016/06/16-17, 2016/06/25, 2017/02/28, 2017/03/09, 2017/03/18, 2017/07/26, 2017/10/03, 2017/11/05

In the quality control procedure for the collected data, four criteria are employed to filter out undesired and unreliable data:

i. Particles whose observed V_T deviates from the expected fall velocity of a raindrop $V_T^{exp.}$, as determined by the equation

$$V_T^{exp.}(D) = -0.1021 + 4.932\mathrm{D} - 0.9551D^2 + 0.07934D^3 - 0.002362D^4 \quad (3.1)$$

(Brandes et al. 2002), by a factor of 0.5 or more are excluded from the D-V_T matrix (e.g., Fig. 3.2), because they may not be raindrops (Tokay et al. 2013).

ii. In addition to the filtering based on V_T deviation, isolated single raindrops without any particles measured in the neighboring eight bins in the matrices are also removed as outliers. Together, these criteria led to the elimination of 30% of the particles.

iii. The remaining data in each D row of the cleaned matrixes are summed up and further averaged using a 5-minute moving window for noise reduction. Note that in this smoothing process, only DSDs recorded in consecutive 5-minute intervals and reporting as precipitation are included. This resulted in a total of 187,211 DSDs. The smoothed datasets are then converted from the measured number to the concentration, namely $N(D)$.

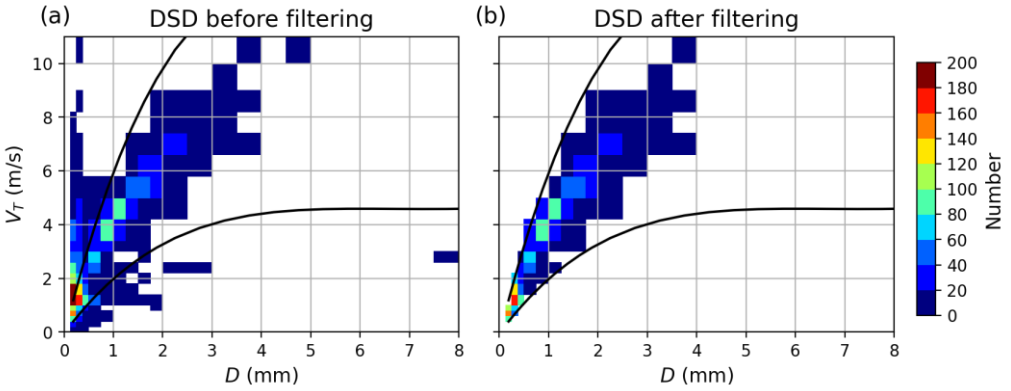

Figure 3.2 Matrices of D and fall velocity V_T of observed particles (a) before and (b) after filtering based on the empirical relation between the measured D and the expected fall velocity $V_T^{exp.}$ of a raindrop from Brandes et al. (2002). The filtering excludes particles whose observed V_T deviates by 0.5 or more from $V_T^{exp.}$ (black lines).

iv. DSDs containing particles identified as solid by the software or with rain intensities calculated from DSDs using Eq. (2.8) less than 0.1 mm h^{-1} are also excluded, resulting in 84,169 DSDs.

Apart from their use in T-matrix simulations, the processed DSDs can be utilized to derive other DSD parameters and integral variables such as N_w, D_m, LWC, and R using Eqs. (2.5)-(2.8). Note that the derived R then can be utilized for QPE evaluations (Fig. 3.1 purple crosses and dots).

3.1.2 Micro Rain Radar

The Micro Rain Radar (MRR) is a K-band (24 GHz) microwave profiler that measures the Doppler spectra of hydrometeors within a sampled volume, providing information on Z and V_T (Figs. 3.3a/b). Using an empirical relation between D and V_T, DSDs are retrieved from the measured Z and V_T profiles at each height bin (Metek 2012). These DSDs are then used to derive integral variable profiles and simulate polarimetric radar variables for the study purposes (Reinoso-Rondinel and Schleiss 2021). Additionally, the DSDs help correct the attenuation of observed Z profiles in an iterative manner starting from bins near the surface towards bins at higher altitudes, assuming negligible PIA at the ground (Figs. 3.3c/d, Peters et al. 2010). This attenuation correction can be made without polarimetric measurements and is available directly from the MRR software. It is, however, only applicable to liquid precipitation and feasible for data with $PIA \leq 10$ dB, as the correction algorithm becomes unstable above this threshold (e.g., right after 1800 UTC in Fig. 3.3d).

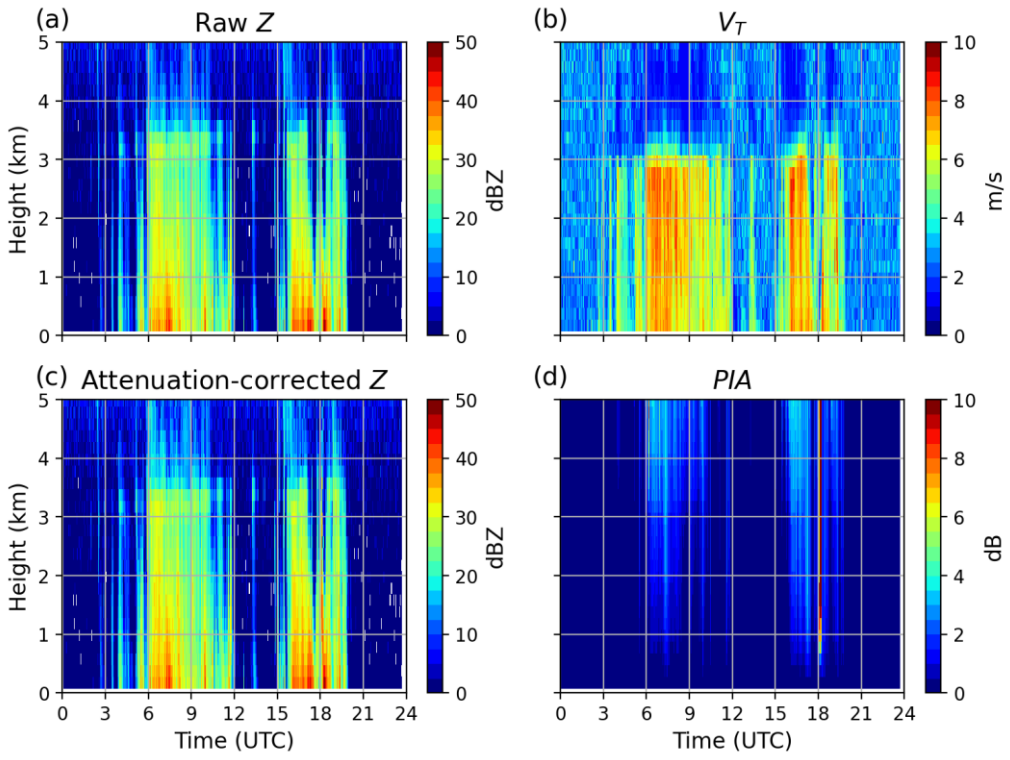

Figure 3.3 Vertical profiles (VP) of MRR-measured (a) reflectivity Z without attenuation correction, (b) V_T, (c) attenuation-corrected Z, and (d) two-way path-integrated specific attenuation (PIA) in Bergheim on 14 July 2021.

In the present case, the ML height is estimated to be 3 km based on the clear vertical gradient of V_T shown in Fig. 3.3b, which signifies the complete transformation of snowflakes into raindrops. The attenuation correction method proposed by Peters et al. (2010), however, becomes invalid above the ML height due to the occurrence of mixed-phase or solid precipitation, leading to considerable weak Z above this height. Furthermore, the DSD retrieval from Doppler velocity spectra may not account for the effects of vertical wind speeds, potentially affecting the results. To ensure high data quality, only observations of stratiform rain events with clear MLs implying weak vertical wind draft, and data with PIA less than 10 dB and below the ML height are used in this study.

The MRR offers thirty bins and allows users to choose a vertical bin resolution between 10 to 200 m, depending on their research needs. In this study, data from two MRRs located in Bonn and Bergheim (Fig. 3.1 cyan dot and square) were used. The data had a bin resolution of 200 m, covering a vertical range of up to 6 km, and were collected at a temporal resolution of 1 minute. The retrieved DSDs were smoothed using a 5-minute moving-window average, similar to the LPM observations, before being input into the T-matrix simulation.

3.2 Radar measurements for precipitation retrieval

This section provides an overview of the DWD C-band radars and a local X-band research radar. Furthermore, it outlines the quality-control procedures utilized to ensure the reliability of data collected by these radars at both frequencies.

3.2.1 German C-band radar network

DWD operates a network of 17 polarimetric Doppler C-band radars, which are named after the towns where they are installed (Fig 3.1 black circles, Helmert et al. 2014). Two scanning strategies, both with a 1-deg azimuthal resolution, are utilized for different applications (Table. 3.2). The precipitation scan is the first choice for generating QPE products, with a radial resolution of 250 m and a measurement range of 150 km. This scan mode involves terrain-following elevation angles that change azimuthally between 0.2 and 1.8 deg to minimize the effects of PBB and most ground clutters (Fig. 3.4). The second strategy is the volume scan mode, which scans at fixed elevation angles and covers a decreasing radial range from 180 km to 60 km as elevation angles increase. The radial resolution of this mode was upgraded from 1,000 m to 250 m in March 2021. Additionally, DWD performs a vertical scan at each time step for Z_{DR} calibration. The precipitation scan is first conducted, followed by the volume scans and the vertical scan in 5-minute cycles.

This study develops the $R(A)$ rainfall algorithm using six rain events, which caused severe local flooding over Germany. Among the six events, four are convective events characterized by organized squall lines and intense rain mixed with small-to-moderate hail, propagating from west to east (case [1], [3], [4], and [7] outlined in Table 3.3), and two are stratiform events characterized by widespread, intense, and continuous rain (case [2] and [11]). Case [11] is additionally chosen to assess the performance of the algorithms aimed at correcting biases from vertical precipitation gradients. Case [5], a stratiform rain event with a very low ML height, is selected for evaluating the efficacy of the correction method attempting to mitigate Z biases within and above the ML. Finally, the polarimetric snowfall algorithm is investigated using the observations made during case [5] and four snowfall events (case [6], [8], [9], and [10]).

Table 3.2 Specification of precipitation and volume scans obtained from the DWD polarimetric Doppler C-band radars.

type of scan	elevation (deg)	radial resolution (m)	number of range bin	max. slant range (km)
precipitation	terrain-following	250	600	150
volume 0	5.5	1000/250	180/720	180
volume 1	4.5	1000/250	180/720	180
volume 2	3.5	1000/250	180/720	180
volume 3	2.5	1000/250	180/720	180
volume 4	1.5	1000/250	180/720	180
volume 5	0.5	1000/250	180/720	180
volume 6	8.0	1000/250	124/496	124
volume 7	12.0	1000/250	60/240	60
volume 8	17.0	1000/250	60/240	60
volume 9	25.0	1000/250	60/240	60

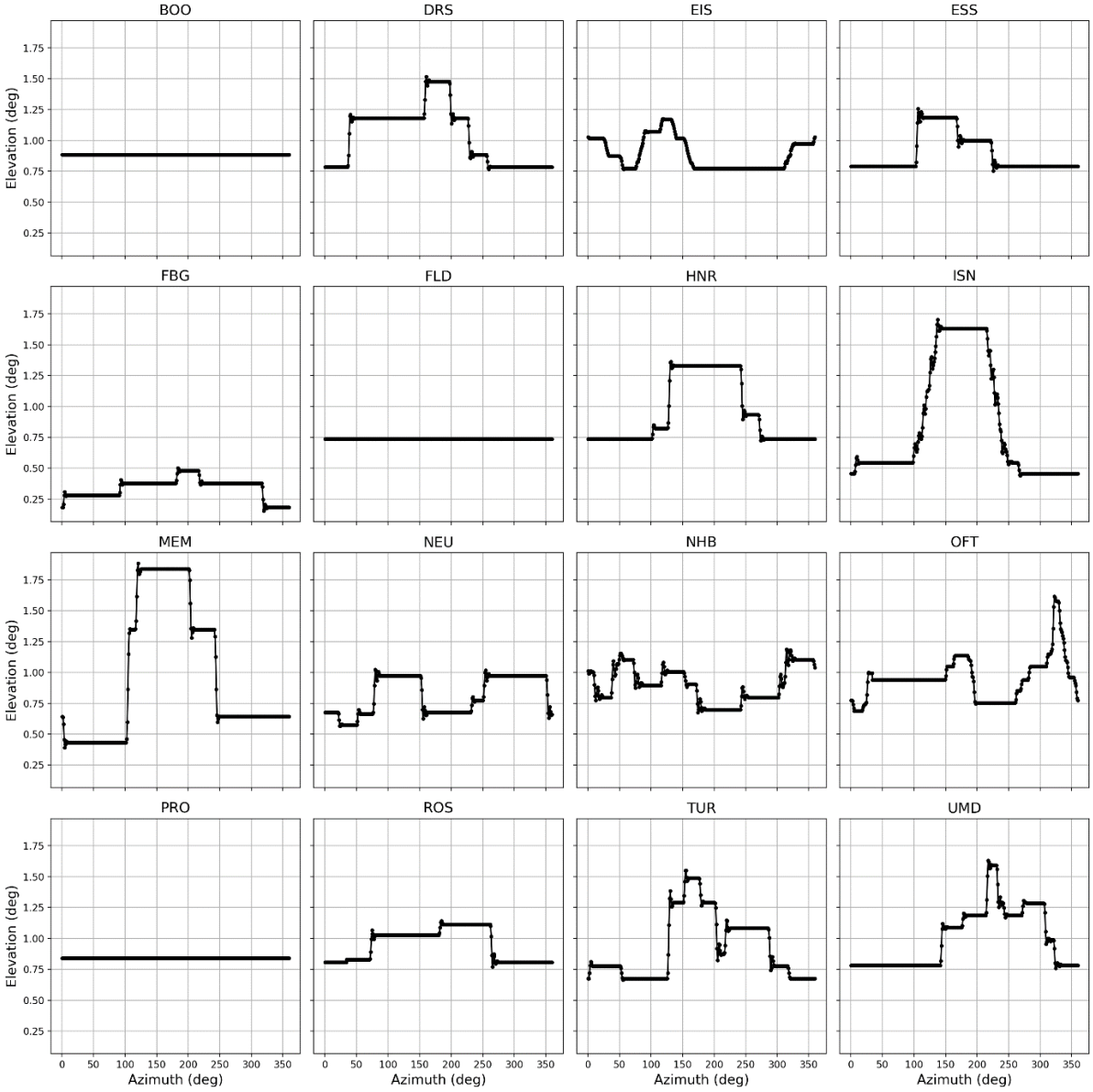

Figure 3.4 Terrain-following elevation angles of the DWD precipitation scans obtained from each radar.

Table 3.3 Information on studied precipitation events, including time period, precipitation type, bottom height of the melting layer (ML) above mean sea level (MSL), denoted as H_b, maximum hourly accumulated precipitation measured by rain gauges, and the radars involved.

No.	time [yyyy/mm/dd] [hh-hh UTC]	precipitation type	lowest H_b (m)	max. hourly precipitation (mm)	used radars
1	2017/07/19 1200-2400	convective rain	2600	48.8	BOO, DRS, ESS, FLD, HNR, NEU, OFT, PRO, ROS, UMD
2	2017/07/25 0000-2400	stratiform rain	1700	38.5	BOO, DRS, ESS, FLD, HNR, NEU, OFT, PRO, ROS, UMD
3	2018/07/28 1200-2400	convective rain	2500	36.7	BOO, DRS, ESS, FLD, HNR, OFT, PRO, ROS, UMD
4	2018/08/09 1200-2400	convective rain	3000	28.2	BOO, DRS, ESS, FLD, HNR, OFT, PRO, ROS, UMD
5	2018/09/23 1000-2400	stratiform rain with low ML	900	24.1	ESS, FLD, HNR, PRO, UMD
6	2019/02/03 0000-2400	snow	x	6.3	DRS, EIS, ISN, MEM
7	2019/07/20 1200-2400	convective rain	2500	30.5	BOO, DRS, ESS, FLD, HNR, OFT, PRO, ROS, UMD
8	2021/01/14 0000-2400	snow	x	5.7	FBG, MEM, TUR
9	2021/01/24 0400-1200	snow	x	4.2	ESS, FLD, OFT
10	2021/02/07-08 0000-2400	snow	x	5.0	DRS, HNR, PRO, UMD
11	2021/07/14 0000-2400	stratiform rain	2500	63.5	ESS, FLD, NHB, OFT

3.2.2 Local X-band radar, JuXPol

JuXPol is a local polarimetric Doppler X-band radar that forms a part of the Laboratory for Clouds and Precipitation Exploration (CPEX-LAB, http://www.cpex-lab.de/) infrastructure. The radar is installed atop the artificial hill Sophienhöhe, which was created as a result of nearby open-pit lignite mining. It is located approximately 6 km east of the city center of Jülich and named accordingly as JuXPol (Fig. 3.1 red circle). In the current study, it functions as a gap-filling radar between the DWD radars ESS and Neuheilenbach (NHB) for the study case [11]. JuXPol provides data with radial and azimuthal resolutions of 25-150 m and 1 deg, respectively (Table. 3.4). A range height indicator (RHI) scan and 11 volume scans, which include a vertical scan, are scheduled every 5 minutes. The lowest elevation scan at 0.6 deg is used here for rainfall estimation.

Table 3.4 Specification of volume and range height indicator (RHI) scans obtained from the local polarimetric Doppler X-band radar, JuXPol.

type of scan	elevation/ azimuth (deg)	radial resolution (m)	number of range bin	max. slant range (km)
volume 0	28.0	100	360	36
volume 1	18.0	100	500	50
volume 2	14.0	100	620	62
volume 3	11.0	100	800	80
volume 4	8.2	100	1050	105
volume 5	6.0	100	1400	140
volume 6	4.5	150	1000	150
volume 7	3.1	150	1000	150
volume 8	1.7	150	1000	150
volume 9	0.6	150	1000	150
vertical	90.0	25	1200	30
RHI	235	75	666	50

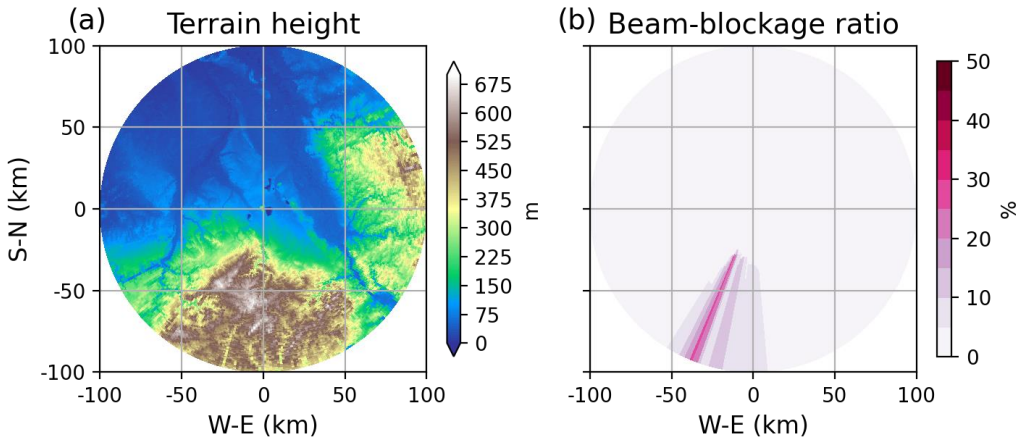

Figure 3.5 (a) Topography height and (b) beam-blockage percentage of the 0.6-deg elevation scan from the local polarimetric Doppler X-band radar JuXPol.

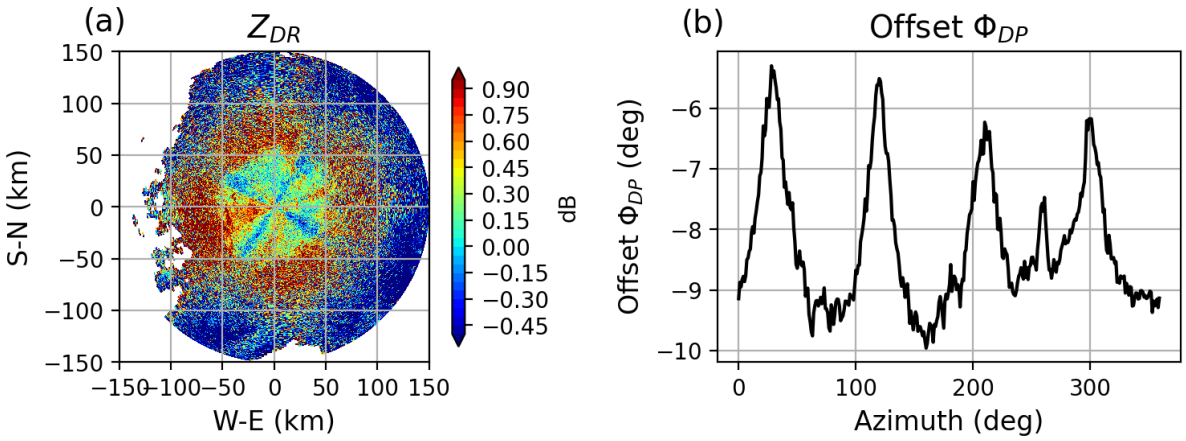

Figure 3.6 (a) Field of differential reflectivity Z_{DR} and (b) azimuthal offset change of differential phase shift Φ_{DP} caused by lightning protection installed in the radome of the Flechtdorf (FLD) radar on 25 July 2017 at 1945 UTC.

3.2.3 Quality control

Since the DWD radars provide scans with terrain-following elevation angles and JuXPol experiences minimal beam blocking (only 25% less in the southwest as shown in Fig. 3.5), this study does not perform additional error correction for PBB. The lightning protection equipped symmetrically around the radome of the DWD radars, however, could result in Z_{DR} biases at the position of lightning rods (Fig. 3.6a), and so far no practical solution has been developed yet for this issue. At the DWD radar sites, signal processors remove undesired echoes using a set of thresholds for noise, signal quality index, signal power, clutter power, ρ_{HV}, and speckle filtering (Werner 2014 and 2017). A similar processing routine is also applied to JuXPol measurements. Consequently, pre-processed Z and Z_{DR} are chosen, and post-processing procedures for the power-based variables are applied to both C-band radars and JuXPol. These procedures include:

i. Noise correction for ρ_{HV} and non-weather signal removal:
   In this study, the noise correction method for ρ_{HV} as described in section 2.3 is employed. Specifically, the constant value C in Eq. (2.45) is determined through an incremental increase of 0.2 dB to C until the corrected ρ_{HV} values within the range of 0.95 and 1.01 have the highest proportion in the dataset with SNR less than 20 dB. In the illustrated example in Fig. 3.7, C is found to be 38 dB, leading to increased ρ_{HV} values particularly in areas where SNR < 10 dB. To eliminate non-meteorological signals, a threshold value of 0.8 for ρ_{HV} is set. Following the noise correction, both the X- and C-band radars are able to retain meteorological signals at far distances where SNR values are low (Fig. 3.8).

ii. Removal of isolated points and patching of small holes:
   Isolated data points refer to cases where the number of valid points from the neighboring eight bins is three or less. Such cases may arise from inadequate elimination of ground clutter with higher ρ_{HV} values relative to the surrounding clutter. Subsequently, the removal of these data points is followed by a hole-filling process using the mean of neighboring data points. Note that at least five out of eight bins must be valid for the interpolation to take place.

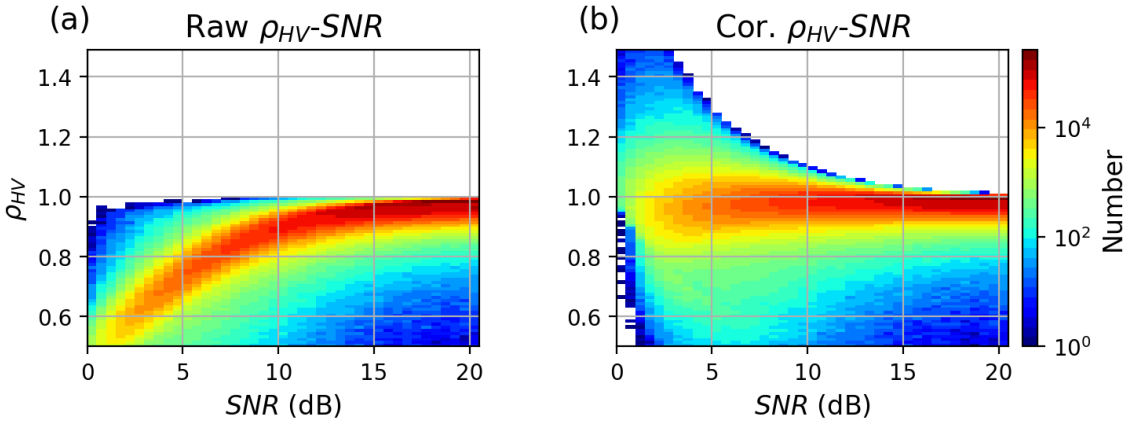

Figure 3.7 Scatterplots of co-polar correlation coefficient ρ_{HV} (a) before, and (b) after noise correction, against the signal-to-noise ratio SNR obtained from the observations of the Ummendorf (UMD) radar on 25 July 2017.

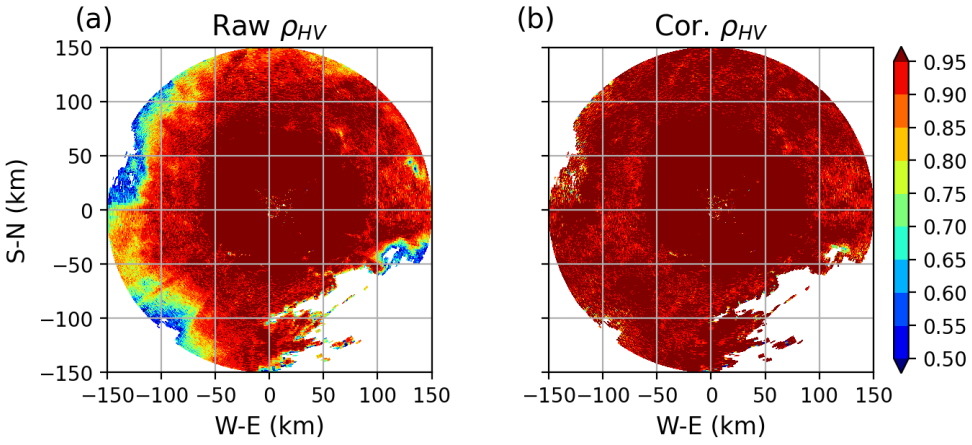

Figure 3.8 Fields of (a) raw ρ_{HV} and (b) ρ_{HV} with noise correction applied, from the observations of UMD on 25 July 2017 at 1230 UTC.

iii. Attenuation correction for Z and Z_{DR}:

During pure rain events, the attenuation of $Z_{H/V}$ below the ML is corrected using PIA. This approach uses preset average values of $\alpha_{H/V}$ at the two polarizations: 0.093 and 0.071 dB deg^{-1} for C-band, and 0.31 and 0.27 dB deg^{-1} for X-band, respectively. These values are estimated via the relation $A_{H/V} = \alpha_{H/V} K_{DP}$ fitted to the simulated $A_{H/V}$ and K_{DP} values from the local LPM-measured DSDs. Correction of Z_{DR} is performed with β values of 0.021 and 0.046 dB deg^{-1} at C- and X-band, respectively. The advanced method proposed by Gu et al. (2011) that considers HS is only applied to the observations from three DWD radars. These radars are deliberately selected to assess the feasibility of segment-wise application in the ZPHI algorithm (see section 4.2).

Regarding the attenuation of melting snow, $\Delta\Phi_{\mathrm{DP}}$ within the ML is multiplied by three for PIA and PIA_{DP} calculations. Since the attenuation caused by snowflakes/crystals is thought to be negligible, only PIA/ PIA_{DP} obtained ahead of the top height of the ML, denoted as H_t, is counted and carried over to the observations above it.

iv. Calibration of Z and Z_{DR}:

The calibration of Z for the DWD radars is achieved through the use of solar radio emissions and is performed on the radar-site computer; therefore, no calibration is required by users. Moreover, Z_{DR} offset values have been archived for each volume scan since August 2017, enabling users to extract them from the files and calibrate the data accordingly. In cases where observations were made prior to this time, the mean value of Z_{DR} in weak-echo regions is used.

JuXPol utilizes a self-consistency method for Z calibration, as detailed in section 2.3. The $K_{DP}(Z_h)$ relation used in the process is given by

$$K_{DP}(Z_h) = 0.0012 Z_h^{0.64} \tag{3.2}$$

at X-band. As a result, an average of 4.8 dBZ was added to the Z_H measurements on 14 July 2021 (Fig. 3.9). As for Z_{DR}, the observed Z_{DR} values were adjusted by subtracting the mean value of Z_{DR} obtained from vertical scans, estimated to be 0.9 dB for the same study day (Fig. 3.10).

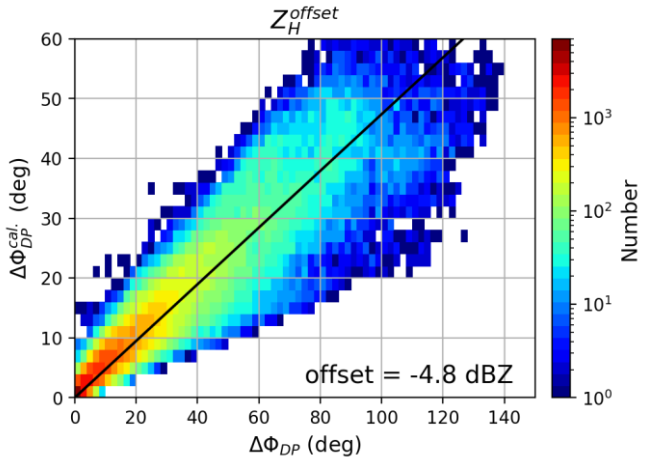

Figure 3.9 Scatterplot of the total span of calculated differential phase shift $\Delta\Phi_{DP}^{cal.}$ against measured differential phase shift $\Delta\Phi_{\mathrm{DP}}$ from JuXPol on 14 July 2021. The ratio of $\Delta\Phi_{DP}^{cal.}$ to measured $\Delta\Phi_{\mathrm{DP}}$ is used to derive the offset of reflectivity at horizontal polarization, Z_H^{offset}.

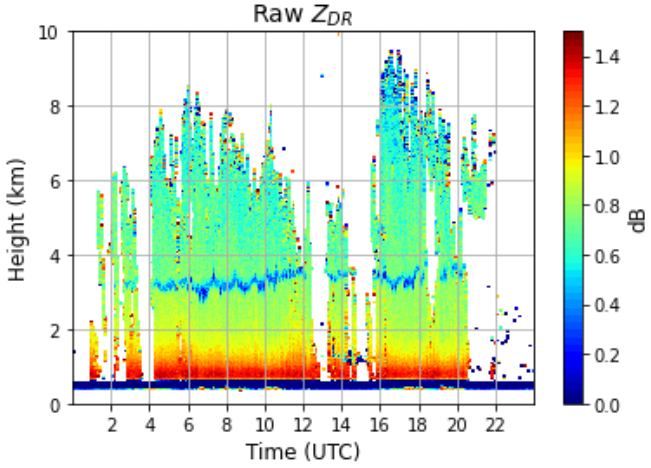

Figure 3.10 Z_{DR} field from vertical scans obtained from JuXPol on 14 July 2021.

v. Areal smoothing:

To enhance the accuracy of snowfall estimates by reducing the impact of wind advection and noise at far ranges from the radar site caused by beam-broadening effects, the Z field in snow undergoes additional smoothing. This process involves averaging each radar bin with its adjacent points within a radius of 3 km, and the smoothing is performed in a linear unit.

The Φ_{DP} processing is critical for the investigated QPE algorithms as the accuracies of both K_{DP} and A strongly depend on the Φ_{DP} quality. In particular, the disturbance originating from strong δ at C-band requires mitigation (Trömel et al. 2013 and 2014b). To this end, this study applies a series of consecutive steps for Φ_{DP} processing and K_{DP} estimation, as outlined below:

i. Unfolding Φ_{DP}:

Due to a folding effect in the Φ_{DP} field, values exceeding 180 deg fold to -180 deg. Thus, 360 deg is added to Φ_{DP} if its value falls below the initial estimated offset value.

ii. First filtering:

To remove radar bins with poor Φ_{DP} quality, those with Φ_{DP} standard deviations above a given value within a moving window of five bins are excluded. For radar data with a 1-km radial resolution, a threshold of 10 deg is applied, while a higher threshold of 20 deg is used for finer-resolved data (i.e., 250 m or less). Additionally, non-weather signals and isolated points are removed as well.

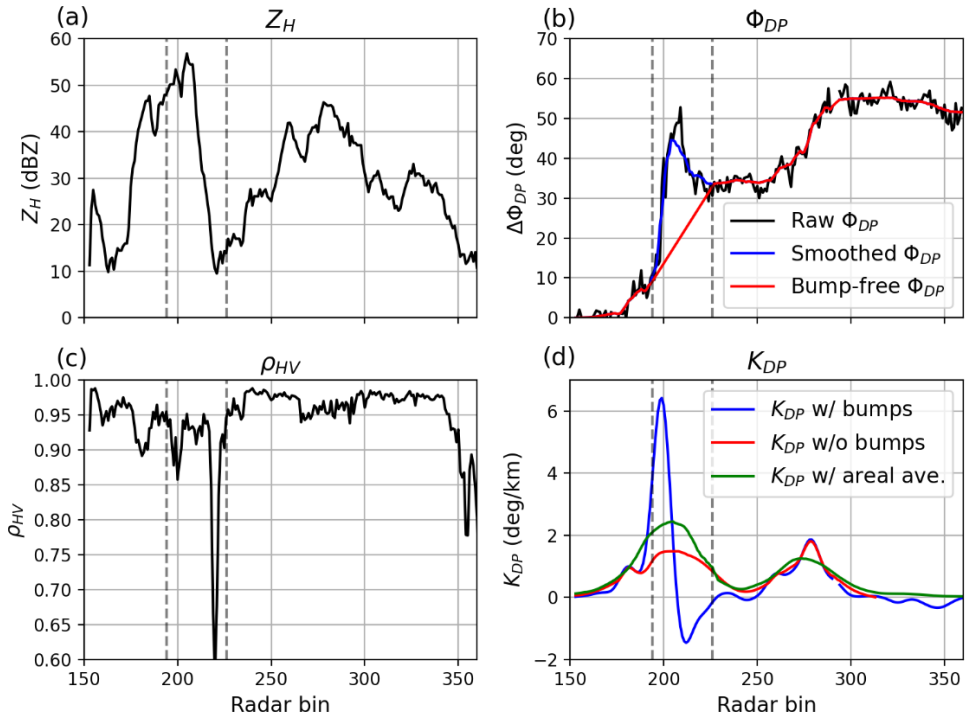

Figure 3.11 Radial profiles of radar variables at the 220.5-deg azimuth from the Boostedt (BOO) radar on 28 July 2018 at 1335 UTC, including (a) reflectivity at horizontal polarization Z_H (in dBZ), (b) raw Φ_{DP} in black, smoothed Φ_{DP} in blue and bump-free Φ_{DP} in red, (c) ρ_{HV}, and (d) K_{DP} in blue/red derived before/after bump removal, and K_{DP} in green with further areal smoothing. The detected Φ_{DP} bump is marked between two gray dashed lines.

iii. Second filtering:

When the Φ_{DP}-difference between an observation and its mean value within a moving window of 17 range bins is larger than 1.25 times the standard deviation of the same window, the observed Φ_{DP} value is replaced with the mean value (Hubbert and Bringi 1995). This filtering process is iterated five times.

iv. Smoothing:

The resulting Φ_{DP} is further smoothed by an unweighted average with a moving window of five range bins (Fig. 3.11b blue line).

v. Correction for Φ_{DP} bumps:

The presence of NBF effects at C-band frequencies, e.g., at the edges of strong convective cells where ρ_{HV} values decrease, can cause considerable excursions from a monotonic increase of Φ_{DP} along the ray (Figs. 3.11a-c black lines, Ryzhkov and Zrnić 2005). In some cases, these bumps may be too large to be corrected through the filtering and smoothing methods introduced earlier, and may lead to wrong estimates of K_{DP}: abnormally high K_{DP} values before the cell followed by small or even negative values within the HS (Fig. 3.11d blue line). Therefore, Φ_{DP} bumps should be identified and corrected before deriving K_{DP}.

To this goal, K_{DP} is temporarily estimated from the smoothed Φ_{DP} (Fig. 3.11b blue line) using a 2-km window size following Vulpiani et al. (2012). The interval below the ML encompassing the segment with Z_H larger than 50 dBZ and negative K_{DP} backside is regarded as the potential location of the bump. As bumps always exhibit a rapid increase in Φ_{DP} in front, the starting point of the interval is determined by searching forward from the segment until the Φ_{DP} difference between two consecutive bins drops less than 1.5 deg. The endpoint is defined as the last bin with a negative value of K_{DP} extending behind the segment. The data within this interval, i.e., between the gray dashed lines in Fig. 3.11, are removed and filled with linear-interpolated values (Fig. 3.11b red line).

vi. $\Delta\Phi_{DP}$ (total span of Φ_{DP} below the ML) calculation:

The offset of Φ_{DP} shows an azimuthal change due to the radome effects. Therefore, the offset is determined for each ray by calculating the median value of the first-five valid Φ_{DP} data along each ray over all time steps (Fig. 3.6b). The $\Delta\Phi_{DP}$ field can then be obtained by subtracting the Φ_{DP} offsets from the smoothed Φ_{DP}.

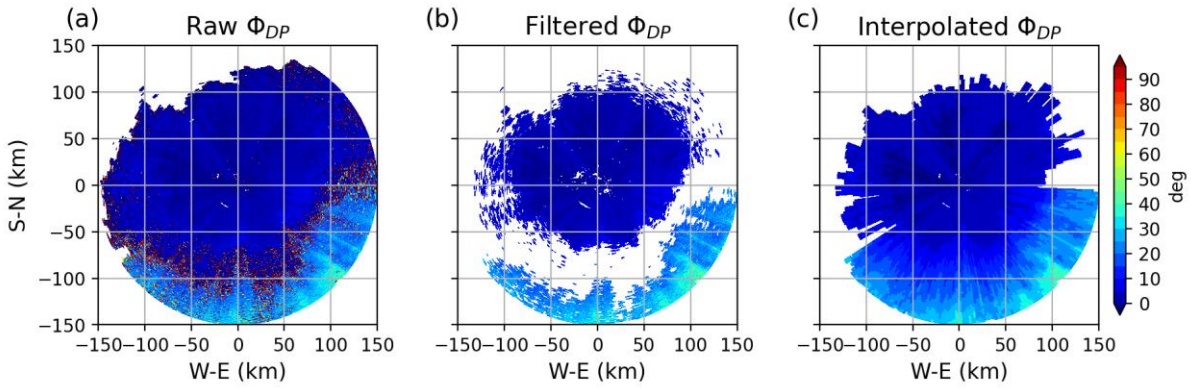

Figure 3.12 Fields of (a) raw, (b) filtered, and (c) interpolated Φ_{DP} from the observations of the Hannover (HNR) radar on 25 July 2017 at 0740 UTC.

vii. Linear interpolation:

It is apparent from the observations of the HNR, Neuhaus (NEU), and Offenthal (OFT) radars that Φ_{DP} experiences significant instability within certain value ranges (Fig 3.12a). Even with the aforementioned procedure, these noises cannot be completely filtered out and thus need manual removal (Fig 3.12b). During weak precipitation, low-quality Φ_{DP} can persist over long distances if it falls within this specific range. In such cases, linear interpolation is employed to fill the gap (Fig 3.12c). The ensuing $\Delta\Phi_{\mathrm{DP}}$ field is then utilized to calculate PIA and PIA_{DP} for attenuation correction and to retrieve K_{DP}.

viii. Correction of noisy $\Delta\Phi_{\mathrm{DP}}$ for the use in the ZPHI method:

In light rain, Φ_{DP} is susceptible to noise and small fluctuations, leading to unreliable values of $\Delta\Phi_{\mathrm{DP}}$ used for PIA calculations. To address this issue, a strategy is adopted to replace $\Delta\Phi_{\mathrm{DP}}$ values below 5 deg within the rainy segment with $\Delta\Phi_{DP}^{cal.}$ derived from quality-controlled Z_h. The $K_{DP}(Z_h)$ relation for obtaining $\Delta\Phi_{DP}^{cal.}$ at X-band is given as Eq. (3.2), while for C-band it is defined as

$$K_{DP}(Z_h) = 0.00016 Z_h^{0.83}. \tag{3.3}$$

Finally, to ensure smoothness and continuity of the resulting data along the azimuth, the final $\Delta\Phi_{\mathrm{DP}}$ is smoothed by the mean of the four closest rays if it remains below 10 deg.

ix. K_{DP} estimation:

In order to better capture the texture of convective cells while reducing noise in light rain, two different window sizes are employed for the K_{DP} calculation during rain events. Specifically, a 2-km window is applied when attenuation-corrected Z_H exceeds 40 dBZ, and a 6-km window is used for Z_H values below 40 dBZ (Fig. 3.11d red line). To mitigate the discontinuities at the switch between these conditions, K_{DP} along the ray is averaged using a 5-bin moving window. In contrast, K_{DP} is always derived using a 6-km window for snow observations.

x. Areal smoothing for K_{DP}:

The process of areal averaging for Z_H in snow is similarly applied to K_{DP}, but for all precipitation conditions. It should be noted that prior to this process, any remaining negative K_{DP} values in rain are set to NaN. Finally, the smoothed K_{DP} field displaying fewer negative values is deemed suitable for QPE (Fig. 3.11d green line).

Even though neither the original Φ_{DP} field (Fig. 3.11b blue line) nor the filled artifact (Fig. 3.11b red line) can provide the true pattern of K_{DP} within the bump interval, the latter does yield less problematic values. Note that Chen et al. (2021a) utilized proxy K_{DP} in heavy rain, which is calculated using quality-controlled Z_h and constraint $\Delta\Phi_{\mathrm{DP}}$ (Lim et al. 2013; Zhang et al. 2013), as a means of mitigating the impact of Φ_{DP} bump on QPE. This proxy, however, is only valid in pure rain and not suitable for the presence of bumps, as it may signify hail. Therefore, it is irrelevant for this study.

Chapter 4

Methodologies for QPE and Their Assessment

This chapter details the methodology employed to establish regional polarimetric rainfall relations using measured DSDs. Subsequently, the proposed radar-based QPE approaches are elaborated, including the modified/optimized $R(A)$ algorithms for C-band radars, the application of VP correction to observations below the ML and gap-filling for warm-rain precipitation, the PVPR correction method aimed at Z biases within and above the ML, and the use of polarimetry for snowfall quantification. Finally, the chapter introduces the compared QPE retrievals and methodologies used for evaluation.

4.1 T-matrix simulation and rainfall algorithms for C-band radar

The T-matrix method is a computational technique for simulating non-spherical scattering (Waterman 1971). In this study, the processed DSDs are used in T-matrix simulations to compute the polarimetric variables at various frequencies and temperature environments. These simulations assist in optimizing the parameters required for radar data quality check and the ZPHI method, as well as coefficients in rainfall relationships for the regional precipitation climatology. One of the publicly available T-matrix code packages is chosen and accessed at https://github.com/jleinonen/pytmatrix.

The simulation of raindrops utilizes size-dependent ar following a fourth-order polynomial equation (Brandes 2002)

$$ar(D) = 0.9951 + 0.0251D - 0.03644D^2 + 0.005303D^3 - 0.0002492D^4 \quad (4.1)$$

when D is larger than 1 mm, and equals one otherwise. Additionally, a canting angle distribution with a mean value of 0 deg and a standard deviation (σ) of 8 deg is assumed. All simulations are restricted to D values below 8 mm, which appears more appropriate for local climate conditions. The simulations are conducted at a temperature of 15°C, as the polarimetric variables, except for A and δ, are relatively insensitive to temperature. Wang et al. (2014) showed that the temperature effects on the attenuation parameter α are opposite to those on the intercept parameter in $R(A)$ relations. Such cancellation of both dependencies in the final retrieved rainfall, however, unlike at S-band is incomplete at C-band. At present, this study does not account for the temperature effects on the $R(A)$ retrieval.

The power-law rainfall relations utilized for the German C-band radar network are established based on the fitting of calculated rain rates and simulated radar variables derived from long-term LPM observations. The corresponding relations are listed below:

$$R(Z_h) = 0.052{Z_h}^{0.57}, \quad (4.2)$$

$$R(Z_h) = 0.022{Z_h}^{0.61}. \quad (4.3)$$

$$R(K_{DP}) = 20.4{K_{DP}}^{0.75}, \tag{4.4}$$

$$R(A_H) = 307{A_H}^{0.92} \text{ and} \tag{4.5}$$

$$R(A_V) = 452{A_V}^{0.98}. \tag{4.6}$$

These relations, as well as any other relations used in this study, are derived via the Levenberg-Marquardt algorithm (Levenberg 1944), which aims to solve nonlinear least squares problems. Unlike least squares polynomial fit, this regression method is less weighted by the more frequent observations with lower rain intensities, and offers a better fit in more relevant heavy rain. The $R(Z_h)$ relation in Eq. (4.2) is derived from the entire database, while Eq. (4.3) is based on data with $Log_{10}(N_w)$ < 3.1 (the 10th percentiles of N_w representing continental rain) to compensate for the absence of simulations for melting graupel and hail. To align with the hybrid rainfall algorithms (see next paragraph), only data with Z_H > 40 dBZ are included for the derivation of the $R(K_{DP})$ relation, while data with Z_H < 40 dBZ are used for the $R(A_{H/V})$ relations.

Four rainfall algorithms are compared and evaluated in this study. The first algorithm is the traditional Z_h-based retrieval, which uses Eq. (4.2) for attenuation-corrected Z_H values below 55 dBZ, and Eq. (4.3) for areas with $Z_H \geq$ 55 dBZ, assuming they are hail cores or rain mixed with hail. The other three hybrid algorithms are $R(Z_h)$ [i.e., Eq. (4.2)] or $R(A_{H/V})$ retrievals in combination with the $R(K_{DP})$ retrieval when Z_H exceeds 40 dBZ, denoted as $R(Z_h, K_{DP})$ and $R(A_{H/V}, K_{DP})$, respectively. The $R(Z_h, K_{DP})$ algorithm serves as a benchmark to assess the proposed $R(A, K_{DP})$ algorithms, given its widespread use in rainfall estimation.

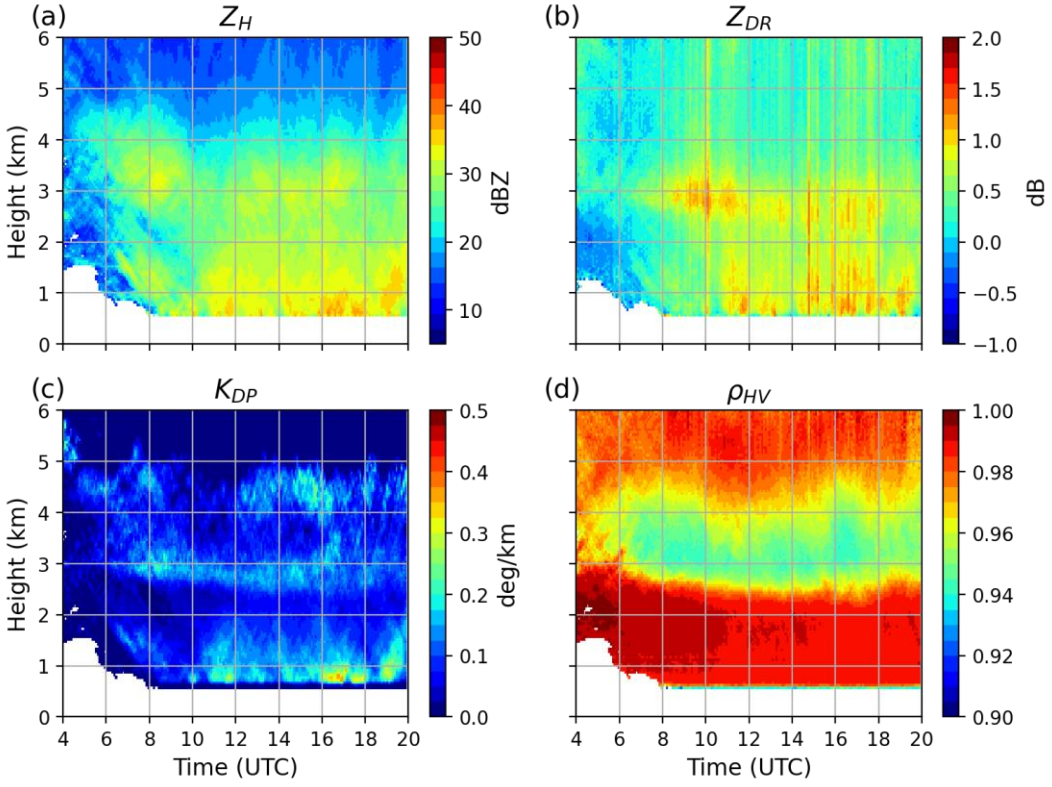

Figure 4.1 Quasi-vertical profiles (QVP) of (a) Z, (b) Z_{DR}, (c) K_{DP}, and (d) ρ_{HV} derived from Neuheilenbach (NHB) radar observations at the 1.5-deg elevation angle on 14 July 2021.

Since rainfall retrievals are only provided for radar observations below H_b, the quasi-vertical profile (QVP, Ryzhkov et al. 2016) methodology is used to detect the ML height. This approach averages radar data at a fixed elevation angle along the azimuths to generate a time-height format with significantly reduced statistical errors. Even though most radar variables exhibit changes in their values with clear bands when the radar beams intersect the ML, ρ_{HV} gives the most robust overview of BB contamination areas (Fig. 4.1 with 0-°C isotherm height at about 3.5 km). Therefore, a threshold value of 0.975 for ρ_{HV} is utilized to identify the lower boundary of the ML from the QVP. To simplify the process, the lowest H_b obtained from the scan data at the 1.5-deg elevation angle over the rain events determines the height, above which data are excluded from the analysis.

4.2 $R(A)$ rainfall retrievals

This study employs the ZPHI algorithm (Testud et al. 2000) to estimate A from C-band observations. This algorithm, however, is limited to pure rain; hence, A is computed for Z_H < 50 dBZ or outside the defined hail cores below the ML. Nevertheless, the reliable estimation of $\Delta\Phi_{\mathrm{DP}}$ over a short ray interval pose a challenge in the segment-wise integration of the ZPHI algorithm, owing to the pronounced resonance effects observed in hailstorms at C-band. As a compromise, this study adopts the approach suggested by Wang et al. (2017), which excludes the hail region from the integration path using Eqs. (6)-(7) in their paper to handle hail contamination. When Φ_{DP} bumps hinder the accurate extraction of $\Delta\Phi_{\mathrm{DP}}$ within the hail cores, the integral over K_{DP} is used as $\Delta\Phi_{\mathrm{DP}}$. Although the segment-wise application of the ZPHI algorithm is not implemented in operational environments due to the trade-off between computational efficiency and accuracy, this study accesses this application by using the data from three radars with better-quality measurements and fewer isolated convective cells.

Two methods are proposed to optimize α for A estimates at C-band: i) adaptive scan-wise α estimators derived from the DSDs through the Z_{DR} slope, and ii) estimation of ray/segment-wise α values based on the $\alpha(Z_{DR})$ relation. The following subsections provide further details on the developments of these methods.

4.2.1 Scan-wise α derived from the Z_{DR} slope

The widely-used average value of α_H at C-band is around 0.08 dB deg^{-1}, but α_H can vary from 0.05 to 0.18 dB deg^{-1} at a certain temperature, depending on the DSDs (Trömel et al. 2014a). Recent studies by Wang et al. (2019) and Zhang et al. (2020a) have shown their success in estimating real-time adjusted α_H values at S-band using the slopes of Z_{DR} dependence on Z_H. This method has been optimized and extended for the C-band algorithm development in this study (also reported in Chen et al. 2021a). The simulations based on locally-observed DSDs are first stratified into different DSD classes using N_w as a proxy, which is determined using Eqs. (2.5)-(2.7). Subsequently, α_H and α_V estimators are derived from the representative $\alpha_{H/V}$ values and Z_{DR} slopes of each class.

The dataset is stratified into eight classes based on the N_w values, using the 10$^{\mathrm{th}}$, 20$^{\mathrm{th}}$, 30$^{\mathrm{th}}$, 40$^{\mathrm{th}}$, 50$^{\mathrm{th}}$, 65$^{\mathrm{th}}$, and 80$^{\mathrm{th}}$ percentiles as thresholds (Fig. 4.2 red dashed lines). For each N_w class, representative values of $\alpha_{H/V}$ are estimated using the relation $A_{H/V} = \alpha_{H/V} K_{DP}$, which best fits the simulated $A_{H/V}$ and K_{DP} data from the DSDs (Fig. 4.3a). In deriving the α_H values, data points with Z_H > 45 dBZ in each class, and with Z_H > 40 dBZ in the first class (i.e., the

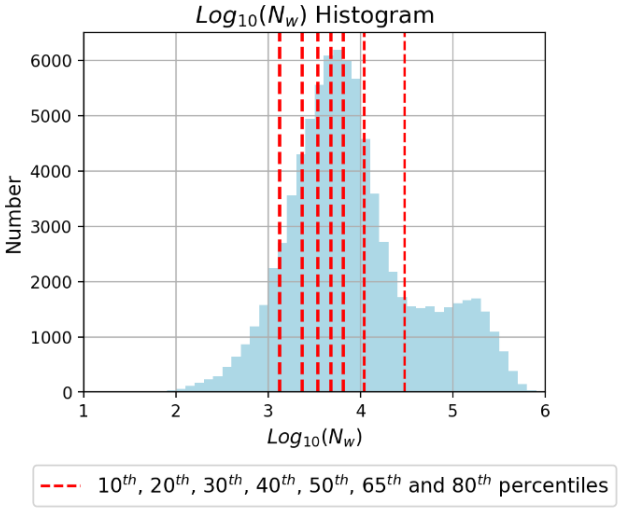

Figure 4.2 Histogram of N_w in logarithmic scale derived from 84,169 DSDs measured by the LPMs from DWD during 2015-2017 and the Institute for Geosciences, Department of Meteorology, University of Bonn during 2011-2019. The red dashed lines indicate the 10th, 20th, 30th, 40th, 50th, 65th and 80th percentiles of N_w.

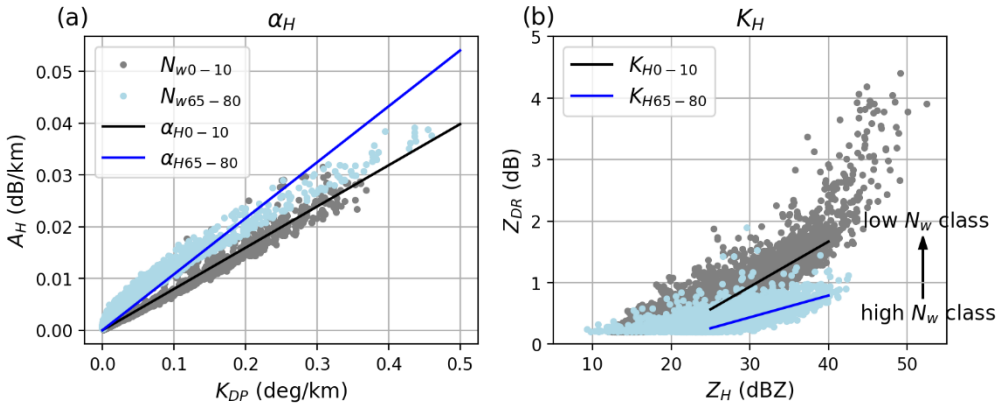

Figure 4.3 Scatterplots of (a) A_H and K_{DP}, and (b) Z_{DR} and Z_H for the two selected N_w classes: the 0th-10th percentile and 65th-80th percentile intervals (marked with subscripts). α_H is an attenuation parameter defined as the ratio of A_H to K_{DP}, and K_H is the Z_{DR} slope with respect to Z_H.

lowest N_w class) are excluded. This is because α_H values in heavy rain are relatively variable due to resonance effects, and they play a minority but influential role in fitting, which needs to be mitigated (Carey and Petersen, 2015). Fortunately, the hybrid QPE algorithms use the K_{DP}-based retrieval in this range of rain intensity. As for vertical polarization, only data points with Z_H > 45 dBZ in the first class are removed to determine the representative α_V value. In the case of the $\alpha_{H/V}$ values from the last class (i.e., N_w > 80th percentile), data points with Z_{DR} < 0.3 dB are additionally eliminated from the calculation in order to reduce the impact of very small raindrops with unrealistically high $\alpha_{H/V}$ values caused by close-to-zero K_{DP} values. Consequently, α_H of 0.153 dB deg^{-1} and α_V of 0.147 dB deg^{-1} are assigned to the last class.

The Z_{DR} slope with respect to Z_H, denoted as K_H, for each class is estimated by fitting a straight line to the median Z_{DR} values derived for each 1 dBZ interval of Z_H between 25 dBZ and 40 dBZ. The Z_H range considered for this analysis is reduced from (20 dBZ, 50 dBZ)

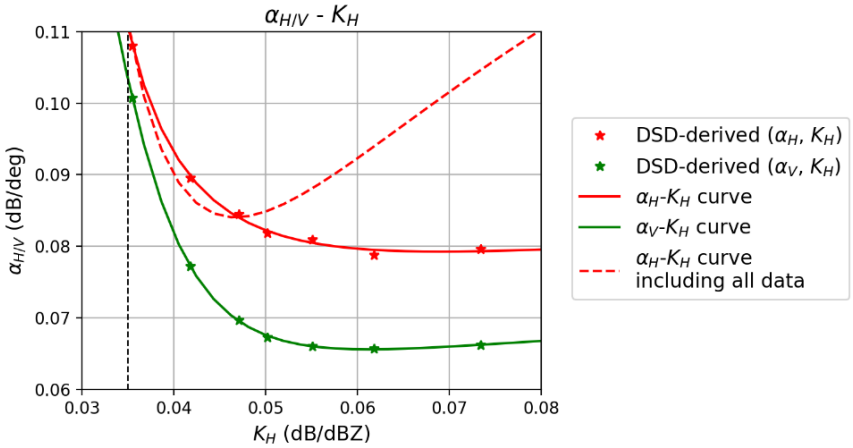

Figure 4.4 Curves of α_H (red solid line) and α_V (green solid line) as a function of K_H. The red dashed line indicates the curve of α_H versus K_H when all data with potential resonance effects are included. The red/green stars mark the ($\alpha_{H/V}$, K_H) pairs derived from the seven N_w classes, respectively. The black dashed line marks the lowest threshold of K_H.

suggested by Wang et al. (2019) to (25 dBZ, 40 dBZ) because of the less pronounced resonance effects in this range and the lower occurrence of Z_H > 40 dBZ in stratiform rain in Germany. Within this range, the dependence of Z_{DR} on Z_H is almost quasi-linear with a distinct slope depending on N_w (Fig. 4.3b). K_H values are found to be higher for lower N_w classes and vice versa. In the final step, the relationships between the derived $\alpha_{H/V}$ and K_H values, namely $\alpha_{H/V}$ estimators, are formulated as ratios of polynomial functions (rational function):

$$\alpha_H(K_H) = \frac{1.36-7.17\times10^{1}K_H+1.36\times10^{3}{K_H}^2}{1\times10^{1}-7.03\times10^{2}K_H+1.57\times10^{4}{K_H}^2} \text{ , and} \quad (4.7)$$

$$\alpha_V(K_H) = \frac{1.05-5.35\times10^{1}K_H+8.40\times10^{2}{K_H}^2}{1\times10^{1}-6.21\times10^{2}K_H+1.12\times10^{4}{K_H}^2}. \quad (4.8)$$

The ($\alpha_{H/V}$, K_H) pair from the last class is excluded from deriving Eqs. (4.7) and (4.8) since the Z_H values in this class are mostly below 30 dBZ, far from the 40-dBZ threshold required for determining the corresponding K_H value. The α estimators presented in this study reveal that, both α_H and α_V values initially decrease with increasing K_H and then remain constant (Fig. 4.4 solid lines). However, incorporating all data points in the fitting of the α_H estimator shows that α_H values first drop and then increase with increasing K_H (Fig. 4.4 dashed line).

In real-time radar observations, K_H value is estimated from the precipitation scan data for each time step. It is determined using the same aforementioned fitting method, but only the median Z_{DR} values derived from more than a hundred samples for each 1 dBZ interval are considered. Despite prior correction for attenuation in Z_H and Z_{DR}, radar bins with Φ_{DP} > 30 deg are excluded from the K_H calculation in order to minimize uncertainties associated with attenuation. To ensure the K_H quality, the derived value is counted only when Pearson's correlation coefficient between the median Z_{DR} and given Z_H values is higher than 0.95; otherwise, the collected data is retained and included in the next time step. K_H values are constrained to be above 0.035 dB dBZ^{-1}, which is close to the value derived from the seventh class (Fig 4.4 black dashed line), to avoid excessively high $\alpha_{H/V}$ values.

The $\alpha_{H/V}$ values are calculated for A estimates using the derived K_H value and Eqs. (4.7) and (4.8). Note that the renewal of α estimates for each scan is contingent upon the availability of over 20,000 valid points for the K_H derivation. If this requirement is not met, the α value from the previous time step is utilized, and the data are collected for the next time step. When there is insufficient data or an absence of valid α from the previous time step, default values of 0.09 and 0.07 dB deg^{-1} for $\alpha_{H/V}$ are applied. These default values are derived from the simulated data with Z_H < 50 dBZ.

Chen et al. (2021a) applied the highest $\alpha_{H/V}$ values from the last N_w class to radar observations when the maximum valid interval of Z_H for fitting K_H is below 30 dBZ. QPE results, however, showed significant negative biases in stratiform rain. Consequently, two additional conditions for the use of these $\alpha_{H/V}$ values are included here. Specifically, when the mean plus one standard deviation of Z_H and Z_{DR} is less than 30 dBZ and 1.5 dB, respectively, $\alpha_{H/V}$ values derived from the last N_w class are used. This criterion is chosen as, in a normal distribution, already around 84% of data fall below these thresholds.

4.2.2 Ray/segment-wise α derived from Z_{DR}

Ryzkhov et al. (2022) recommended using ray/segment-wise α value derived from Z_{DR} for A estimates, but its practical implementation has not yet been achieved. This can be attributed to several factors: i) the derivation of segment-wise α involves segment-wise integration in the ZPHI method, which is hindered by the unreliability of $\Delta\Phi_{\mathrm{DP}}$ within short bin intervals or light rain, ii) at C-band significant attenuation uncertainties still exist in attenuation-corrected Z_{DR} in hailstorms, and iii) for the DWD radars radome effects from lightning pods on Z_{DR} cannot be ignored. Despite these challenges, this study aims to explore the potential benefits of this methodology using observations from the BOO, HNR, and Ummendorf (UMD) radar in five rain events. These radars were selected because of their minimal radome effects and fewer scattering isolated convective cells, which could complicate obtaining reliable $\Delta\Phi_{\mathrm{DP}}$.

Accurate estimation of α strongly relies on precise measurement of Z_{DR} as well as Z_H, particularly during hailstorms where additional attenuation from hail is a concern. To account for this, the attenuation correction method proposed by Gu et al. (2011), as described in section 2.3, is applied. The HS segment is defined using the following steps:

i. Search for bins with attenuation-corrected Z_H > 50 dBZ (the correction using PIA with a default value of 0.093 dB deg^{-1} for α_H).

ii. Concatenate the adjacent bins/intervals that are within five bins of each other.

iii. Retain intervals with $\Delta\Phi_{DP}$ greater than 10 deg and a length of more than 10 bins.

This ensures that the defined HS segment is not too fragmented, avoiding unnecessary algorithmic complexity and conserving computational resources. During the correction process, if $\Delta\Phi_{DP}$(OHS) in Eq. (2.40) is negative due to backscattering effects or noisy Φ_{DP} in light rain, it is replaced with $\Delta\Phi_{DP}^{cal.}$ using Eq. (3.3). The $Z_{DR}(Z_H)$ relation in Eq. (2.42) follows the equation

$$Z_{DR}(Z_H) = 0.20335179 - 0.02225738 Z_H + 0.00122115 {Z_H}^2, \quad (4.9)$$

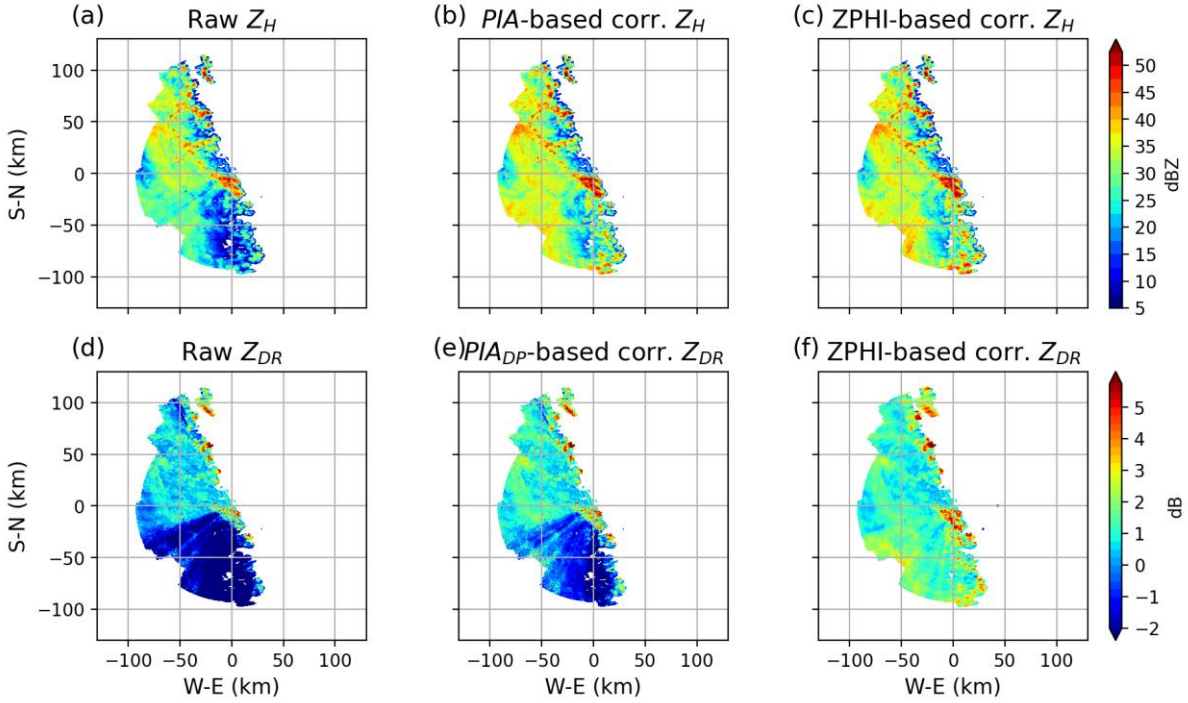

Figure 4.5 Fields of Z_H and Z_{DR} obtained from the UMD radar on 19 July 2017 at 1945 UTC. These include (a) raw Z_H, (b) Z_H corrected for attenuation using PIA, and (c) Z_H corrected for attenuation using the ZPHI method considering hot spots (HS, hail cores), and (d)-(f) the same for Z_{DR} fields.

which is derived from the measured DSDs with Z_H below 40 dBZ. If multiple HSs are present within a ray, sufficient data points need to be well-assigned behind each HS to derive $\Delta\beta$ in Eq. (2.43). Therefore, the rainy segment between two HSs is evenly separated into two parts, attaching the closest HS individually, so that each HS is enclosed by two rainy segments. If data behind the HS are all above 40 dBZ, a mode value of 0.05 dB deg^{-1} is assigned to $\Delta\beta$. No correction is applied to the HS located at the end of the ray below the ML, as $R(K_{DP})$ takes responsibility there. This method successfully restores the Z and Z_{DR} fields behind the HS (Figs. 4.5c/f) compared to the PIA-/PIA_{DP}-based method, which still gives negative Z_{DR} values after the HS (Fig. 4.5e). It is also observed that the attenuation effects of HS impact Z_{DR} more than Z (Figs. 4.5a/b and d/e), highlighting the potential danger of using Z_{DR} at C- and X-band.

The net α value within a given rainy segment (r_1, r_2), denoted as $\langle\alpha\rangle$, can be estimated from Z_h and Z_{DR} corrected for attenuation. The estimation of $\langle\alpha\rangle$ begins with the formula

$$\langle\alpha\rangle = \frac{PIA}{\Delta\Phi_{DP}} = \frac{\int_{r_1}^{r_2} A(r)dr}{\int_{r_1}^{r_2} K_{DP}(r)dr} = \frac{\int_{r_1}^{r_2} A(r)dr}{\int_{r_1}^{r_2} \frac{A(r)}{\alpha(r)}dr}, \tag{4.10}$$

where $\alpha(r)$ is the local α primarily dependent on Z_{DR}, and thus is expressed as $\alpha[Z_{DR}(r)]$. The ZPHI method assumes $A = aZ_h{}^b$, and hence, Eq. (4.10) can be reformulated as

$$\langle\alpha\rangle = \frac{\int_{r_1}^{r_2} Z_h^b(r)dr}{\int_{r_1}^{r_2} \frac{Z_h^b(r)}{\alpha[Z_{DR}(r)]}dr}. \tag{4.11}$$

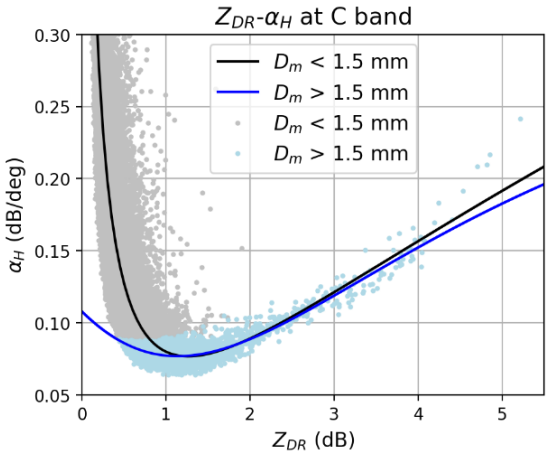

Figure 4.6 Scatterplot of α_H against Z_{DR} at C-band.

The simulated data from the measured DSDs show that α_H values vary from several orders of magnitude down to 0.6 dB deg^{-1} when the raindrop size is small (Fig. 4.6). This variability may bias the ensuing A if a single $\alpha(Z_{DR})$ relation is used. Therefore, two $\alpha_H(Z_{DR})$ relations and two $\alpha_V(Z_{DR})$ relations are used depending on the D_m value. The relations for horizontal polarization, as indicated by the black and blue lines in Fig. 4.6, are given by

$$\alpha_H(Z_{DR}) = \frac{9.84\times10^{-1}-6.08\times10^{-1}Z_{DR}+6.12\times10^{-1}Z_{DR}^2}{1-1.08\times10^{1}Z_{DR}+5.62\times10^{-1}Z_{DR}^2} \quad if\ D_m < 1.5, \text{ and} \tag{4.12}$$

$$\alpha_H(Z_{DR}) = \frac{1.08\times10^{-1}-4.68\times10^{-2}Z_{DR}+2.96\times10^{-2}Z_{DR}^2}{1+9.68\times10^{-2}Z_{DR}+7.48\times10^{-2}Z_{DR}^2} \quad if\ D_m > 1.5, \tag{4.13}$$

and for vertical polarization

$$\alpha_V(Z_{DR}) = \frac{1.74-5.95\times10^{-1}Z_{DR}+7.96\times10^{-1}Z_{DR}^2}{1+2.40\times10^{1}Z_{DR}+2.33Z_{DR}^2} \quad if\ D_m < 1.5, \text{ and} \tag{4.14}$$

$$\alpha_V(Z_{DR}) = \frac{9.60\times10^{-2}-4.20\times10^{-2}Z_{DR}+1.60\times10^{-2}Z_{DR}^2}{1-4.96\times10^{-2}Z_{DR}+7.40\times10^{-2}Z_{DR}^2} \quad if\ D_m > 1.5. \tag{4.15}$$

The D_m values can be estimated from Z_h and Z_{DR} (Cao et al. 2008) following the equation

$$\frac{D_m}{Z_h^{0.042}} = 6.82\times10^{-2}Z_{DR}^3 - 4.60\times10^{-1}Z_{DR}^2 + 1.33Z_{DR} + 4.83\times10^{-1}, \tag{4.16}$$

which is derived based on the local DSDs. The threshold of 1.5 mm for D_m is due to being close to the midpoint between the means of stratiform and convective D_m presented in Fig. 6 of Wen et al. (2016).

The Z_{DR} observation is susceptible to noise, which can introduce errors that bias $\langle\alpha\rangle$. To minimize the impact of noise, two boundaries are used to constrain Z_{DR} observations. These boundaries are determined based on the $Z_{DR}(Z_H)$ relations derived from the 0th-20th percentile (upper bound) and 80th-100th percentile (lower bound) intervals of N_w, respectively, given by

$$Z_{DR}(Z_H) = 5.51\times10^{-4}Z_H^{2.18}, \text{ and} \tag{4.17}$$

$$Z_{DR}(Z_H) = 3.06 \times 10^{-7} Z_H^{3.44} \,. \tag{4.18}$$

Accordingly, any observed Z_{DR} value that is greater than 1.25 times the value derived from Eq. (4.17) or smaller than 0.75 times the value derived from Eq. (4.18) is set to the derived value (Fig. 4.7).

In heavy rain, resonance effects at C-band can cause considerable variability in Z_{DR} values for a given Z_H. To mitigate this uncertainty, $\langle \alpha \rangle$ is computed only within a segment where Z_H is below 40 dBZ. The segment-wise integration is also based on this limit. To ensure reliable corresponding $\Delta\Phi_{DP}$ within the segment, its value is replaced with $\Delta\Phi_{DP}^{cal.}$ when it is either two times larger or half times lower than $\Delta\Phi_{DP}^{cal.}$.

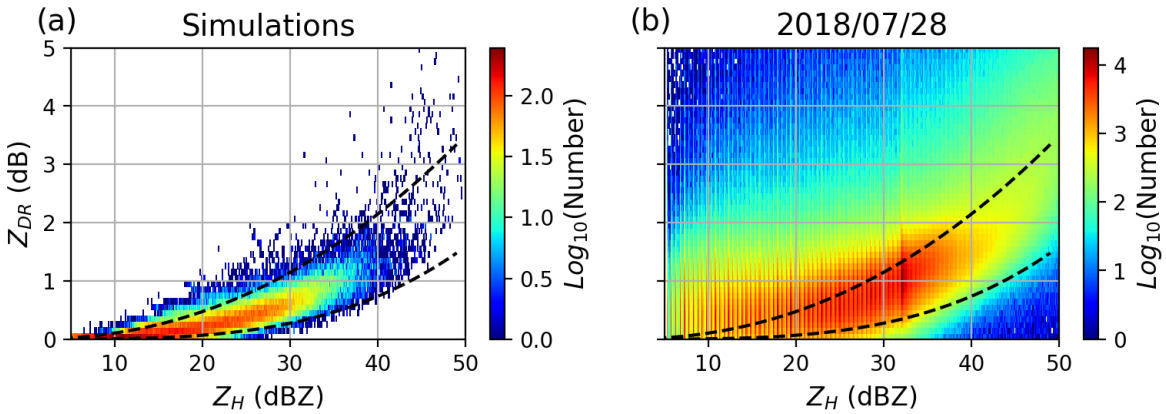

Figure 4.7 Scatterplots of Z_{DR} against Z_H based on (a) simulations at C-band, and (b) observations from UMD, HNR, and BOO on 28 July 2018. The dashed lines indicate the constraint lines for Z_{DR} observation.

4.3 Warm-rain precipitation

In warm rain, vertical precipitation gradients increasing towards the surface are a common occurrence. However, radar beams, which monitor precipitation at increasing heights above the ground with increasing distance from the site, often fail to detect such gradients. Furthermore, the current rainfall relations are derived mainly from simulated radar variables at the surface, rather than those observed aloft and matched to surface-measured rain rates. This can result in a large underestimation of rainfall due to the high variability in the vertical structure of precipitation. Warm-rain processes are often associated with flooding (Chen et al. 2011; Grams et al. 2014), and climate change has increased the frequency and intensity of such extreme events (Nissen and Ulbrich 2017; Myhre et al. 2019; Tabari 2020). The propagation of these errors into forecast models can lead to significant deviations from actual precipitation patterns and potentially severe consequences. As a result, it becomes mandatory to correct for the vertical gradients of radar variables utilized to estimate rainfall below the ML in operational applications. To this end, two mitigation strategies are proposed and evaluated for a heavy rain event on 14 July 2021. The first strategy involves a VP correction method that includes vertical projections of Z and K_{DP} to low altitudes and the use of MRR-DSD-derived rainfall relations. The second strategy entails the inclusion of observations from an X-band radar to fill gaps in low-altitude coverage. This section briefly summarizes the impact and microphysical

characteristics of the investigated rain event, followed by a description of the two methodologies, as presented by Chen et al. (2022).

4.3.1 Overview of the study case

The 14 July 2021 witnessed heavy precipitation across western Europe, with western Germany being particularly affected, as well as neighboring countries Belgium, Luxembourg, and the Netherlands (Puca et al. 2021). The intense and prolonged stratiform rain produced more than 160 mm of precipitation over the German states of Rhineland-Palatinate and North Rhine-Westphalia, causing extreme flash floods, especially but not only in the Ahr river. In July of that year, the floods resulted in at least 196 fatalities and left 1,300 people missing in Germany (Eddy and Specia 2021). Moreover, the estimated cost of the damage incurred reached $40 billion (Libatique 2022). This disaster underscores the critical need for accurate and timely QPE products to enable reliable flash-flood predictions.

The precipitation event occurring on 14 July 2021 was characterized by warm-rain processes during rain formation. Its vertical structure shows a different pattern from the stratiform rain on 25 July 2017, with the latter having little Z_H gradient (Fig. 4.8). Data retrieved from observations of the MRR indicate that D_m, K_{DP}, R, and LWC increase towards the ground with decreasing N_w (Fig. 4.9). Analysis of the contributions of drizzle (defined as D < 0.5 mm) and raindrops with D between 2 and 4 mm to the DSDs reveals that the former shows a secondary peak right below 1 km height, followed by a rapid decrease downwards (Fig. 4.10a). In contrast, the mean number concentration of big raindrops constantly increases towards the ground below the ML (Fig. 4.10b). Thus, the observed increases in R and LWC towards the surface can be attributed to the transformation of water vapor into droplets above 1 km, which subsequently transform into rainwater via warm-rain processes below. However, due to the geometry of radar measurements, the DWD weather radar network was unable to measure the lower atmosphere below up to 2.5 km above the ground over parts of the affected region, even with the largest overlap of the four operational radars: ESS, Flechtdorf (FLD), NHB, and OFT (Pejcic et al. 2020). As a result, rainfall was significantly underestimated.

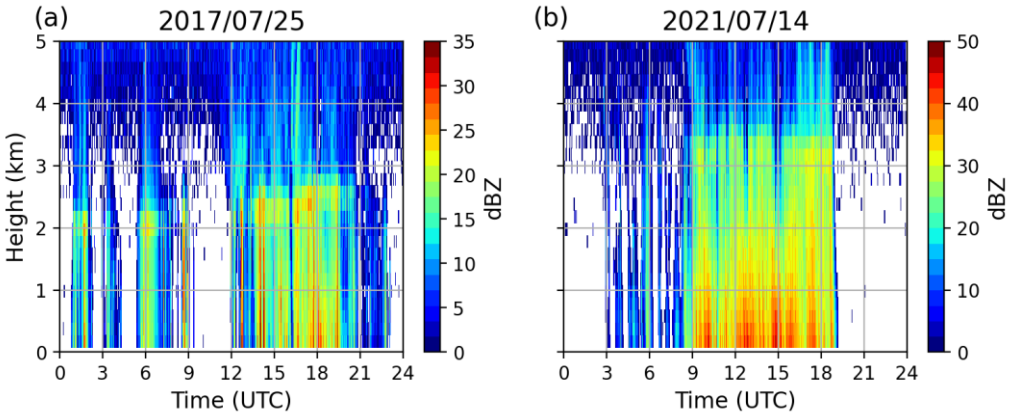

Figure 4.8 Simulated Z_H profiles based on MRR measurements from the University of Bonn on (a) 25 July 2017 and (b) 14 July 2021.

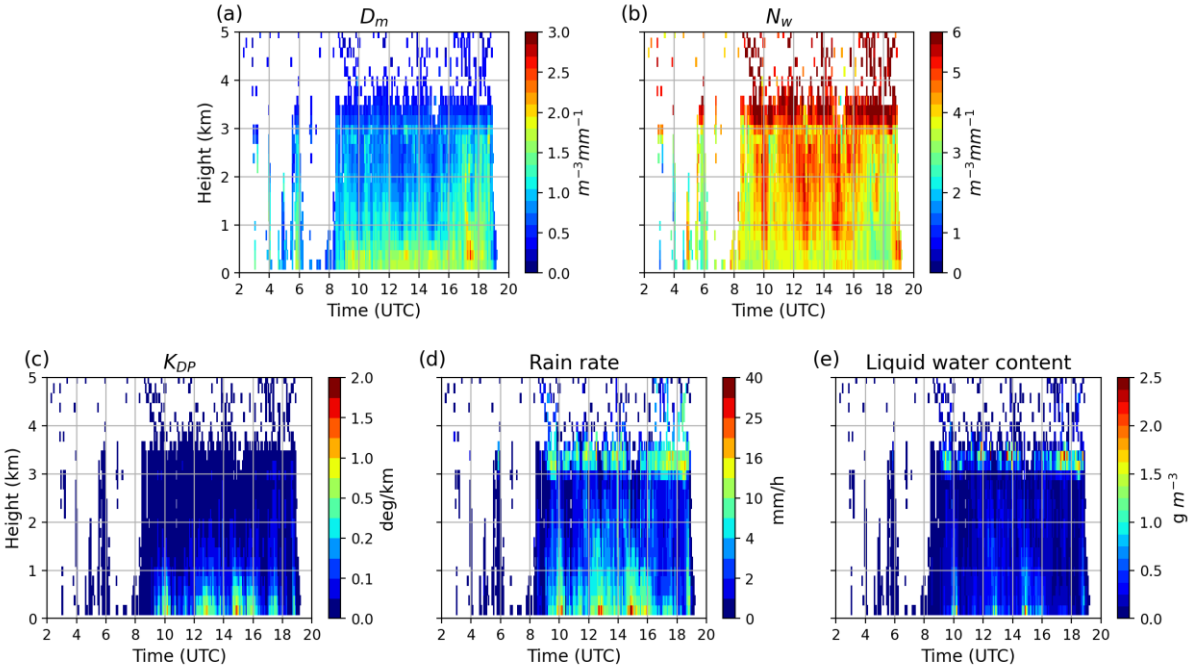

Figure 4.9 Retrieved profiles from the MRR-derived DSDs on 14 July 2021, including (a) D_m, (b) N_w, (c) K_{DP}, (d) R, and (e) liquid water content (LWC).

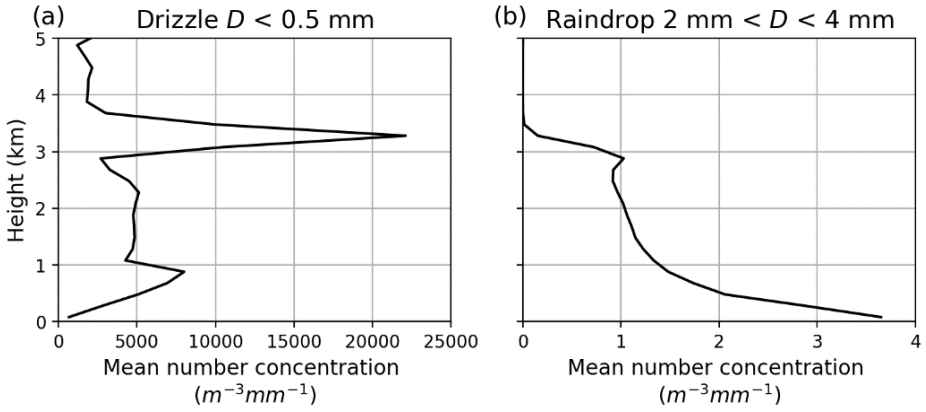

Figure 4.10 Mean number concentration profiles of (a) drizzle with D < 0.5 mm, and (b) raindrops with 2 mm < D < 4 mm calculated from the DSDs retrieved from the two MRR observations.

4.3.2 Vertical profile correction

Chen et al. (2022) investigated the efficacy of two QPE methodologies for warm rain: i) vertical projection of observations to low altitudes, and ii) the use of rainfall relations derived from MRR observations. The present study combines these two methodologies by regarding projection as an explicit VP correction and MRR-DSD-derived relations as an implicit VP correction. Additionally, the K_{DP} in the $R(A, K_{DP})$ retrieval is also corrected using the explicit method, which was not included in the previous study by Chen et al. (2022).

Explicit VP correction

Chen et al. (2020) employed profiler radar observations as a reference to explicitly correct the VPR. This work proposes an extension of their approach by using the real-time RD-QVP as a reference, and correcting the K_{DP} measurements in the same manner. The correction involves adding the difference of radar variable values between a pre-defined lower altitude and the observing height as seen in the RD-QVPs to the observations. However, the explicit correction for A is impractical due to its partial correlation with temperature dependence (Trömel et al. 2014a), making it difficult to separate its dependencies on the temperature and the rain rates.

An RD-QVP is a range-defined average of QVPs from several elevation scans using inverse distance weighting (IDW) beyond the specified range from the radar. The resulting RD-QVPs are influenced by the elevations of the scans included in the analysis and the specified range. To identify the most appropriate scans for inclusion, two different procedures are compared. The first procedure uses data from all volume scans, while the second procedure only uses the two lowest scans, that may encompass the elevation angle ranges of the precipitation scans. The former method produces more reliable and finer resolved profiles at higher altitudes, primarily due to smaller beam-broadening effects. The specified range of 75 km is chosen for this event because it provides the best coverage of the scans with precipitation. The ensuing RD-QVPs of Z_H, K_{DP} and Z_{DR} (Figs. 4.11a-c) agree well with the MRR retrievals (Figs. 4.8b and 4.9), indicating a high likelihood of collision-coalescence processes occurring below the ML during this event. Note that the Z_H gradient observed in the RD-QVP is unlikely to be caused by attenuation accumulated at high altitudes (far ranges), as attenuation correction is already applied, and 90% of the data show PIA values below 2.5 dB during this stratiform rain event.

The explicit correction for Z_H and K_{DP} fields is restricted to a minimum height of 700 m above MSL, as it is close to the highest altitude (628 m) of the contributing radars, and to avoid the contamination of ground clutter in the VP correction. Radar variables observed above 700 m are projected to this height, and no correction is applied to data below 700 m and above H_b. The values of H_b range from 2 to 2.7 km as indicated by the RD-QVP of ρ_{HV} from each radar (e.g., $\approx$ 2.5 km for the NHB radar in Fig. 4.11d). For each radar bin and every time step, the final corrected Z_H or K_{DP} value is the weighted average using IDW of the estimates, that take different radar-derived RD-QVPs as references for projection (Fig. 4.12). Only when precipitation covers more than one-third of the radar domain, the referred RD-QVPs are included for correction. Since K_{DP} value scales with the inverse of radar wavelength, the ratio 0.64 of K_{DP} at C-band to at X-band is considered for calculating the K_{DP}-difference when the RD-QVP is derived from radar observations at a different wavelength. Finally, the corrected Z_H values are truncated at 55 dBZ, as these values are considered unrealistic for pure rain.

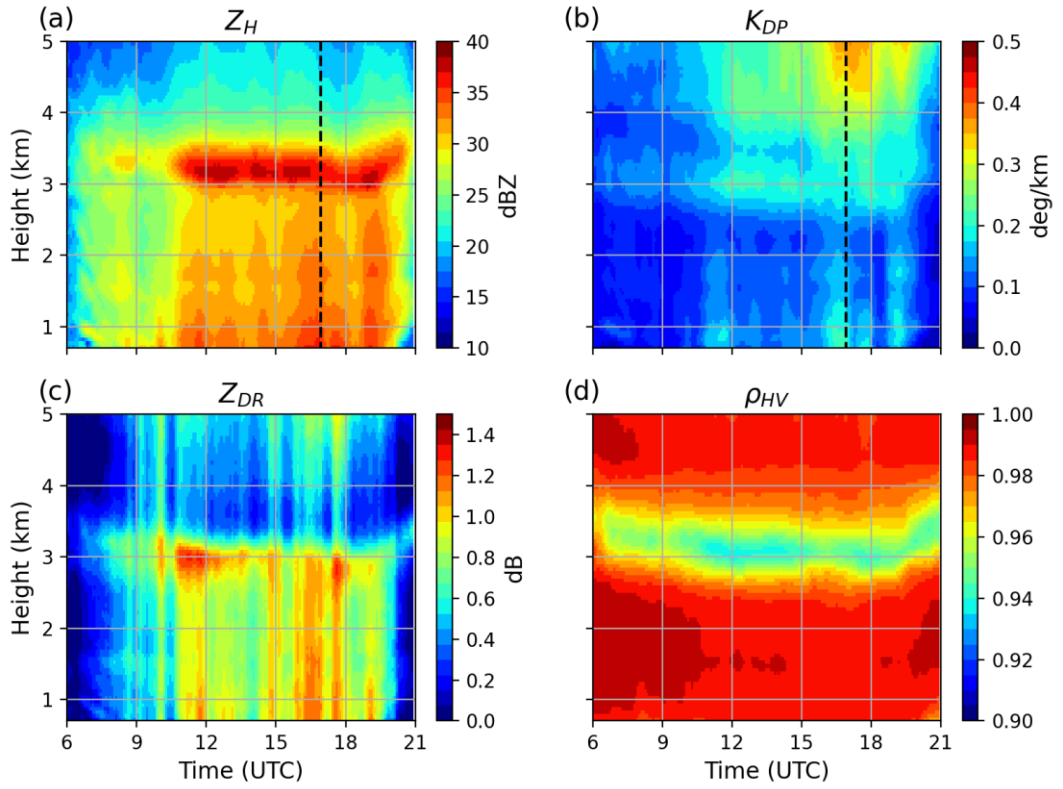

Figure 4.11 Range-defined quasi-vertical profiles (RD-QVP) of (a) Z_H, (b) K_{DP}, (c) Z_{DR}, and (d) ρ_{HV} derived from the NHB radar observations on 14 July 2021. The black dashed lines in (a) and (b) mark the time step of VPs at 1655 UTC, which are shown in Fig. 4.12.

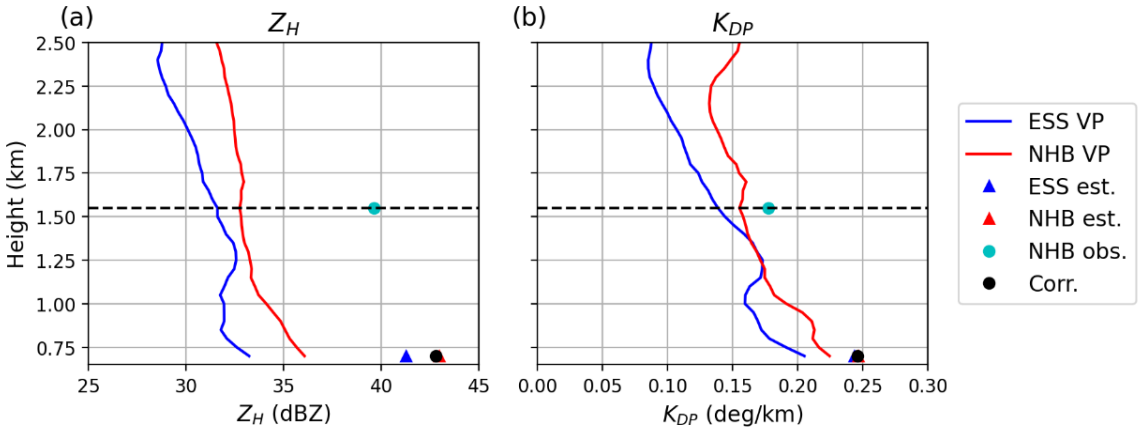

Figure 4.12 VPs of (a) Z_H and (b) K_{DP} obtained from the RD-QVPs of the Essen (ESS, blue line) and NHB (red line) radars on 14 July 2021 at 1655 UTC. The cyan dot is the NHB-observed Z_H (K_{DP}) located 30 km northwest of the radar and 119 km southwest of ESS. The blue and red triangles denote the estimated Z_H (K_{DP}) using the corresponding blue and red lines as VP references. The black dot represents the final corrected, i.e., weighted average using inverse distance weighting, Z_H (K_{DP}) at a height of 700 m.

Implicit VP correction

The above-mentioned VP correction is only applicable to radar data above 700 m height. To account for the vertical gradients of precipitation below that height, rainfall relations derived from 1,728 DSDs observed by two MRRs during this event are used. These relations link radar variables (e.g., Figs.4.8b and 4.9c) in the lowest three resolved levels to rainfall rates measured at the surface, and are given by

$$R(Z_h) = 0.026{Z_h}^{0.69}, \tag{4.19}$$

$$R(K_{DP}) = 30.4{K_{DP}}^{0.7}, \tag{4.20}$$

$$R(A_H) = 427{A_H}^{0.94}, \text{ and} \tag{4.21}$$

$$R(A_V) = 572{A_V}^{0.97}. \tag{4.22}$$

The heights of the MRR sites plus the three resolved levels spanning 600 m correspond to a height of 675 m above MSL. This height covers the altitude range between 185 and 628 m of the four DWD radar sites and is in close proximity to the 700 m height. While it may seem optimal to establish rainfall relations for each height level using MRR data and apply them to radar observations at the corresponding height, there are limitations to this approach. The uncertainties associated with attenuation in MRR measurements increase with height, which may significantly bias the relations at high levels. In addition, the limited number of MRRs available during the event and the insufficient sample collected from each level to derive robust relations are also concerns. Hence, the MRR-based relations are used solely to adjust the projected radar data up to 700 m height.

To estimate error contributions caused by using DSDs from long-term observations and neglecting vertical changes in rainfall intensities near the surface, the QPE relations derived using 2,588 LPM-measured DSDs during the event within the domain of interest are compared to Eqs. (4.19)-(4.22):

$$R(Z_h) = 0.023{Z_h}^{0.68}, \tag{4.23}$$

$$R(K_{DP}) = 24.4{K_{DP}}^{0.75}, \tag{4.24}$$

$$R(A_H) = 320{A_H}^{0.93} \text{ and} \tag{4.25}$$

$$R(A_V) = 438{A_V}^{0.98}. \tag{4.26}$$

The findings indicate that during light rain, the long-term LPM-based $R(Z_h)$ relation yields higher rain rates, while in moderate-to-heavy rain, it produces lower rates compared to the event-specific $R(Z_h)$ relations (Fig. 4.13a). For the relations derived from the measurements during this event, the MRR-based $R(Z_h)$ relation gives slightly higher rain rates than the LPM-based $R(Z_h)$ relation for the entire Z_h range. In light-to-moderate rain conditions where $R(A)$ is derived, the different DSD statistics between this rain event and the climatology does not significantly affect the $R(A_{H/V})$ relations, whereas their MRR-based relations as well as $R(K_{DP})$'s produce the highest rain intensities for the entire range (Figs.

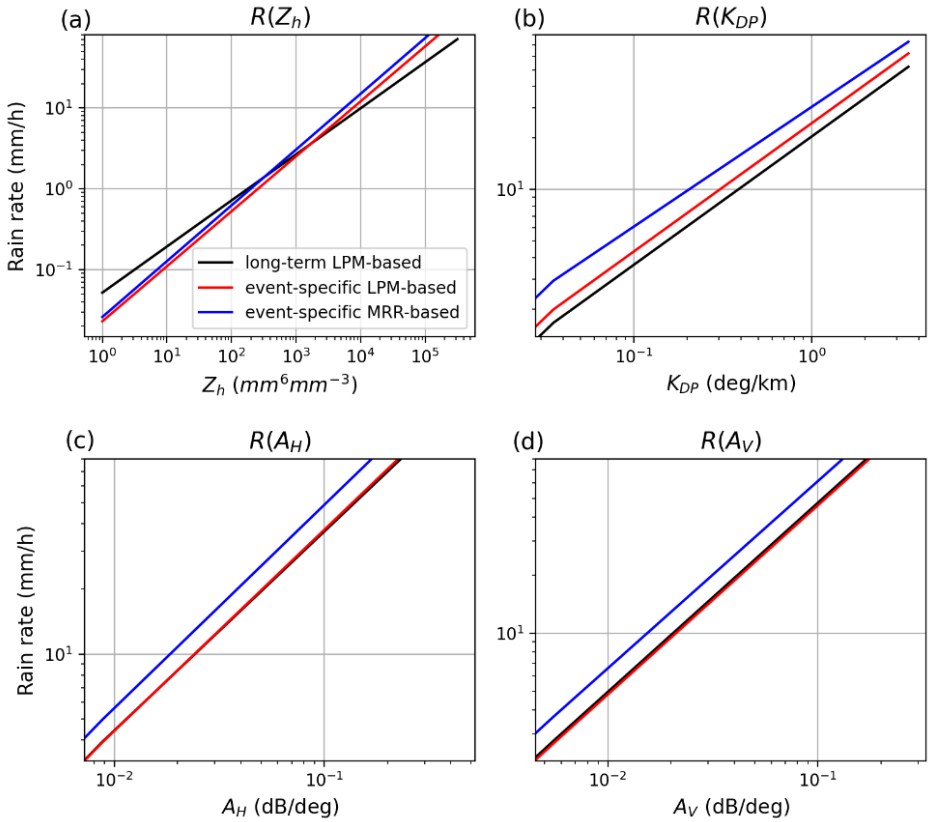

Figure 4.13 Rainfall relations at C-band based on (a) Z_h, (b) K_{DP}, (c) A_H, and (d) A_V derived from long-term LPM-measured DSDs (black), and from DSDs observed by LPMs (red) and by MRRs (blue) during the rain event.

4.13b-d). Thus, these comparisons suggest that the choice of MRR-based rainfall relations could significantly impact rainfall estimates.

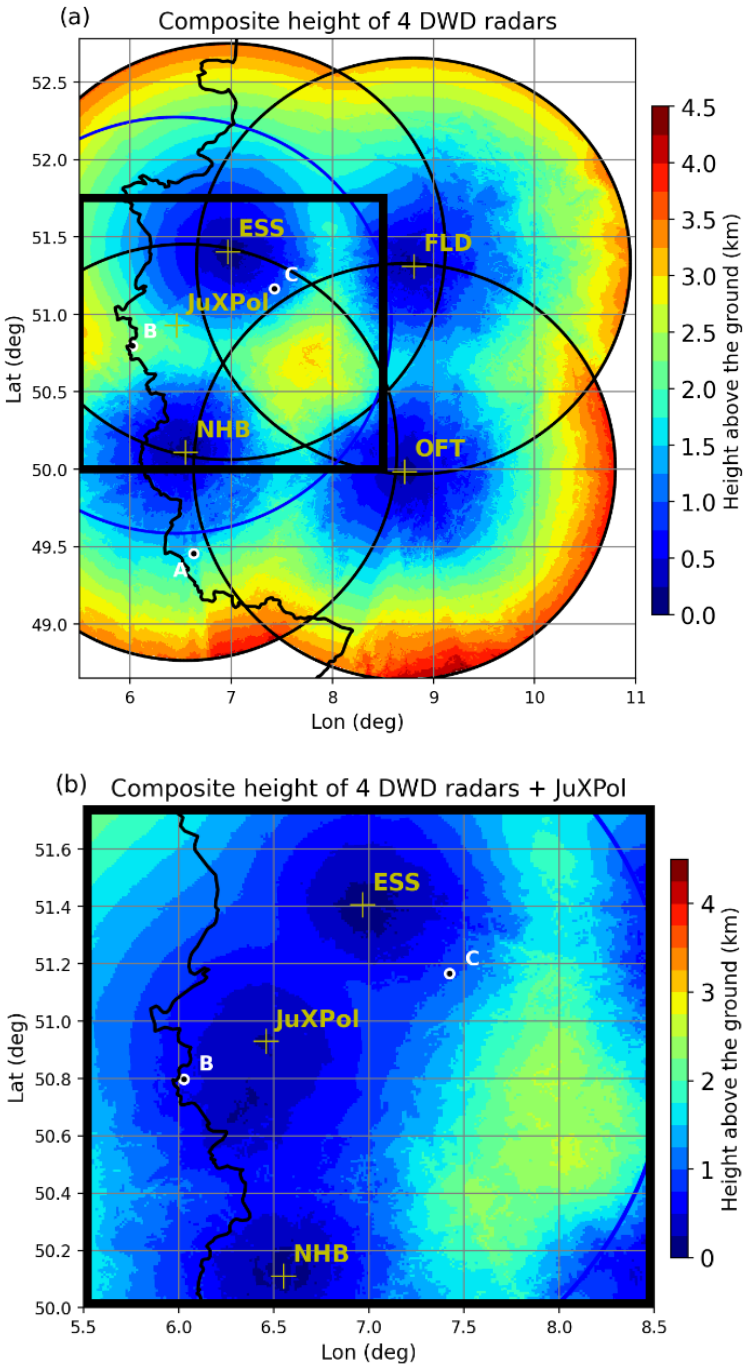

Figure 4.14 Observation heights for (a) the composite of the four C-band radars operated by DWD, namely ESS, FLD, NHB, and Offenthal (OFT), and (b) the same composite with the additional measurements from JuXPol. The white circles are the locations of rain gauges selected for further analysis (IDs 03263, 15000, and 05619, hereafter named A, B, and C). The black frame in (a) indicates the area shown in (b).

4.3.3 Inclusion of the gap-filling radar, JuXPol

In the flood-affected region, the radar sampling volume can reach up to 3 km height at a range of 100 km from the radar sites in the radar composite obtained from the DWD precipitation scan data (Fig. 4.14a). The use of JuXPol as a gap filler between the ESS and NHB radar, however, can reduce observation heights by up to 1.5 km (Fig. 4.14b), which is anticipated to improve QPE performance.

The X-band rainfall relations derived using the long-term LPM-measured DSDs are given by

$$R(Z_h) = 0.098{Z_h}^{0.47}, \tag{4.27}$$

$$R(K_{DP}) = 15.0{K_{DP}}^{0.88}, \tag{4.28}$$

$$R(A_H) = 38{A_H}^{0.69} \text{ and} \tag{4.29}$$

$$R(A_V) = 47{A_V}^{0.73}. \tag{4.30}$$

The corresponding relations based on the MRR-retrieved DSDs are

$$R(Z_h) = 0.058{Z_h}^{0.57}, \tag{4.31}$$

$$R(K_{DP}) = 22.9{K_{DP}}^{0.71}, \tag{4.32}$$

$$R(A_H) = 67{A_H}^{0.78} \text{ and} \tag{4.33}$$

$$R(A_V) = 74{A_V}^{0.78}. \tag{4.34}$$

For A estimates at X-band, the fixed average $\alpha_{H/V}$ values of 0.31 and 0.27 dB deg^{-1} are used. Similar to the C-band algorithm, data with Z_H > 50 dBZ are excluded from the integration path in the ZPHI method, and a Z_H threshold of 40 dBZ is utilized in the QPE hybrid approach.

4.4 Snow quantification

Algorithms based on polarimetric radar variables are believed to be more accurate in quantifying melting snow within the ML and snowfall at the surface, compared to those relying solely on Z_h. This potential, however, has not yet been put into practice. When the radar beams reach BB at a short distance from the radar and experience bean-broadening issues at far ranges, the area of exploitable radar observations shrinks. To overcome this limitation and take full advantage of observations made over long ranges, such as those obtained by the DWD radars up to 180 km away, many VPR correction methods have been proposed. This study adopts the first polarimetric method for correcting the blurring of VPR, as recommended by Ryzkhov et al. (2022). Nonetheless, the QPE results based on the corrected Z_h have not been validated yet in their study. In the presence of snow at the surface, the polarimetric approach suggested by Bukovčić et al. (2020) is extended and adapted to C-band radars to improve the accuracy of snowfall estimates. These two novel methodologies for the two different situations are elaborated in the following subsections.

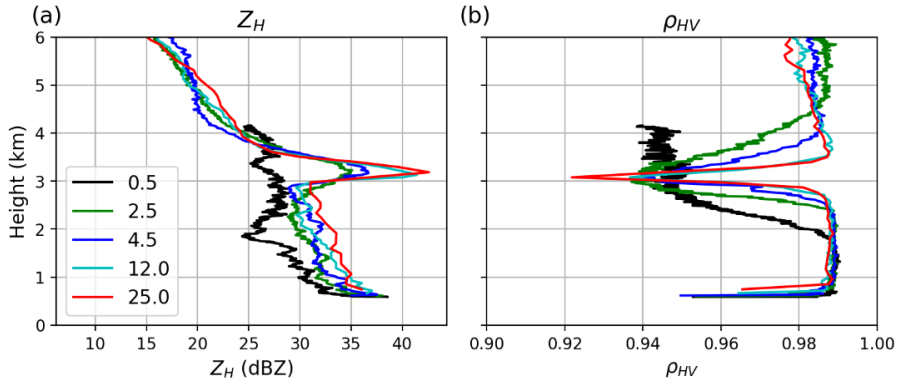

Figure 4.15 VPs of (a) Z_H and (b) ρ_{HV} with noise correction. These profiles are derived from the QVPs of NHB at different elevation angles shown in different colors on 14 July 2021 at 1445 UTC.

4.4.1 Polarimetric vertical profile of reflectivity correction

In the context of monitoring snow-to-rain transformation within the ML of a typical stratiform cloud, the Z_H field exhibits artificial enhancements, followed by rapid decreases at longer distances due to beam-broadening effects and weak echoes of snowflakes and ice crystals. In contrast, the presence of mixed-phase hydrometeors within the ML causes ρ_{HV} to drop. The radial profile of ρ_{HV} is found to correlate well with that of Z_H within the ML, albeit with some variability owing to different microphysical characteristics (Trömel et al. 2019; Griffin et al. 2020). Furthermore, ρ_{HV} provides a more reliable BB discrimination than Z_H. Consequently, the PVPR correction method reconstructs intrinsic Z_H profiles from the observed ρ_{HV} profiles to correct for Z_H.

In addition to the precipitation microphysics process, changes in radar variables within and above the ML are also affected by the radar elevation angle. This dependence arises because the elevation angle determines the width of the radar beam, and thus, the extent of beam-broadening effects at the observation point. Fig. 4.15a demonstrates that the VPR at the 0.5-deg elevation angle loses the BB signature and has the lowest Z_H values, implying the greatest Z biases amongst other profiles due to severe beam-broadening effects (black line). The same problem occurs for ρ_{HV} as the ρ_{HV} curve at the 0.5-deg elevation angle is the first one that responds to the BB contamination but never increases beyond the ML, even after applying the noise correction (Fig. 4.15b black line). On the other hand, the highest elevation scan at 25 deg shows the maximum (minimum) value of Z_H (ρ_{HV}) caused by the BB contamination (Fig. 4.15 red lines). Thus, the differences in radar measurements at various elevation angles need to be considered in the PVPR correction.

The PVPR correction method is designed to reconstruct the intrinsic profile of Z_H from ρ_{HV} and correct Z_H using estimated Z_H biases. To achieve this, the intrinsic profiles of ρ_{HV} and Z_H with respect to the ML are first modeled through statistical analysis of QVPs. Based on the obtained intrinsic profiles, the observed profiles of ρ_{HV} and Z_H are then simulated, taking into account the effects of beam broadening. Subsequently, several parameters associated with simulated ρ_{HV} are stored in lookup tables to facilitate the reconstruction process. Additionally, reflectivity biases relative to the intrinsic Z_H value below the ML, denoted as $Z_H^{vp.bias}$, are estimated and also stored in lookup tables for given elevation angles.

The entire process is detailed below:

i. Model the intrinsic profiles of ρ_{HV} and Z_H:

According to Ryzhkov and Krause (2022), the intrinsic profiles of ρ_{HV} and Z_H are modeled as piecewise linear functions, parameterized by a number of microphysical parameters as shown in Fig. 4.16 and given by

a. the minimum value of co-polar correlation coefficient within the ML (ρ_{HV}^{min}),

b. reflectivity in rain below the ML (Z_H^{rain}),

c. the maximum value of reflectivity within the ML (Z_H^{max}),

d. reflectivity in snow right above the ML (Z_H^{snow}),

e. the vertical gradient of reflectivity above the melting layer (β_{ML}), and

f. the ML depth (ΔH in km) determined by the value of ρ_{HV} (i.e., $H_t - H_b$ where H_b and H_t are defined as the heights at which ρ_{HV} starts decreasing below 0.975 and exceeds again 0.975 after crossing the ML).

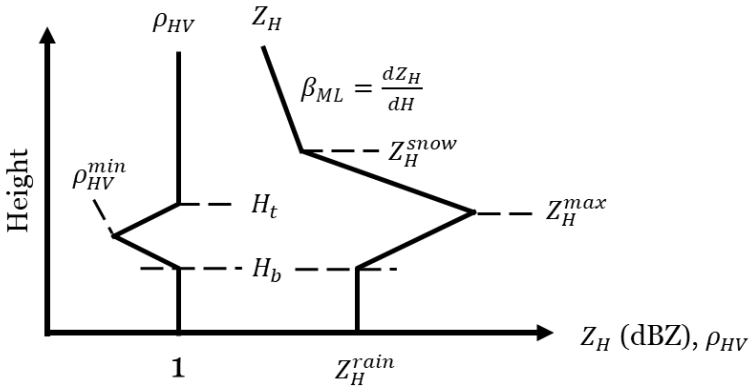

Figure 4.16 Model intrinsic VPs of ρ_{HV} and Z_H with respect to the melting layer (ML).

QVPs offer a systematic examination of high-resolved features within and above the ML. In this regard, ΔH and the difference in values between Z_H^{max} and Z_H^{rain}, denoted as ΔZ_H^{ML}, are estimated using the functions of ρ_{HV}^{min} obtained from S-band observation-based QVPs (Griffin et al. 2020) as follows

$$\Delta Z_H^{ML}(\rho_{HV}^{min}) = 4.27 + 6.89\left(1 - \rho_{HV}^{min}\right) + 341(1 - \rho_{HV}^{min})^2, \text{ and} \quad (4.35)$$

$$\Delta H\left(\rho_{HV}^{min}\right) = -0.64 + 30.8\left(1 - \rho_{HV}^{min}\right) + 315\left(1 - \rho_{HV}^{min}\right)^2 + 1115\left(1 - \rho_{HV}^{min}\right)^3. \quad (4.36)$$

Note that such analysis at C-band has never been performed yet and herein the statistics at S-band are assumed to be valid at C-band. In addition to ρ_{HV} and Z_H, the intrinsic Z_{DR} profile is also modeled. Other associated assumptions include

a. ρ_{HV} is equal to one below H_b and above H_t,

b. Z_H^{rain} is a constant,

c. Z_H^{max} is 36 dBZ,

d. the height of Z_H^{max} is at $H_b + 0.8\Delta H$,

e. the top height of the ML in terms of Z_H is at $H_b + 1.6\Delta H$,

f. $Z_H^{snow} = Z_H^{rain} - 2$ dBZ,

g. β_{ML} is equal to 4 dB km^{-1},

h. differential reflectivity in rain below the ML (Z_{DR}^{rain}) is expressed as a function of Z_H^{rain}, where $Z_{DR}^{rain} = 0.75 - 0.0623Z_H^{rain} + 0.00184{Z_H^{rain}}^2$,

i. the maximum value of differential reflectivity within the ML (Z_{DR}^{max}) is determined by ρ_{HV}^{min} as per the formula $Z_{DR}^{max} = 16.65 - 17\rho_{HV}^{min}$,

j. Z_{DR}^{max} is at the same height as ρ_{HV}^{min}, and

k. differential reflectivity in snow right above the ML (Z_{DR}^{snow}) is equal to 0 dB.

ii. Simulate the observed profiles of ρ_{HV} and Z_H:

Fig. 4.15 illustrates the necessity to account for distortion caused by range-dependent beam broadening at arbitrary antenna elevation. Consequently, the simulated observed reflectivity factors at two channels, referred to as $Z_{h/v}^{s.obs.}$, are determined using the formula from Ryzhkov (2007):

$$Z_{h/v}^{s.obs.}(r_0) = \int Z_{h/v}^{i.}(r_v) I\,(r_v, r_0) dr_v, \tag{4.37}$$

where r_0 and r_v refer to the distance from the radar site to the center of a radar beam volume and to any point within a beam volume, respectively, and $Z_{h/v}^{i.}$ correspond to the intrinsic values of reflectivity factors at two channels. The illumination function $I(r_v, r_0)$ relies on the radar pulse length and beam width at r_0 and is strongly linked to the elevation angles.

The beam-broadening effects on ρ_{HV}, however, cannot be estimated by the computation of the integral similar to Eq. (4.37). Instead, the simulated observed co-polar correlation coefficient, denoted as $\rho_{HV}^{s.obs.}$, is calculated at r_0 using the ratio of

$$\rho_{HV}^{s.obs.}(r_0) = \frac{|R_{HV}^{s.obs.}|(r_0)}{\left[Z_h^{s.obs.}(r_0) Z_v^{s.obs.}(r_0)\right]^2}, \tag{4.38}$$

where $R_{HV}^{s.obs.}$ is the simulated observed complex covariance given by

$$R_{HV}^{s.obs.}(r_0) = \int R_{HV}^{i.}(r_v)\, I(r_v, r_0) dr_v. \tag{4.39}$$

In Eq. (4.39), $R_{HV}^{i.}$ is the intrinsic complex covariance depending on several radar variables and is expressed as (Ryzhkov et al. 2017):

$$R_{HV}^{i.} = Z_h^{i.} {Z_{dr}^{i.}}^{-1/2} \rho_{HV}^{i.} exp[j(\Phi_{DP} - \Phi_{DP}^t - \Phi_{DP}^r)] + Z_h^{i.} L_{dr}^{i.} exp[j(\Phi_{DP}^t - \Phi_{DP}^r)], \tag{4.40}$$

where $Z_{dr}^{i.}$, $L_{dr}^{i.}$ and $\rho_{HV}^{i.}$ represent the intrinsic values of differential reflectivity, linear

depolarization ratio in linear units, and co-polar correlation coefficient, respectively. Φ_{DP}^{t} indicates the transmitted system differential phase, and Φ_{DP}^{r} is the received system differential phase. If cross-coupling effects are negligible (i.e., $L_{dr}^{i.}$ is small), the second term in Eq. (4.40) can be ignored and the value of $\rho_{HV}^{s.obs.}$ only relies on $Z_{h/v}^{s.obs.}$, $Z_{dr}^{i.}$, and $\rho_{HV}^{i.}$. This simulation also considers attenuation effects.

iii. Generate comprehensive lookup tables:

Lookup tables are utilized to determine ΔH and H_b (i.e., the intrinsic profile of Z_H) from radar-observed ρ_{HV} and to obtain the corresponding $Z_H^{vp.bias}$ for PVPR correction. Once the radial profiles of $\rho_{HV}^{s.obs.}$ are calculated using Eqs. (4.38)-(4.40), three parameters are assigned to their respective lookup tables:

a. the distance r_b to the starting point of the $\rho_{HV}^{s.obs.}$ dip (< 0.975) caused by the ML,

b. the distance r_t to the endpoint of the $\rho_{HV}^{s.obs.}$ dip, and

c. the melting layer strength S_{ML} defined as

$$S_{ML} = \int_{r_b}^{r_t} \rho_{HV}^{th.} - \rho_{HV}^{s.obs.}(r)dr, \tag{4.41}$$

where $\rho_{HV}^{th.}$ is the threshold of ρ_{HV} set to 0.975 at C-band.

Additionally, $Z_H^{vp.bias}$ is estimated using

$$Z_H^{vp.bias}(r) = Z_H^{s.obs.}(r) - Z_H^{rain}, \tag{4.42}$$

and stored in lookup tables.

To accommodate variations in precipitation microphysics processes, the lookup tables for the parameters r_b, r_t and S_{ML} are generated with 15 values of H_b and 8 values of ΔH (indexed as ih and id), as shown in Tables 4.1-4.3 for a certain elevation scan. It is found that the values of r_b for a given H_b are a function of ΔH, and decrease for thicker ΔH. Similarly, S_{ML} depends on both H_b and ΔH. Moreover, the vectors a and b required to compute H_b are stored for the given elevation angle (Table 4.4).

For the DWD radars, it is recommended to estimate ih and id from the elevation scan data at 1.5 deg, and use these indices for PVPR correction at various elevation angles. Data from the lowest elevation angle at 0.5 deg should be avoided since the radial profile of ρ_{HV} may not rebound to values exceeding the threshold of 0.975 above the ML, making reliable estimation of S_{ML} impossible. Furthermore, Z may become too weak due to beam-broadening effects to be identified as ML. The approach may also be hindered by contamination from ground clutter, PBB, and any other potential artifacts at the 0.5-deg elevation scan.

Ideally, these lookup tables should be provided for the same antenna elevation. However, if the ML parameters (i.e., ih and id) do not significantly change with distance from the radar, then lookup tables generated for one elevation angle can be used for PVPR correction at another elevation angle. As the elevation angle of the DWD precipitation scans is adjusted to the terrain azimuthally, the lookup tables of $Z_H^{vp.bias}$ are created for angles ranging from 0.1 to 2 deg with an interval of 0.1 deg and a radial resolution of 250 m.

Table 4.1 Lookup table for the radial distance r_b (km) from the radar to the starting point of the simulated observed co-polar correlation coefficient $\rho_{HV}^{s.obs.}$ dip caused by the ML at both S- and C-bands for an elevation angle of 1.5 deg.

		ML depth ΔH (km)							
		0.55	0.53	0.51	0.49	0.45	0.40	0.36	0.32
H_b (km)	0.2	8	8	8	8	8	8	9	9
	0.4	14	14	14	14	14	14	15	15
	0.6	19	19	19	20	20	20	21	21
	0.8	24	24	25	25	25	26	26	27
	1.0	29	29	30	30	31	31	32	33
	1.2	34	34	35	35	36	36	37	39
	1.4	38	39	39	40	41	42	43	45
	1.6	43	43	44	45	46	47	48	51
	1.8	47	48	49	50	51	52	54	58
	2.0	52	53	53	55	56	57	59	64
	2.2	56	57	58	59	61	62	65	70
	2.4	60	61	63	64	65	67	70	77
	2.6	65	66	67	69	70	72	76	84
	2.8	69	70	72	73	75	77	81	92
	3.0	73	74	76	78	80	82	86	86

Table 4.2 Lookup table for the radial distance r_t from the radar to the endpoint of the $\rho_{HV}^{s.obs.}$ dip caused by the ML at both S- and C-bands for an elevation angle of 1.5 deg.

		ML depth ΔH (km)							
		0.55	0.53	0.51	0.49	0.45	0.40	0.36	0.32
H_b (km)	0.2	47	42	38	34	30	26	22	19
	0.4	60	55	50	45	40	35	32	28
	0.6	72	66	60	56	50	45	40	35
	0.8	84	77	71	65	60	54	48	43
	1.0	94	87	81	75	69	62	56	50
	1.2	105	97	90	84	77	70	64	57
	1.4	115	107	99	92	85	78	71	63
	1.6	125	116	108	101	93	85	78	69
	1.8	130	125	117	109	101	93	85	75
	2.0	130	130	125	117	109	100	91	80
	2.2	130	130	130	125	116	106	97	85
	2.4	130	130	130	130	123	113	104	90
	2.6	130	130	130	130	130	120	109	94
	2.8	130	130	130	130	130	126	115	97
	3.0	130	130	130	130	130	130	121	121

Table 4.3 Lookup table for the melting layer strength S_{ML} at both S- and C-bands for an elevation angle of 1.5 deg.

H_b (km) \ ML depth ΔH (km)	0.55	0.53	0.51	0.49	0.45	0.40	0.36	0.32
0.2	2.10	1.72	1.37	1.08	0.79	0.52	0.32	0.17
0.4	2.36	1.90	1.48	1.15	0.83	0.52	0.31	0.15
0.6	2.62	2.09	1.60	1.23	0.87	0.53	0.30	0.13
0.8	2.87	2.28	1.73	1.31	0.91	0.54	0.29	0.11
1.0	3.11	2.45	1.84	1.37	0.94	0.55	0.28	0.10
1.2	3.34	2.61	1.94	1.44	0.97	0.55	0.27	0.08
1.4	3.55	2.77	2.04	1.49	0.99	0.55	0.26	0.07
1.6	3.76	2.91	2.13	1.54	1.01	0.55	0.25	0.05
1.8	3.94	3.04	2.21	1.59	1.03	0.54	0.23	0.04
2.0	4.04	2.89	2.29	1.63	1.04	0.54	0.22	0.03
2.2	4.05	3.22	2.35	1.66	1.05	0.53	0.21	0.02
2.4	3.98	3.20	2.37	1.70	1.06	0.52	0.19	0.01
2.6	3.84	3.11	2.33	1.69	1.07	0.51	0.18	0.01
2.8	3.66	2.98	2.25	1.64	1.05	0.51	0.17	< 0.01
3.0	3.44	2.80	2.12	1.56	1.01	0.50	0.16	0.16

Table 4.4 Predetermined eight-element vectors a and b for an elevation angle of 1.5 deg.

vector a	-0.230	-0.215	-0.206	-0.194	-0.183	-0.164	-0.150	-0.089
vector b	0.044	0.043	0.042	0.040	0.039	0.038	0.036	0.033

To reconstruct the intrinsic profile of Z_H, the values of r_b and S_{ML} at each ray are first estimated based on the radar-observed ρ_{HV} at 1.5 deg. The value of S_{ML} is then utilized to determine ΔH. Finally, the known values of r_b and ΔH, along with the vectors a and b, enable the derivation of H_b. The overall process involves the use of a melting layer detection algorithm (MLDA), which follows a specific sequence of steps:

i. Estimate the range interval ($r_b,\ r_t$):

The estimated H_b value based on the QVP of ρ_{HV}, denoted as H_0, is used to identify the initial value of ih in the lookup tables of r_b and r_t. Following that, the range interval (i_{min}, i_{max}) utilized to search for the possible interval of ($r_b,\ r_t$) is determined, given by

$$(i_{min}, i_{max}) = (\frac{2}{3}\frac{r_b[ih,4]}{dr}, \frac{5}{4}\frac{r_t[ih,4]}{dr}), \tag{4.43}$$

where dr represents the radial resolution of radar beams in km. The value in the middle column ($id = 4$) of the lookup tables is assumed in Eq. (4.43) since the value of ΔH is still unknown at this stage. Moreover, the range interval (i_{min}, i_{max}) is defined as slightly larger than the first guess of ($r_b,\ r_t$), namely ($r_b[ih, 4],\ r_t[ih, 4]$), by factors 2/3 and 5/4.

ii. Determine r_b:

The data within the range interval (r_b, r_t) are expected to meet the criteria of 0.8 < ρ_{HV} < 0.975 and 20 dBZ < Z_H < 50 dBZ. If the count of bins satisfying these criteria within the interval (i_{min}, i_{max}) is less than five, $r_b[ih, 4]$ is assigned as r_b. Otherwise, the median of the five lowest qualified bins is set as r_b.

iii. Determine ΔH from S_{ML}:

Determining r_b alone is not adequate to estimate H_b due to the considerable variation of r_b with ΔH, even when H_b is held constant. Therefore, the value of ΔH is estimated using S_{ML}. If less than 80% of the expected valid bins are found within the interval (i_{min}, i_{max}), the default value of $S_{ML}[ih, 4]$ is used. Otherwise, S_{ML} is calculated by summing the differences between 0.975 and the observed ρ_{HV} values from the valid bins. The index of ΔH (id) can then be determined by identifying the column in the S_{ML} table having the values closest to the calculated S_{ML}.

iv. Determine H_b:

Obtaining r_b and id is sufficient to confirm the true value of H_b using the equation of

$$H_b = a(id) + b(id)\, r_b. \tag{4.44}$$

Subsequently, H_t can be computed using the known value of ΔH in addition to H_b. Both H_b and H_t are smoothed along the azimuth by averaging with a moving window of 21 rays.

Once the indices of ih and id are identified in the lookup table, the value of $Z_H^{vp.bias}$ can be retrieved and used to correct Z_H for rainfall retrieval. The resulting reflectivities, referred to as $Z_H^{vp.cor.}$, can be expressed as

$$Z_H^{vp.cor.}(r) = Z_H^{obs.} - Z_H^{vp.bias}(ih, id, r), \tag{4.45}$$

where $Z_H^{obs.}$ represents the observed reflectivities, and r is the range bin. Note that if data above the ML are classified as graupel or hail by the HCA (as introduced later in section 4.5), no PVPR correction is applied.

4.4.2 K_{DP}-based snowfall estimator

Bukovčić et al. (2020) developed a generalized bivariate relationship for $S(Z_h, K_{DP})$ based on 2-dimensional video disdrometer (2DVD) data. This relation is applicable for particles with ar values ranging from 0.5 to 0.8 and σ values ranging from 0 to 40 deg, and for radars at various frequencies. The relation is formulated using Eqs. (2.2), (2.10)-(2.12), (2.17), and (2.26), and is given by

$$S(Z_h, K_{DP}) = \frac{27.9\times10^{-3}}{[F_o(L_a - L_b)]^{0.615}} \left(\frac{P_0}{P}\right)^{0.5} Z_h^{0.33} (K_{DP}\lambda)^{0.615}. \tag{4.46}$$

Fig. 4.17 demonstrates that the intercept parameter in the $S(Z_h, K_{DP})$ relation is proportional to the values of ar and σ. Bukovčić et al. (2020) also proposed a generalized relationship for $S(Z_{dr}, K_{DP})$, but its use with DWD radars is not recommended due to radome effects.

The intercept value of the C-band $S(Z_h, K_{DP})$ relation can be determined using a given λ value and the provided information of P, ar, and σ for each radar bin. As previously mentioned, ar is associated with the shape factors L_a and L_b, while σ is related to the orientation factor F_o. The value of P is obtained from the radiosonde observations available on the platform administered by the Department of Atmospheric Sciences at the University of Wyoming (http://weather.uwyo.edu/upperair/sounding.html). As for ar, its value is assumed to be 0.6 based on the previous studies of Korolev and Isaac (2003) and Hogan et al. (2012), as their findings suggested average values of ar between 0.5 and 0.7 for irregular and aggregated snowflakes. The uncertainty regarding orientation, however, remains an issue. The value of σ for ice particles varies from 10 deg for pristine or lightly aggregated ice crystals to 40 deg for heavily aggregated snowflakes, as indicated by Hendry et al. (1987), Matrosov et al. (2005b),

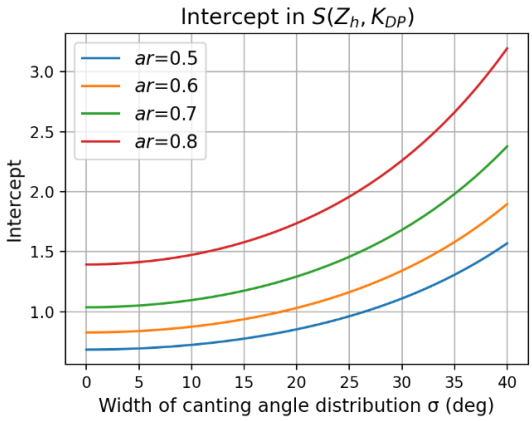

Figure 4.17 Impact of the particle aspect ratio ar and canting angle distribution width σ on the intercept parameter of the snowfall relation $S(Z_h, K_{DP})$. The mean canting angle is set to 0 deg and the atmospheric pressure P is assumed to be 1013.25 mb.

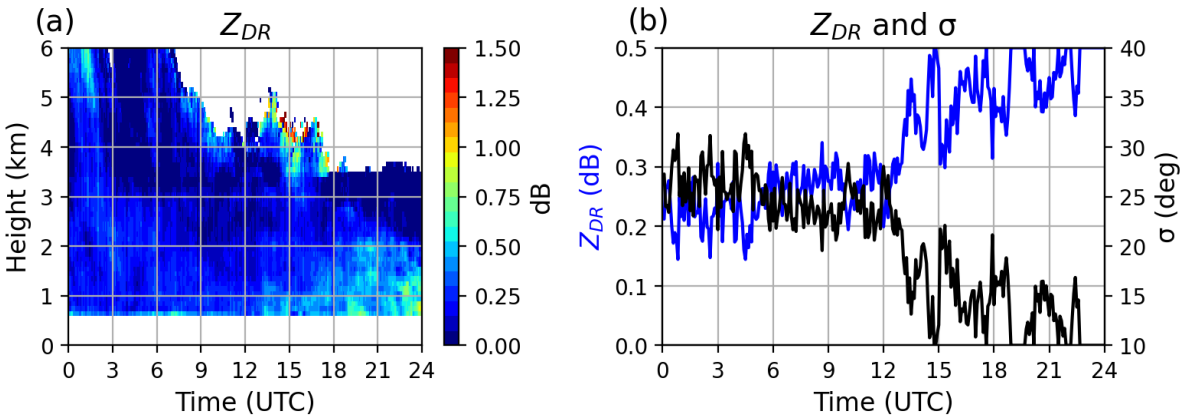

Figure 4.18 (a) QVP of Z_{DR} obtained from the Isen (ISN) radar at a 1.5-deg elevation angle on 3 February 2019 and (b) time series of Z_{DR} (blue) and corresponding σ (black) values at the lowest levels of the QVP.

and Melnikov and Straka (2013). This variability affects the intercept value in the $S(Z_h, K_{DP})$ relation significantly, and thus, this study estimates σ based on Z_{DR}. Picca et al. (2014) have reported that the Z_{DR} value of dry snow aggregates ranges from 0 to 0.5 dB, while heavily aggregated snowflakes have a near-zero value. Assuming a negative linear relationship between Z_{DR} and σ within the range of (0 dB, 0.5 dB) for Z_{DR} and (10 deg, 40 deg) for σ, the σ value near the surface or above H_t is determined using the median of Z_{DR} at the lowest five QVP levels above the ground or H_t (Fig. 4.18). When the Z_{DR} value exceeds 0.5 dB, it is capped at 0.5 dB. At higher levels, specifically within and above the dendritic growth layer (DGL), σ is equal to 10 deg. The DGL typically spans between -10° and -20°C height, and thus its altitude is determined based on the radiosonde observations. Once the location of the DGL and the value of σ near the surface or above H_t are confirmed, the values of σ are then linearly interpolated into each height level. This process allows for the adjustment of the intercept value in the $S(Z_h, K_{DP})$ relation at each radar bin and time step. In the case of K_{DP} being zero or negative, the Z_h-based snowfall retrieval given by

$$S(Z_h) = 0.115 Z_h^{0.5} \tag{4.47}$$

is applied instead. This equation is currently implemented in the operational Multi-Radar Multi-Sensor (MRMS) system in the U.S.A. (Vasiloff 1997; Zhang et al. 2016).

4.5 QPE comparison and evaluation

The QPE retrievals obtained in the present study are assessed using ground-based measurements collected by the rain gauges and disdrometers operated by DWD. In addition, the performance of these retrievals is compared against both DWD's operational QPE products and other retrievals documented in the existing literature. The rain gauge information, the compared retrievals and the evaluation methodologies are described below.

The DWD runs one of the world's most densely distributed networks of rain gauges, consisting of over 7,500 stations (Zolina et al. 2014). The DWD Climate Data Center platform (CDC, https://opendata.dwd.de/climate_environment/CDC/) provides access to data from 1032 of these gauges (Fig. 3.1 green crosses) that have undergone quality control and offer temporal

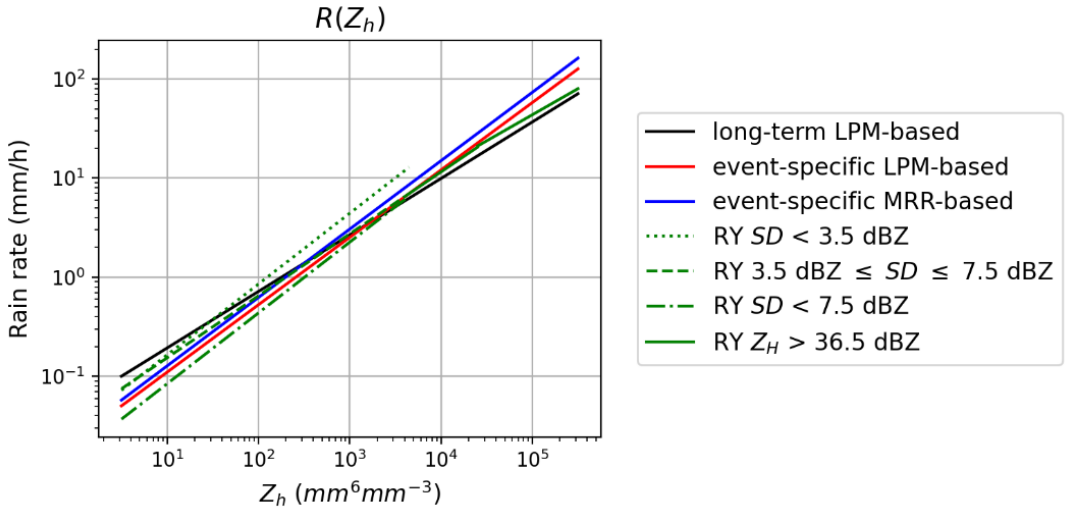

Figure 4.19 Comparison of the Z_h-based rainfall relations, referred to as $R(Z_h)$, derived in this study (black, red, and blue) and those used in the DWD QPE product Radar-Online-Aneichung (RADOLAN) RY (green). SD represents the standard deviation (texture) within the nearest 12 radar bins.

resolutions ranging from 1 minute to annual. Hundreds of them are used for QPE evaluation, with the exact number dependent on the precipitation events. The gauges are of the weighing OTT Pluvio type, which enables its use in measuring various forms of precipitation, including rain, hail, and snow, without the need for additional heating equipment. As compared to tipping-bucket precipitation gauges, this gauge type yields higher accuracy (Habib et al., 2001).

This study includes a comparison between the proposed precipitation retrievals and DWD's RADOLAN product RY. The RY product has a high temporal and spatial resolution of five minutes and 1 km, respectively, but it is not publicly available. The RY algorithm consists of several $R(Z_h)$ relations, formulated based on different thresholds of Z_H intensities and standard deviations (texture) calculated from the nearest 12 radar bins (Bartels et al. 2004). As depicted in Fig. 4.19, the $R(Z_h)$ relations utilized in RY for heavy rain lie between those derived in this study from the long-term and event-specific (i.e., warm-rain event) LPM measurements, whereas they differ significantly for light-to-moderate rain.

Another RADOLAN product RW is available from the CDC platform 30 minutes after the completion of an hour. RW is based on RY, but adjusted to hourly rain gauge measurements using a weighted average of radar-gauge differences and ratios. During the processing of the RW product, each hour 20% of the gauges are randomly chosen and reserved as audit data, which do not contribute to the adjustment. In addition, radar and gauge data from neighboring countries are included (further details about the RADOLAN products can be found at http://www.dwd.de/RADOLAN). Although RW has a long processing time, limiting its use for nowcasting and flashflood warnings, it serves as an ideal benchmark for evaluating the proposed QPE algorithms. A coding error, however, caused potential 10-minute precipitation accumulations to be missing from RW between 25 April 2018 and 17 August 2021. Therefore, a corrected version of RW was ordered from DWD specifically for evaluation during the flooding event on 14 July 2021. It is important to note that the conclusion drawn by Chen et al. (2021a) regarding the comparison of proposed QPE retrievals with RW is incorrect due to this error.

The evaluation of QPE retrievals involves a comparison of their hourly or event-accumulated precipitation sums against gauge measurements. This comparison utilizes three statistical measures, including the normalized root-mean-square error (NRMSE), normalized mean bias (NMB), and Pearson's correlation coefficient (CC), and defined as

$$\text{NRMSE} = \frac{\sqrt{\frac{\sum_{i=1}^{N}(R_i - G_i)^2}{N}}}{\sigma(\text{G})} \times 100\ \%, \tag{4.48}$$

$$\text{NMB} = \frac{\frac{\sum_{i=1}^{N}(R_i - G_i)}{N}}{\bar{\text{G}}} \times 100\ \%, \text{ and} \tag{4.49}$$

$$\text{CC} = \frac{\sum_{i=1}^{N}(R_i - \bar{R})(G_i - \bar{\text{G}})}{\sqrt{\sum_{i=1}^{N}(R_i - \bar{R})^2 \sum_{i=1}^{N}(G_i - \bar{\text{G}})^2}}. \tag{4.50}$$

In Eqs. (4.48)-(4.50), N represents the total number of QPE-gauge/disdrometer pairs compared, while R_i and G_i denote the radar-estimated and gauge/disdrometer-observed precipitation sums at the i[th] station. $\bar{R}$ and $\bar{G}$ refer to the mean values of R_i and G_i, respectively, and $\sigma(G)$ is the standard deviations of G_i.

In the evaluation of QPE performance over a wide area, radar observations are transformed into 1-km-resolution composites, following the same grid format as RY and RW. The WRADLIB package, an open-source library for processing weather radar data, is employed to calculate the weighted average radar-estimated precipitation rates or other input variables and subsequently generate the corresponding composite data (Heistermann et al. 2013, https://docs.wradlib.org/en/stable/comp.html). In the overlap areas with observations from two radars or more, the weight is determined based on the sampling volume of the radar beam per bin that varies depending on the range and beam width. The locations of gauges and disdrometers are also converted into the same grid format for pairing. On the other hand, when analyzing and discussing the performance of individual radars, the gauge-measured rainfall/snowfall sums are paired with the mean of radar-retrieved sums within a horizontal range of 1 km from the gauge locations in the original radar polar coordinate grid. The RY and RW products are excluded from this comparison.

The other compared QPE algorithms, including those summarized in Table 4.5, are described below, along with their respective evaluation methodologies.

i. $R(A)$ algorithm based on scan-wise α derived from the Z_{DR} slope:

This study compares the accuracy of the proposed $R(A, K_{DP})$ algorithms, which use scan-wise adjusted α values for A estimates and are henceforth referred to as $R(A^{adj.}, K_{DP})$, with $R(Z_h)$ and $R(Z_h, K_{DP})$. Additionally, the fixed $\alpha_{H/V}$ values of 0.093 dB deg^{-1} and 0.071 dB deg^{-1}, respectively, obtained from the entire database are used to derive $A_{H/V}$ values, and the resulting hybrid QPEs, denoted as $R(A^{fix.}, K_{DP})$, serve as another benchmark to determine whether the scan-wise adjustment of α can enhance radar-based QPE. To further assess the improvements from the German-regime relations, the $R(A_{H/V})$ and $R(K_{DP})$ relations derived from Oklahoma's DSDs (Ryzhkov et al. 2014; Ryzhkov and Zrnić 2019) are also employed. They are given by

$$R(A_H) = 294A_H^{0.89}, \tag{4.51}$$

$$R(A_V) = 393A_V^{0.93}, \text{ and} \tag{4.52}$$

$$R(K_{DP}) = 25.3K_{DP}^{0.78}. \tag{4.53}$$

The gauge-adjusted RW product is anticipated to yield the lowest errors when evaluated using the same gauge data. To compare RW with other rainfall retrievals, additional measurements from sixty LPMs, collected by DWD (Fig. 3.1 purple dots and crosses) and the University of Bonn on 19 July 2017, are used as rain gauges for evaluation (Fehlmann et al. 2020). All evaluations are performed in the RADOLAN grid and by the data below the ML only.

ii. $R(A)$ algorithm based on ray/segment-wise α derived from Z_{DR}:

Due to the limited number of radars selected for algorithm development, the evaluation of the presented algorithm is conducted in polar coordinates without composing. The application of ray/segment-wise α, i.e., $\langle\alpha\rangle$, requires segment-wise integration in the ZPHI method, which creates an opportunity to investigate the feasibility of this integration approach and the impact of HS on A estimation. Consequently, the study compares the performance of $R(A^{adj.}, K_{DP})$ with two equivalents that derive A using i) $\langle\alpha\rangle$ and segment-wise integration, denoted as $R(A^{\langle\alpha\rangle}, K_{DP})$, and ii) scan-wise adjusted α values and segment-wise integration, denoted as $R(A^{\langle adj.\rangle}, K_{DP})$.

iii. QPE for warm-rain precipitation:

In order to identify the primary causes of underestimation in the investigated rainfall event, five additional rainfall algorithms are evaluated alongside the original algorithm that uses DWD radar observations and rainfall relations derived from long-term LMP measurements. These algorithms are as follows: i) utilizing rainfall relations obtained from event-specific LPM-measured DSDs, ii) applying explicit VP correction (projection) down to a height of 700 m, iii) combing explicit VP correction with implicit VP correction, which involves the use of MRR-DSD-derived relations, as a complete VP correction, iv) including JuXPol observations as gap-filling, and v) using both complete VP correction and JuXPol data. The last two algorithms are assessed only in the domain where JuXPol provides measurements at lower altitudes than the DWD radars. The comparison is carried out in the RADOLAN grid.

To evaluate the accuracy of QPE in regions where DWD radar beams reach high altitudes above the ML but JuXPol observations fill gaps below, precipitation estimates above H_b are included in the composite. The PVPR correction, however, is ineffective in this case, as the ML height is already quite high (> 2.5 km), making the signature of BB less apparent for data with low scanning angles. Therefore, QPE within and above the ML height, which is defined by the QVP of ρ_{HV}, is calculated using the $R(Z_h)$ relation of Eq. (4.2) along with additional multipliers of 0.6 and 2.8, respectively. To mitigate the discontinuity in the rain-field map between areas below and within the ML, a 15-km-wide transition zone is defined from the lower bounds of the ML towards the radar. Within this zone, the results of the $R(Z_h)$ and $R(A^{adj.}, K_{DP})$ retrievals are averaged using IDW.

iv. QPE with PVPR correction:

The accuracy of the rainfall retrieval derived from PVPR-corrected Z_h fields is compared to that derived from uncorrected Z_h fields, and that generated using the $R(Z_h)$ relation with multipliers of 0.6 and 2.8. Unlike the previous application of the multipliers merely based on the ML height, they are assigned in this case based on the results of an HCA developed at Colorado State University (code package available at https://github.com/CSU-RadarMet/CSU_RadarTools). The HCA employs a fuzzy-logic method and in this study the classification process utilizes default settings for assigning weights to the temperature information and radar observations, with the exception of L_{DR} which is not provided by the used radar. The $R(Z_h)$ relation is then multiplied by different factors according to the respective hydrometeor types, i.e., 0.6 for wet snow and 2.8 for any solid particles except for hail and graupel.

To evaluate the performance of QPE with the PVPR correction, the focus is on areas at far distances from the radar site (within and above the ML). Therefore, the evaluation is based on measurements of individual radars in polar coordinates.

v. Snowfall polarimetric algorithm:

To investigate the potential increase in the accuracy of snowfall estimates through the use of polarimetry, the $S(Z_h, K_{DP})$ algorithm is compared with the $S(Z_h)$ algorithm from Vasiloff (1997), i.e., Eq. (4.47). In four snowfall events, both algorithms are applied to observations from the DWD precipitation scans and volume scans at the 1.5- and 2.5-deg angles, respectively, in order to evaluate their performance at different heights (given the possible impact of decreasing K_{DP} values towards the surface). Additionally, the proposed snowfall retrieval is compared to the RY product, and thus the data are converted into the RADOLAN grid for analysis.

Furthermore, the performance of $S(Z_h, K_{DP})$ is compared with that of PVPR-corrected $R(Z_h)$ in areas above the low ML height during a stratiform rain event. This validation is based on the assumed conservation of the precipitation flux through the ML. This allows the rain rates measured by gauges at the surface to be utilized as the ground truth for the snow flux just above the ML. The comparison is evaluated in polar coordinates.

Table 4.5 A set of QPE retrieval algorithms compared in this study. It includes i) $R(Z_h)$, a rainfall retrieval based on linear reflectivity at horizontal polarization Z_h, ii) $R(Z_h, K_{DP})$, a hybrid rainfall retrieval based on both Z_h and specific differential phase K_{DP}, and iii) $R(A_{H/V}, K_{DP})$, hybrid rainfall retrievals based on specific attenuation at horizontal or vertical polarizations $A_{H/V}$ and K_{DP}. For the $R(A_{H/V}, K_{DP})$ algorithms, four different approaches to estimate $A_{H/V}$ in the ZPHI method are compared: i) $A_{H/V}^{fix.}$, derived using fixed values of attenuation parameter $\alpha_{H/V}$ and a ray-wise integration technique, ii) $A_{H/V}^{adj.}$, derived using scan-wise adjusted $\alpha_{H/V}$ values and the ray-wise integration technique, iii) $A_{H/V}^{\langle adj.\rangle}$, the same as ii) but using a segment-wise integration technique, and iv) $A_{H/V}^{\langle\alpha\rangle}$, derived using segment-wise $\alpha_{H/V}$ values, i.e., net $\alpha_{H/V}$ within the rainy segment denoted as $\langle\alpha\rangle$, and the segment-wise integration technique. Additionally, two snowfall retrieval algorithms are included: one based on Z_h, denoted as $S(Z_h)$, and the other based on both Z_h and K_{DP}, denoted as $S(Z_h, K_{DP})$.

QPE algorithm	description
$R(Z_h)$	A rainfall retrieval based on attenuation-corrected Z_h. The attenuation correction is performed using the path-integrated specific attenuation (PIA) with an α_H value of 0.093 dB deg^{-1}. This value is derived from the entire data set of drop size distributions (DSD) measured in Germany.
$R(Z_h, K_{DP})$	A hybrid rainfall retrieval based on Z_h and combined with $R(K_{DP})$ when the attenuation-corrected reflectivity at horizontal polarization in dBZ, referred to as Z_H, exceeds 40 dBZ.
$R(A_{H/V}^{fix.}, K_{DP})$	Hybrid rainfall retrievals based on $A_{H/V}$ and combined with $R(K_{DP})$ when attenuation-corrected Z_H exceeds 40 dBZ. The $A_{H/V}$ values are obtained using fixed $\alpha_{H/V}$ values of 0.093 and 0.071 dB deg^{-1}, respectively, and a ray-wise integration technique suggested by Wang et al. (2017). This technique excludes the contribution of intense convective cells (defined as those with Z_H > 50 dBZ) from the integration path to avoid potential hail contamination.
$R(A_{H/V}^{adj.}, K_{DP})$	The same as $R(A_{H/V}^{fix.}, K_{DP})$ but with the $A_{H/V}$ values derived using scan-wise adjusted $\alpha_{H/V}$ values based on the changes in differential reflectivity Z_{DR} with respect to Z_H.
$R(A_{H/V}^{\langle adj.\rangle}, K_{DP})$	Hybrid rainfall retrievals based on $A_{H/V}$ and combined with $R(K_{DP})$ when attenuation-corrected Z_H exceeds 40 dBZ. The $A_{H/V}$ values are obtained using scan-wise adjusted $\alpha_{H/V}$ values and a segment-wise integration technique in the ZPHI method. The segment-wise integration is limited to rain with Z_H values of less than 40 dBZ.
$R(A_{H/V}^{\langle\alpha\rangle}, K_{DP})$	The same as $R(A_{H/V}^{\langle adj.\rangle}, K_{DP})$ but with the $A_{H/V}$ values derived using $\langle\alpha\rangle$, which is determined by the local Z_{DR} values.
$S(Z_h)$	A snowfall retrieval based on Z_h (Vasiloff 1997).
$S(Z_h, K_{DP})$	A snowfall retrieval based on both Z_h and K_{DP}.

Chapter 5

Application to Real Precipitation Events

The study assesses the performance of various proposed QPE algorithms, which target different hydrometeor types including rain, melting graupel/hail, mixed-phase hydrometeors within the ML, and snowflakes. This assessment is conducted by evaluating these algorithms using both gauge and LPM measurements, and comparing them with existing QPE retrievals.

5.1 Phase-based retrievals below the melting layer

For measurements observed below the ML, the hybrid rainfall estimators $R(A_{H/V}, K_{DP})$ are utilized. To achieve precise estimates of A using the ZPHI method, two types of approaches for deriving α are proposed: i) scan-wise adjustment of α based on Z_{DR} slopes, and ii) segment/ray-wise α derived from local Z_{DR} values.

5.1.1 $R(A)$ retrievals using scan-wise α

The rain events listed in Table 3.3 are analyzed, excluding the one with low ML height on 23 September 2018. The evaluation statistics by gauge measurements for all compared algorithms and the RADOLAN RY product from the six events are summarized in Table 5.1. The convective and stratiform events are first examined separately, followed by a performance comparison of rainfall relations derived from DSDs measured in Germany and Oklahoma.

Convective rain

Based on the rain gauge observations, the Z_h-based retrievals, including the proposed $R(Z_h)$ retrieval and RY, exhibit the highest NRMSE values above 70% and the lowest CC values for all cases. The $R(Z_h)$ retrieval, however, demonstrates a more stable performance than RY, which gives large positive biases ranging from 13% to 32%. With regards to the hybrid retrievals, it is noticeable that $R(A_H^{fix.}, K_{DP})$ consistently results in the highest NMB values, while the use of scan-adjusted α reduces NMB values compared to the use of fixed α, with a more pronounced improvement seen for the horizontal polarization. As a consequence, $R(A_H^{adj.}, K_{DP})$ shows success in reducing the impact of relatively large DSD variability on A_H by the scan-wise adjustment of α_H and produces accuracy similar to $R(A_V^{adj.}, K_{DP})$. Overall, $R(A^{adj.}, K_{DP})$ surpass in quality the RY product with a reduction in NRMSE of 13% and in NMB of 16%. The lowest NRMSE values are obtained by $R(Z_h, K_{DP})$, but it also yields larger negative NMB values compared to $R(A^{adj.}, K_{DP})$. When evaluated using LPM observations, Fig. 5.1 indicates that the score numbers of RY remain the worst, while those of the proposed hybrid retrievals are significantly improved and approach RW's scores.

Stratiform rain

The RY product stands out in terms of having the least biases among all algorithms, whereas $R(Z_h)$ significantly underestimates rainfall amounts. $R(Z_h, K_{DP})$ performs similarly to or

Table 5.1 Evaluation of six proposed QPE retrievals and DWD's operational product Radar-Online-Aneichung (RADOLAN) RY against rain gauge measurements for hourly accumulations in six rain events. The evaluation metrics include the normalized root-mean-square error (NRMSE), normalized mean bias (NMB), and Pearson's correlation coefficient (CC). The retrievals with the top (second to top) quality measures from the compared retrievals are highlighted in bold (bold-italics), while RY is not included in the ratings. The total numbers of data points N available for the evaluation are also noted.

		$R(Z_h)$	$R(Z_h, K_{DP})$	$R(A_H^{fix.}, K_{DP})$	$R(A_H^{adj.}, K_{DP})$	$R(A_V^{fix.}, K_{DP})$	$R(A_V^{adj.}, K_{DP})$	RY
		convective rain						
2017/07/19 $N = 1194$	NRMSE (%)	72.8	**64.4**	68.6	66.5	66.5	***66.0***	74.6
	NMB (%)	*12.8*	**6.8**	20.0	***12.8***	15.7	14.0	16.4
	CC	0.71	0.77	0.76	0.76	0.77	0.77	0.68
2018/07/28 $N = 991$	NRMSE (%)	73.8	***65.5***	66.1	66.1	**65.2**	65.7	79.5
	NMB (%)	-5.5	-8.8	6.0	**1.4**	***3.1***	3.4	27.4
	CC	0.68	0.76	0.75	0.75	0.76	0.76	0.68
2018/08/09 $N = 1003$	NRMSE (%)	70.6	**63.3**	64.1	63.6	***63.4***	63.5	71.3
	NMB (%)	-14.7	-11.0	2.7	-1.3	***-0.5***	**-0.2**	13.3
	CC	0.72	0.78	0.77	0.77	0.78	0.78	0.72
2019/07/20 $N = 1306$	NRMSE (%)	77.4	**67.7**	70.3	69.7	***68.0***	69.0	93.5
	NMB (%)	**-1.1**	-6.1	9.6	***3.1***	7.4	5.9	32.8
	CC	0.68	0.75	0.75	0.75	0.77	0.76	0.67
		stratiform rain						
2017/07/25 $N = 5299$	NRMSE (%)	66.5	68.1	71.8	**63.5**	79.9	***65.5***	63.8
	NMB (%)	-26.1	-27.1	-40.8	***-22.5***	-51.0	**-22.1**	-9.6
	CC	0.82	0.81	0.82	0.81	0.82	0.79	0.78
2021/07/14 $N = 2114$	NRMSE (%)	69.8	68.8	58.3	***57.0***	61.3	**56.6**	66.0
	NMB (%)	-44.8	-45.0	-34.9	***-30.8***	-41.8	**-30.2**	-26.0
	CC	0.89	0.90	0.88	0.88	0.89	0.87	0.80

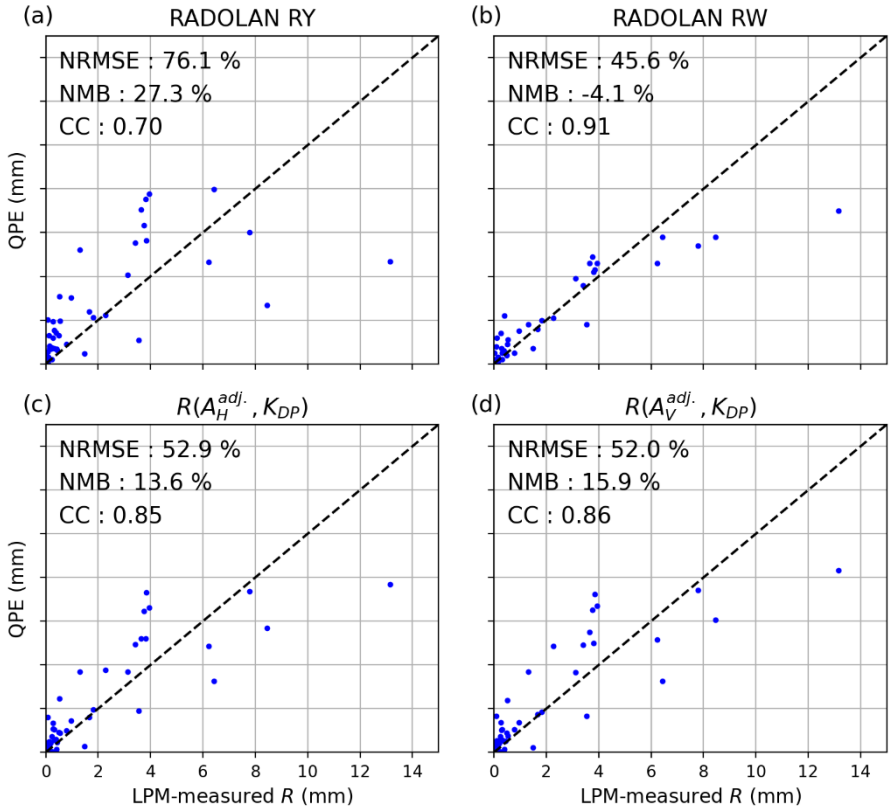

Figure 5.1 Scatterplots of hourly rainfall sums for the convective rain event on 19 July 2017, obtained from four different sources against LPM-measured rainfall sums. These sources include the RADOLAN (a) RY, and (b) RW products, and (c) and (d) hybrid rainfall retrievals based on K_{DP} and $A_{H/V}$, with the latter derived using scan-wise adjusted $\alpha_{H/V}$ and ray-wise integration in the ZPHI method, denoted as $R(A_{H/V}^{adj.}, K_{DP})$. The evaluation statistics normalized root-mean-square error (NRMSE), normalized mean bias (NMB), and Pearson's correlation coefficient (CC) are shown in each panel. The total number of data points evaluated is 55.

slightly worse than $R(Z_h)$, likely due to the limited number of data points with Z_H > 40 dBZ and insensitivity of K_{DP} to stratiform rain. The significant underestimation by $R(A^{fix.}, K_{DP})$ is attributed to too low α values. The adjustment of α on a scan-wise basis increases QPE accuracy, resulting in the lowest errors of all proposed algorithms. It, however, still yields negative biases of up to 30%. The improvements achieved by adjusted α are smaller for the case on 14 July 2021 than for those on 25 July 2017. The underestimation of rainfall in the former case comes from vertical gradients of rain intensities near the surface observed during warm rain, which will be discussed in the next subsection.

The impact of PBB on the Z_h-based retrievals, including RW and $R(Z_h, K_{DP})$, is mostly alleviated by employing the precipitation scan. Consequently, the immunity of A-based retrievals to this impact is not particularly advantageous, as observed in a few rays from the measurements of the HNR and Rostock (ROS) radars (Fig. 5.2 black arrows). Note that in those rainfall maps, some radar coverages deviate from the circular shape due to the terrain-following scan strategy and the constraint of retrievals to observations below the ML. Nevertheless, in the mountainous southern region of Germany, specifically in the measurement rage of the Feldberg (FBG) radar where PBB cannot be entirely avoided by applying a terrain-following elevation angle, great benefits can be expected from the utilization of $R(A)$ algorithms.

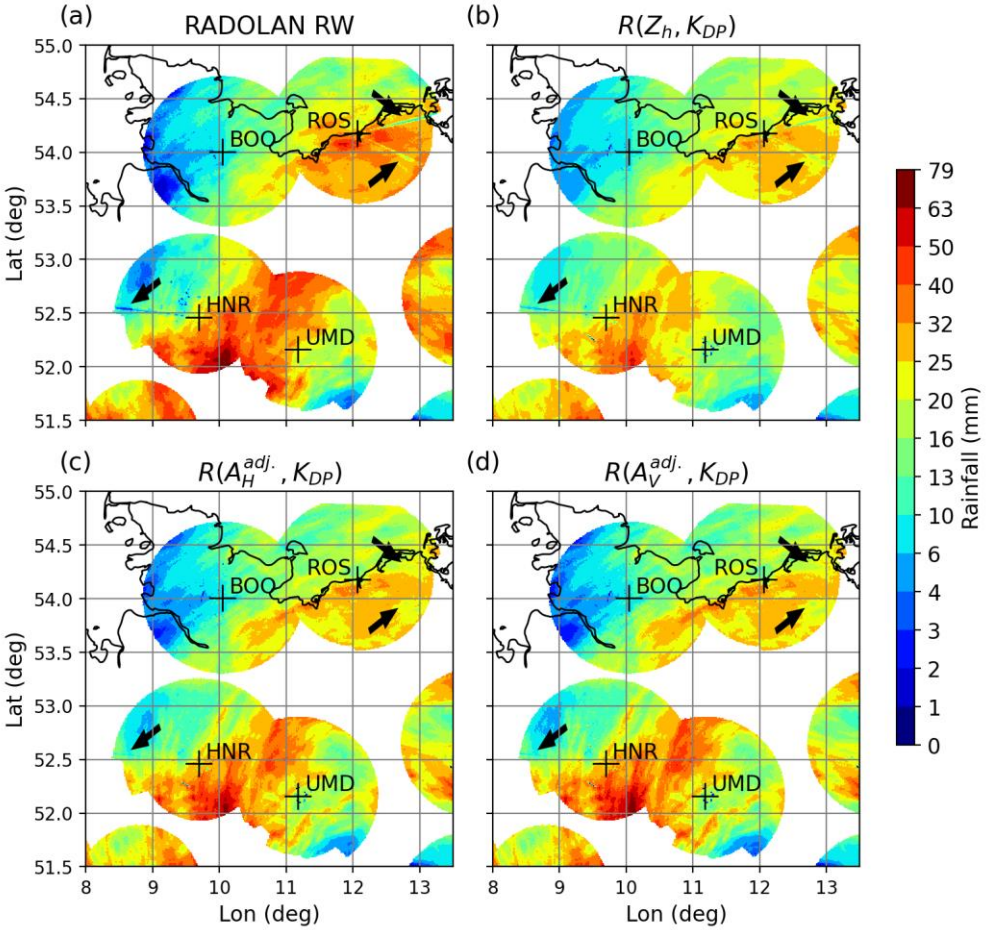

Figure 5.2 Daily-accumulated rainfall composite maps of the stratiform rain event on 25 July 2017, generated from (a) RADOLAN RW, (b) $R(Z_h, K_{DP})$, (c) $R(A_H^{adj.}, K_{DP})$, and (d) $R(A_V^{adj.}, K_{DP})$. The black arrows indicate the rays affected by partial beam blockage (PBB) in the Z_h-based rainfall retrieval fields.

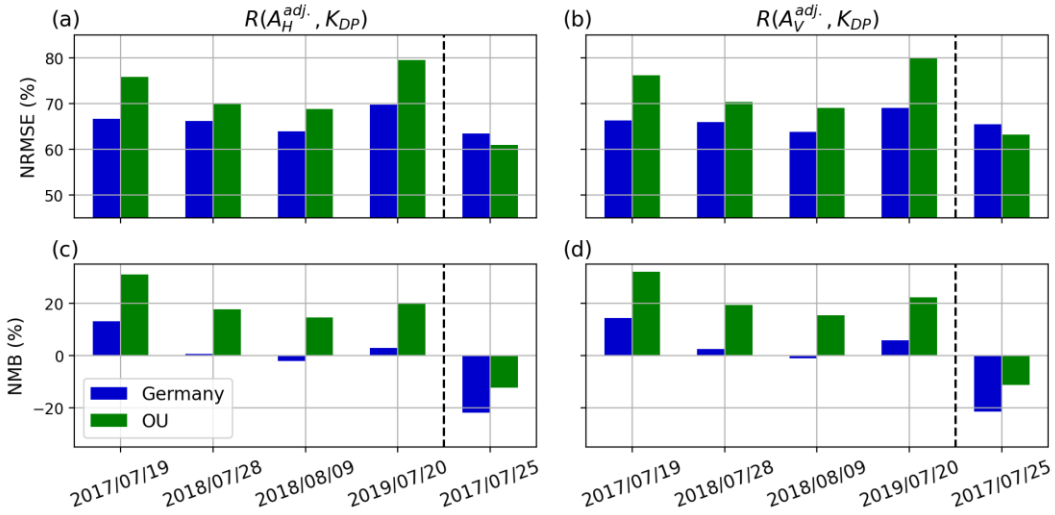

Figure 5.3 Comparison of the hourly NRMSE (upper panel) and NMB (bottom panel) for the $R(A_H^{adj.}, K_{DP})$ (left column) and $R(A_V^{adj.}, K_{DP})$ (right column) retrievals evaluated by gauge data. The blue and green bars mark the $R(A, K_{DP})$ retrievals obtained using rainfall relations derived from DSDs measured in Germany and Oklahoma in the U.S.A., respectively. The bars on the left/right-hand side of the dashed lines represent the convective/stratiform rain events.

Oklahoma rainfall relations

The utilization of $R(A, K_{DP})$ relations obtained from Oklahoma leads to increased errors in the convective events, with higher NMB values by over 10% compared to those derived from local DSD measurements (Fig. 5.3). Despite lower errors observed in the stratiform event when using Oklahoma's relations, the improvements, especially in NRMSE, are relatively minor and insufficient to counterbalance their substandard performance in convective precipitation. In general, the rainfall relations established in this study provide a better representation of the German region, indicating the need for regional precipitation relationships.

5.1.2 $R(A)$ retrievals using ray/segment-wise α

Table 5.2 reveals that neither the use of $\langle\alpha\rangle$ for each rainy segment nor the segment-wise integration technique in the ZPHI method can reliably enhance the accuracy of the derived A and thus $R(A)$ for convective rain. Instead, the $R(A, K_{DP})$ algorithms using $A^{\langle\alpha\rangle}$, $A^{\langle adj.\rangle}$, and $A^{adj.}$, respectively, perform on a case-by-case basis. On the other hand, $R\left(A^{\langle\alpha\rangle}, K_{DP}\right)$ provides the lowest errors during the stratiform rain event, while the segment-wise integration technique does not work effectively because of the limited detected HS.

Nevertheless, Fig. 5.4 illustrates that the rain field obtained from $R(A_H^{adj.}, K_{DP})$ displays several bundles of rays with notably underestimated rain rates in areas behind the strongly attenuating hail cores, whereas $R(A_H^{\langle adj.\rangle}, K_{DP})$ generates less biased rays (black circles). Upon closer examination of the radial profiles in Fig. 5.5, $A_H^{\langle adj.\rangle}$ rectifies the overestimated values of $A_H^{adj.}$ before and the underestimated values after the HS (i.e., the range within two black dashed lines). Note that the imbalance of $A_H^{adj.}$ occurs because the attenuation from the intense cell is missed in the integration path, resulting in less PIA erroneously assigned to the bins located behind.

Table 5.2 Evaluation (NRMSE, NMB, and CC) of $R(A_{H/V}, K_{DP})$ retrievals for five rain events against hourly gauge measurements.

		$A_H^{\langle\alpha\rangle}$	$A_H^{\langle adj.\rangle}$	$A_H^{adj.}$	$A_V^{\langle\alpha\rangle}$	$A_V^{\langle adj.\rangle}$	$A_V^{adj.}$
convective rain							
2017/07/19 $N = 641$	NRMSE (%)	64.0	63.6	64.1	**62.3**	***63.1***	63.5
	NMB (%)	17.7	14.8	***13.5***	14.3	**11.7**	15.0
	CC	0.80	0.79	0.79	0.80	0.79	0.80
2018/07/28 $N = 651$	NRMSE (%)	69.8	70.0	***69.6***	69.8	70.0	**69.4**
	NMB (%)	5.4	**-1.0**	4.5	4.7	***-3.8***	6.1
	CC	0.72	0.72	0.72	0.72	0.72	0.73
2018/08/09 $N = 524$	NRMSE (%)	***67.5***	67.9	**67.4**	67.8	69.0	67.9
	NMB (%)	-11.3	-13.1	***-7.4***	-12.1	-14.7	**-5.4**
	CC	0.74	0.74	0.74	0.74	0.73	0.74
2019/07/20 $N = 688$	NRMSE (%)	62.1	**61.6**	62.4	62.2	***61.9***	62.3
	NMB (%)	4.8	**-0.2**	4.4	3.4	***-3.0***	6.1
	CC	0.79	0.79	0.79	0.79	0.79	0.80
stratiform rain							
2017/07/25 $N = 1789$	NRMSE (%)	***56.3***	59.5	59.5	**54.7**	59.8	60.2
	NMB (%)	***-11.8***	-20.0	-20.1	**-8.7**	-18.1	-17.9
	CC	0.85	0.83	0.83	0.85	0.82	0.82

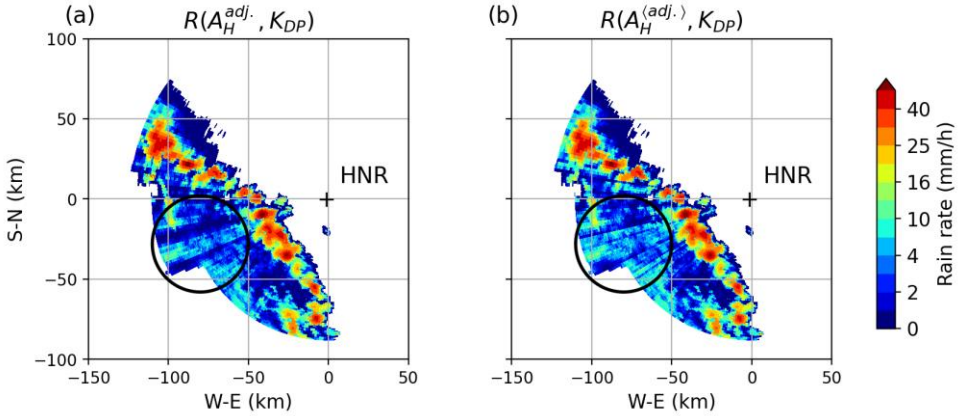

Figure 5.4 Instantaneous rainfall maps on 19 July 2017 at 1725 UTC, obtained from HNR radar observations using (a) $R(A_H^{adj.}, K_{DP})$ and (b) $R(A_H^{\langle adj.\rangle}, K_{DP})$ with A_H calculated using scan-wise adjusted α_H and segment-wise integration in the ZPHI method. The black circles mark rays with underestimated rain rates behind the HSs.

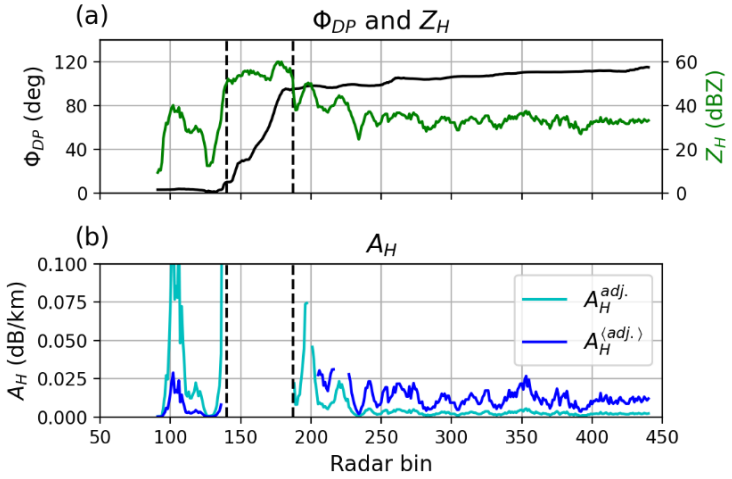

Figure 5.5 Radial profiles of (a) Φ_{DP} in black and Z_H in green, and (b) $A_H^{adj.}$ in cyan and $A_H^{\langle adj.\rangle}$ in blue. These profiles are obtained at the 255-deg azimuth of HNR radar observations on 19 July 2017 at 1725 UTC.

5.2 Warm-rain precipitation

During the flooding event on 14 July 2021, the rainfall algorithms presented in subsection 5.1.1, which rely on climatological DSDs and DWD radar data, exhibit noticeable deficiencies (Figs. 5.6 and 5.7 left column). As demonstrated in the first row group of Table 5.3, even the most favorable $R(A^{adj.}, K_{DP})$ retrievals have an NMB value of approximately -30%. To mitigate such underestimation, the VP correction and gap-filling methods thus are proposed.

Quantitative analysis

For daily rainfall totals exceeding 40 mm, the deviation from the one-to-one line for rainfall totals derived at high altitudes is greater than those obtained at low altitudes in all QPE algorithms (Fig. 5.7 left column). This discrepancy can be attributed to the increased rain rates towards the ground during this event. Of all the rainfall retrievals, RY displays the widest scatter against gauge-measured rainfall sums and gives the lowest CC value (Fig. 5.8a). The other DWD QPE product RW with gauge adjustments also yields a negative bias with an NMB value

close to -12% (Fig. 5.8b). Note that an isolated point within its scatter originates from DWD's ground clutter removal processing (red arrow). By excluding this point from the evaluation, the NRMSE and NMB values of RW slightly decrease to 17.7% and -10.9%, respectively.

According to the second row group of Table 5.3, the use of event-specific LPM-based relations leads to limited improvements in NMB, and only slightly better NRMSE compared to the relations derived from long-term DSD observations. However, the explicit VP correction for the Z_h-based retrievals, including $R(Z_h)$ and $R(Z_h, K_{DP})$, does improve the results as indicated in the third row group. Furthermore, the addition of MRR-DSD-derived relations, i.e., the implicit VP correction, significantly reduces errors by around 20% for all retrievals (see the last row group). Accordingly, the middle column of Fig. 5.6 clearly depicts enhanced rainfall amounts, and large differences in rainfall accumulations between the Z_h-based and A-based retrievals are mitigated, especially in the southwest region where the gaps between radar observations and the surface are vast due to the high location of NHB (black circles). The $R(A^{adj.}, K_{DP})$ algorithms with the VP correction outperform the others and even produce qualities comparable to RW. Therefore, considering the vertical precipitation gradients in QPE has a more positive and apparent impact than taking into account differences in DSD types between this event and climatology. Finally, Fig. 5.6 also illustrates that the phase-based $R(A^{adj.}, K_{DP})$ retrievals eliminate the notable radome effect of NHB caused by lightning protections, which is not the case for the Z_h-based retrievals.

Using only the data acquired from the lowest elevation scan of JuXPol for rainfall estimation causes rain fields with some holes near the southwest of the radar site due to ground clutter removal (Fig. 5.6 right column). Nonetheless, incorporating observations from the gap-filling radar leads to higher and thus more accurate rainfall estimates in the domain ranging from 50.5° to 51.0°N and from 6.0° to 7.5°E (black squares). Although the decreases in errors achieved by gap-filling are smaller than those obtained from the VP correction, the CC values overall increase further (the second and third row groups of Table. 5.4). In contrast to the Z_h-based algorithms, the inclusion of JuXPol data results in greater improvement in QPE quality for the phase-based algorithms. This difference can be attributed to the high sensitivity of Φ_{DP} to rain rates at X-band, leading to less noise than C-band. Moreover, the shorter-wavelength radars have stronger attenuation uncertainties in power-related variables, further contributing to the superior performance of phase-based algorithms with JuXPol data. The advantage of gap-filling is most pronounced in areas where JuXPol provides observations at considerably lower height levels than the DWD radars, as evidenced by the strong correlation between the reductions of normalized bias [defined as NB $= (R_i - G_i)/G_i \times 100\,\%$] and the height difference (Fig. 5.9). These correlations are lower for the A-based retrievals than for the $R(Z_h)$ and $R(Z_h, K_{DP})$ retrievals because at some points, the NB values of $R(A^{adj.}, K_{DP})$ remain similar regardless of the height levels from which they are obtained.

The VPs of JuXPol observations are also corrected, and the final QPE retrievals are generated by fusing the VP-corrected data from JuXPol with those from the DWD radars. As a result, the errors in QPE are reduced by at least 45% of NRMSE and 30% of NMB compared to the original QPE algorithms (see the first and last row groups in Table 5.4). The scatters of ensuing accumulated retrievals against gauge-measured rain totals are also much closer to the one-to-one line (Fig. 5.7 right column). Overall, the performance of the final $R(A^{adj.}, K_{DP})$ retrievals surpasses that of RW.

Table 5.3 Evaluation of four QPE retrievals obtained from DWD radar observations against gauge-measured daily accumulations for the rain event on 14 July 2021. These retrievals are derived using long-term or event-specific rainfall relations, and with explicit vertical profile (VP) correction, or complete VP correction (i.e., the combination of explicit and implicit VP correction). The evaluation is based on 306 data points.

		$R(Z_h)$	$R(Z_h, K_{DP})$	$R(A_H^{adj.}, K_{DP})$	$R(A_V^{adj.}, K_{DP})$
long-term relation (original version)	NRMSE (%)	59.8	59.9	***45.0***	**44.3**
	NMB (%)	-41.2	-41.4	***-30.3***	**-29.8**
	CC	0.97	0.97	0.97	0.97
event-specific relation	NRMSE (%)	54.5	56.8	**42.6**	***43.6***
	NMB (%)	-39.6	-41.4	**-29.5**	***-30.4***
	CC	0.97	0.97	0.97	0.97
long-term relation explicit VP Cor.	NRMSE (%)	51.2	52.8	**44.5**	***45.4***
	NMB (%)	-33.2	-34.2	**-29.6**	***-30.5***
	CC	0.97	0.97	0.97	0.97
VP Cor. (explicit + implicit)	NRMSE (%)	29.9	33.7	***25.6***	**23.8**
	NMB (%)	-14.3	-17.5	***-9.6***	**-6.3**
	CC	0.97	0.97	0.97	0.98

Table 5.4 Evaluation of four QPE retrievals derived from DWD radar data with additional JuXPol measurements against gauge-measured daily accumulations on 14 July 2021. The evaluation is based on 32 data points.

		$R(Z_h)$	$R(Z_h, K_{DP})$	$R(A_H^{adj.}, K_{DP})$	$R(A_V^{adj.}, K_{DP})$
long-term relation	NRMSE (%)	93.0	91.8	***73.2***	**72.9**
	NMB (%)	-44.9	-44.7	**-34.3**	***-34.4***
	CC	0.93	0.94	0.93	0.93
VP Cor.	NRMSE (%)	**38.8**	45.5	43.4	***41.0***
	NMB (%)	***-12.3***	-16.2	-12.8	**-10.9**
	CC	0.95	0.94	0.93	0.93
long-term relation + JuXPol	NRMSE (%)	78.9	77.3	***55.3***	**54.5**
	NMB (%)	-37.1	-37.6	**-24.9**	***-25.1***
	CC	0.94	0.96	0.97	0.97
+ JuXPol VP Cor.	NRMSE (%)	34.1	35.1	***26.1***	**24.7**
	NMB (%)	***-4.1***	-8.5	**4.0**	4.6
	CC	0.94	0.95	0.97	0.97

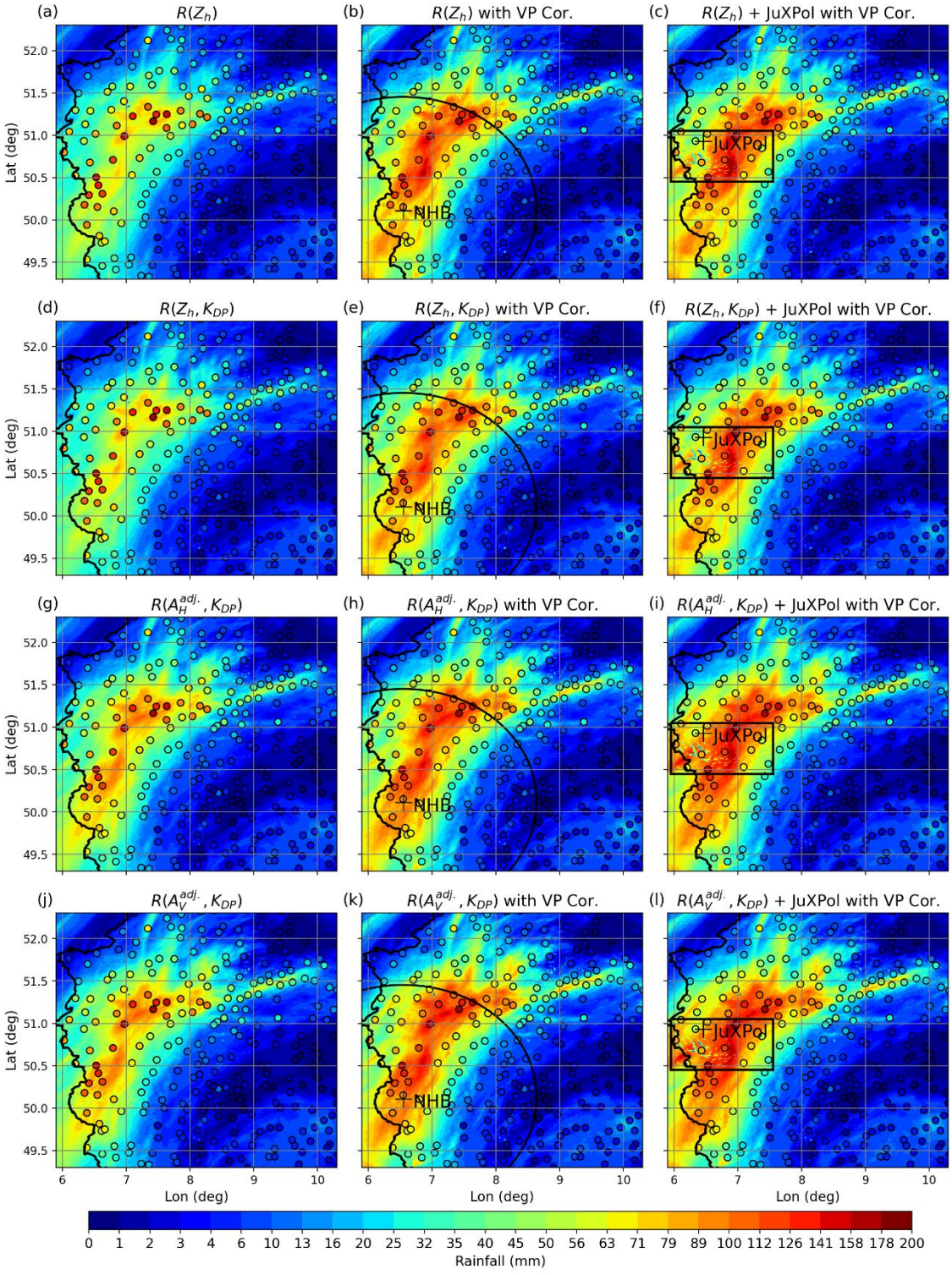

Figure 5.6 Composite maps of daily-accumulated rainfall sums on 14 July 2021 obtained using $R(Z_h)$, $R(Z_h, K_{DP})$, $R(A_H^{adj.}, K_{DP})$, and $R(A_V^{adj.}, K_{DP})$ algorithms (top to bottom). The three columns from left to right represent the rainfall estimates derived based on four DWD C-band radar data, with VP correction, and with the additional inclusion of JuXPol data and VP correction, respectively. The measurement range of NHB is depicted by black circles in the middle column, while the black squares in the right column highlight areas where JuXPol provides lower-altitude observations than the DWD radars with enhanced rainfall sums. The colored dots indicate the rainfall accumulations measured by 306 DWD gauges.

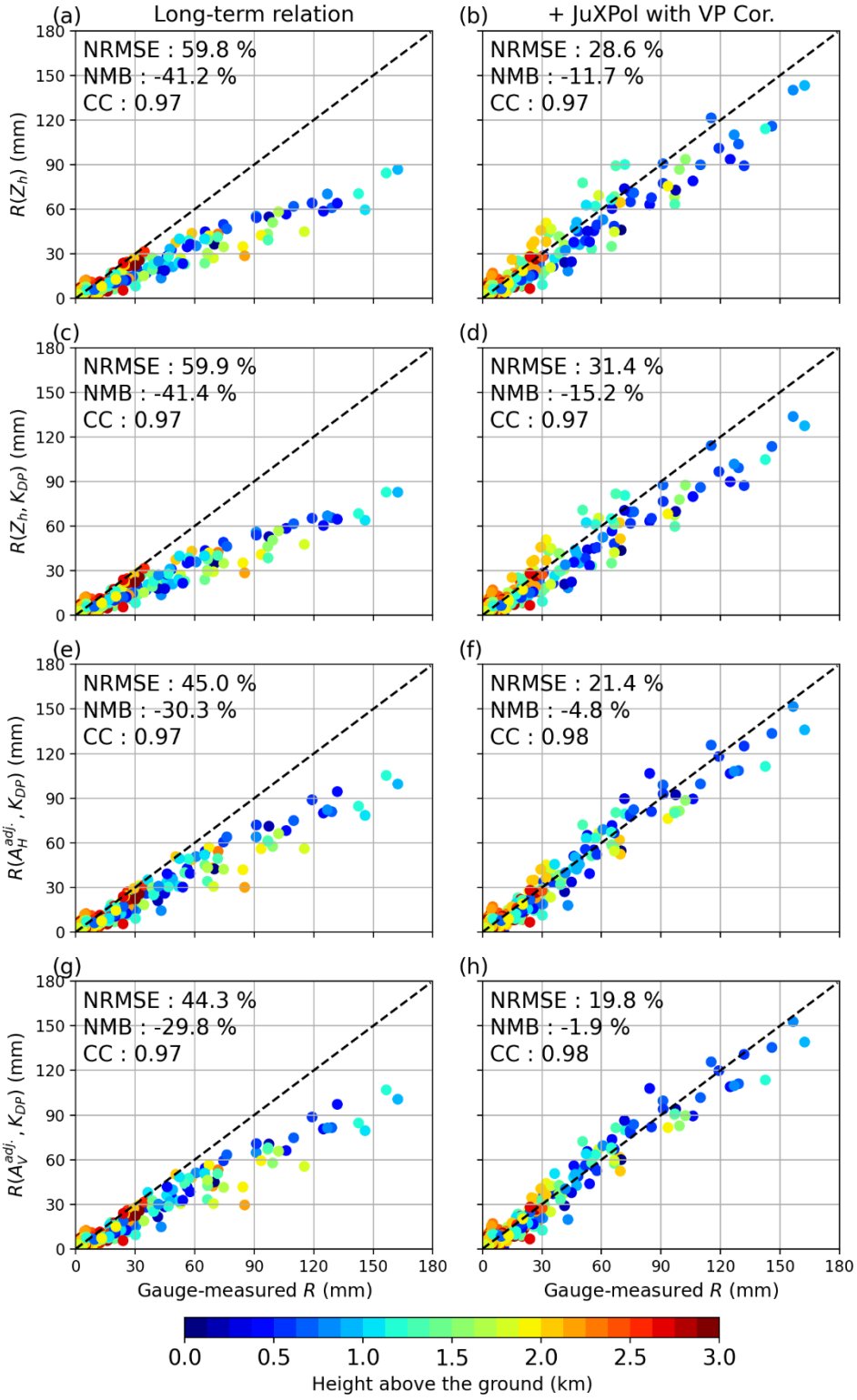

Figure 5.7 Scatterplots of daily-accumulated QPE retrievals and gauge-measured rain totals on 14 July 2021. The retrievals are generated using the $R(Z_h)$, $R(Z_h, K_{DP})$, $R(A_H^{adj.}, K_{DP})$, and $R(A_V^{adj.}, K_{DP})$ algorithms (top to bottom). The left column shows the rainfall estimates obtained based on the DWD radar data, while the right column displays the estimates with the inclusion of JuXPol observations and VP correction. The color of the dots represents the heights of radar observations above the ground.

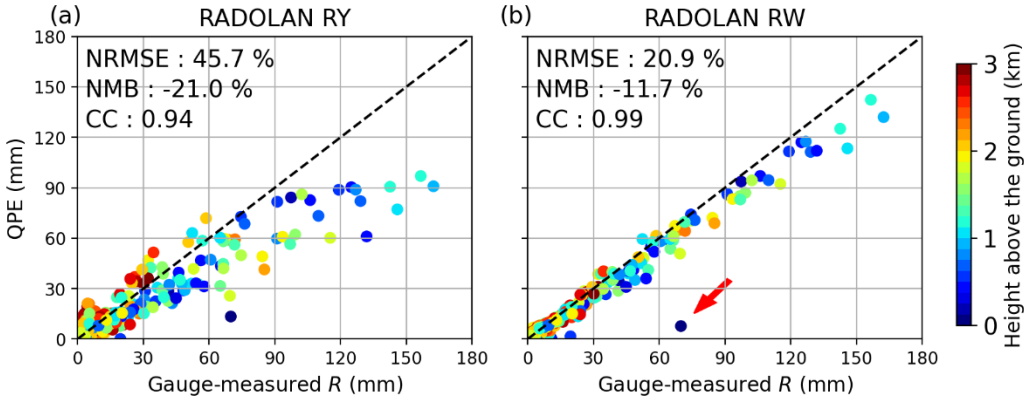

Figure 5.8 As in Fig. 5.7, but for the DWD RADOLAN (a) RY and (b) RW products.

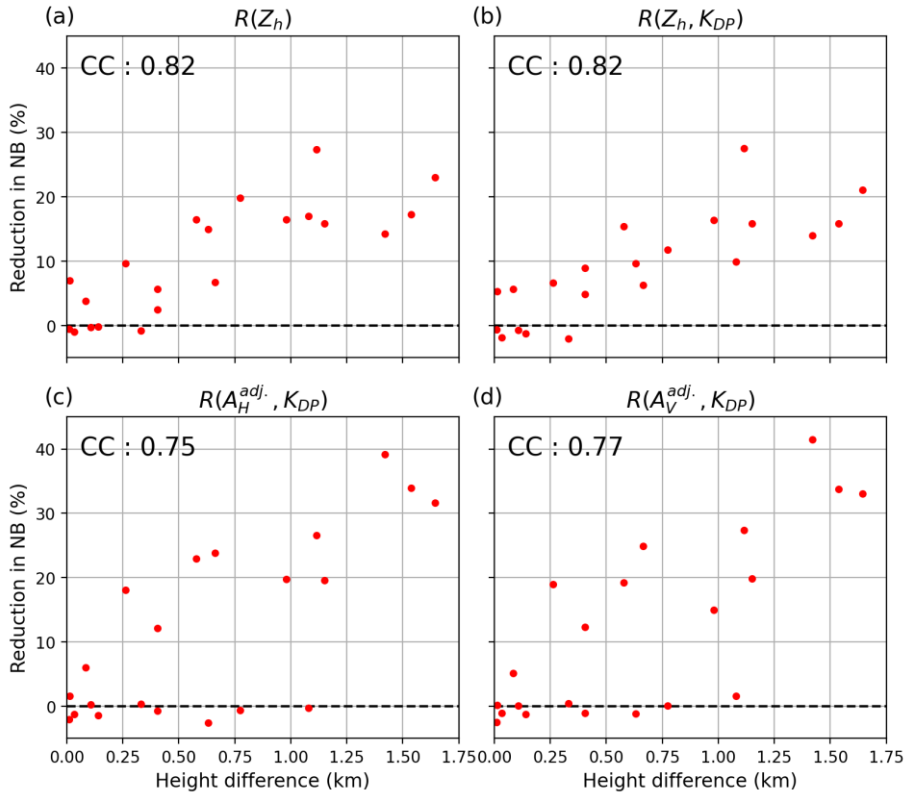

Figure 5.9 Scatterplots of the reduction in normalized bias (NB) achieved by including JuXPol data against the measurement height difference for the (a) $R(Z_h)$, (b) $R(Z_h, K_{DP})$, (c) $R(A_H^{adj.}, K_{DP})$, and (d) $R(A_V^{adj.}, K_{DP})$ algorithms. Only data points with rainfall totals exceeding 40 mm are included in the analysis. Pearson's correlation coefficient between the reduction in NB and the height difference is given in each panel.

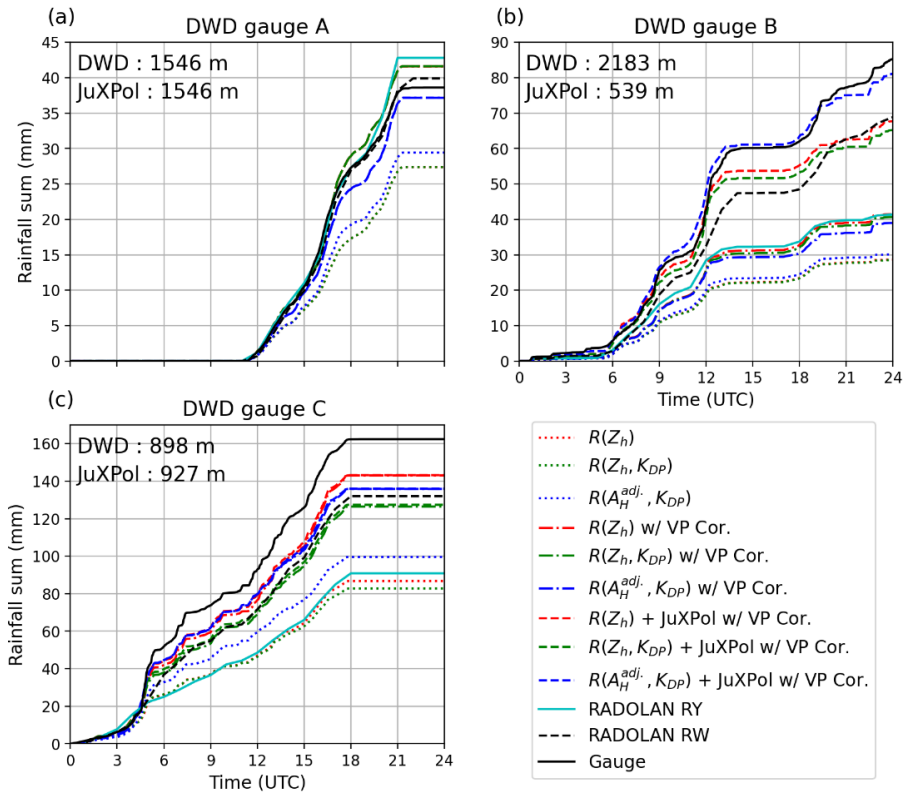

Figure 5.10 Time series of accumulated rain totals on 14 July 2021, as measured by three DWD rain gauges (a) A, (b) B, and (c) C (full black lines) compared to RY (full cyan lines), RW (dashed black lines), and the proposed rainfall retrievals. The dotted, dashed-dotted, and dashed lines depict the original retrievals based on the DWD radar data, retrievals with VP correction, and retrievals with both VP correction and inclusion of JuXPol data, respectively. The lines in red, green, and blue correspond to the $R(Z_h)$, $R(Z_h, K_{DP})$, $R(A_H^{adj.}, K_{DP})$ algorithms. The heights of radar observations above the ground, before and after the inclusion of JuXPol data, are indicated in each panel.

Time series of accumulated rainfall from different QPE algorithms

For further analysis, three DWD gauges, with IDs 03263, 15000, and 05619, are exemplary selected and referred to as gauges A, B, and C, respectively (Fig. 4.14 white circles). These gauges have radar coverages at varying heights and have recorded different rainfall intensities throughout the day. The objective of this analysis is to compare the rain total time series of these gauges with those of the proposed retrievals and DWD QPE products. Note that the $R(A_V^{adj.}, K_{DP})$ algorithm is not included in this comparison due to its high similarity to $R(A_H^{adj.}, K_{DP})$.

Gauge A is located outside of JuXPol's coverage, and thus the retrievals derived from VP-corrected DWD radar measurements and from radar measurements with additional JuXPol data coincide in Fig. 5.10a. The Z_H values observed above gauge A consistently remain below 40 dBZ, indicating that $R(K_{DP})$ does not contribute to the rainfall estimates. Consequently, the curves of $R(Z_h)$ and $R(Z_h, K_{DP})$ also coincide. In line with the above evaluation, the Z_h-based algorithms produce the lowest estimated rainfall, and the less DSD-sensitive $R(A_H^{adj.}, K_{DP})$ algorithm performs slightly better. The $R(A_H^{adj.}, K_{DP})$ retrieval with VP correction displays the curve closest to gauge A among all the proposed retrievals, followed by the others which have also corrected for VP.

For gauge B, which is situated between the ESS and NHB radar and near JuXPol, the results are opposite to gauge A when the VP correction method is applied to DWD radar data alone. The ensuing retrievals are not significantly improved and have similar performance to RY (Fig. 5.10b). This could be due to the fact that the altitude of the DWD radar observations is already beyond 2 km height, where the representativeness of RD-QVP fades as data from wider and farther areas are averaged. In such cases, the gap-filling radar plays a crucial role and all associated curves closely follow the gauge observations: the Z_h-based retrievals, although lagging behind in the second half of the period, give rainfall sums close to the RW product in the end; the curve of $R(A_H^{adj.}, K_{DP})$ is shifted upwards, leading to improvements of two factors and the best agreement with the gauge.

At locations where both JuXPol and DWD radars monitor precipitation at similar height levels, gap-filling is not as effective. Hence, the $R(A_H^{adj.}, K_{DP})$ retrieval including the JuXPol measurements cannot fully replicate the highest daily-accumulated rainfall amount of up to 160 mm during the day, as measured by gauge C (Fig. 5.10c). In contrast to gauge B, where larger height differences need to be bridged, rainfall retrievals with VP correction exhibit better correlation with the gauge observations throughout the entire time span.

5.3 Snow quantification

To assess the potential of PVPR correction to reduce Z_H biases within and above the ML for surface rainfall estimation, a rainfall event with an ML height of around 0.9 km is chosen. The resulting PVPR-corrected $R(Z_h)$ retrieval is compared to the uncorrected $R(Z_h)$ and hydrometeor-type-specific $R(Z_h)$ retrievals. In addition, the performance of the polarimetric snowfall algorithm $S(Z_h, K_{DP})$ is evaluated by applying it to four snowfall events, and comparing the outcomes to those obtained from the traditional $S(Z_h)$ algorithm. This section presents the preliminary results of these two methodologies.

5.3.1 Polarimetric vertical profile of reflectivity correction

Both the HCA and PVPR correction methods demonstrate increased accuracy of QPE in comparison to the uncorrected $R(Z_h)$ retrieval (Table 5.5). The success of the PVPR correction method in rainfall estimation is highlighted by the HNR and Prötzel (PRO) radars, with improvements of over 30% in NRMSE and up to 0.3 in CC as compared to the uncorrected $R(Z_h)$ retrieval. In the case of the PRO radar as shown in Fig. 5.11, the HCA-based retrieval method mitigates overestimated rainfall caused by BB contamination and underestimated rainfall at far distances. The appearance of discontinuities in the rain field, however, is visible and strongly depends on the temperature information (Fig. 5.12). On the other hand, the PVPR correction method reduces the Z_H biases within and above the ML without any discontinuity, which leads to more accurate rainfall estimates than the other two retrieval methods.

For the remaining three radars, the PVPR correction method, however, yields the greatest negative biases among all retrievals (Table 5.5 and Fig. 5.13). The BB signature observed by ESS, enclosed by the dashed line in Fig. 5.13d, is limited to the north and is not as clear and symmetrical as it appears in Fig. 5.11d. This discrepancy can be due to the spatial heterogeneity of the ML, which can hinder the efficacy of ML detection. Moreover, severe underestimation in the south results from diminished convective cells due to erroneous ML detection (Fig. 5.13f). A further discussion on the causes of this outcome will be presented in subsection 6.3.1.

Table 5.5 Evaluation of three Z_h-based rainfall retrievals against hourly rain gauge measurements on 23 September 2018 using five radar observations. These retrievals are based on uncorrected Z_h, hydrometeor classification algorithm (HCA), and Z_h with polarimetric vertical profile of reflectivity (PVPR) correction, respectively. Bold numbers mark retrievals with the top-quality measures.

		$R(Z_h)$	HCA-based $R(Z_h)$	PVPR-Cor. $R(Z_h)$
ESS $N = 1035$	NRMSE (%)	86.3	**80.6**	91.6
	NMB (%)	-44.5	**-34.7**	-54.9
	CC	0.64	**0.67**	**0.67**
FLD $N = 1684$	NRMSE (%)	82.9	**76.8**	85.0
	NMB (%)	-47.8	**-32.6**	-52.3
	CC	0.70	0.71	**73**
HNR $N = 1340$	NRMSE (%)	105.5	83.4	**62.7**
	NMB (%)	-15.7	**7.4**	-12.6
	CC	0.49	0.68	**0.79**
PRO $N = 789$	NRMSE (%)	91.6	73.4	**60.8**
	NMB (%)	15.8	17.0	**-6.3**
	CC	0.67	0.74	**0.80**
UMD $N = 1430$	NRMSE (%)	90.6	**74.9**	84.6
	NMB (%)	-34.4	**-23.9**	-40.0
	CC	0.51	**0.70**	0.65

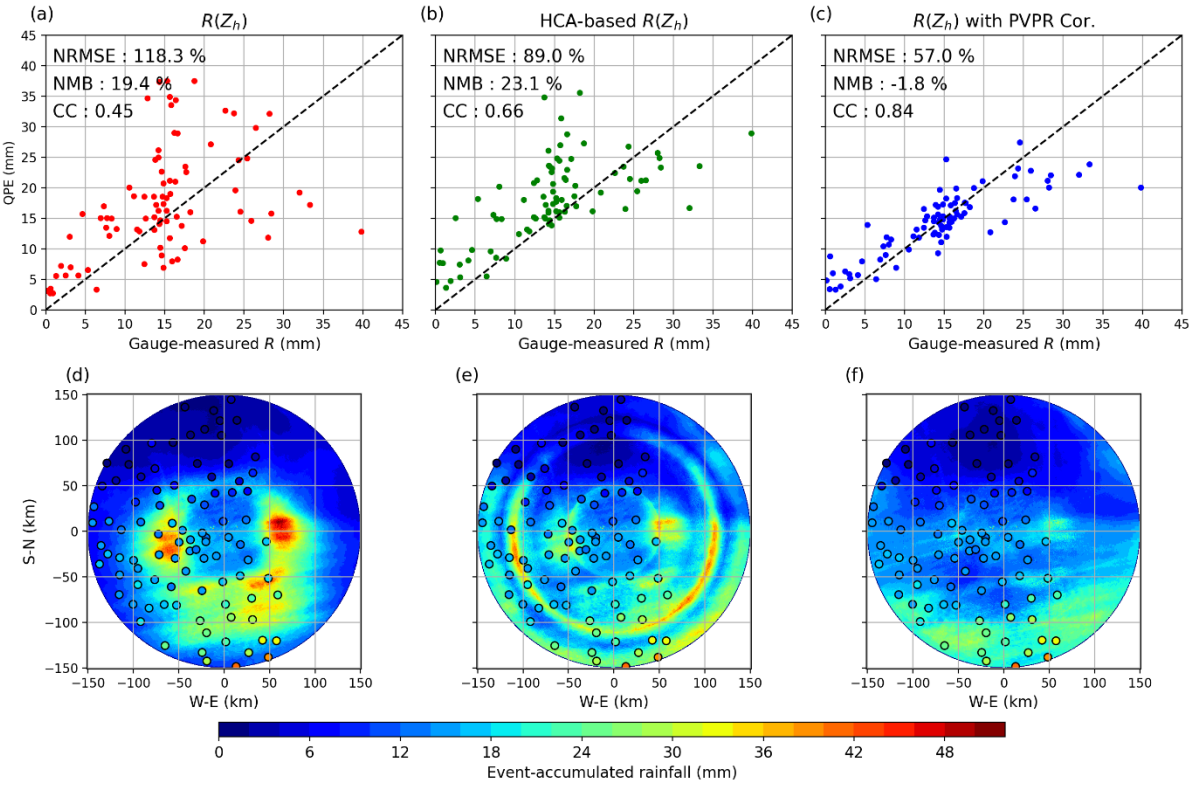

Figure 5.11 Scatterplots (upper panel) and rainfall maps (bottom panel) of event-accumulated rainfall sums derived from three $R(Z_h)$ retrievals using Prötzel (PRO) radar observations against gauge-measured rainfall sums on 23 September 2018. These retrievals are obtained using uncorrected Z_h, based on the results of a hydrometeor classification algorithm (HCA), and from Z_h with polarimetric vertical profile of reflectivity (PVPR) correction, respectively, from left to right.

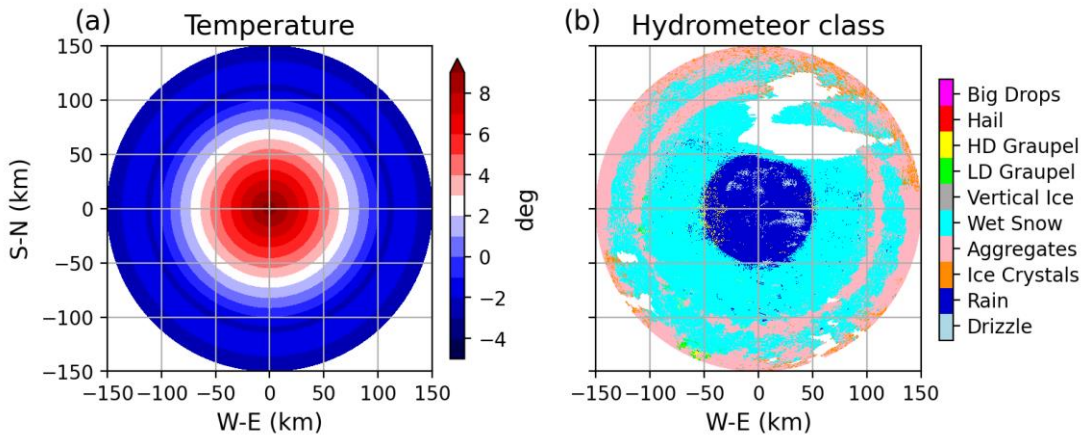

Figure 5.12 Maps of the (a) interpolated temperature field derived from radiosonde measurements on 23 September 2018 at 1200 UTC, and (b) hydrometeor types classified based on PRO radar observations on the same day at 1355 UTC.

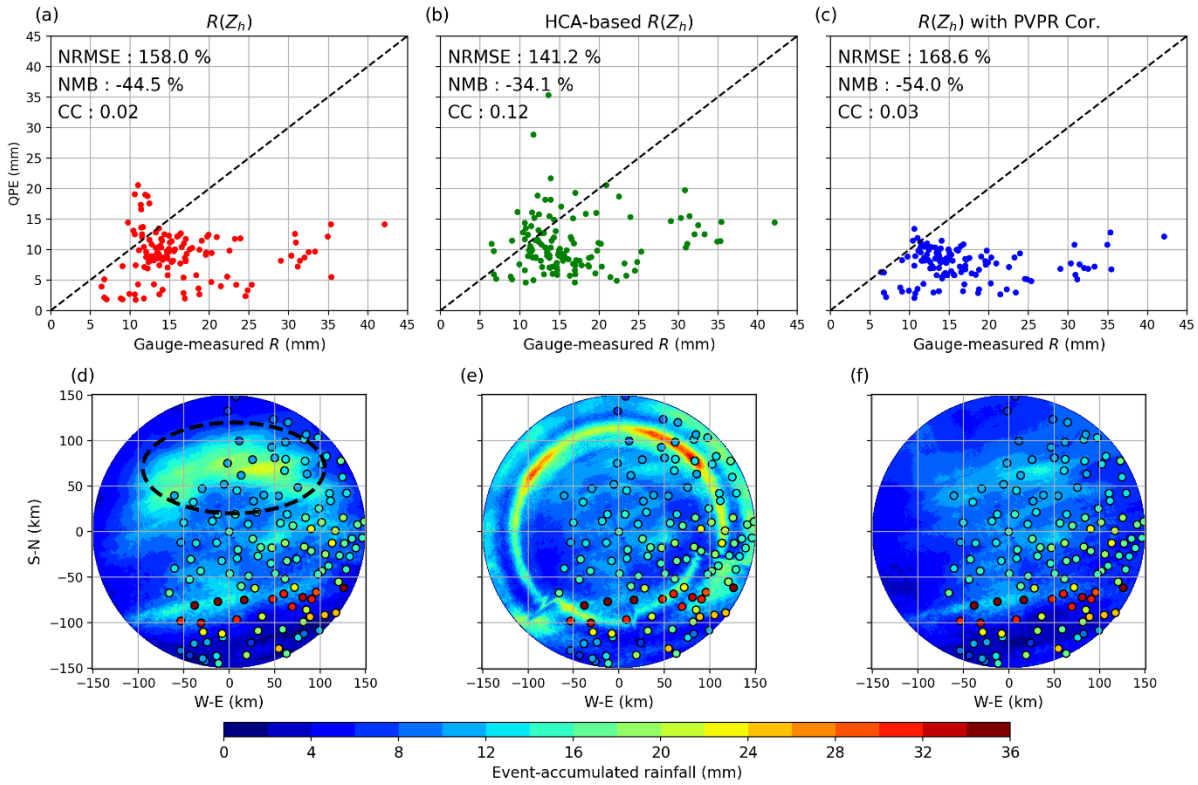

Figure 5.13 As in Fig. 5.11 but using the observations from the ESS radar. The black dashed line in (d) encloses the enhanced rainfall caused by bright-band (BB) contamination.

5.3.2 K_{DP}-based snowfall estimator

In all snowfall events except for the one occurring on 14 January 2021, the $S(Z_h, K_{DP})$ algorithm performs better than the $S(Z_h)$ algorithm (Table 5.6). The results indicate that $S(Z_h, K_{DP})$ yields a minimum improvement of 0.1 in CC values and a reduction of up to 20% in NRMSE values. Conversely, the RY product generally produces the least accurate estimates of snowfall.

On 14 January 2021, the event-accumulated snowfall maps reveal a spatial shift between radar-estimated and gauge-measured snowfall fields from the northeast to the southwest (Figs. 5.14d-f). This shift becomes more pronounced with increasing observation heights, as depicted by the black dashed lines, leading to an overestimation of up to 32% in NMB values. Note that this shift is not a consequence of beam-broadening effects or an inappropriate σ assumption of 10 deg at far ranges (i.e., high altitudes within the DGL), as both factors tend to produce smaller snowfall estimations. Instead, it may be attributed to the influence of wind advection on snowflake falling trajectories. Correcting for horizontal advection of snowflakes is challenging, particularly in the presence of strong vertical wind, or when radar data are not interpolated into the same height (e.g., constant altitude plan position indicator, CAPPI) for further examination. In the case of the other event on 7-8 February 2021, a noticeable overestimation of snowfall is observed in the north (Figs. 5.14j-l). Nonetheless, there is no clear tendency regarding the possible contributing factors mentioned above, such as the snowfall algorithms used, radar-observing heights, or spatial shift, to this phenomenon. Thus, further investigation into this matter falls outside the scope of the present study.

To investigate the QPE performance at various heights and antenna angles, the snowfall event on 3 February 2019 is selected due to its less spatial shift. Regardless of the snowfall algorithms or elevation scans used, the precipitation amounts are typically underestimated when radar observations are taken above 2.5 km height as a result of weak echoes of dry snow as well as beam-broadening effects (Fig. 5.15). This underestimation is more pronounced for $S(Z_h)$ than for $S(Z_h, K_{DP})$ at all elevation angles, while at the 1.5- and 2.5-deg angles, the $S(Z_h, K_{DP})$ retrieval obtained at lower altitudes produces smaller snowfall sums compared to those derived from the $S(Z_h)$ retrieval (Fig. 5.16). Additional analysis of the QPE performance as a function of height levels, as depicted in Fig. 5.17, indicates that $S(Z_h)$ derived using the precipitation scan data consistently has lower NRMSE values and higher CC values than those obtained from the data at higher elevation angles across the entire height range. This, however, is not the case for $S(Z_h, K_{DP})$. At the first height level, the $S(Z_h, K_{DP})$ retrievals at different elevation angles perform similarly to each other, but slightly worse than the $S(Z_h)$ retrievals in terms of NRMSE values. At the second level, the $S(Z_h, K_{DP})$ retrievals at both the 1.5- and 2.5-deg angles display a significant jump/drop in NRMSE/CC values (red arrows), giving the worst scores of all the compared retrievals. In contrast, at the third and fourth levels, $S(Z_h, K_{DP})$ at the 1.5-deg angle yields the lowest NRMSE values among all retrievals. Finally, beyond the fifth level, the retrieval of $S(Z_h, K_{DP})$ derived using the precipitation scan data outperforms those at the higher elevation angles, due to the expected decrease in QPE accuracy caused by wind drift above a certain height. The change in the performance of $S(Z_h, K_{DP})$ retrievals at different height levels and elevation scans can also be attributable to deficiencies in K_{DP}, which will be discussed in subsection 6.3.2.

Table 5.6 Evaluation of two snowfall quantification retrievals and the RY product derived from the DWD precipitation scan data against hourly gauge measurements in four snowfall events. The ratings include RY.

		$S(Z_h)$	$S(Z_h, K_{DP})$	RY
2019/02/03 $N = 3714$	NRMSE (%)	82.7	**76.0**	90.9
	NMB (%)	-17.0	**-4.3**	-39.2
	CC	0.60	**0.70**	0.61
2021/01/14 $N = 1946$	NRMSE (%)	**105.4**	112.4	113.6
	NMB (%)	**18.7**	32.4	20.6
	CC	0.34	**0.49**	0.43
2021/01/24 $N = 1159$	NRMSE (%)	111.7	**89.6**	111.8
	NMB (%)	**-4.5**	-11.7	-36.6
	CC	0.43	**0.59**	0.42
2021/02/07-08 $N = 6080$	NRMSE (%)	101.8	**92.1**	102.5
	NMB (%)	14.4	16.7	**6.6**
	CC	0.43	**0.58**	0.55

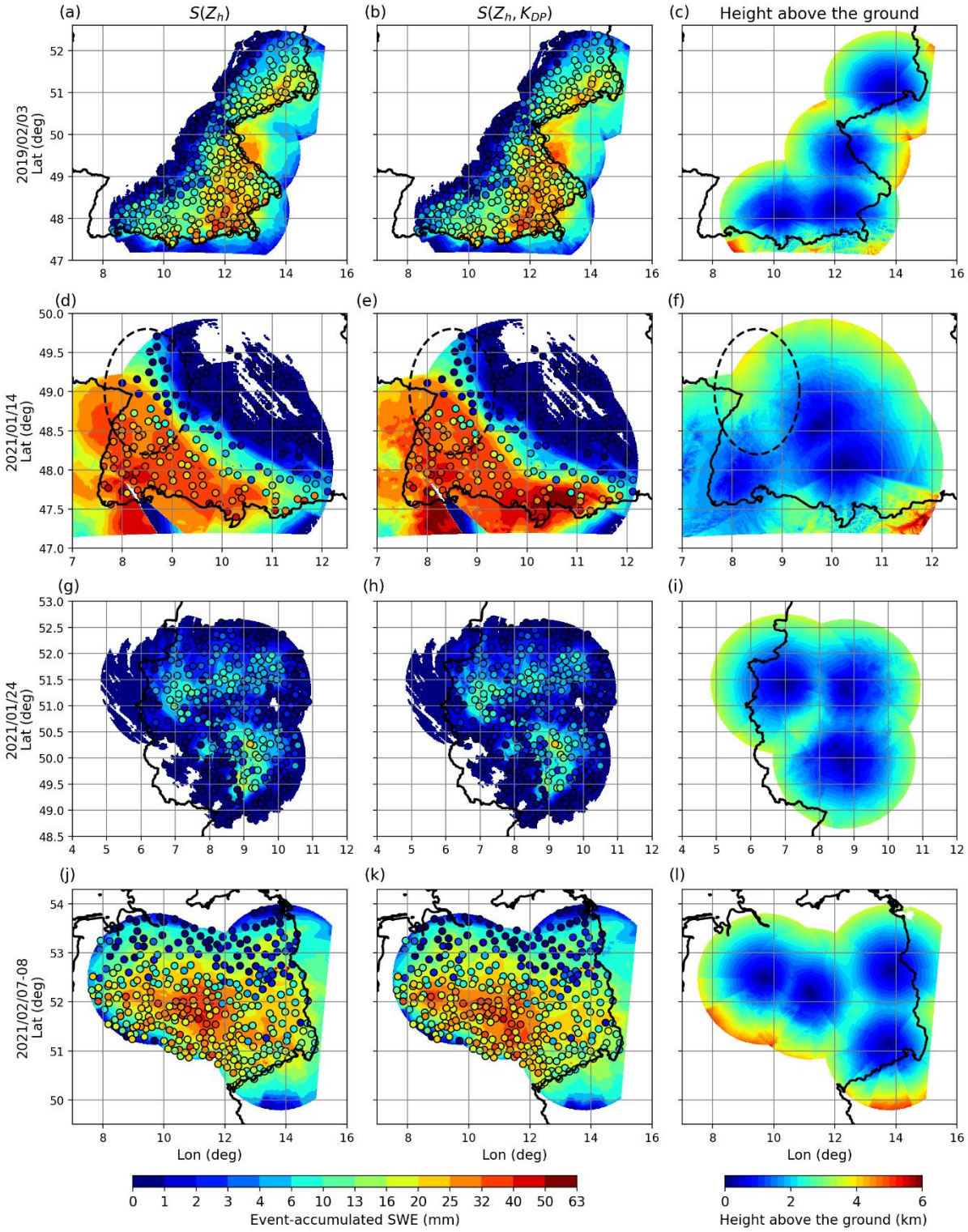

Figure 5.14 Event-accumulated snowfall composite maps obtained from the $S(Z_h)$ (left column) and $S(Z_h, K_{DP})$ (middle column) algorithms, and the observation heights of precipitation scans above the ground (right column) for four snowfall events (each row).

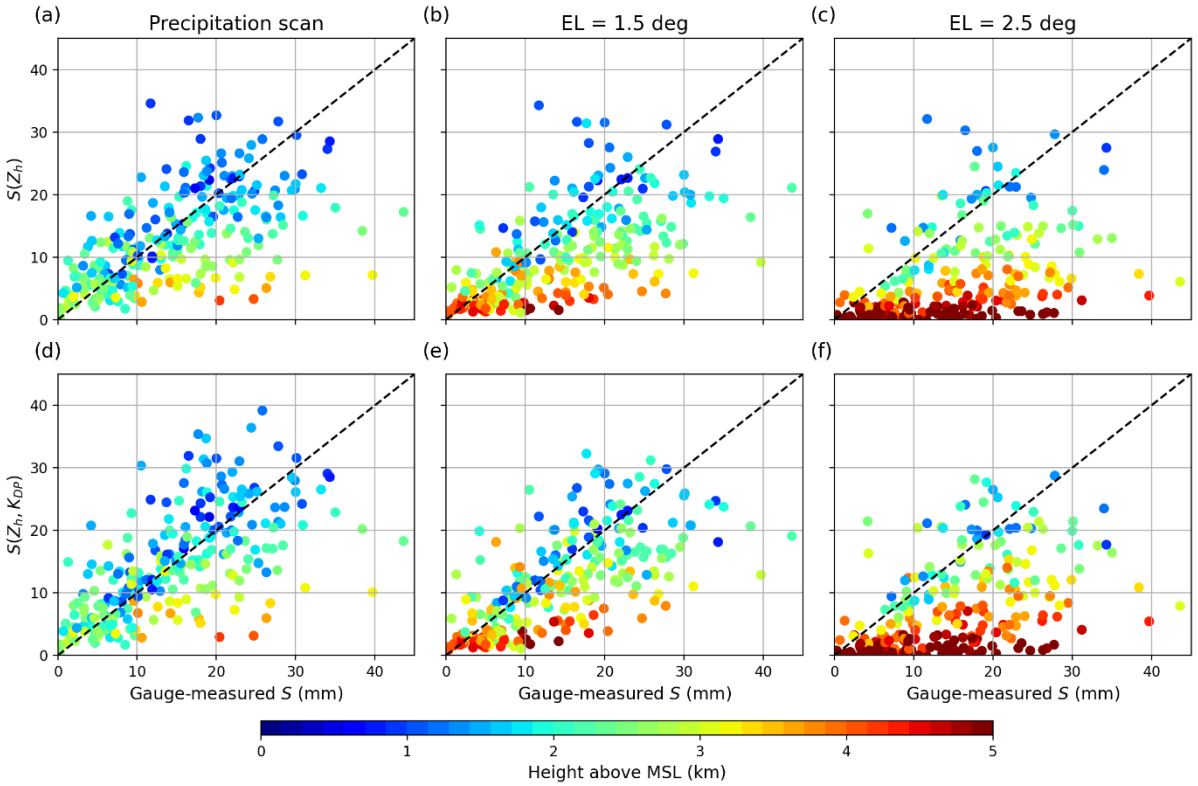

Figure 5.15 Scatterplots of event-accumulated snowfall sums derived from the $S(Z_h)$ and $S(Z_h, K_{DP})$ retrievals (up and bottom), against gauge-measured snowfall sums on 3 February 2019. The retrievals are obtained using data from the precipitation scan, 1.5-deg elevation scan, and 2.5-deg elevation scan, respectively, from left to right. The color of the dots represents the heights of radar observations above mean sea level (MSL).

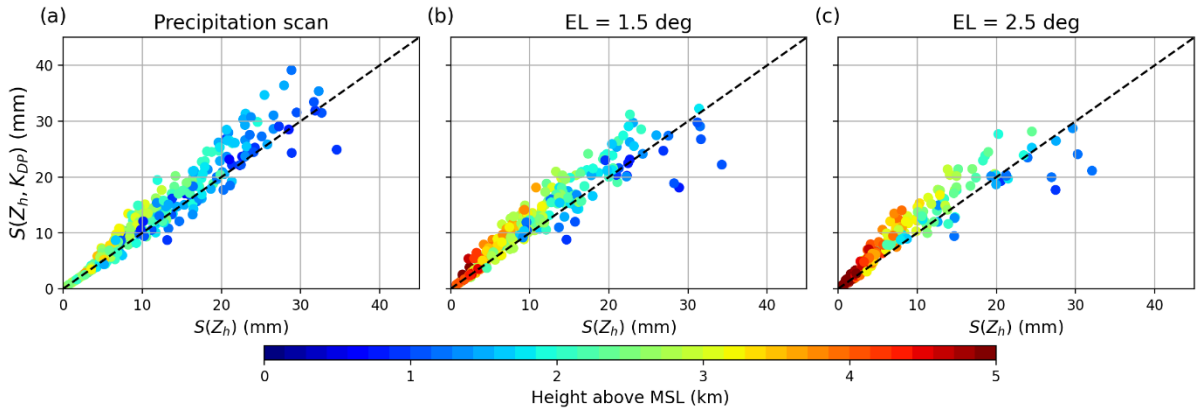

Figure 5.16 As in Fig.5.15 but for scatterplots of $S(Z_h, K_{DP})$ against $S(Z_h)$.

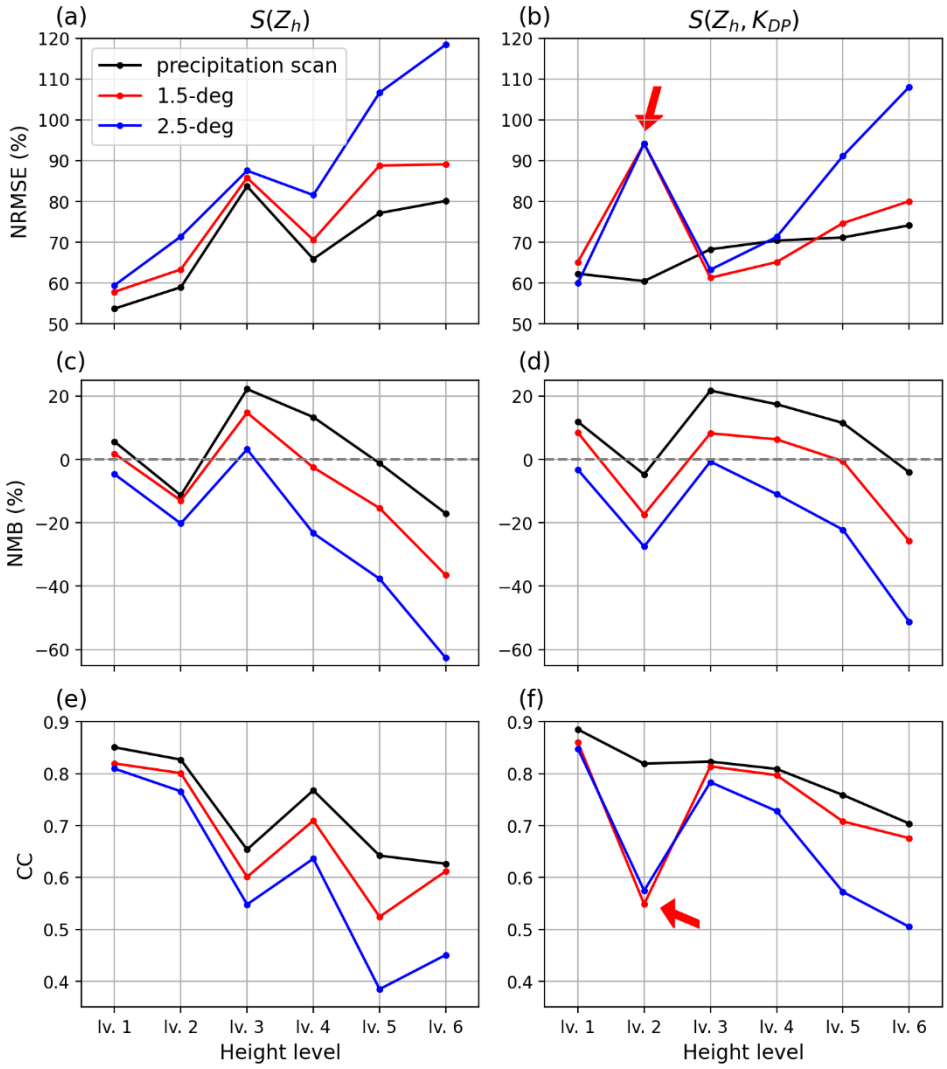

Figure 5.17 NRMSE, NMB, and CC (top to bottom) of event-accumulated snowfall sums derived from $S(Z_h)$ and $S(Z_h, K_{DP})$ (left and right) against gauge measurements on 3 February 2019. The performance metrics at different elevation scans, indicated by the colors, are shown as a function of the observing heights of the precipitation scan above the ground. The first height level pertains to altitudes below 0.7 km, the second to fifth levels refer to altitudes from 0.7 km to 1.7 km with an interval of 0.2 km, and the sixth level corresponds to altitudes from 1.7 km to 2.5 km.

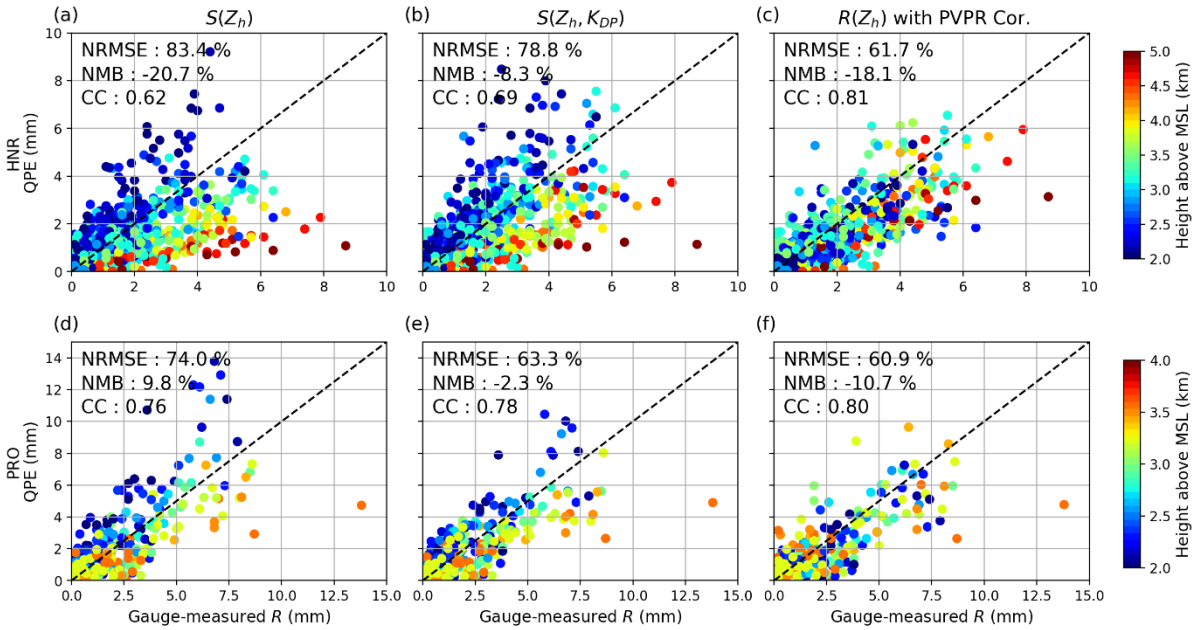

Figure 5.18 Scatterplots of precipitation sums derived from three QPE retrievals using the HNR data above the ML against hourly gauge measurements on 23 September 2018. These retrievals include (a) $S(Z_h)$, (b) $S(Z_h, K_{DP})$, and (c) PVPR-corrected $R(Z_h)$. (d)-(f) display the same analysis but using the measurements from the PRO radar.

When estimating surface precipitation using measurements above the ML, the $S(Z_h, K_{DP})$ retrieval is additionally compared to the $R(Z_h)$ retrieval with the PVPR correction. The PVPR-corrected $R(Z_h)$ retrieval demonstrates the highest consistency with gauge observations and the least pronounced error dependency on observation heights among all retrievals (Fig. 5.18). Overestimated points in $S(Z_h)$ may result from the overcorrection of Z_h for attenuation within the ML, which propagates to the data above the ML. Similarly, overestimation in $S(Z_h, K_{DP})$ may occur due to small Z_{DR} values without appropriate attenuation correction within the ML, leading to excessive intercept values in the relation. Therefore, uncertainties arising from attenuation, especially for data within the ML, affect not only the direct use of Z_h in snowfall retrieval algorithms, but also Z_{DR} used for estimating σ right above the ML. Consequently, the preference for the $R(Z_h)$ algorithm with the PVPR correction in such cases is further justified.

Chapter 6

Advantages/Disadvantages, and Potential Improvement

The approaches presented in this study aim to enhance QPE quality beyond the current DWD RY product, or even the gauge-adjusted RW product. This chapter summarizes the benefits and drawbacks of these approaches, and discusses potential solutions for open problems that must be addressed before implementing these algorithms in operational applications of C-band radar networks.

6.1 Phase-based retrievals below the melting layer

In the ZPHI method, an incorrect α value will cause an erroneous estimation of PIA from Φ_{DP}, leading to incorrect values of A or $R(A)$ along a ray. To avoid this problem, the use of scan-wise adjusted α values derived from the Z_{DR} slope is suggested, as it is immune to radar miscalibration and less susceptible to noise and resonance effects of Z_{DR} owing to its statistical approach. The improvement achieved by using $R(A^{adj.}, K_{DP})$ over $R(A^{fix.}, K_{DP})$, however, is limited to reducing biases in convective rain events. This is because a scan-wise α value represents an average value and cannot distinguish between different precipitation types within an azimuthal scan. An illustration of coexisting convective and stratiform rain in the radar domain is demonstrated in the BOO observations on 20 July 2019 (Figs. 6.1a-c). The data depicts two distinct Z_{DR} slopes: a steeper slope originating from the squall line in the east, and a flatter slope arising from stratiform regions located behind the convective rain band. The merging of these two slopes results in an intermediate K_H value. Higher (lower) K_H values typically correspond to lower (higher) α values, which usually happen in continental convection (tropical or marine stratiform). As a consequence, the scan-wise α values tend to overestimate the heavier convective rain and underestimate the lighter stratiform rain. Similar experiences have been documented for the $R(A)$ algorithm at S-band (e.g., Wang et al. 2019). Note that in the derivation of Z_{DR} slopes, only data with $\Delta\Phi_{\mathrm{DP}}$ less than 30 deg are included to minimize the effects of attenuation at C-band. Thus, in the case of heavy rain, data closer to the radar site may dominate the results and cause a loss of representativeness in the derived K_H values.

The $R(A^{adj.}, K_{DP})$ algorithms offer substantial mitigation to the underestimation of rainfall caused by the $R(A^{fix.}, K_{DP})$ algorithms in two stratiform rain events. It, however, still generates an NMB value greater than 20%. Specifically, the underestimation during the event on 25 July 2017 remains unresolved, despite the absence of pronounced vertical precipitation gradients below the radar-observing heights, that are typically associated with warm-rain processes and were observed in the other investigated stratiform rain event. Located at the center of the involved radars and effectively monitoring precipitation during the event, the UMD radar data is further examined and indicates that more than 90% of observations are below 30 dBZ. The small percentage of higher Z_H with higher Z_{DR} from embedded

convection, however, strongly dominates the fitting of Z_{DR} slope, producing smaller α values and subsequently underestimated rainfall estimates (Figs. 6.1d-f).

Based on the findings of Chen et al. (2021a), the performance of their $R(A^{adj.}, K_{DP})$ algorithms in stratiform rain deteriorated when using scan-wise α values. Hence, modifications have been made in this study to the conditions for applying the most tropical and highest α values derived from the last N_w class, leading to significant improvements in QPE quality. During the adjustment of α, these high α values are employed when one standard deviation of Z_H above the mean collected from each scan exceeds 30 dBZ. This, however, can cause significant fluctuations in α values from one scan to another when the referred Z_H values (mean plus a standard deviation) move around the threshold of 30 dBZ (Fig. 6.2 red arrows). The α estimators are also highly sensitive to the change of K_H in low-value regions. Thus, when K_H fluctuates below 0.05 dB dBZ^{-1}, the derived α value can exhibit oscillations (Fig. 6.2 black arrow). These two factors can lead to noticeable temporal discontinuity in derived rainfall fields. By utilizing the most tropical $\alpha_{H/V}$ values of 0.153 and 0.147 dB deg^{-1}, respectively, for $A_{H/V}$ estimates throughout the rain event on 25 July 2017, the resulting NRMSE and NMB values are reduced by 10% and 15%, respectively, compared to those obtained using scan-wise α values (Fig. 6.3). This finding suggests that higher α values better represent the average in this specific case, underscoring the need to establish more robust criteria for the use of most tropical α values based on a larger database.

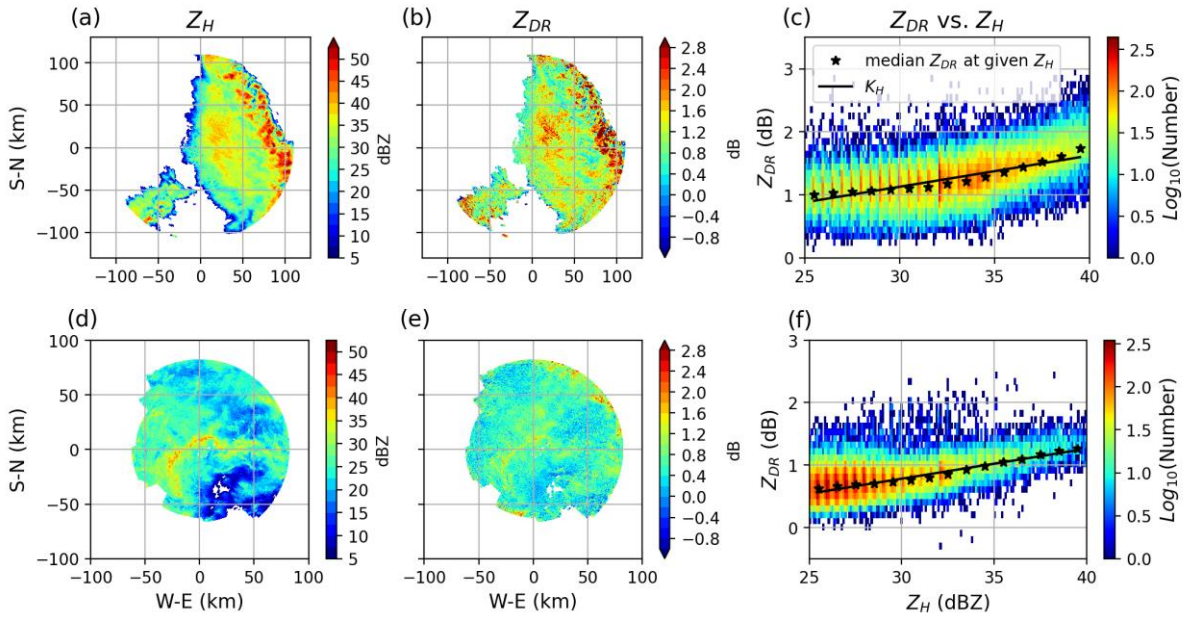

Figure 6.1 Fields of (a) Z_H and (b) Z_{DR}, and (c) scatterplot of Z_{DR} against Z_H acquired from the BOO radar on 20 July 2019 at 0445 UTC. Panels (d)-(f) demonstrate the same data as (a)-(c) but obtained from the UMD radar on 25 July 2017 at 0820 UTC. The black stars in (c) and (f) depict the median values of Z_{DR} at given Z_H values, while the black lines are the resulting Z_{DR} slope (i.e., K_H).

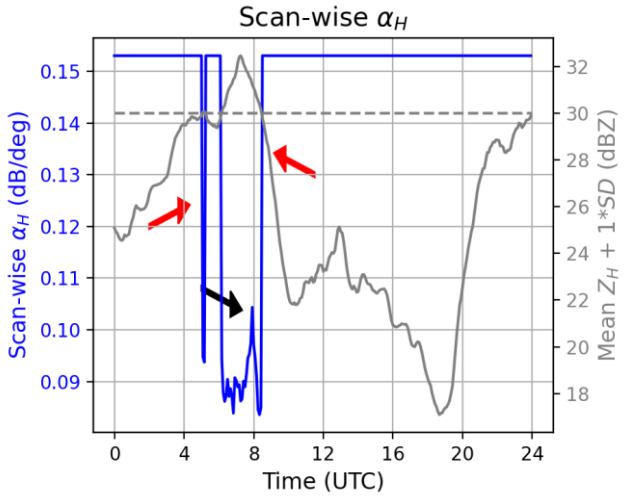

Figure 6.2 Time series of scan-wise α values (blue) derived from the observations of UMD on 25 July 2017. The gray solid line corresponds to the mean Z_H plus one standard deviation for each scan, and the gray dashed line marks the value of 30 dBZ.

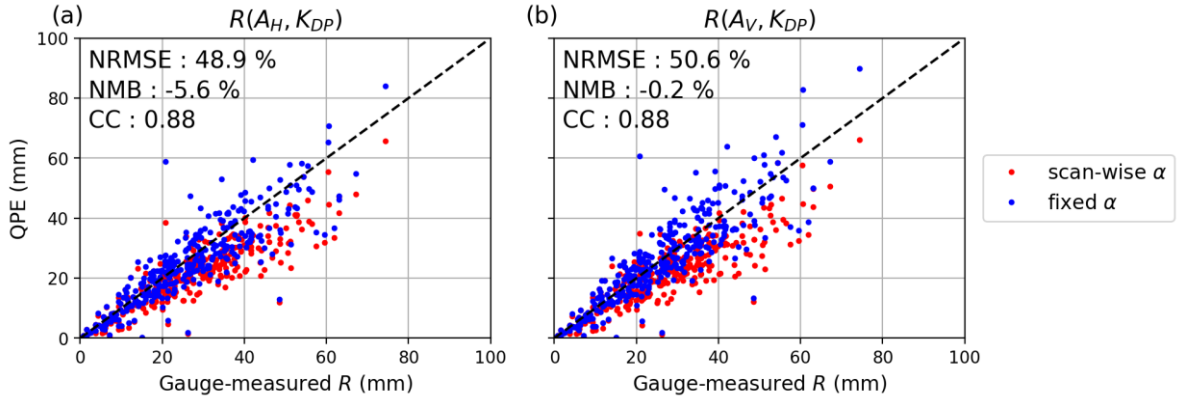

Figure 6.3 Scatterplots of daily-accumulated rainfall sums derived from (a) $R(A_H, K_{DP})$, and (b) $R(A_V, K_{DP})$ against rain gauge measurements for the stratiform event on 25 July 2017. The red dots represent the use of scan-wise $\alpha_{H/V}$ values, while the blue dots refer to the use of fixed $\alpha_{H/V}$ values of 0.153 and 0.147 dB deg^{-1}. The evaluation statistics are based on the 336 blue dots.

Optimizing $\langle\alpha\rangle$ along individual rays or within segments has the potential to provide a better representation of local α in heterogeneous precipitation (e.g., the comparison between Figs. 6.4d and f) and thus increase the accuracy of A estimates. The efficacy of this approach, however, cannot be guaranteed in all cases. The derivation of ray/segment-wise α values, in particular, requires precise measurements of both Z_{DR} and Z_H through calibration and attenuation correction. Additionally, obtaining reliable estimations of $\Delta\Phi_{\mathrm{DP}}$ within a short rainy range interval poses another obstacle. As a result, the benefits of utilizing ray/segment-wise α values in A estimates are limited.

The application of ray/segment-wise α values in stratiform rain has shown improved QPE, likely due to reduced uncertainties in attenuation and the decreased need for complex segment-wise integration in the ZPHI method. In such cases, the performance of $R(A^{\langle\alpha\rangle}, K_{DP})$ heavily

depends on the accuracy of Z_{DR} calibration. Fig. 6.4 illustrates that a Z_{DR} offset of about 0.3 dB has already a considerable impact on the resulting $\langle\alpha\rangle$. For observations made prior to August 2017, the Z_{DR} offsets are determined by taking the mean values of Z_{DR} in the weak-echo regions. For rain events occurring after August 2017, the available archived Z_{DR} offsets provided by DWD, however, can differ by up to 0.5 dB from the values obtained using this method. Using different sources for Z_{DR} offset results in a change of at most 10% in NMB values. Nevertheless, it is difficult to conclude which source is more accurate, as there is no clear pattern indicating which value leads to better QPE performance.

In convective rain, the presence of scattered and isolated strong cells can impede the efficacy of the attenuation correction method proposed by Gu et al. (2011). Moreover, to avoid resonance effects in heavy rain, only segments with Z_H values less than 40 dBZ are considered in the ZPHI method, which further complicates the estimation of reliable $\Delta\Phi_{\mathrm{DP}}$. To ensure the quality of $\Delta\Phi_{\mathrm{DP}}$, $\Delta\Phi_{DP}^{cal.}$ values calculated from Z_h with quality control replace observed values that are either two times larger or 0.5 times smaller than the former. It is observed, however, that up to 40% of noisy $\Delta\Phi_{\mathrm{DP}}$ values within the segments can be substituted. This indicates that a large proportion of A values are derived based on Z_H instead of the phase-based variable, making the advantages of $R(A)$ underutilized.

In light of the importance of using more representative α values for local regions and the resistance of the scan-wise α adjustment to measurement errors, it is more favorable to utilize a rain-type classifier on the entire scan and optimize α values individually for each hydrometeor type through Z_{DR} slopes. Implementing this approach successfully necessitates the development of an HCA that is specifically tailored to German climatology.

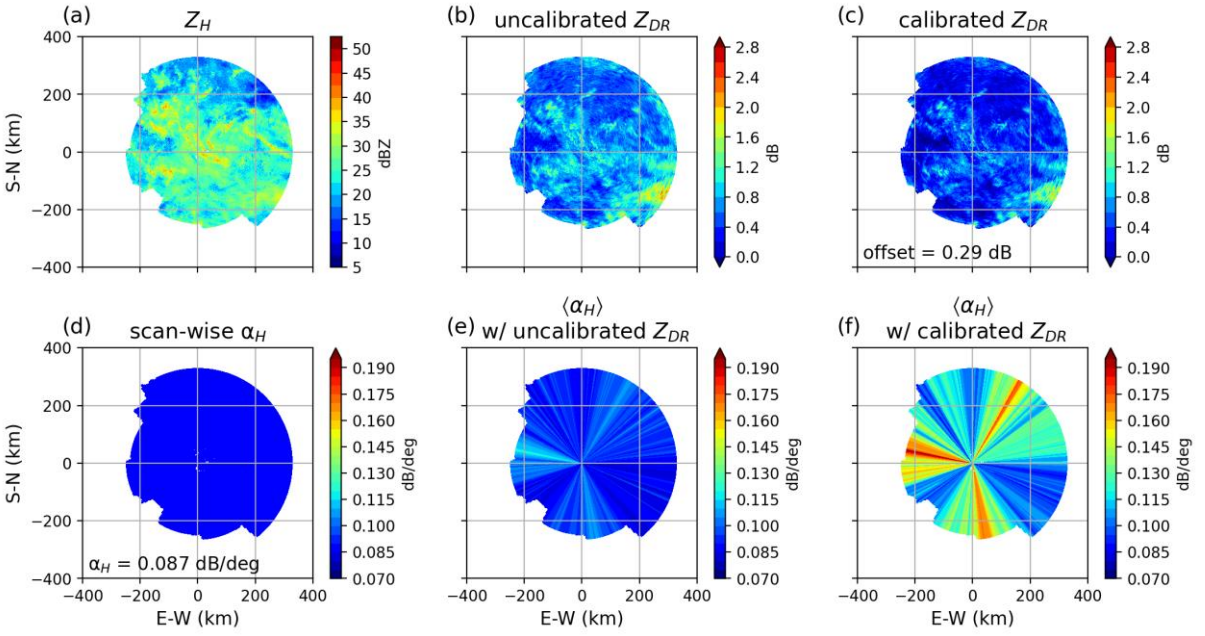

Figure 6.4 Fields of (a) Z_H, (b) uncalibrated Z_{DR}, (c) calibrated Z_{DR}, (d) scan-wise α_H (equal to 0.087 dB deg^{-1}), (e) segment-wise α_H derived from uncalibrated Z_{DR}, and (f) segment-wise α_H derived from calibrated Z_{DR} on 25 July 2017 from the UMD radar.

6.2 Warm-rain precipitation

The application of long-term LPM-based rainfall relations to DWD C-band radar measurements yields significant underestimation in a warm rain event on 14 July 2021, especially when employing Z_h-based algorithms. Despite better performance, the hybrid polarimetric retrievals $R(A^{adj}, K_{DP})$ still exhibit a bias (NMB) of around -30%. The use of event-specific LPM-based relations only results in minor enhancement in NRMSE. The underestimation tendency increases with radar observation height, and the vertical gradients of radar variables and rain rates, as observed in both MRR observations and RD-QVPs, are identified as sources of errors.

The evaluation of the VP correction method reveals that the utilization of MRR-DSD-derived rainfall relations (implicit correction) yields more considerable reductions in NRMSE and NMB values compared to the projection of radar observations (explicit correction). This finding underscores the importance of the DSD profiles obtained from MRR observations at lower altitudes in optimizing rainfall relations in such scenarios. The implementation of the implicit correction method in practical settings, however, requires more robust and generalized relations of this kind. Such relations can be established based on a larger dataset that includes various rain intensity gradients near the surface. In addition to DWD, several universities and research institutions in Germany have MRR measurements available, which can be utilized for this purpose. Once optimized, the relations can be applied to certain rain regimes when distinct precipitation gradients below the ML are identified via real-time RD-QVPs. Notably, deploying MRRs in areas with high observation altitudes of operational radars is particularly recommended, as it offers an affordable means of addressing vertical precipitation gradients in stratiform rain.

The complete VP correction method has been found to reduce retrieval errors by a minimum of 20%, with the $R(A^{adj.}, K_{DP})$ algorithms showing the most pronounced improvements. In the case of heterogeneous precipitation, however, very local gradients or the decreased representativeness of RD-QVPs for a larger area of interest may limit the efficacy of the VP correction. Thus, further research to investigate the spatiotemporal variabilities of vertical gradients is necessary. To facilitate wide-area explicit VP corrections, it is anticipated that small, embedded convective cells in stratiform rain must be identified and excluded from RD-QVPs. For precipitation within convective cores, VP correction should either be ignored or estimated and applied separately. The VP of convective cells can be described using the columnar vertical profile (CVP, Murphy et al. 2020) methodology. CVPs, however, are valid at low altitudes only when the data are collected in close proximity to radar sites. To extend their utility, a feasible strategy is to assume that the profiles derived from convective cells located near the radar are representative of cells within the entire scan. As for stratiform rain, the profiles generated from RD-QVPs are sensitive to the defined range, and require careful adjustment based on the evolution of the precipitation system.

The explicit VP correction has been applied to Z and K_{DP}, but not to A because of its temperature dependence. With decreasing temperature, the value of the parameter α (and consequently A) increases, while the intercept parameter in power-law $R(A)$ relations decreases. At C-band, however, these opposing effects only partially cancel out. In addition, in practice α is treated as a constant within each segment or ray in the ZPHI method, and thus its change with temperature is usually not accounted for in A estimation. Similarly, the selection of $R(A)$ relations based on environment temperature is not considered. Nonetheless, it can be

inferred that the temperature factor has a lesser impact on the derived $R(A)$ compared to A. To enable the exploitation, at least to some extent, of $R(A)$ in warm-rain processes, an alternative approach is investigated within a Master thesis. This approach involves projecting the derived $R(A)$ to lower altitudes using the VP of $R(Z_h)$, $R(Z_h, K_{DP})$ or any other rainfall retrieval without temperature effects. Note that in situations where rain intensities increase towards the ground, the VP of observation-derived A shows a steeper slope than that of intrinsic A. Therefore, the implicit VP correction for A is particularly advantageous in warm rain.

In heterogeneous precipitation conditions, the utilization of cost-effective X-band radars as gap fillers is highly recommended to enhance the accuracy of precipitation measurements near the surface (recall the improvements achieved at the location of gauge B by including JuXPol data, as demonstrated in section 5.2). The $R(Z_h)$ and $R(Z_h, K_{DP})$ algorithms exhibit smaller improvements from gap-filling compared to the $R(A^{adj.}, K_{DP})$ algorithms due to the favorable application of phase-based variables at X-band and, on the other hand, higher attenuation uncertainties in power-related radar measurements at shorter wavelengths. The attenuation of Z can cause complete extinction at short ranges, as observed in the case of BoXPol, another local X-band radar in Bonn, during this event. It is encouraging to note that in Germany, four additional operational X-band radars will soon complement the existing network of C-band radars, a positive step towards improved precipitation monitoring, particularly during warm-rain processes.

6.3 Snow quantification

Section 4.4 introduces innovative PVPR correction and polarimetric snowfall retrieval techniques at C-band frequencies. Section 5.3 demonstrates their potential in improving surface precipitation estimations in scenarios where the radar beams are monitoring at a certain distance within and above the ML, and when snowfall is reaching the ground, respectively. This section also evaluates their limitations and explores possible pathways for further development.

6.3.1 Polarimetric vertical profile of reflectivity correction

The rain event on 23 September 2018 displays various spatial characteristics of the ML within radar domains. This offers an opportunity to assess the efficacy of the proposed MLDA and PVPR correction methods under different precipitation conditions. It is found that the success of the PVPR correction method relies on accurate estimations of r_b and H_b.

In the case of pure and uniform stratiform rain, an initial estimate of H_b, i.e., H_0, is determined using QVPs of ρ_{HV} with sufficient quality. Thus, the method effectively mitigates BB contaminations and corrects negative Z_H biases above the ML. Figs. 6.5a/b and d/e illustrate the regions affected by BB contamination, which are clearly visible in the ρ_{HV} field at the higher antenna elevation of 1.5 deg. The increase in Z_H associated with hydrometeor mixtures within the ML is strongly correlated with S_{ML}. At the lower elevation angle of 0.83 deg, the BB areas are less pronounced and more diffused compared to 1.5 deg. Nonetheless, consistent results achieved for different elevation angles confirm the applicability of the PVPR method (Figs. 6.5c/f). This implies that when observations from the lowest elevation scan are severely contaminated by ground clutter, the Z_H measurements at successive elevation angles can improve the estimates of Z_H and $R(Z_h)$ near the surface.

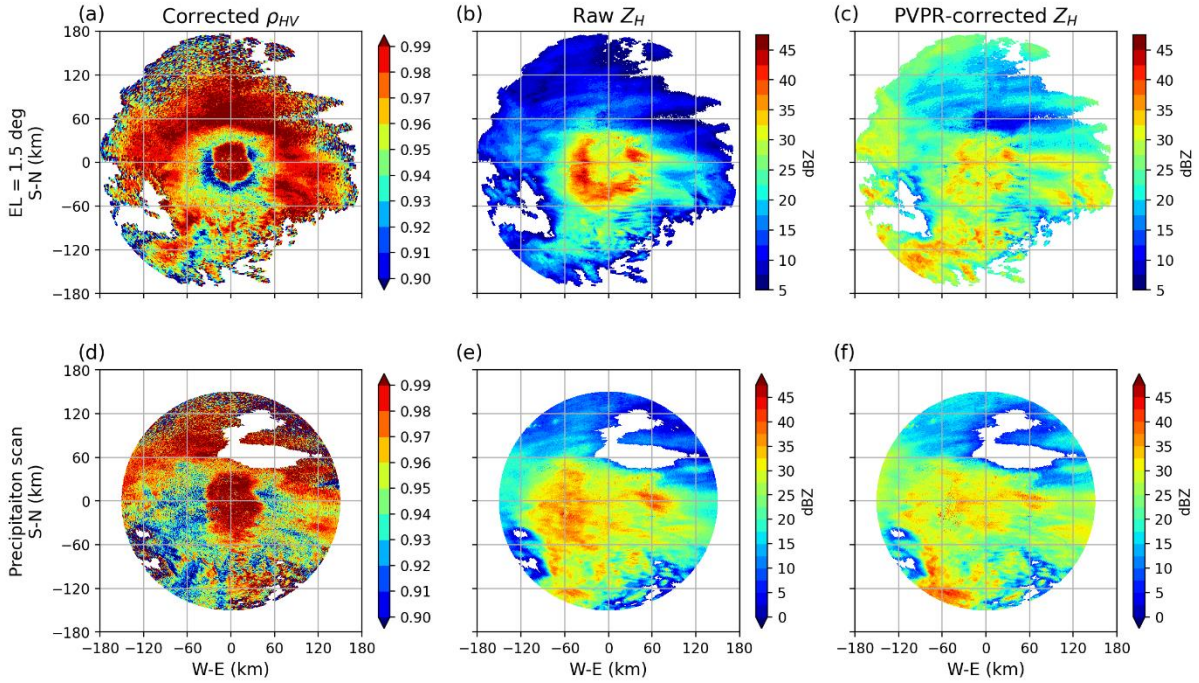

Figure 6.5 Fields of (a) noise-corrected ρ_{HV}, (b) raw Z_H, and (c) PVPR-corrected Z_H at the 1.5-deg elevation angle of PRO, and (d)-(f) the same but from the precipitation scan at 0.83 deg on 23 September 2018 at 1355 UTC.

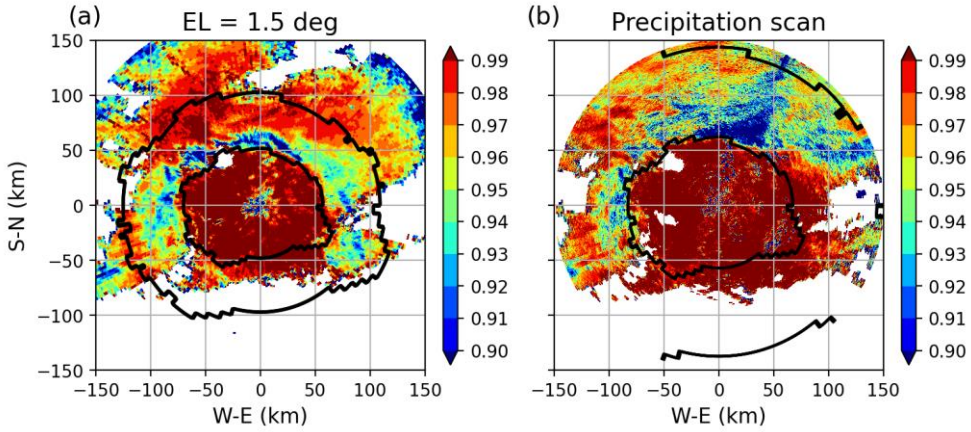

Figure 6.6 Fields of ρ_{HV} (a) at the 1.5-deg elevation angle, and (b) from the precipitation scan obtained by the FLD radar on 23 September 2018 at 1215 UCT. The black lines depict the areas contaminated by BB.

Nevertheless, significant azimuthal variations of the ML height complicate BB detections. In such situations, the BB appears weaker but thicker in the QVPs due to the averaging of the signature observed at different height levels. This results in a lower defined value of H_0 than the average true H_b. The MLDA searches for r_b within an estimated interval based on H_0, i.e., (i_{min}, i_{max}) in Eq. (4.43). However, when r_b exceeds i_{max} on the side where the ML height tiles upwards, the algorithm wrongly determines r_b using the default value. Fig. 6.6 provides an example where H_b increases from northwest to southeast, causing the rain in the southeast to be mistakenly identified as being within the ML (depicted by black lines). Subsequently, a presumed positive bias is subtracted, leading to an underestimation of rainfall. To overcome this issue, sector-specific QVPs are suggested to detect H_0 within smaller azimuthal ranges. Moreover, precise modeling of the ML that takes into account potential height variations can enable a spatially resolved detection of the BB, thereby improving the correction.

This study uses observations at the higher elevation angle of 1.5 deg to determine H_b and ΔH, as lower elevation scans are subject to ground clutter contamination and reduced information of ρ_{HV} at far ranges, rendering the estimation of S_{ML} unreliable. The obtained H_b and ΔH are then utilized to estimate and correct Z_H biases at various scanning angles, e.g., the precipitation scans. Inconsistent H_b between the two elevation scans, however, can affect the correction accuracy at the precipitation scans and thus result in substantial errors in QPE. In Fig. 6.6, for example, the ML height measured by the precipitation scan is higher towards the east than that measured by the 1.5-deg elevation scan. Consequently, a mismatch arises between the detected BB area and the low-ρ_{HV} region in the east at the precipitation scan (Fig. 6.6b).

The coexistence of the ML and strong convection within the estimated BB ranges can also pose a challenge for the MLDA, because both conditions cause reductions in ρ_{HV} at C-band. As a consequence, the convective cell is misinterpreted as the ML, leading to a significant underestimation of rainfall in the ESS, FLD, and UMD radars (Fig. 6.7 black dashed circles). Although the PVPR correction is not applied to observations classified as rain, graupel, or hail, the current HCA struggles to distinguish between ice particles and moderate/heavy rain due to its strong dependency on temperature (Fig. 6.7c). To resolve this issue, it is recommended to include the texture information (i.e., standard deviations) of Z_{DR} and the vertical gradients of radar variables as additional membership functions in the current HCA (Penide et al. 2013; Powell et al. 2016). These features are highly distinguishable between the ML and convective cores, and are expected to improve the accuracy of QPE based on the PVPR-corrected Z_H fields.

The PVPR correction method estimates Z_H biases within and above the ML based on certain assumptions in a model. However, one deficiency in the current model is the usage of a constant value for β_{ML}, which may not adequately account for the diversity of precipitation types. Therefore, the variability of β_{ML} needs to be considered through statistical analysis. Moreover, the model employed in this study relies on QVP statistics at S-band, but for more precise lookup tables, it is crucial to perform such statistics at C-band.

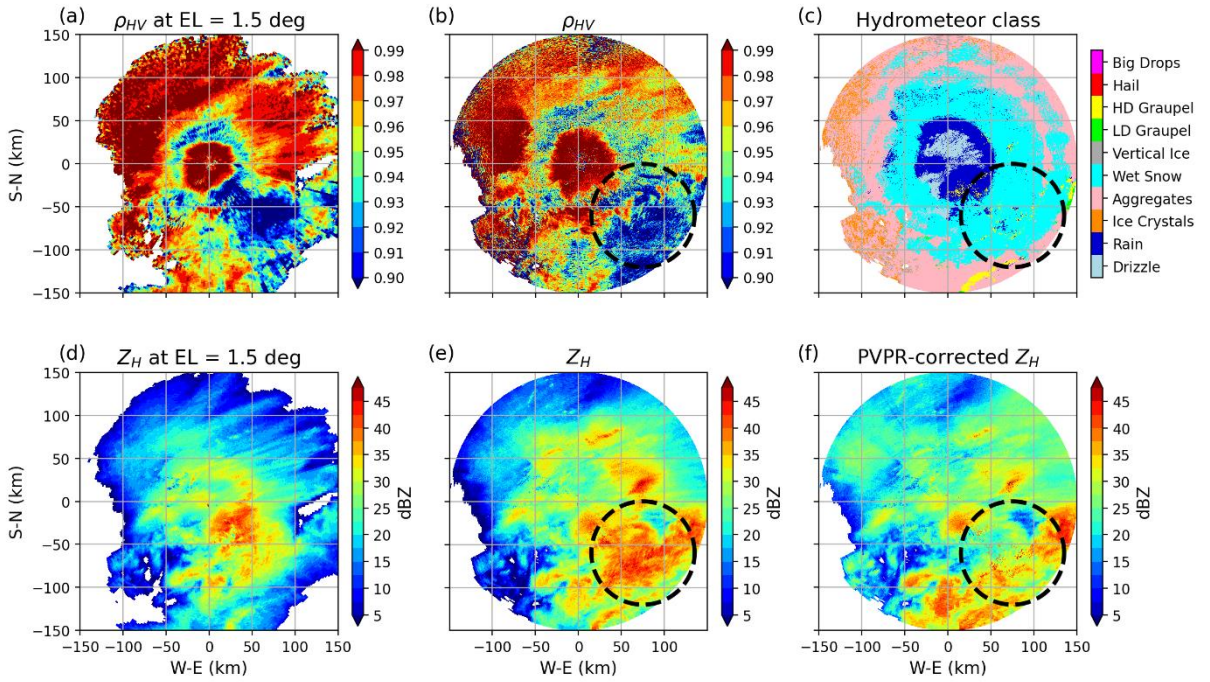

Figure 6.7 Observations from the UMD radar on 23 September 2018 at 1515 UCT. It includes ρ_{HV} and Z_H fields at the 1.5-deg elevation angle (top to bottom in the left column), and ρ_{HV} and Z_H fields from the precipitation scan (middle column). The right upper panel shows the results of hydrometeor classification, and the right lower panel displays the PVPR-corrected Z_H field. The black dashed lines mark the convective cells near the BB.

6.3.2 K_{DP}-based snowfall estimator

The aggregation of snowflakes during their fall causes a decrease in K_{DP} values. To estimate snowfall, this decrease is compensated for by the assumption of a linear increase in σ towards the ground in Eq. (4.46), which in turn increases the intercept parameter in the $S(Z_h, K_{DP})$ relation. Moreover, the potential to exploit K_{DP} is greater at C-band than at S-band, as K_{DP} value is inversely proportional to the radar wavelength. Nonetheless, a rapid decline in the $S(Z_h, K_{DP})$ retrieval in lower layers is still apparent in all snowfall events (e.g., Fig. 6.8f). This is because the K_{DP} retrieval process amplifies the extent of K_{DP} values decreasing towards the ground, leading to near-zero values at low altitudes (Fig. 6.8b). Specifically, in the case of snow observations, K_{DP} is derived using a window size of 25 gates, which allows for relatively reliable estimates after at least 6 km in radial distance from the first valid bin. Hence, K_{DP} is less usable below about 350 m height above the DWD radar locations at the lowest two to four elevation angles. This explains the smaller snowfall sums obtained from $S(Z_h, K_{DP})$ compared to those from $S(Z_h)$ at low altitudes, as shown in Fig. 5.16, and the worsened NRMSE and CC values of $S(Z_h, K_{DP})$ at the second height level in Fig. 5.17. Note that the discontinuity of the $S(Z_h, K_{DP})$ retrieval below 1 km height in Fig. 6.8f is a result of the replacement of $S(Z_h, K_{DP})$ with $S(Z_h)$ as K_{DP} values become zero or negative. This also clarifies why the performance of $S(Z_h, K_{DP})$ is better at the first height level than at the second level in Fig. 5.17.

Validation of snowfall estimates at higher altitudes using ground-based gauges can be challenging, due to the horizontal movement of snowflakes during their descent. Despite the scarcity of in-situ observations at these heights, the expected intensification of snowfall rates in

the DGL provides insight into the efficacy of the polarimetric snowfall algorithm. On 14 January 2021 between 0400 and 0800 UTC, a clear DGL was observed at altitudes of 3-4 km, characterized by enhanced K_{DP} and Z_{DR} values, and relatively low Z_H and ρ_{HV} values (Figs. 6.8a-d). The $S(Z_h, K_{DP})$ algorithm produces higher snowfall estimates within the DGL than below it, mainly owing to reduced and less reliable K_{DP} at lower altitudes (Fig. 6.8f). In contrast, snowfall rates calculated using $S(Z_h)$ exhibit an increase below the DGL, eventually reaching the surface with some delay (Fig. 6.8e). Previous studies by Kennedy and Rutledge (2011) and Trömel et al. (2019) have demonstrated a strong correlation between K_{DP} in the DGL and subsequent precipitation rates near the surface. Therefore, it is reasonable to conclude that $S(Z_h, K_{DP})$ gives superior QPE accuracy within the DGL than $S(Z_h)$, while $S(Z_h)$ provides better quality near the surface compared to $S(Z_h, K_{DP})$. This conclusion is also supported by the evaluation of the other snowfall event presented in Fig. 5.17, where the $S(Z_h)$ retrieval yields smaller errors than the $S(Z_h, K_{DP})$ retrieval at the first height level. However at the third and fourth levels, the $S(Z_h, K_{DP})$ retrieval based on observations at the higher elevation angle of 1.5 deg performs the best among all retrievals. Consequently, further analyses on the height-dependent combination of $S(Z_h, K_{DP})$ and $S(Z_h)$ are required.

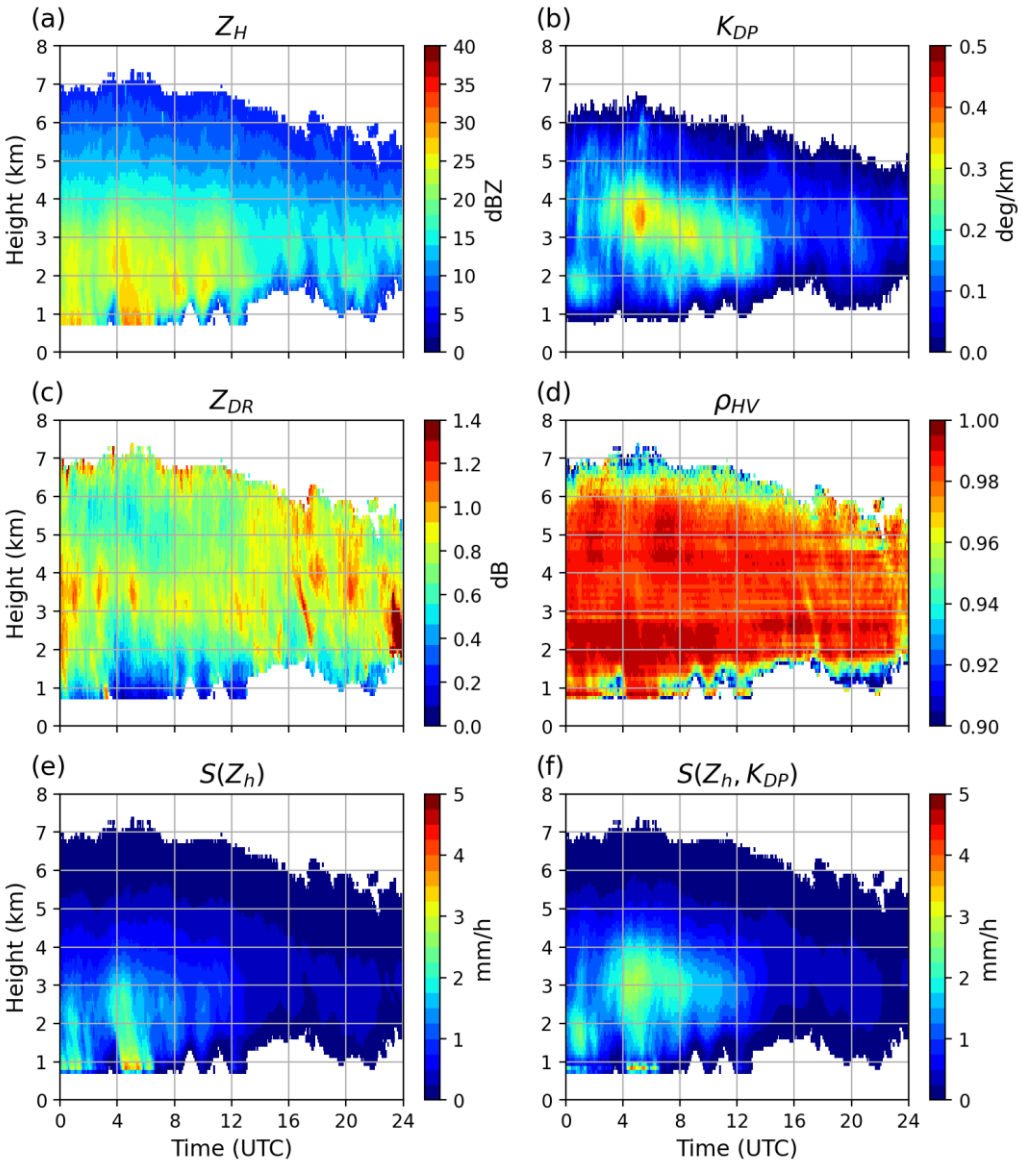

Figure 6.8 QVPs at the 2.5-deg elevation angle of (a) Z_H, (b) K_{DP}, (c) Z_{DR}, (d) ρ_{HV}, (e) $S(Z_h)$, and (f) $S(Z_h, K_{DP})$ from the Memmingen (MEM) radar on 14 January 2021.

Chapter 7

Conclusions, and Outlook

The current real-time QPE product RY from DWD has limited accuracy due to its reliance on $R(Z_h)$ relations alone. Although the alternative gauge-adjusted product RW is of higher quality than RY, it is made on an hourly basis and thus cannot provide timely output for certain applications. To overcome these deficiencies, this study proposes several advanced polarimetric QPE algorithms at C-band. The performance of the final QPE retrievals for different precipitation types is evaluated using DWD gauge and disdrometer measurements, and compared with those obtained from other benchmark algorithms and DWD products. The findings demonstrate that the proposed algorithms hold promise in improving the accuracy and timeliness of the precipitation estimations. Some suggestions are also presented for refining and optimizing the algorithms to explore their potential applications in a wider range of precipitation conditions.

Rainfall retrieval algorithms

The successful application of $R(A)$ algorithms to the operational S-band radars in the U.S.A. prompts the need to adapt and optimize them for widely-used C-band radar networks in Europe. The implementation of C-band $R(A)$ algorithms, however, poses several challenges, including the higher sensitivity of both α and $R(A)$ relations to the DSD variability, and stronger resonance effects and attenuation in rain mixed with hail compared to S-band. To address these challenges, this study derives various regional relationships and parameters for optimizing the algorithms, based on the DSDs measured in Germany. The classification of DSDs and radar observations according to N_w and Z_{DR} slope is also exploited to adjust α values for each radar scan. Moreover, $R(A)$ is combined with $R(K_{DP})$ when Z_H exceeds 40 dBZ. The ensuing hybrid $R(A^{adj.}, K_{DP})$ algorithms perform better than the benchmark algorithm $R(Z_h, K_{DP})$ and the RY product, as evidenced by reduced NRMSE and NMB values by more than 20% when evaluated with gauge measurements. Additional evaluation with independent disdrometer observations shows that these $R(A^{adj.}, K_{DP})$ algorithms have the potential to provide near-online QPE products with accuracy approaching RW's.

The use of scan-wise α estimators is found to reduce biases in QPE when compared to fixed α values, but their ability to improve NRMSE and CC values is limited. This limitation is attributed to the inhomogeneity of precipitation within a scan, which corrupts adequate Z_{DR}-slope estimates. One possible solution is the optimization of $\langle\alpha\rangle$ along each ray or segment by deriving local α values based on Z_{DR}. Stratiform rain benefits from this approach, showing an improvement of approximately 10% in NMB values. The approach, however, is less reliable in convective rain due to the larger uncertainties in Z_{DR} and the increased requirement for complex segment-wise integration in the ZPHI method. To account for varying precipitation types within a scan and minimize the impact of radar miscalibration, attenuation, and noisy $\Delta\Phi_{\mathrm{DP}}$ on A estimates, this study recommends the adjustment of α based on Z_{DR} slopes,

which are obtained from areas classified as the same precipitation types within the scan. These adjusted α values can then be applied to the corresponding observations, as a more efficient and effective approach in practical applications.

Warm-rain precipitation

The recent notorious flooding event in western Germany has highlighted the crucial role of accurate QPE products in hydrological models and flash-flood predictions, especially in light of escalating climate change impacts. However, the proposed QPE algorithms exhibited significant negative biases of up to 30% in the estimated rainfall amounts during this event, mainly due to warm-rain processes that led to intensified rain rates near the surface and were not captured by operational radars at their observing heights.

To compensate for these observation limitations, this study proposes two approaches: the VP correction, and the inclusion of measurements from the JuXPol X-band radar for gap-filling. The VP correction approach involves i) projecting the data below the ML down to a height of 700 m using RD-QVPs as VP references, and ii) utilizing rainfall relationships derived from the rain rates measured near the surface and DSD profiles in the lowest three bin levels of MRR, specifically at heights of 675 m and below. The results show that the VP correction approach achieves larger error reductions than the inclusion of JuXPol data, while the latter approach further increases the CC values. The proposed $R(A^{adj.}, K_{DP})$ algorithms, which incorporate both the VP correction and gap-filling approaches, yield the lowest errors (an NMB value of less than 2%) among all QPE retrievals, including the gauge-adjusted RW product. Moreover, these improved QPE retrievals have been demonstrated to increase the accuracy of hydrological models and associated flash flooding warnings (Saadi et al. 2022).

The need for identifying and taking into account vertical gradients in precipitation flux for QPE and nowcasting has been overlooked in many operational environments (Bringi et al. 2023). This study underscores the importance of this consideration and serves as a pilot investigation into the application of gap-filler radars in such cases, as the DWD is currently installing four additional X-band radars in its radar network. To enhance the efficacy and usability of the VP correction approach in heterogeneous precipitation, it is advisable to exclude embedded convection from stratiform rain during the correction process. Additionally, local VPs derived from convective cores near the radar can be utilized as references to carry out the correction for convective cores across the scan.

The PVPR correction

Unlike the previous VP correction method for warm rain, most of the available VPR correction techniques are designed to target measurements within and above the ML. In this study, a novel PVPR correction method that employs polarimetry is introduced as the first of its kind. Specifically, the method uses the statistical analysis of QVP obtained from S-band to characterize the VP properties of Z_H and ρ_{HV} regarding the impact of the ML at C-band, for which QVP statistics are currently lacking. Based on these properties, the biases of Z_H caused by BB contamination and beam-broadening effects are estimated. To identify areas where biases need correction in radar observations, an MLDA is utilized to search for the BB-contaminated areas along each radial ray using initial estimates from QVP.

In pure uniform stratiform rain, the PVPR correction method is highly effective in mitigating the enhanced Z_H within the BB and increasing the weak Z_H above the ML at any

given elevation angle. Similar patterns are observed in the Z_H fields across different elevation scans, indicating the possibility of integrating data from the lowest antenna tilts to ensure an optimal quality of Z_H for conversion to rain rate. Furthermore, the PVPR-corrected $R(Z_h)$ retrieval demonstrates noticeable advantages, with the highest CC values reaching about 0.8, over other existing techniques, e.g., the hydrometeor-type-specific $R(Z_h)$ retrieval introduced by Giangrande and Ryzhkov (2008) and the polarimetric snowfall retrieval presented in this study.

However, the PVPR correction method encounters difficulties in situations where the current MLDA cannot accurately estimate the BB-contaminated areas. This is particularly true when the height of the ML significantly varies with azimuth, or when a convective cell penetrates the estimated BB zone. The latter case occurs because the C-band ρ_{HV} values drop during intense convection, similar to the behavior of mixtures within the ML. To handle the tilted ML issue, sector-specific QVP, which provides highly-resolved initial estimates of the BB range, is recommended. As for the problem with embedded convection, a new HCA is required to differentiate convective cores from the ML. These modifications will enable the extension of the PVPR correction method to more heterogeneous scenarios. Finally, it is suggested to perform the PVPR correction based on the QVP statistics at C-band to better represent the BB features at this frequency.

Snowfall estimation

In the absence of the ML, the PVPR correction method loses its utility. Furthermore, traditional $S(Z_h)$ relations suffer from great uncertainties due to their large sensitivity to the PSD variability. Bukovčić et al. (2020) thereby proposed a generalized $S(Z_h, K_{DP})$ relationship, which dynamically includes changes in the shape and orientation of snowflakes and ice crystals. In this study, its first application to C-band radar data is discussed, resulting in considerably increased CC values by up to 0.15 compared to the Z_h-based retrieval and RY. Additionally, the enhanced precipitation band within the DGL, where ice is generated, can only be observed from the QVP of $S(Z_h, K_{DP})$. An analysis of QPE performance with respect to height reveals that $S(Z_h, K_{DP})$ surpasses $S(Z_h)$ at high altitudes, while $S(Z_h)$ produces smaller errors than $S(Z_h, K_{DP})$ at low altitudes where K_{DP} is less reliable. Therefore, a height-dependent combination of $S(Z_h)$ and $S(Z_h, K_{DP})$ is recommended, which offers new insights into improved QPE in snow.

The ultimate objective of this research is to develop a robust and operational QPE algorithm that maximizes the benefits of A in synergistic use with K_{DP} and Z_h for C-band radar networks. The study has provided valuable outcomes and findings that contribute to this development. Currently, the proposed QPE algorithms are being integrated into the DWD software framework "Polarimetric Radar Algorithms (POLARA)" under the program "Near-Realtime Quantitative Precipitation Estimation and Prediction (RealPEP)". As the presented results are based on a limited number of case studies, a comprehensive evaluation of the algorithms will soon follow, using an extended database covering a more diverse range of rain types in POLARA. This evaluation will ensure the practical implementation of the algorithms and facilitate their future use with a positive impact on various applications, including weather nowcasting, flood forecasting, agriculture, hydrology, and disaster management.

List of Abbreviations

2DVD	2-Dimensional Video Disdrometer	61
AI	Artificial Intelligence	22
AVPR	Apparent Vertical Profile of Reflectivity	21
BB	Bright Band	3
BOO	the BOOstedt radar	23
BoXPol	a local Polarimetric Doppler X-band radar from the University of Bonn, Germany	96
CAPPI	Constant Altitude Plan Position Indicator	84
CC	Pearson's Correlation Coefficient (specifically refers to the evaluation of precipitation estimation)	64
CDC	German Climate Data Center	62
CPEX-LAB	LABoratory for Clouds and Precipitation EXploration in Germany	30
CVP	Columnar Vertical Profile	95
DGL	Dendritic Growth Layer	62
DSD	Drop Size Distribution	1
DWD	German Meteorological Service (Deutscher WetterDienst)	1
EIS	the EISberg radar	23
ESS	the ESSen radar	23
FBG	the FeldBerG radar	71
FLD	the FLechtDorf radar	46
HCA	Hydrometeor Classification Algorithm	20
HNR	the HanNoveR radar	23
HS	Hot Spot (convective cell)	15
IDW	Inverse Distance Weighting	48
ISN	the ISeN radar	23
JuXPol	a local Polarimetric Doppler X-band radar located about 6 km east of the city center of Jülich, Germany	30
LPM	Thies Clima Laser Precipitation Monitor disdrometer	23
MEM	the MEMmingen radar	23
ML	Melting Layer	1
MLDA	Melting Layer Detection Algorithm	60
MRMS	an operational Multi-Radar Multi-Sensor system in the U.S.A.	62
MRR	Micro Rain Radar	26
MSL	Mean Sea Level	7
NB	Normalized Bias	75
NBF	Non-uniform Beam Filling	11
NEU	the NEUhaus radar	36
NHB	the NeuHeilenBach radar	30
NMB	Normalized Mean Bias	64
NRMSE	Normalized Root-Mean-Square Error	64
NSSL	National Severe Storms Laboratory in the U.S.A.	8
OFT	the OfFenThal radar	36
OHS	Outside Hot Spot (convective cell)	15
PBB	Partial Beam Blockage	1
POLARA	POLArimetric Radar Algorithm	105
PPI	Plan Position Indicator	14

PRO	the PRÖtzel radar	81
PSD	ice Particle Size Distributions	1
PVPR	Polarimetric Vertical Profile of Reflectivity	1-2
QPE	Quantitative Precipitation Estimation	1
QVP	Quasi-Vertical Profile	39
RADOLAN	the operational German radar-based and gauge-adjusted quantitative precipitation estimation products (RADar-OnLine-ANeichung)	1
RealPEP	a research program named “near-Realtime quantitative Precipitation Estimation and Prediction”	105
RD-QVP	Range-Defined Quasi-Vertical Profile	21
RHI	Range Height Indicator	30
ROS	the ROStock radar	71
SWE	Snow Water Equivalent	7
UMD	the UmMenDorf radar	42
VIL	Vertical Integrated Liquid	21-22
VP	Vertical Profile	1
VPR	Vertical Profile of Reflectivity	3
WRADLIB	an open-source LIBrary for Weather RADar data processing	64
ZPHI	an attenuation correction algorithm for measured reflectivity Z using the total constraint differential phase shift Φ_{DP}	2

List of Symbols

α	attenuation parameter, a ratio of A to K_{DP}	dB deg^{-1}	2
$\langle\alpha\rangle$	net α within a rainy segment or ray	dB deg^{-1}	43
α_0	α in rain	dB deg^{-1}	14
$\alpha_{H/V}$	attenuation parameter, a ratio of A_H or A_V to K_{DP}	dB deg^{-1}	32
β	attenuation parameter, a ratio of A_{DP} to K_{DP}	dB deg^{-1}	15
β_{ML}	vertical gradient of Z_H above the melting layer	dB km^{-1}	55
δ	backscatter differential phase	degree	10
λ	radar wavelength	mm	8
Λ	slope of the exponential raindrop size distribution	mm^{-1}	5
μ	shape parameter of the Gamma raindrop size distribution		5-6
ρ_i	density of solid ice	g cm^{-3}	8
ρ_s	density of ice crystals or snowflakes	g cm^{-3}	7
ρ_w	density of water	g cm^{-3}	6
ρ_{HV}	co-polar correlation coefficient		11
ρ_{HV}^{i}	intrinsic co-polar correlation coefficient		56-57
ρ_{HV}^{min}	minimum co-polar correlation coefficient within the ML		55
$\rho_{HV}^{obs.}$	radar-observed co-polar correlation coefficient		17
$\rho_{HV}^{s.obs.}$	simulated observed co-polar correlation coefficient		56
σ	width of the canting angle distribution	radian	10
$\sigma(G)$	standard deviation of G_i	mm h^{-1}	64
φ_{DP}	propagation differential phase	degree	10
Φ_{DP}	differential phase shift	degree	2
$\Phi_{DP}^{cal.}$	calculated differential phase shift from Z_h	degree	13
Φ_{DP}^{r}	received system differential phase	degree	56-57
Φ_{DP}^{t}	transmitted system differential phase	degree	56-57
$\Phi_{H/V}$	cumulative phase shift at horizontal or vertical polarization	degree	10
ar	aspect ratio of hydrometeor		10
A	specific attenuation	dB km^{-1}	1
A_{DP}	specific differential attenuation	dB km^{-1}	12
$A_{H/V}$	specific attenuation at horizontal or vertical polarization	dB km^{-1}	12
$A_{H/V}^{\langle\alpha\rangle}$	specific attenuation derived using $\langle\alpha\rangle$ and segment-wise integration in the ZPHI method	dB km^{-1}	65
$A_{H/V}^{adj.}$	specific attenuation derived using scan-wise adjusted $\alpha_{H/V}$ values and ray-wise integration in the ZPHI method	dB km^{-1}	64
$A_{H/V}^{\langle adj.\rangle}$	specific attenuation derived using scan-wise adjusted $\alpha_{H/V}$ values and segment-wise integration in the ZPHI method	dB km^{-1}	65
$A_{H/V}^{fix.}$	specific attenuation derived using fixed values of $\alpha_{H/V}$ and ray-wise integration in the ZPHI method	dB km^{-1}	64
C	noise level	dB	17
dr	radial resolution of radar beams	km	60
D	hydrometeor diameter	mm	5
D_m	mass-weighted mean diameter	mm	6
D_{max}	maximum diameter of hydrometeor	mm	5

D_{min}	minimum diameter of hydrometeor	mm	5
F_o	orientation factor of spheroidal particle		10
$\bar{G}$	mean value of G_i	mm h^{-1}	64
G_i	gauge/disdrometer-observed precipitation sum at the i^{th} station	mm h^{-1}	64
H_0	first guess of H_b defined based on the QVP of ρ_{HV}		60
H_b	bottom height of the ML		10
H_t	top height of the ML		32
ΔH	ML depth, $H_t - H_b$		55
i_{min}	possibly lowest point of r_b	km	60
i_{max}	possibly highest point of r_t	km	60
$I(r_v, r_0)$	illumination function		56
IWC	ice water content	g m^{-3}	7
k	dielectric constant factor		8
k_i	dielectric constant factor of solid ice		8
k_w	dielectric constant factor for water		8
K_{DP}	specific differential phase	deg km^{-1}	1
K_H	Z_{DR} slope with respect to Z_H	dB dBZ^{-1}	40
$L_{a.b}$	shape factors of spheroidal particle		10
$L_{dr}^{i.}$	intrinsic linear depolarization ratio	linear units	56-57
L_{DR}	linear depolarization ratio	dBZ	12
LWC	liquid water content	g m^{-3}	6
N	total number of QPE-gauge/disdrometer pairs compared		64
$N(D)$	drop size distribution, volume density of drops per unit drop diameter	$m^{-3}mm^{-1}$	5
N_0	intercept parameter of the exponential and gamma size distribution of raindrops	$m^{-3}mm^{-1}$	5
N_i	normalized ice particle size distribution	$m^{-3}mm^{-1}$	7
N_w	normalized raindrop size distribution	$m^{-3}mm^{-1}$	6
P	measured atmospheric pressures	mb	7
P_0	atmospheric pressures at MSL	mb	7
PIA	two-way path-integrated specific attenuation in rain	dB	14
PIA_{HS}	two-way path-integrated specific attenuation in rain mixed with hail	dB	15
PIA_{DP}	two-way path-integrated specific differential attenuation	dB	15
r	range distance from the radar to scatter	km	11
r_0	range distance from the radar to the center of a radar beam volume	km	56
r_b	distance to the starting point of the $\rho_{HV}^{s.obs.}$ dip (< 0.975) caused by the ML	km	57
r_t	distance to the endpoint of the $\rho_{HV}^{s.obs.}$ dip (< 0.975) caused by the ML	km	57
r_v	range distance from the radar to any point within a beam volume	km	56
R	rain rate	mm h^{-1}	1, 5
$\bar{R}$	mean value of R_i	mm h^{-1}	64
R_i	radar-estimated precipitation sum at the i^{th} station	mm h^{-1}	64
$R_{HV}^{i.}$	intrinsic complex covariance		56
$R_{HV}^{s.obs.}$	simulated observed complex covariance		56
s	slant range	km	14
snr	signal-to-noise ratio	linear units	17

S	liquid equivalent snowfall rate	mm h^{-1}	2, 7
$S_{HH/VV}$	co-polar backscatter coefficient at horizontal or vertical polarization		8, 9
S_{HV}	cross-polar scatterers with the transmission at horizontal polarization and reception at vertical one		12
S_{ML}	melting layer strength		57
SNR	signal-to-noise ratio	dB	14
V_T	fall velocity of hydrometeor	m s^{-1}	23
V_{Ts}	fall velocity of snowflakes	m s^{-1}	7
$V_T^{exp.}$	expected fall velocity of raindrops	m s^{-1}	25
W	Doppler velocity	m s^{-1}	17
Z	reflectivity factor		1
Z_a	measured, uncorrected apparent Z_h or Z_v	mm^6m^{-3}	14
Z_{dr}	differential reflectivity	linear units	9
Z_{dr}^i	intrinsic differential reflectivity	linear units	56
$Z_{h/v}$	reflectivity factors at horizontal or vertical polarization	mm^6m^{-3}	1, 9
$Z_{h/v}^i$	intrinsic (true) reflectivity factors at horizontal or vertical polarization	mm^6m^{-3}	56
$Z_{h/v}^{s.obs.}$	simulated observed reflectivity factors at horizontal or vertical polarization	mm^6m^{-3}	56
Z_{DR}	differential reflectivity	dB	1
$Z_{DR}^{obs.}$	radar-observed differential reflectivity	dB	15
Z_{DR}^{max}	maximum differential reflectivity within the ML	dB	56
Z_{DR}^{rain}	differential reflectivity in rain below the ML	dB	56
Z_{DR}^{snow}	differential reflectivity in snow right above the ML	dB	56
$Z_{H/V}$	reflectivity factors at horizontal or vertical polarization	dBZ	8, 9
Z_H^{max}	maximum reflectivity at horizontal polarization within the ML	dBZ	55
$Z_H^{obs.}$	radar-observed reflectivity at horizontal polarization	dBZ	61
Z_H^{offset}	offset of reflectivity at horizontal polarization	dBZ	13
Z_H^{rain}	reflectivity at horizontal polarization in rain below the ML	dBZ	55
Z_H^{snow}	reflectivity at horizontal polarization in snow right above the ML	dBZ	55
$Z_H^{vp.bias}$	reflectivity biases caused by BB contamination and beam-broadening effects relative to the intrinsic Z_H	dBZ	54
$Z_H^{vp.cor.}$	reflectivity with the PVPR correction	dBZ	60-61
ΔZ_H^{ML}	reflectivity difference between Z_H^{max} and Z_H^{rain}	dBZ	55

List of Figures

List of Tables

Bibliography

Anagnostou, M., J. Kalogiros, E. Anagnostou, M. Tarolli, A. Papadopoulos, and M. Borga, 2010: Performance evaluation of high-resolution estimation from X-band dual-polarization radar for flash flood applications in mountainous basins. *J. Hydrology*, **394**, 4-16, https://doi.org/10.1016/j.jhydrol.2010.06.026.

Andrieu, H., and J. D. Creutin, 1995: Identification of vertical profiles of radar reflectivity for hydrological applications using an inverse method. Part I: Formulation. *J. Appl. Meteor.*, **34**, 225-239, https://doi.org/10.1175/1520-0450(1995)034,0225:IOVPOR.2.0.CO;2.

Antonini, A., S. Melani, M. Corongiu, S. Romanelli, A. Mazza, A. Ortolani, and B. Gozzini, 2017: On the implementation of a regional X-band weather radar network. *Atmosphere*, **8**, 25, https://doi.org/10.3390/atmos8020025.

Atlas, D., and C. Ulbrich, 1977: Path- and area-integrated rainfall measurements by microwave attenuation in the 1-3 cm band. *J. Appl. Meteor.*, **16**, 1322-1331, https://doi.org/10.1175/1520-0450(1977)016,1322:PAAIRM.2.0.CO;2.

——, 2002: Radar calibration. *Bull. Amer. Meteor. Soc.*, **83**, 1313-1316, https://doi.org/10.1175/1520-0477-83.9.1313.

Aydin, K., T. Seliga, and V. Balaji, 1986: Remote sensing of hail with a dual linear polarization radar. *J. Clim. Appl. Meteorol.*, **25**, 1475-1484, https://doi.org/10.1175/1520-0450(1986)025<1475:RSOHWA>2.0.CO;2.

——, and Y. Zhao, 1990: A computational study of polarimetric radar observables in hail. *IEEE Trans. Geosci. Remote Sens.*, **28**, 412-422, https://doi.org/10.1109/TGRS.1990.572906.

——, V. Giridhar, and Y. Zhao, 1991: Polarimetric C-band radar observables in melting hail: A computational study. Preprints, *25th Int. Conf. on Radar Meteorology*, Paris, France, Amer. Meteor. Soc., 733-736.

Balakrishnan, N., and D. S. Zrnić, 1990: Use of polarization to characterize precipitation and discriminate large hail. *J. Atmos. Sci.*, **47**, 1525-1540, https://doi.org/10.1175/1520-0469(1990)047<1525:UOPTCP>2.0.CO;2.

Bartels, H., E. Weigl, T. Reich, P. Lang, A. Wagner, O. Kohler, and N. Gerlach, 2004: Projekt RADOLAN–Routinever fahren zur Online-Aneichung der Radarniederschlagsdaten mit Hilfe von automatischen Bodenniederschlagsstationen (Ombrometer). Tech. Rep., Deutscher Wetterdienst, Abteilung Hydrometeorologie, 111 pp.

Battan, L. J., 1973: *Radar Observation of the Atmosphere*. University of Chicago Press, 324 pp.

Bechini, R., R. Cremonini, E. Gorgucci, L. Baldini, 2006: Dual-pol radar calibration and correction of the bias introduced by nonuniform radome wetting. *4th European Conf. on Radar in Meteorology and Hydrology*, Barcelona, Spain, ERAD, 593-596.

Bellon, A., I. Zawadzki, and F. Fabry, 1997; Measurements of melting layer attenuation at X-band frequencies. *Radio Sci.*, **32**, 943-955, https://doi.org/10.1029/97RS00492.

Berndt, C., E. Rabiei, and U. Haberlandt, 2014: Geostatistical merging of rain gauge and radar data for high temporal resolutions and various station density scenarios. *J. Hydrol.*, **508**, 88-101, https://doi.org/10.1016/j.jhydrol.2013.10.028.

Bloemink, H. I., and E. Lanzinger, 2005: Precipitation type from the Thies disdrometer. *WMO Tech. Conf. on Meteorological and Environmental Instruments and Methods of Observation*, IOM Rep. 82/WMO/TD 1265, Bucharest, Romania, WMO, 3 pp.

Boodoo, S., D. Hudak, A. V. Ryzhkov, P. Zhang, N. Donaldson, D. Sills, and J. Reid, 2015: Quantitative precipitation estimation from a C-band dual-polarized radar for the 8 July 2013 flood in Toronto, Canada. *J. Hydrometeor.*, **16**, 2027-2044, https://doi.org/10.1175/JHM-D-15-0003.1.

Brandes, E. A., G. Zhang, and J. Vivekanandan, 2002: Experiments in rainfall estimation with a polarimetric radar in a subtropical environment. *J. Appl. Meteor.*, **41**, 674-685, https://doi.org/10.1175/1520-0450(2002)041,0674:EIREWA.2.0.CO;2.

——, and K. Ikeda, 2004: Freezing-level estimation with polarimetric radar. *J. Appl. Meteor. Climatol.*, **43**, 1541-1553, https://doi.org/10.1175/JAM2155.1.

——, ——, G. Zhang, M. Schonhuber, and R. M. Rasmussen, 2007: A statistical and physical description of hydrometeor distributions in Colorado snowstorms using a video disdrometer. *J. Appl. Meteor. Climatol.*, **46**, 634-650, https://doi.org/10.1175/JAM2489.1.

——, ——, G. Thompson, and M. Schönhuber, 2008: Aggregate terminal velocity/temperature relations. *J. Appl. Meteor. Climatol.*, **47**, 2729-2736, https://doi.org/10.1175/2008JAMC1869.1.

Bringi, V. N., T. A. Seliga, and W. A. Cooper, 1984: Analysis of aircraft hydrometeor spectra and differential reflectivity (Z_{DR}) radar measurements during the cooperative convective precipitation experiment. *Radio Sci.*, **19**, 157-167, https://doi.org/10.1029/RS019i001p00157.

——, and V. Chandrasekar, 2001: *Polarimetric Doppler Weather Radar: Principles and Applications*. Cambridge University Press, 636pp.

——, ——, J. Hubbert, E. Gorgucci, W. L. Randeu, and M. Schoenhuber, 2003: Raindrop size distribution in different climatic regimes from disdrometer and dual-polarized radar analysis. *J. Atmos. Sci.*, **60**, 354-365, https://doi.org/10.1175/1520-0469(2003)060<0354:RSDIDC>2.0.CO;2.

——, K. Mishra, and M. Thurai, 2023: *Advances in weather and applications*. IET press. Manuscript under review.

Bukovčić, P., A. V. Ryzhkov, D. S. Zrnić, and G. Zhang, 2018: Polarimetric radar relations for quantification of snow based on disdrometer data. *J. Appl. Meteor. Climatol.*, **57**, 103-120, https://doi.org/10.1175/JAMC-D-17-0090.1.

——, ——, and ——, 2020: Polarimetric relations for snow estimation—radar verification. *J. Appl. Meteor. Climatol.*, **59**, 991-1009, https://doi.org/10.1175/JAMC-D-19-0140.1.

Cao, Q., G. Zhang, E. Brandes, T. Schuur, A. V. Ryzhkov, and K. Ikeda, 2008: Analysis of video disdrometer and polarimetric radar data to characterize rain microphysics in Oklahoma. *J. Appl. Meteor. Climatol.*, **47**, 2238-2255, https://doi.org/10.1175/2008JAMC1732.1.

Carey, L. D., and W. A. Petersen, 2015: Sensitivity of C-band polarimetric radar-based drop size estimates to maximum diameter. *J. Appl. Meteor. Climatol.*, **54**, 1352-1371, https://doi.org/10.1175/JAMC-D-14-0079.1.

Chandrasekar, V., L. Baldini, N. Bharadwaj and P. L. Smith, 2015: Calibration procedures for global precipitation-measurement ground-validation radars. *Radio Sci. Bull.*, **2015**, 45-73, https://doi.org/10.23919/URSIRSB.2015.7909473.

Chang, W.-Y., J. Vivekanandan, K. Ikeda, and P.-L. Lin, 2016: Quantitative precipitation estimation of the Epic 2013 Colorado flood event: Polarization radar-based variational scheme. *J. Appl. Meteorol. Clim.*, **55**, 1477-1495, https://doi.org/10.1175/JAMC-D-15-0222.1.

Chen, R., Z. Li, R. J. Kuligowski, R. Ferraro, and F. Weng, 2011: A study of warm rain detection using A-Train satellite data. *Geophys. Res. Lett.*, **38**, L04804, https://doi.org/10.1029/2010GL046217.

Chen, B., J. Yang, and J. Pu, 2013: Statistical characteristics of raindrop size distribution in the Meiyu season observed in eastern China, *J. Meteorol. Soc. Jpn.*, **91**, 215-227, https://doi.org/10.2151/jmsj.2013-208.

Chen, H., R. Cifelli, and A. B. White, 2020: Improving operational radar rainfall estimates using profiler observations over complex terrain in Northern California. *IEEE Trans. Geosci. Remote Sens.*, **58**, 1821-1832, https://doi.org/10.1109/TGRS.2019.2949214.

Chen, J.-Y., S. Trömel, A. V. Ryzhkov, and C. Simmer, 2021a: Assessing the benefits of specific attenuation for quantitative precipitation estimation with a C-band radar network. *J. Hydrometeor.*, **22**, 2617-2631, https://doi.org/10.1175/JHM-D-20-0299.1.

——, W.-Y. Chang, P.-L. Chang, 2021b: A synthetic quantitative precipitation estimation by integrating S- and C-band dual-polarization radars over northern Taiwan. *Remote Sens.*, **13**, 154, https://doi.org/10.3390/rs13010154.

——, R. Reinoso-Rondinel, S. Trömel, C. Simmer, and A. V. Ryzhkov, 2022: A radar-based quantitative precipitation estimation algorithm to overcome the impact of vertical gradients of warm-rain precipitation: the flood in western Germany on 14 July 2021. *J. Hydrometeor.*, https://doi.org/10.1175/JHM-D-22-0111.1, in press.

Clark, R. A., Y. J. Canipe, and D. R. Greene, 1972: Applications of digital radar data in both meteorology and hydrology. *Bull. Amer. Meteor. Soc.*, **53**, 687, https://doi.org/10.1175/1520-0477-53.7.677.

Cocks, S., A. V. Ryzhkov, P. Zhang, Y. Wang, J. Zhang, K. Howard, 2017: Precipitation rate estimation based on specific attenuation: Validation using WSR-88D dual-pol radars. 2017 *International Symposium on Weather Radar and Hydrology*, Seoul, Korea, WRaH.

Cooper, S. J., N. B. Wood, and T. S. L'Ecuyer, 2017: A variational technique to estimate snowfall rate from coincident radar, snowflake, and fall-speed observations, *Atmos. Meas. Tech.*, **10**, 2557-2571, https://doi.org/10.5194/amt-10-2557-2017.

Delanoë, J., A. Protat, J. Testud, D. Bouniol, A. J. Heymsfield, A. Bansemer, P. R. A. Brown, and R. M. Forbes, 2005: Statistical properties of the normalized ice particle size distribution, *J. Geophys. Res.*, **110**, D10201, https://doi.org/10.1029/2004JD005405.

——, A. J. Heymsfield, A. Protat, A. Bansemer, and R. J. Hogan, 2014: Normalized particle size distribution for remote sensing application, *J. Geophys. Res. Atmos.*, **119**, 4204- 4227, https://doi.org/10.1002/2013JD020700.

Diederich, M., A. V. Ryzhkov, C. Simmer, P. Zhang, and S. Trömel, 2015a: Use of specific attenuation for rainfall measurement at X-band radar wavelengths. Part I: Radar calibration and partial beam blockage estimation. *J. Hydrometeor.*, **16**, 487-502, https://doi.org/10.1175/JHM-D-14-0066.1.

——, ——, ——, ——, and ——, 2015b: Use of specific attenuation for rainfall measurement at X-band radar wavelengths. Part II: Rainfall estimates and comparison with rain gauges. *J. Hydrometeor.*, **16**, 503-516, https://doi.org/10.1175/JHM-D-14-0067.1.

Doviak, R. J., V. N. Bringi, A. V. Ryzhkov, A. Zahrai, and D. S. Zrnić, 2000: Considerations for polarimetric upgrades to operational WSR-88D radars. *J. Atmos. Oceanic Technol.*, **17**, 257-278, https://doi.org/10.1175/1520-0426(2000)017<0257:CFPUTO>2.0.CO;2.

——, and D. S. Zrnic, 2006: *Doppler Radar and Weather Observations* (2nd ed.). Dover, 562pp.

Eddy, M., and M. Specia, 2021: Hundreds missing in Europe floods are safe, even as death toll rises. The New York Times, 19 July, https://www.nytimes.com/2021/07/19/world/europe/europe-floods-germany-belgium.html.

Fabry, F., and W. Szyrmer, 1999: Modeling of the melting layer. Part II: Electromagnetic. *J. Atmos. Sci.*, **56**, 3593-3600, https://doi.org/10.1175/1520-0469(1999)056<3593:MOTMLP>2.0.CO;2.

Fehlmann, M., M. Rohrer, A. von Lerber, and M. Stoffel, 2020: Automated precipitation monitoring with the Thies disdrometer: Biases and ways for improvement. *Atmos. Meas. Tech.*, **13**, 4683-4698, https://doi.org/10.5194/amt-13-4683-2020.

Figueras i Ventura, J., and P. Tabary, 2013: The new French operational polarimetric radar rainfall rate product. *J. Appl. Meteor. Climatol.*, **52**, 1817-1835, https://doi.org/10.1175/JAMC-D-12-0179.1.

Frech, M., 2009: The effect of a wet radome on dualpol data quality. 34th *Int. Conf. on Radar Meteorology*, Wiliamsburg, VA, Amer. Meteor. Soc., P13.15.

Gatlin, P. N., M. Thurai, V. N. Bringi, W. Petersen, D. Wolff, A. Tokay, L. Carey, and M. Wingo, 2015: Searching for large raindrops: A global summary of two-dimensional video disdrometer observations. *J. Appl. Meteor. Climatol.*, **54**, 1069-1089, https://doi.org/10.1175/JAMC-D-14-0089.1.

Gehring, J., A. Ferrone, A.-C. Billault-Roux, N. Besic, K. D. Ahn, G. Lee, and A. Berne, 2021: Radar and ground-level measurements of precipitation collected by the École Polytechnique Fédérale de Lausanne during the International Collaborative Experiments for PyeongChang 2018 Olympic and Paralympic winter games, *Earth Syst. Sci. Data*, **13**, 417-433, https://doi.org/10.5194/essd-13-417-2021.

Germann, U., and J. Joss, 2002: Mesobeta profiles to extrapolate radar precipitation measurements above the Alps to the ground level. *J. Appl. Meteor. Climatol.*, **41**, 542-557, https://doi.org/10.1175/1520-0450(2002)041<0542:MPTERP>2.0.CO;2.

Giangrande, S. E., and A. V. Ryzhkov, 2008: Estimation of rainfall based on the results of polarimetric echo classification. *J. Appl. Meteor. Climatol.*, **47**, 2445-2462, https://doi.org/10.1175/2008JAMC1753.1.

——, R. McGraw, and L. Lei, 2013: An application of linear programming to polarimetric radar differential phase processing. *J. Atmos. Oceanic Technol.*, **30**, 1716-1729, https://doi.org/10.1175/JTECH-D-12-00147.1.

——, S. Collis, A. Theisen, and A. Tokay, 2014: Precipitation estimation from the ARM distributed radar network during the MC3E campaign. *J. Appl. Meteor. Climatol.*, **53**, 2130-2147, https://doi.org/10.1175/JAMC-D-13-0321.1.

Goddard, J., J. Tan, and M. Thurai, 1994: Technique for calibration of meteorological radars using differential phase. *Electron. Lett.*, **30**, 166-167, https://doi.org/10.1049/el:19940119.

Gorgucci, E., G. Scarchilli, and V. Chandrasekar, 1992: Calibration of radars using polarimetric techniques. *IEEE Trans. Geosci. Remote Sens.*, **30**, 853-858, https://doi.org/10.1109/36.175319.

——, ——, and ——, 1999: A procedure to calibrate multiparameter weather radar using properties of the rain medium. *IEEE Trans. Geosci. Remote Sens.*, **37**, 269-276, https://doi.org/10.1109/36.739161.

Gou, Y., and H. Chen, 2021: Combining radar attenuation and partial beam blockage corrections for improved quantitative application. *J. Hydrometeor.*, **22**, 139-153, https://doi.org/10.1175/JHM-D-20-0121.1.

Gourley, J. J., A. J. Illingworth, and P. Tabary, 2009: Absolute calibration of radar reflectivity using redundancy of the polarization observations and implied constraints on drop shapes. *J. Atmos. Oceanic Technol.*, **26**, 689-703, https://doi.org/10.1175/2008JTECHA1152.1.

Grams, H. M., J. Zhang, and K. L. Elmore, 2014: Automated identification of enhanced rainfall rates using the near-storm environment for radar precipitation estimates. *J. Hydrometeor.*, **15**, 1238-1254, https://doi.org/10.1175/JHM-D-13-042.1.

Griffin, E. M., T. J. Schuur, and A. V. Ryzhkov, 2020: A polarimetric radar analysis of ice microphysical processes in melting layers of winter storms using S-band quasi-vertical profiles. *J. Appl. Meteor. Climatol.*, **59**, 751-767, https://doi.org/10.1175/JAMC-D-19-0128.1.

Gu, J., A. V. Ryzhkov, P. Zhang, P. Neilley, M. Knight, B. Wolf, and D. Lee, 2011: Polarimetric attenuation correction in heavy rain at C Band. *J. Appl. Meteor. Climatol.*, **50**, 39-58, https://doi.org/10.1175/2010JAMC2258.1.

Gunn, K. L. S., and J. S. Marshall, 1955: The effect of wind shear on falling precipitation. *J. Atmos. Sci.*, **12**, 339-349, https://doi.org/10.1175/1520-0469(1955)012<0339:TEOWSO>2.0.CO;2.

Habib, E., W. F. Krajewski, and A. Kruger, 2001: Sampling errors of tipping-bucket raingauge measurements. *J. Hydrol. Eng.*, **6(2)**, 159-166, https://doi.org/10.1061/(ASCE)1084-0699(2001)6:2(159).

Hassan, D., P. A. Taylor, and G. A. Isaac, 2017: Snowfall rate estimation using C-band polarimetric radars. *Meteor. Appl.*, 24, 142-156, https://doi.org/10.1002/met.1613.

——, G. A. Isaac, P. A. Taylor, D. Michelson, 2022: Optimizing radar-based rainfall estimation using machine learning models. *Remote Sens.*, **14**, 5188, https://doi.org/10.3390/rs14205188.

Heistermann, M., S. Jacobi, and T. Pfaff, 2013: Technical Note: An open source library for processing weather radar data (wradlib). *Hydrol. Earth Syst. Sci.*, **17**, 863-871, https://doi.org/10.5194/hess-17-863-2013.

Helmert, K., and Coauthors, 2014: DWDs new radar network and post-processing algorithm chain. *Proc. 8th European Conf. on Radar in Meteorology and Hydrology*, Garmisch-Partenkirchen, Germany, ERAD, 6 pp., https://www.pa.op.dlr.de/erad2014/programme/ExtendedAbstracts/237_Helmert.pdf.

Hendry, A., Y. Antar, and G. McCormick, 1987: On the relationship between the degree of preferred orientation in precipitation and dual-polarization radar echo characteristics. *Radio Sci.*, **22**, 37-50, https://doi.org/10.1029/RS022i001p00037.

Herzegh, P., and A. Jameson, 1992; Observing precipitation through dual-polarization radar measurements. *Bull. Amer. Meteor. Soc.*, **73**, 1365-1374, https://doi.org/10.1175/1520-0477(1992)073<1365:OPTDPR>2.0.CO;2.

Hiley, M. J., M. S. Kulie, and R. Bennartz, 2011: Uncertainty analysis for cloudSat snowfall retrievals. *J. Appl. Meteor. Climatol.*, **50**, 399-418, https://doi.org/10.1175/2010JAMC2505.1.

Hogan, R. J., L. Tian, P. R. A. Brown, C. D. Westbrook, A. J. Heymsfield, and J. D. Eastment, 2012: Radar scattering from ice aggregates using the horizontally aligned oblate spheroid approximation. *J. Appl. Meteor. Climatol.*, **51**, 655-671, https://doi.org/10.1175/JAMC-D-11-074.1.

Huang, G.-J., V. N. Bringi, D. Moisseev, W. Petersen, L. Bliven, and D. Hudak, 2015: Use of 2D-video disdrometer to derive mean density-size and Z_e–SR relations: Four snow cases from the light precipitation validation environment. *Atmos. Res.*, **153**, 34-48, https://doi.org/10.1016/j.atmosres.2014.07.013.

——, ——, A. Newman, G. Lee, D. Moisseev, B. Notaroš, 2019: Dual-wavelength radar technique development for snow rate estimation: A case study from GCPEx. *Atmos. Meas. Tech.*, **12**, 1409-1427, https://doi.org/10.5194/amt-12-1409-2019.

Huang, H., and Coauthors, 2018: Quantitative precipitation estimation with operational polarimetric radar measurements in southern China: A differential phase–based variational approach. *J. Atmos. Oceanic Technol.*, **35**, 1253-1271, https://doi.org/10.1175/JTECH-D-17-0142.1.

——, K. Zhao, H. Chen, D. Hu, P. Fu, Q. Lin, and Z. Yang, 2020: Improved attenuation-based radar precipitation estimation considering the azimuthal variabilities of microphysical properties. *J. Hydrometeor.*, **21**, 1605-1620, https://doi.org/10.1175/JHM-D-19-0265.1.

Hubbert, J. C., and V. N. Bringi, 1995: An iterative filtering technique for the analysis of copular differential phase and dual-frequency radar measurements. *J. Atmos. Oceanic Technol.*, **12**, 643-648, https://doi.org/10.1175/1520-0426(1995)012<0643:AIFTFT>2.0.CO;2.

——, ——, and D. Brunkow, 2003: Studies of the polarimetric covariance matrix. Part I: Calibration methodology. *J. Atmos. Oceanic Technol.*, **20**, 696-706, https://doi.org/10.1175/1520-0426(2003)20<696:SOTPCM>2.0.CO;2.

——, F. Pratte, M. Dixon, and R. Riiling, 2008: The uncertainty of Z_{DR} calibration. Preprints, *5th European Conf. on Radar in Meteorology and Hydrology*, Helsinki, Finland, ERAD, http://erad2008.fmi.fi/proceedings/extended/erad2008-0285-extended.pdf.

Hudak, D., P. Rodrigues, G.-W. Lee, A. V. Ryzhkov, F. Fabry, and N. Donaldson, 2006: Winter precipitation studies with a dual polarized C-band radar. *4th European Conf. on Radar in Meteorology and Hydrology*, Barcelona, Spain, ERAD, 9-16.

Illingworth, A. J., and T. M. Blackman, 2002: The need to represent raindrop size spectra as normalized gamma distributions for the interpretation of polarization radar observations. *J. Appl. Meteor. Climatol.*, **41**, 286-297, https://doi.org/10.1175/1520-0450(2002)041<0286:TNTRRS>2.0.CO;2.

IPCC, 2022: *Climate Change 2022: Impacts, Adaptation, and Vulnerability*. H.-O. Pörtner et al., eds., Cambridge University Press, 3056 pp., https://doi.org/10.1017/9781009325844.

Jameson, A., 1991: A comparison of microwave techniques for measuring rainfall. *J. Appl. Meteor.*, **30**, 32-54, http://www.jstor.org/stable/26185490.

Jung, S.-H., M.-K. Suk, S. Lee, Y.-A. Oh, and K. Jang 2018: Development of radar rainfall estimation system using S-band polarization weather radar network in Korea. *Hybrid Surface Rainfall, 9th Workshop of the International Precipitation Working Group*, Seoul,

Korea, HSR IPWG, https://www.isac.cnr.it/~ipwg/meetings/seoul-2018/Orals/3-7_Jung.pdf.

Kennedy, P. C., and S. A. Rutledge, 2011: S-band dual-polarization radar observations of winter storms. *J. Appl. Meteor. Climatol.*, **50**, 844-858, https://doi.org/10.1175/2010JAMC2558.1.

Kitchen, M., R. Brown, and A. G. Davies, 1994: Real-time correction of weather radar data for the effects of bright band, range and orographic growth in widespread precipitation. *Quart. J. Roy. Meteor. Soc.*, **120**, 1231-1254, https://doi.org/10.1002/qj.49712051906.

Koistinen, J., 1991: Operational correction of radar rainfall errors due to vertical reflectivity profile. Preprints, *25th Int. Conf. on Radar Meteorology*, Paris, France, Amer. Meteor. Soc., 91-94.

Korolev, A., and G. Isaac, 2003: Roundness and aspect ratio of particles in ice clouds. *J. Atmos. Sci.*, **60**, 1795-1808, https://doi.org/10.1175/1520-0469(2003)060<1795:RAAROP>2.0.CO;2.

Kulie, M. S., and R. Bennartz, 2009: Utilizing spaceborne radars to retrieve dry snowfall. *J. Appl. Meteor. Climatol.*, **48**, 2564-2580, https://doi.org/10.1175/2009JAMC2193.1.

Kumjian, M. R., and A. V. Ryzhkov, 2010: The impact of evaporation on polarimetric characteristics of rain: Theoretical model and practical implications. *J. Appl. Meteor. Climatol*, **49**, 1247-1267, http://www.jstor.org/stable/26173815.

——, and O. P. Prat, 2014: The impact of raindrop collisional processes on the polarimetric radar variables. *J. Atmos. Sci.*, **71**, 3052-3067, https://doi.org/10.1175/JAS-D-13-0357.1.

Kurri, M., and A. Huuskonen, 2008: Measurements of the transmission loss of a radome at different rain intensities. *J. Atmos. Oceanic Technol.*, **25**, 1590-1599, https://doi.org/10.1175/2008JTECHA1056.1.

Lang, T. J., D. A. Ahijevych, S. W. Nesbitt, R. E. Carbone, S. A. Rutledge, and R. Cifelli, 2007: Radar-observed characteristics of precipitating systems during NAME 2004. *J. Climate*, **20**, 1713-1733, https://doi.org/10.1175/JCLI4082.1.

Lauri, T., J. Koistinen, and D. Moisseev, 2012: Advection-based adjustment of radar measurements. *Mon. Wea. Rev.*, **140**, 1014-1022, https://doi.org/10.1175/MWR-D-11-00045.1.

Lee, J.-K., J.-H. Kim, and M.-K. Suk, 2015: Application of bias correction methods to improve the accuracy of quantitative radar rainfall in Korea. *Atmos. Meas. Tech. Discuss.*, **8**, 4011-4047, https://doi.org/10.5194/amtd-8-4011-2015.

Lee, J.-T., K.-Y. Ko, D.-I. Lee, C.-H. You, Y.-C. Liou, 2018: Enhancement of orographic precipitation in Jeju Island during the passage of Typhoon Khanun (2012), *Atmos. Res.*, **201**, 58-71, https://doi.org/10.1016/j.atmosres.2017.10.013.

Levenberg, K., 1944: A method for the solution of certain nonlinear problems in least squares. *Q. Appl. Math.*, **2**, 164-168, https://doi.org/10.1090/qam/10666.

Libatique, R., 2022: Munich Re: Natural catastrophe losses soar in 2021. Insurance Business, 10 January, https://www.insurancebusinessmag.com/uk/news/breaking-news/naturalcatastrophe-losses-soar-in-2021–munich-re-321579.aspx.

Lim, S., R. Cifelli, V. Chandrasekar, and S. Matrosov, 2013: Precipitation classification and quantification using X-band dual-polarization weather radar: Application in the Hydrometeorology Testbed. *J. Atmos. Oceanic Technol.*, **30**, 2108-2120, https://doi.org/10.1175/JTECH-D-12-00123.1.

Liu, G., 2008: Deriving snow cloud characteristics from cloudsat observations. *J. Geophys. Res.*, **113**, D00A09, https://doi.org/10.1029/2007jd009766.

Lu, Y., and J. Kumar, 2019: Convolutional neural networks for hydrometeor classification using dual polarization Doppler radars. *Int. Conf. on Data Mining Workshops*, Beijing, China, ICDMW, 288-295, https://doi.org/10.1109/ICDMW.2019.00050.

Maesaka, T., K. Iwanami, and M. Maki, 2012: Non-negative K_{DP} estimation by monotone increasing Φ_{DP} assumption below melting layer. *7th European Conf. on Radar in Meteorology and Hydrology*, Toulouse, France, ERAD, http://www.meteo.fr/cic/meetings/2012/ERAD/extended_abs/QPE_233_ext_abs.pdf.

Marshall, J. S., and W. Palmer, 1948: The distribution of raindrops with size. *J. Meteorol.*, **5**, 165-166, https://doi.org/10.1175/1520-0469(1948)005<0165:TDORWS>2.0.CO;2.

Matrosov, S. Y., D. Kingsmill, and F. Ralph, 2005a: The utility of X-band polarimetric radar for quantitative estimates of rainfall parameters. *J. Hydrometeor.*, **6**, 248-262, https://doi.org/10.1175/JHM424.1.

——, 2005b: Attenuation-based estimates of rainfall rates aloft with vertically pointing Ka-band radars. *J. Atmos. Oceanic Technol.*, **22**, 43-54, https://doi.org/10.1175/JTECH-1677.1.

——, K. A. Clark, and D. E. Kingsmill, 2007: A polarimetric radar approach to identify rain, melting-layer, and snow regions for applying corrections to vertical profiles of reflectivity. *J. Appl. Meteor. Climatol.*, **46**, 154-166, https://doi.org/10.1175/JAM2508.1.

——, C. Campbell, D. Kingsmill, and E. Sukovich, 2009: Assessing snowfall rates from X-Band radar reflectivity measurements. *J. Atmos. Oceanic Technol.*, **26**, 2324-2339, https://doi.org/10.1175/2009JTECHA1238.1.

McLaughlin, D., and Coauthors, 2009: Short-wavelength technology and the potential for distributed networks of small radar systems. *Bull. Amer. Meteor. Soc.*, **90**, 1797-1817, https://doi.org/10.1175/2009BAMS2507.1.

Melnikov, V. M., R. J. Doviak, D. S. Zrnić, and D. J. Stensrud, 2011: Mapping Bragg scatter with a polarimetric WSR-88D. *J. Atmos. Oceanic Technol.*, **28**, 1273-1285, https://doi.org/10.1175/JTECH-D-10-05048.1.

——, and J. M. Straka, 2013: Axis ratios and flutter angles of cloud ice particles: Retrievals from radar data. *J. Atmos. Oceanic Technol.*, **30**, 1691-1703, https://doi.org/10.1175/JTECH-D-12-00212.1.

——, D. S. Zrnić, A. Free, R. Ice, R. Macemon, 2017: Monitoring radar calibration using ground clutter. *NSSL internal report*, https://www.nssl.noaa.gov/publications/wsr88d_reports/Z_ZDRcal_ROC_MOU_report_2017.pdf.

Metek, 2012: *MRR physical basics*. Metek, 13 March 2012, 20 pp, https://mpimet.mpg.de/fileadmin/atmosphaere/barbados/Instrumentation/MRR-physical-basics_20090707.pdf.

Murphy, A. M., A. V. Ryzhkov, and P. Zhang, 2020: Columnar Vertical Profile (CVP) methodology for validating polarimetric radar retrievals in ice using in situ aircraft measurements. *J. Atmos. Oceanic Technol.*, **37**, 1623-1642, https://doi.org/10.1175/JTECH-D-20-0011.1.

Myhre, G., and Coauthors, 2019: Frequency of extreme precipitation increases extensively with event rareness under global warming. *Sci. Rep.*, **9**, 16063, https://doi.org/10.1038/s41598-019-52277-4.

Nissen, K. M., and U. Ulbrich, 2017: Increasing frequencies and changing characteristics of heavy precipitation events threatening infrastructure in Europe under climate change. *Nat. Hazards Earth Syst. Sci.*, **17**, 1177-1190, https://doi.org/10.5194/nhess-17-1177-2017.

Park, H. S., A. V. Ryzhkov, D. S. Zrnić, and K. Kim, 2009: The hydrometeor classification algorithm for the polarimetric WSR-88D: Description and application to an MCS. *Wea. Forecasting*, **24**, 730-748, https://doi.org/10.1175/2008WAF2222205.1.

Pejcic, V., P. S. Garfias, K. Mühlbauer, S. Trömel, and C. Simmer, 2020: Comparison between precipitation estimates of ground-based weather radar composites and GPM's DPR rainfall product over Germany. *Meteor. Z.*, **29**, 451-466, https://doi.org/10.1127/metz/2020/1039.

Penide, G., A. Protat, V. V. Kumar, and P. T. May, 2013: Comparison of two convective/stratiform precipitation classification techniques: Radar reflectivity texture versus drop size distribution–based approach. *J. Atmos. Oceanic Technol.*, **30**, 2788-2797, https://doi.org/10.1175/JTECH-D-13-00019.1.

Peters, G., B. Fischer, and M. Clemens, 2010: Rain attenuation of radar echoes considering finite-range resolution and using drop size distributions. *J. Atmos. Oceanic Technol.*, **27**, 829-842, https://doi.org/10.1175/2009JTECHA1342.1.

Picca, J. C., D. M. Schultz, B. A. Colle, S. Ganetis, D. R. Novak, and M. J. Sienkiewicz, 2014: The value of dual-polarization radar in diagnosing the complex microphysical evolution of an intense snowband, *Bull. Amer. Meteor. Soc.*, **95**, 1825-1834, https://doi.org/10.1175/BAMS-D-13-00258.1.

Porcacchia, L., P. E. Kirstetter, J. J. Gourley, V. Maggioni, B. L. Cheong, and M. N. Anagnostou, 2017: Toward a polarimetric radar classification scheme for coalescence-dominant precipitation: Application to complex terrain. *J. Hydrometeor.*, **18**, 3199-3215, https://doi.org/10.1175/JHM-D-17-0016.1.

Powell, S. W., R. A. Houze, and S. R. Brodzik, 2016: Rainfall-type categorization of radar echoes using polar coordinate reflectivity data. *J. Atmos. Oceanic Technol.*, **33**, 523-538, https://doi.org/10.1175/JTECH-D-15-0135.1.

Puca, S., and Coauthors, 2021: A slow moving upper-level low brought devastating floods to parts of north west Germany and other parts of western Europe in July 2021. EUMETSAT, 26 July, https://www.eumetsat.int/devastating-floods-western-europe.

Reimel, K. J., and M. Kumjian, 2021: Evaluation of K_{DP} estimation algorithm performance in rain using a known-truth framework. *J. Atmos. Oceanic Technol.*, **38**, 587-605, https://doi.org/10.1175/JTECH-D-20-0060.1.

Reinoso-Rondinel, R., and M. Schleiss, 2021: Quantitative evaluation of polarimetric estimates from scanning weather radars using a vertically pointing micro rain radar. *J. Atmos. Oceanic Technol.*, **38**, 481-499, https://doi.org/10.1175/JTECH-D-20-0062.1.

Rinehart, R. E., 2004: *Radar for Meteorologists*. Rinehart, 482pp.

Roberto, N., L. Baldini, E. Adirosi, L. Facheris, F. Cuccoli, A. Lupidi, A. Garzelli, 2017: A support vector machine hydrometeor classification algorithm for dual-polarization radar. *Atmosphere.*, **8**, 134, https://doi.org/10.3390/atmos8080134.

Ryzhkov, A. V., and D. S. Zrnić, 1998: Discrimination between rain and snow with a polarimetric radar. *J. Appl. Meteor.*, **37**, 1228-1240, https://doi.org/10.1175/1520-0450(1998)037<1228:DBRASW>2.0.CO;2.

——, and ——, 2005: Radar polarimetry at S, C, and X bands comparative analysis and operational implications. *32nd Int. Conf. on Radar Meteorology*, Albuquerque, NM, Amer. Meteor. Soc., 9R.3, https://ams.confex.com/ams/32Rad11Meso/techprogram/paper_95684.htm.

——, and ——, 2019: *Radar Polarimetry for Weather Observations*. Springer, 486 pp.

——, T. J. Schuur, D. W. Burgess, P. L. Heinselman, S. E. Giangrande, and D. S. Zrnić, 2005: The joint polarization experiment: Polarimetric rainfall measurements and hydrometeor classification. *Bull. Amer. Meteor. Soc.*, **86**, 809-824, https://doi.org/10.1175/BAMS-86-6-809.

——, 2007: The impact of beam broadening on the quality of radar polarimetric data. *J. Atmos. Oceanic Technol.*, **24**, 729-744, https://doi.org/10.1175/JTECH2003.1.

——, M. R. Kumjian, S. M. Ganson, and A. P. Khain, 2013a: Polarimetric radar characteristics of melting hail. Part I: Theoretical simulations using spectral microphysical modeling. *J. Appl. Meteor. Climatol.*, **52**, 2849-2870, https://doi.org/10.1175/JAMC-D-13-073.1.

——, ——, ——, and P. Zhang, 2013b: Polarimetric radar characteristics of melting hail. Part II: Practical implications. *J. Appl. Meteor. Climatol.*, **52**, 2871-2886, https://doi.org/10.1175/JAMC-D-13-074.1.

——, M. Diederich, P. Zhang, and C. Simmer, 2014: Potential utilization of specific attenuation for rainfall estimation, mitigation of partial beam blockage, and radar networking. *J. Atmos. Oceanic Technol.*, **31**, 599-619, https://doi.org/10.1175/JTECH-D-13-00038.1.

——, P. Zhang, H. Reeves, M. Kumjian, T. Tschallener, S. Trömel, and C. Simmer, 2016: Quasi-vertical profiles—A new way to look at polarimetric radar data. *J. Atmos. Oceanic Technol.*, **33**, 551-562, https://doi.org/10.1175/JTECH-D-15-0020.1.

——, ——, P. Bukovčić, J. Zhang, and S. Cocks, 2022: Polarimetric radar quantitative precipitation estimation. *Remote Sens.*, **14**, 1695, https://doi.org/10.3390/rs14071695.

——, and Coauthors, 2017: Estimation of depolarization ratio using weather radars with simultaneous transmission/reception. *J. Appl. Meteor. Climatol.*, **56**, 1797-1816, https://doi.org/10.1175/JAMC-D-16-0098.1.

——, and J. Krause, 2022: New polarimetric radar algorithm for melting layer detection and determination of its height. *J. Atmos. Ocean. Technol.*, **39**, 529-543, https://doi.org/10.1175/JTECH-D-21-0130.1.

Saadi, M., C. Furusho-Percot, A. Belleflamme, J.-Y. Chen, S. Trömel, S. Kollet, 2022: How uncertain are precipitation and peakflow estimates for the July 2021 flooding event? *Nat. Hazards Earth Syst. Sci.*, **23**, 159-177, https://doi.org/10.5194/nhess-2022-111.

Sachidananda, M., and D. S. Zrnić, 1986: Differential propagation phase shift and rainfall rate estimation. *Radio Sci.*, **21**, 235-247, https://doi.org/10.1029/RS021i002p00235.

——, and ——, 1987: Rain rate estimates from differential polarization measurements. *J. Atmos. Oceanic Technol.*, **4**, 588-598, https://doi.org/10.1175/1520-0426(1987)004<0588:RREFDP>2.0.CO;2.

Scarchilli, G., E. Gorucci, V. Chandrasekar, and T. A. Seliga, 1993: Rainfall estimation using polarimetric techniques at C-band frequencies. *J. Appl. Meteor.*, **32**, 1150-1160, https://doi.org/10.1175/1520-0450(1993)032,1150:REUPTA.2.0.CO;2.

——, ——, ——, and A. Dobaie, 1996: Self-consistency of polarization diversity measurements of rainfall. *IEEE Trans. Geosci. Remote Sens.*, **34**, 22-26, https://doi.org/10.1109/36.481887.

Schmidt, M., 2020: Improvement of hail detection and nowcasting by synergistic combination of information from polarimetric radar, model predictions, and in-situ observations. Ph.D. dissertation, Universität Bonn, 150 pp.

Schneebeli, M., J. Grazioli, and A. Berne, 2014: Improved estimation of the specific differential phase shift using a compilation of Kalman filter ensembles. *IEEE Trans. Geosci. Remote Sens.*, **52**, 5137-5149, https://doi.org/10.1109/TGRS.2013.2287017.

Sekelsky, S. M., 2002: Near-field reflectivity and antenna boresight gain corrections for millimeter-wave atmospheric radars. *J. Atmos. Oceanic Technol.*, **19**, 468-477, https://doi.org/10.1175/1520-0426(2002)019<0468:NFRAAB>2.0.CO;2.

Seliga, T. A. and V. N. Bringi, 1976: Potential use of radar differential reflectivity measurements at orthogonal polarizations for measuring precipitation. *J. Appl. Meteorol.*, **15**, 69-76, https://doi.org/10.1175/1520-0450(1976)015<0069:PUORDR>2.0.CO;2.

——, ——, and H. Al-Khatib, 1981: A preliminary study of comparative measurement of rainfall rate using the differential reflectivity radar technique and a raingauge network. *J. Appl. Meteor.*, **20**, 1362-1368, https://doi.org/10.1175/1520-0450(1981)020<1362:APSOCM>2.0.CO;2.

Seo, D., J. Breidenbach, R. Fulton, D. Miller, and T. O'Bannon, 2000: Real-time adjustment of range-dependent biases in WSR-88D rainfall estimates due to nonuniform vertical profile of reflectivity. *J. Hydrometeor.*, **1**, 222-240, https://doi.org/10.1175/1525-7541(2000)001<0222:RTAORD>2.0.CO;2.

Shakti, P. C., M. Maki, S. Shimizu, T. Maesaka, D.-S. Kim, D. I. Lee, and H. Iida, 2013: Correction of reflectivity in the presence of partial beam blockage over a mountainous region using X-band dual polarization radar. *J. Hydrometeor.*, **14**, 744-764, https://doi.org/10.1175/JHM-D-12-077.1.

Shen, Y., Y. Chen, Y. Bi, D. Lyu, H. Chen, S. Duan, 2022: Snowfall microphysics characterized by PARSIVEL disdrometer observations in Beijing from 2020 to 2022. *Remote Sens.*, **14**, 6025, https://doi.org/10.3390/rs14236025.

Siggia, A., and R. Jr. Passarelli, 2004: Gaussian model adaptive processing (GMAP) for improved ground clutter cancellation and moment calculation. *3rd European Conf. on Radar in Meteorology and Hydrology*, Visby, Island of Gotland, Sweden, ERAD, 63-73.

Steinert, J., M. Werner, and P. Tracksdorf, 2013: Hydrometeor classification and quantitative precipitation estimation from quality assured radar data for the DWD C-band weather radar network. *36th Int. Conf. on Radar Meteorology*, Breckenridge, CO, Amer. Meteor. Soc., 363, https://ams.confex.com/ams/36Radar/webprogram/Paper228477.html.

Stephan, K., S. Klink, and C. Schraff, 2008: Assimilation of radar-derived rain rates into the convective-scale model COSMO-DE at DWD. *Q.J.R. Meteorol. Soc.*, **134**, 1315-1326, https://doi.org/10.1002/qj.269.

Sun, J., 2005: Initialization and numerical forecasting of a supercell storm observed during STEPS. *Mon. Wea. Rev.*, **133**, 793-813, https://doi.org/10.1175/MWR2887.1.

Tabari, H., 2020: Climate change impact on flood and extreme precipitation increases with water availability. *Sci. Rep.*, **10**, 13768, https://doi.org/10.1038/s41598-020-70816-2.

Tao, R., K. Zhao, H. Huang, L. Wen, G. Zhang, A. Zhou, H. Chen, 2021: Snow particle size distribution from a 2-D video disdrometer and radar snowfall estimation in east China. *IEEE Trans. Geosci. Remote Sens.*, **59**, 196-207, https://doi.org/10.1109/TGRS.2020.2990920.

Testud, J., E. Le Bouar, E. Obligis, and M. Ali-Mehenni, 2000: The rain profiling algorithm applied to polarimetric weather radar. *J. Atmos. Oceanic Technol.*, **17**, 332-356, https://doi.org/10.1175/1520-0426(2000)017,0332:TRPAAT.2.0.CO;2.

——, S. Oury, R. A. Black, P. Amayenc, and X. Dou, 2001: The concept of ‘‘normalized’’ distribution to describe raindrop spectra: A tool for cloud physics and cloud remote sensing. *J. Appl. Meteor.*, **40**, 1118-1140, https://doi.org/10.1175/1520-0450(2001)040,1118:TCONDT.2.0.CO;2.

Thorndahl, S., J. E. Nielsen, M. R. Rasmussen, 2014: Bias adjustment and advection interpolation of long-term high resolution radar rainfall series. *J. Hydrol.*, **508**, 214-226, https://doi.org/10.1016/j.jhydrol.2013.10.056.

Tobin, D., and M. Kumjian, 2017: Polarimetric radar and surface-based precipitation-type observations of ice pellet to freezing rain transitions. *Wea. Forecasting*, **32**, 2065-2082, https://doi.org/10.1175/WAF-D-17-0054.1.

Tokay, A., P. G. Bashor, E. Habib, and T. Kasparis, 2008: Raindrop size distribution measurements in tropical cyclones. *Mon. Wea. Rev.*, **136**, 1669-1685, https://doi.org/10.1175/2007MWR2122.1.

——, W. A. Petersen, P. Gatlin, and M. Wingo, 2013: Comparison of raindrop size distribution measurements by collocated disdrometers. *J. Atmos. Oceanic Technol.*, **30**, 1672-1690, https://doi.org/10.1175/JTECH-D-12-00163.1.

Trömel, S., M. Kumjian, A. V. Ryzhkov, and C. Simmer, 2013: Backscatter differential phase—Estimation and variability. *J. Appl. Meteor. Climatol.*, **52**, 2529-2548, https://doi.org/10.1175/JAMC-D-13-0124.1.

——, M. Ziegert, A. V. Ryzhkov, C. Chwala, and C. Simmer, 2014a: Using microwave backhaul links to optimize the performance of algorithms for rainfall estimation and attenuation correction. *J. Atmos. Oceanic Technol.*, **31**, 1748-1760, https://doi.org/10.1175/JTECH-D-14-00016.1.

——, A. V. Ryzhkov, P. Zhang, and C. Simmer, 2014b: Investigations of backscatter differential phase in the melting layer. *J. Appl. Meteor. Climatol.*, **53**, 2344-2359, https://doi.org/10.1175/JAMCD-14-0050.1.

——, ——, B. Hickman, K. Mühlbauer, and C. Simmer, 2019: Polarimetric radar variables in the layers of melting and dendritic growth at X band—Implications for a nowcasting strategy in stratiform rain. *J. Appl. Meteor. Climatol.*, **58**, 2497-2522, https://doi.org/10.1175/JAMC-D-19-0056.1.

Ulaby, F., R. Moore, and A. Fung, 1982: *Microwave Remote Sensing: Active and Passive*. Reading: Addison – Wesley, **2**, 1064 pp.

Ulbrich, C. (1983). Natural variations in the analytical form of the raindrop size distribution. *J. Clim. Appl. Meteorol.*, **22**, 1764-1775, https://doi.org/10.1175/1520-0450(1983)022<1764:NVITAF>2.0.CO;2.

Vasiloff, S., 1997: *Interpretation of radar data during snow events in mountainous terrain*. Western Region Tech, Attachment 97-35, 16 pp, https://www.weather.gov/media/wrh/online_publications/TAs/ta9735.pdf.

Vivekanandan, J., G. Zhang, S. M. Ellis, D. Rajopadhyaya, and S. K. Avery, 2003: Radar reflectivity calibration using differential propagation phase measurement, *Radio Sci.*, **38**, 8049, https://doi.org/10.1029/2002RS002676.

von Lerber, A., D. Moisseev, L. F. Bliven, W. Petersen, A. Harri, and V. Chandrasekar, 2017: Microphysical properties of snow and their link to $Z_e - S$ relations during BAECC 2014. *J. Appl. Meteor. Climatol.*, **56**, 1561-1582, https://doi.org/10.1175/JAMC-D-16-0379.1.

Vulpiani, G., M. Montopoli, L. Delli Passeri, A. G. Gioia, P. Giordano, and F. S. Marzano, 2012: On the use of dual-polarized C-band radar for operational rainfall retrieval in mountainous areas. *J. Appl. Meteor. Climatol.*, **51**, 405-425, https://doi.org/10.1175/JAMC-D-10-05024.1.

——, L. Baldini, and N. Roberto, 2015: Characterization of Mediterranean hail-bearing storms using an operational polarimetric X-band radar. *Atmos. Meas. Tech.*, **8**, 4681-4698, https://doi.org/10.5194/amt-8-4681-2015.

Wang, Y., P. Zhang, A. V. Ryzhkov, J. Zhang, and P.-L. Chang, 2014: The application of specific attenuation for tropical rainfall estimation in complex terrain. *J. Hydrometeor.*, **15**, 2250-2266, https://doi.org/10.1175/JHM-D-14-0003.1.

——, J. Zhang, P. Zhang, A. V. Ryzhkov, and C. Fritts, 2017: The impact of different precipitation types on the polarimetric radar QPE using specific attenuation. *38th Int. Conf. on Radar Meteorology*, Chicago, IL, Amer. Meteor. Soc., 265, https://ams.confex.com/ams/38RADAR/webprogram/Paper321106.html.

——, S. Cocks, L. Tang, A. V. Ryzhkov, P. Zhang, J. Zhang, and K. Howard, 2019: A prototype quantitative precipitation estimation algorithm for operational S-Band polarimetric radar utilizing specific attenuation and specific differential phase. Part I: Algorithm description. *J. Hydrometeor.*, **20**, 985-997, https://doi.org/10.1175/JHM-D-18-0071.1.

Wang, L.-P., S. Ochoa-Rodríguez, J. V. Assel, R. D. Pina, M. Pessemier, S. Kroll, P. Willems, C. Onof, 2015: Enhancement of radar rainfall estimates for urban hydrology through optical flow temporal interpolation and Bayesian gauge-based adjustment, *J. Hydrol.*, **531**, 408-426, https://doi.org/10.1016/j.jhydrol.2015.05.049.

Wang, H., Y. Ran, Y. Deng, X. Wang, 2017: Study on deep-learning-based identification of hydrometeors observed by dual polarization Doppler weather radars. *J. Wireless Com. Network.*, **173**, https://doi.org/10.1186/s13638-017-0965-5.

Waterman, P. C., 1971: Symmetry, unitarity and geometry in electromagnetic scattering. *Phys. Rev. D*, **3**, 825-839, https://doi.org/10.1103/PhysRevD.3.825.

Wen, L., K. Zhao, G. Zhang, M. Xue, B. Z Liu, and X. Chen, 2016: Statistical characteristics of raindrop size distributions observed in East China during the Asian summer monsoon season using 2D-video disdrometer and micro-rain radar data. *J Geophysical Res: Atmospheres*, **121**, 2265-2282, https://doi.org/10.1002/2015jd024160.

Werner, 2014: A new radar data post-processing quality control workflow for the DWD weather radar network. *8th European Conf. on Radar in Meteorology and Hydrology*, Garmisch-Partenkirchen, Germany, ERAD, https://www.pa.op.dlr.de/erad2014/programme/ExtendedAbstracts/079_Werner.pdf.

——, 2017: Post processing radar data quality control at Deutscher Wetterdienst (DWD). *Weather Radar Calibration and Monitoring Workshop*, Offenbach, Germany, WXRCalMon, https://rcc.dwd.de/EN/specialusers/research_education/met_applications_specials/wxrcal

mon2017_presentations/presentation_downloads/14_mwerner_wxrcalmon2017.pdf?__blob=publicationFile&v=2.

Wolfe, J. P., and J. R. Snider, 2012: A relationship between reflectivity and snow rate for a high-altitude S-Band radar. *J. Appl. Meteor. Climatol.*, **51**, 1111-1128, https://doi.org/10.1175/JAMC-D-11-0112.1.

Xie, X., R. Evaristo, S. Troemel, P. Saavedra, C. Simmer, and A. V. Ryzhkov, 2016: Radar observation of evaporation and implications for quantitative precipitation and cooling rate estimation. *J. Atmos. Oceanic Technol.*, **33**, 1779-1792, https://doi.org/10.1175/JTECH-D-15-0244.1.

Yo, T. S., S. H. Su, J. L. Chu, C. W. Chang, H. C. Kuo, 2021: A deep learning approach to radar-based QPE. *Earth Space Sci.*, **8**, e2020EA001340, https://doi.org/10.1029/2020EA001340.

Zacharov, P., and D. Rezacova, 2010: The effect of radar-based QPE on the fractions skill score used at the QPF verification. *Adv. Geosci.*, **25**, 91-95, https://doi.org/10.5194/adgeo-25-91-2010.

Zawadzki, I., W. Szyrmer, C. Bell, and F. Fabry, 2005: Modeling of the melting layer. Part III: The density effect. *J. Atmos. Sci.*, **62**, 3705-3723, https://doi.org/10.1175/JAS3563.1.

Zhang, G., J. Vivekanandan, and E. Brandes, 2001: A method for estimating rain rate and drop size distribution from polarimetric radar measurements. *IEEE Trans. Geosci. Remote Sens.*, **39**, 830-840, https://doi.org/10.1109/36.917906.

——, 2016: *Weather Radar Polarimetry*. CRC Press. 304pp.

Zhang, J., and Y. Qi, 2010: A real-time algorithm for the correction of brightband effects in radar-derived QPE. *J. Hydrometeor.*, **11**, 1157-1171, https://doi.org/10.1175/2010JHM1201.1.

——, and Coauthors, 2016: Multi-Radar Multi-Sensor (MRMS) quantitative precipitation estimation: Initial operating capabilities. *Bull. Amer. Meteor. Soc.*, **97**, 621-638, https://doi.org/10.1175/BAMS-D-14-00174.1.

——, L. Tang, S. Cocks, P. Zhang, A. V. Ryzhkov, K. Howard, C. Langston, and B. Kaney, 2020a: A dual-polarization radar synthetic QPE for operations. *J. Hydrometeor.*, **21**, 2507-2521, https://doi.org/10.1175/JHM-D-19-0194.1.

——, ——, ——, ——, ——, 2020b: A Specific Attenuation Based Radar QPE for Operations. *Precipitation and Flash Flood Prediction from Minutes to Days*, Bonn, Germany, https://indico.scc.kit.edu/event/883/contributions/7483/attachments/3679/5423/PcpFFconf_Zhang_RAQPE.pdf.

Zhang, P., D. S. Zrnić, and A. V. Ryzhkov, 2013: Partial beam blockage correction using polarimetric radar measurements. *J. Atmos. Oceanic Technol.*, **30**, 861-872, https://doi.org/10.1175/JTECH-D-12-00075.1.

Zhang, Y., S. Bi, L. Liu, H. Chen, Y. Zhang, P. Shen, F. Yang, Y. Wang, Y. Zhang, S. Yao, 2021: Deep learning for polarimetric radar quantitative precipitation estimation during landfalling typhoons in south China. *Remote Sens.*, **13**, 3157, https://doi.org/10.3390/rs13163157.

Zhang, J., J. Xu, X. Dai, H. Ruan, X. Liu, W. Jing, 2022: Multi-source precipitation data merging for heavy rainfall events based on cokriging and machine learning methods. *Remote Sens.*, **14**, 1750, https://doi.org/10.3390/rs14071750.

Zolina, O., C. Simmer, A. Kapala, P. Shabanov, P. Becker, H. Mächel, S. Gulev, and P. Groisman, 2014: Precipitation variability and extremes in central Europe: New view from STAMMEX results. *Bull Am Meteorol Soc.*, **95(7)**, 995-1002. http://www.jstor.org/stable/26219377.

Zrnić, D. S., and A. V. Ryzhkov, 1996: Assessment of rainfall measurement that uses specific differential phase. *J. Appl. Meteor.*, **35**, 2080-2090, https://doi.org/10.1175/1520-0450(1996)035<2080:AORMTU>2.0.CO;2.

——, and ——, 1999: Polarimetry for weather surveillance radars. *Bull. Amer. Meteor. Soc.*, **80**, 389-406, https://doi.org/10.1175/1520-0477(1999)080,0389:PFWSR.2.0.CO;2.

——, T. D. Keenan, L. D. Carey, and P. May, 2000: Sensitivity analysis of polarimetric variables at a 5-cm wavelength in rain. *J. Appl. Meteor.*, **39**, 1514-1526, https://doi.org/10.1175/1520-0450(2000)039,1514:SAOPVA.2.0.CO;2.

Acknowledgments

Reflecting on the past four years, I have realized that my journey to this point may have appeared smooth sailing, but it was far from easy. Thus, I am deeply grateful to all those who supported and encouraged me along the way, helping me to reach this significant milestone in my academic career.

First and foremost, I would like to express my profound gratitude to my supervisors, Silke Trömel and Clemens Simmer, for welcoming me into the radar family and allowing me to research a topic that truly interested me. The invaluable guidance, expertise, and support from them helped me overcome numerous challenges during the course of my study. Their constructive comments and criticism were pivotal in shaping my thinking, refining my arguments, and enriching the quality of my work. They also provided me with abundant resources for participating in conferences and visiting research institutions worldwide, broadening my horizons and exposing me to new ideas.

I also extend my thanks to Alexander V. Ryzhkov for his informative insights and feedback on my study. Our discussions were always inspiring, and his enthusiasm for science was infectious. During my stay at the University of Oklahoma, he graciously hosted me and introduced me to many exceptional scientists. I particularly appreciated Pengfei Zhang and Tian-You Yu for sharing their experiences and offering me opportunities to expand my professional network.

In addition, I am indebted to the Institute for Geosciences, Department of Meteorology, University of Bonn, for their powerful IT support led by Kai Mühlbauer, as well as the helpful administrative personnel. Their assistance facilitated my research with efficiency and effectiveness.

Furthermore, I owe a debt of gratitude to my colleagues and peers who created a stimulating academic community throughout my doctoral studies. Their emotional support was also important to me, especially during the early stages of my arrival and the pandemic. Their patience and understanding allowed me to be myself even in moments of frustration. Attending conferences and social events with them was always productive and enjoyable, and I will always treasure the wonderful memories of my time in Bonn with all of them. I will miss you all!

Finally, my thanks go to the unwavering support and encouragement of my family, friends, and former supervisors, Yu-Chieng Liou and Wei-Yu Chang, from Taiwan. While they may not fully grasp the intricacies of my work, their unconditional love and belief in me have been the foundation of my success, equipping me with the strength to face more difficulties and embrace greater dreams in the future.

This study was conducted as part of Project 1 in the RealPEP research unit, which stands for Near-Realtime Quantitative Precipitation Estimation and Prediction. The project was funded by the German Research Foundation under Grant TR 1023/9-2. I acknowledge the support of the German Meteorological Service, which provided data used in the study, including disdrometer, rain gauge, and C-band dual-polarimetric radar measurements. Additionally, I express my appreciation to the Cloud and Precipitation Exploration Laboratory for providing measurements from the polarimetric X-band research radar, JuXPol.